STUDIES ON TRANSPORT AND MAGNETIC PROPERTIES OF AMBIENT PRESSURE SYNTHESIZED $NdFeAsO_{1-x}F_x$ BASED IRON PNICTIDE SUPERCONDUCTORS

Thesis submitted to the

UNIVERSITY OF KERALA

For the Award of the Degree of

DOCTOR OF PHILOSOPHY IN PHYSICS

Under the faculty of Science

By

PILLAI ASWATHY MOHAN

National Institute for Interdisciplinary Science and Technology

Council of Scientific & Industrial Research

Trivandrum, India

August 2015

DECLARATION

I, Pillai Aswathy Mohan, hereby declare that the work presented in the Ph.D. thesis entitled "***Studies on transport and magnetic properties of ambient pressure synthesized $NdFeAsO_{1-x}F_x$ based iron pnictide superconductors***" is an independent research work carried out by me for the award of degree of Doctor of Philosophy in Physics of the University of Kerala, under the guidance of Dr. U. Syamaprasad, Chief Scientist (Rtd.), Applied Superconductivity Group, Materials Science and Technology Division, CSIR - National Institute for Interdisciplinary Science and Technology (NIIST), Trivandrum. I further declare that this thesis or any part of it has not been submitted anywhere else for any other degree, diploma or other similar title.

Pillai Aswathy Mohan

Place : Trivandrum

Date : 25-08-2015

COUNCIL OF SCIENTIFIC & INDUSTRIAL RESEARCH
NATIONAL INSTITUTE FOR INTERDISCIPLINARY SCIENCE AND TECHNOLOGY
(CSIR-NIIST)
Industrial Estate P.O., Pappanamcode,
Trivandrum - 695 019
Kerala, INDIA

ISO 9001 REGISTERED
DNV Certification B.V., The Netherlands

Dr. U. Syamaprasad
Chief Scientist (Rtd.)
Materials Science and Technology Division

Tel: 91-471-2741830
Fax: +91-471-2491712
E-mail: syamcsir@gmail.com

CERTIFICATE

Certified that the work embodied in the thesis entitled, "***Studies on transport and magnetic properties of ambient pressure synthesized $NdFeAsO_{1-x}F_x$ based iron pnictide superconductors***" is an authentic record of the research work carried out by Ms. Pillai Aswathy Mohan, Applied Superconductivity Group, Materials Science and Technology Division, CSIR - National Institute for Interdisciplinary Science and Technology (NIIST), Trivandrum, under my supervision in partial fulfillment of the requirement for the degree of Doctor of Philosophy of the University of Kerala. It is further certified that no part of this thesis has been presented previously anywhere else for the award of any other degree.

U. Syamaprasad

(Research Guide)

Place : Trivandrum

Date : 25-08-2015

Acknowledgements

With great pleasure and humility let me acknowledge all those who helped me in achieving all that I wanted to. I would like to thank the Almighty for giving me a wonderful family who have always understood the meaning of every flicker of my mind and helped me in differentiating between the good and the bad. I commemorate the blessings of my father Late Mr. S. Mohanan Pillai and the unconditional love he gave me till the last breath of his life. My mother is my constant source of inspiration, driving force, role model and my first teacher; my vocabulary won't be adequate to thank her enough. My uncle (Valyachan), Late Mr. Nagappan Nair was the person who took a fatherly responsibility after the untimely demise of my father and extended timely moral and financial support which helped me to be a post graduate. I believe that his heavenly blessings and the unconditional support of my aunt (Valyammachi) Mrs. Syamala were also there throughout my Ph.D. program for which I am very much obliged. Our family and relatives have a significant role in making us reach a stature where we become able enough to choose a career especially being a full time researcher. But apart from them, my teachers from Fatima High School, Ambarnath, Mumbai, Maharashtra; Bethany Balika High School, Nangiarkulangara; Bishop Hodges Higher Secondary School, Mavelikkara; St Aloysius College, Edathua; and last but not the least Department of Physics, Kariavattom Campus, University of Kerala; laid the basics of whatever I know which spans from the spellings of each word to the understanding of a concept. I thank all of them from the bottom of my heart.

After reaching CSIR-NIIST, the person whom I met first turned out to be the most distinguished person of my research career. It was none other than Dr. U. Syamaprasad, Chief Scientist (Rtd.), Applied Superconductivity Group, Materials Science and Technology Division, NIIST, who agreed to guide me towards Ph.D. by giving an interesting and challenging topic in the area of superconductivity. Since we were working on a new class of superconductors, both me and my guide were patiently learning together from the flaws until we achieved the desired. It was his profound knowledge, practical expertise and commendable technical skill which helped us to make easy advances in the new area. Apart from being a guide who gives timely and fruitful instructions, he was always a support to our personal issues and was there for all of us like a father. I sincerely thank him for being there at all the odds of our research life, with a cheerful smile.

I am also very obliged and thankful to Dr. Manoj Raama Varma, Senior Principal Scientist, Magnetism Group, for taking care of us in all aspects, after the superannuation of our guide Dr. Syamaprasad.

I also extend my sincere gratitude to our Director Dr. A. Ajayghosh for providing us the excellent facilities at NIIST. I also thank with due regards the former Directors of NIIST, especially Dr. Suresh Das and Dr. B. C. Pai. I also acknowledge Dr. P. Prabhakar Rao, Head of the Division, Materials Science and Technology Division, for his timely help and valuable suggestions. The former Heads of the Division especially Dr. M. L. P. Reddy, Dr. M. T. Sebastian and Dr. K. G. K Warrier are also remembered with regards for their support and valuable suggestions.

I am thankful to Mr. P. Guruswamy, Technical officer (Rtd.) for his technical and personal support at Applied Superconductivity Group. I am also very grateful to Mr. M. R. Chandran and Ms. Soumya, Mr. Prithviraj and Mr. Ajeesh Paulose for their timely technical support by extending the research facilities such as SEM, XRD and PPMS. I also express my sincere gratitude to Mr. Sisupalan and Mr. Brahmakumar for their timely technical support to vacuum seal the quartz tubes.

I take this opportunity to thank Dr. A. Sundaresan, Professor, Chemistry and Physics of Materials Unit, Jawaharlal Nehru Centre for Advanced Scientific Research (JNCASR), Bangalore; Dr. Devendra Kumar, University of Cambridge, UK; Dr. A. Bharati, IGCAR, Kalpakkam, Dr. R. P. Aloysius, Senior Scientist, National Physical Laboratory, New Delhi; Mr. C. K. Chandrakanth, Senior Scientist, CSIR-NIIST, Trivandrum; for their valuable scientific discussions and experimental support.

I also extend my warm regards and gratitude to Dr. V. Biju, Head of the Department, Department of Physics, Kariavattom Campus, University of Kerala, for his timely help, valuable suggestions and academic support. My sincere thanks are also to all the present and former teachers of our department.

I also record my gratitude to the staff in the administration section of NIIST, who extended their timely support in carrying out different administrative procedures effortlessly. The canteen staff, Hamsikkas kiosk and seva members are also acknowledged for making the research life comfortable.

I also sincerely thank all the anonymous reviewers and editors of the journals who gave critical and productive comments to my research publications, the funding agency Department of Science and Technology (DST) and finally for the invaluable research fellowships provided by Kerala State Council for Science, Technology and Environment (KSCSTE) and Council for Scientific and Industrial Research (CSIR) which was really helpful to withstand as a researcher.

I was accompanied to NIIST by Ms. Anooja J. Babu, my M. Sc. classmate and close friend, on the very first day. Apart from the two years of M. Sc., she was my colleague for the last six years sharing the ups and downs of my research and personal life. I think she is now almost like a family member who knows both the dark and bright shades of my personality. I thank her for being the best companion.

I thank all my senior colleagues beginning from Dr. A. Biju, Dr. P. M. Sarun, Dr. Vinu S., Dr. R. Shabna, Dr. Vinod K. and Dr. Neson Varghese; for teaching me the basics and working principles of each instrument and for warmly accommodating me to their research world, Room No. 320. Even after leaving NIIST, Dr. Sarun and Dr. Vinod were approachable at any hour of the day for research discussions, for which I am always indebted. Dr. Neson Varghese still continues to be a big brother and a sincere advisor for all my research and personal concerns. I thank him sincerely for being there for me along with Anooja.

I also warmly acknowledge the cordial support of my junior colleagues Mr. Anees P., Mr. Rahul S., Mr. Devadas K. M., Mr. Syju Thomas, Ms. Anuraghi G. R. and Mr. Vishnu M. T. I also gratefully acknowledge the praiseworthy technical support extended by Mr. Sivaprakash A., Mr. Santhosh S., Mr. Sajith S. S., Mr. Jakson K. T., Mr. Firozhan M., Late Mr. Rinu V. F., Mr. Maheshkumar M., Mr. Vinu S. L. and Mr. Dinesh Jose.

I also thank all the members of the magnetism group especially Dr. Senoy Thomas, Ms. Neenulekshmi P., Ms. Raji G. R., Ms. Bhagya Uthaman, Ms. Jasnamol P. P. and Mr. Rajesh for their support and valuable suggestions.

Apart from the colleagues in my department, all other NIISTians are duly recorded for their moral support especially my roommates Dr. Arya Nandan, Ms. Rakhi A.M., Ms. Sreedevi K., Ms. Linsha Vazhayal, Ms. Neethu K. S. and Ms. Ramya A. N. who made my life at NIIST and its premises more colorful and memorable with lots of love, fun, silly fights and hugs.

At last but not the least let me remember two other special members of my family: my sister Anjali Mohan (Chinnus) and my husband Mr. Sajeev Philip. Chinnus is younger by age; so she is my daughter especially when under stress, ill health or when she needs to be pampered. But, when I need her, she switches to a strong support with ideas and advice having an elderly touch. I love her for being a part of my life and being a constant motivation. Sajeev is more a friend than a husband and that explains the value of his companionship. He has fought for me and stood for me always and I hope he will do the same in future. I guess I won't thank him because he is bound to be there with me for the rest of my life.

Pillai Aswathy Mohan

CONTENTS

List of figures

List of tables

List of Abbreviations

GL	Ginzburg-Landau
BCS	Bardeen Cooper and Schrieffer
SQUID	Superconducting Quantum Interference Devices
MRI	Magnetic Resonance Imaging
NMR	Nuclear Magnetic Resonance Spectroscopy
LTS	Low Temperature Superconductors
HTS	High temperature superconductors
YBCO	YBaCuO
RVB	Resonating Valence bond
ARPES	Angle Resolved Photoemission Spectroscopy
LHC	Large Hadron Collider
UXO	Unexploded Ordinance
ITER	International Thermonuclear Experimental Reactor
Maglev	Magnetically Levitating
RE	Rare Earth
Ch	Chalcogen
BZ	Brillouin zone
DFT	Density Functional Theory
LDA	Local Density Approximation
SDW	Spin Density Wave
DOS	Density of States
2D	Two Dimensional
3D	Three dimensional
WHH	Werthamer-Helfand-Hohenberg
BN	Boron nitride
PIT	Powder in Tube
OD	Outer Diameter
ID	Inner Diameter
wt.%	Weight percentage
Vol.%	Volume percentage
MBE	Molecular Beam Epitaxy
CMOS	Complementary Metal Oxide Semiconductors
CCD	Charge Coupled Device
ac	Alternating Current

dc	Direct Current
SS	Stainless Steel
XRD	X-ray Diffraction
FWHM	Full Width at Half Maximum
SEM	Scanning Electron Microscope
BSE	Back-Scattered Electrons
CL	Cathodoluminescence
SEI	Secondary Electron Imaging
TEM	Transmission Electron Microscopy
HRTEM	High Resolution Transmission Electron microscope
EDS/EDX	Energy Dispersive X-ray Spectroscopy
PPMS	Physical Property Measurement System
VSM	Vibrating Sample Magnetometer
ARS	Advanced Research Systems
JNCASR	Jawaharlal Nehru Centre for Advanced Science and Research
AGG	Abnormal Grain Growth
RE1111	$REFeAsO_{1-x}F_x$
122	$A_{1-x}B_xFe_2As_2$ (A-alkaline earth metal, B-alkali metal)
111	AFeAs, A – alkaline earth metals
11	FeCh
Nd1111	$NdFeAsO_{1-x}F_x$
Sm1111	$SmFeAsO_{1-x}F_x$
MPa	Mega Pascal
RRR	Residual resistivity ratio

List of symbols

K	Kelvin
ºC	degree Celsius
h	hours
T_C	Critical temperature
T_S	Structural transition temperature
H_C	Critical field
J_C	Critical current density
$J_C(H)$	In-field Critical Current density
λ	London penetration depth
ξ	Coherence length
α, β	Expansion coefficients
A	Vector potential
H, B	Magnetic field
H_{C1}	Lower critical field
H_{C2}	Upper critical field
H_{irr}	Irreversibility field
ρ	Resistivity
ρ_{300}	Normal state resistivity
χ	Magnetic susceptibility
χ', χ''	Real and imaginary component of χ
H_{ac}	*ac* magnetic field
f	Frequency
f_0	An attempt frequency
$\Psi(\mathbf{r})$	Wave function
n	Total number of free electrons
n_s, n_n	Number of superconducting, normal electrons
T	Temperature
I	Current
V	Voltage
R	Resistance
T	Tesla
mT	Milli tesla
K	Ginzburg-Landau parameter
Φ_0	Magnetic flux quantum

Ω	Unit of resistance
a, c	Lattice parameters
a, b	Sample dimensions
T_{Conset}	Temperature corresponding to Onset of transition
$T_{Coffset}$	Temperature corresponding to Offset of transition
ΔT_C	Width of Transition
Θ_D	Debye temperature
Δ	Energy gap
V	Average matrix element of electron interaction
Λ	Coupling constant between the electrons and phonons
$N(E_F)$	Electronic density near the Fermi surface in the normal state
Å	Angstrom unit
θ	Angle of diffraction
l_{el}	Electron mean free path
ω_D	Phonon frequency
gN(0)	BCS coupling constant
c , $c^\dagger$	Creation and annihilation operators
σ	σ bands
π	π bands
d	Inter-atomic spacing
h, k, l	Miller indices of crystal planes
⟨d⟩	Average grain size
M	Magnetization
M_P	Paramagnetic moment
ΔM	Width of the M-H Loop
M^+	Magnetic moment on the field increasing branch of the M-H Loop
M^-	Magnetic moment on the field decreasing branch of the M-H Loop
F_P	Flux pinning force density
F_{Pmax}	Maximum flux pinning force density
C_P	Specific heat capacity
T_P	Peak Temperature
R_H	Hall coefficient
ρ_{xy}	Transverse resistivity

PREFACE

Superconductivity is a fascinating phenomenon in which a material, cooled to very low temperature, allows a persistent frictionless flow of current. Ever since the discovery of superconductivity in Mercury at 4.2 K, a series of metals, alloys and compounds were screened for superconductivity. The recent breakthrough in this area was the discovery of superconductivity in an iron based compound $LaFeAsO_{1-x}F_x$ with a critical temperature (T_C) of 26 K by a Japanese group led by Hideo Hosono in February 2008. The display of superconductivity even in the presence of a well-known ferromagnetic element 'Fe' distinguishes the significance of this discovery, which then prompted the physicists to work with the motto "Strike iron while it is hot" giving rise to lots of classes. The similarity in features of different classes of iron pnictides to cuprates as well as MgB_2 again generates interest in theoreticians. Features such as layered structure, antiferromagnetic parent compound, relatively smaller anisotropy, different order symmetry and less sensitive conductive layer allowing substitution at all sites, are found to be the main characteristics of this system. Among the four major classes of iron pnictides, the $REFeAsO_{1-x}F_x$ (RE1111) compounds are found to be potential candidates for high field applications. Though these compounds show promising characteristics, the volatility of arsenic and fluorine and the trickier chemistry involved in the synthesis of these compounds make the development of practical conductors more difficult.

The present thesis work focuses on the enhancement of transport and magnetic properties of $NdFeAsO_{1-x}F_x$ based iron pnictide superconductors synthesized at ambient pressure through a novel pre-processing technique. Initially, bulk samples were prepared with properties at par with international status and thereafter wire and tape forms of the bulk sample having better transport J_C were also developed. The first chapter is an overview on the fundamentals of superconductivity and its applications and the second chapter introduces the features of iron based superconductors in detail. The preparation and characterization techniques adopted throughout the work are discussed in chapter 3.

Chapter 4 discusses the synthesis of $NdFeAsO_{1-x}F_x$ (Nd1111) iron pnictide superconductors in bulk form with varying fluorine stoichiometry (x=0 to 0.4) and it also details the impact of fluorine variation on the structural and superconducting properties of Nd1111. A maximum T_C of 52 K and a transport J_C of 1050 A/cm^2 at 12 K were obtained for the samples with x = 0.3 and 0.4, respectively. The transport and magnetic properties observed for each stoichiometry showed remarkable correlation with their corresponding structural and microstructural aspects. Moreover, the superconducting properties exhibited in this material, processed at a relatively low temperature of 1000 °C, were competitive as

compared to the existing reports wherein high pressures (~6 GPa) and temperatures (~1300 ^{o}C) were employed inevitably.

Chapter 5 focuses on the synthesis of rare earth modified $NdFeAsO_{0.7}F_{0.3}$ superconductors and the studies on their magneto-transport properties. Selected rare earths such as Yttrium (non 4f element) and 4f elements such as Cerium and Gadolinium having ionic radii in the order Ce>Nd>Gd were doped at Nd^{3+} site in $Nd_{1-x}RE_xFeAsO_{0.7}F_{0.3}$ so as to enhance the critical parameters such as T_C, J_C and H_{C2}. All the rare earth doped samples exhibited enhanced transport and magnetic properties as compared to the undoped sample $NdFeAsO_{0.7}F_{0.3}$. Maximum T_Cs of 53.3, 53.6 and 55.1 K were obtained at x= 0.3, 0.1 and 0.15 for Y, Ce and Gd doped samples, respectively. The magnetic J_C of Ce doped sample was enhanced by a factor of two as compared to that of the undoped sample. It was found that the substitution of a relatively smaller ion at Nd site created inner chemical pressure due to lanthanide contraction thereby favoring the enhancement of T_C in Nd1111. However, the lattice defects due to the substitution of a larger ion (Ce) had a significant influence on the vortex pinning in Nd1111 which in turn enhanced the magnetic J_C. However, the lattice defects due to Y, Ce and Gd doping at Nd site, irrespective of their ionic size, assisted in effective pinning of the flux lines thereby exhibiting an enhanced $J_C(H)$ performance especially at high fields. Moreover, very high upper critical fields of 335 T and 360 T were also estimated for Gd and Ce doped samples, respectively.

Besides isovalent doping, simultaneous doping at two sites i.e. binary doping at Nd and O sites with a single source was also tried using alkaline earth metal fluorides especially CaF_2 and MgF_2 in NdFeAsO and the results are presented in chapter 6. The synthesis of $Nd_{1-x}Ca_xFeAsO_{1-2x}F_{2x}$ superconductors using CaF_2 as a binary dopant provides both holes and electrons by simultaneous substitution of Ca^{2+} ions and F^- ions at Nd^{3+} and O^{2-} sites, respectively. The sample with x=0.2 exhibited a maximum critical temperature (T_C) of 52.3 K and transport critical current density of 1240 A/cm^2 at 12 K. An interesting feature observed for binary doped samples is the preferential alignment of (*00l*) planes and the refinement of microstructure both in terms of grain size and grain connectivity. While using MgF_2 as a binary dopant, a similar refinement in microstructure was observed in addition to an increase in T_C up to 54.7 K. The $J_C(H)$ behavior derived through magnetization measurements and upper critical fields estimated using magneto-transport measurements were also presented. It was observed that lattice defects due to binary doping acted as effective flux pinning centres and enhanced the $J_C(H)$ performance of the samples as compared to the corresponding F alone doped samples. Moreover, very high H_{C2} values of 300 and 310 T were also achieved for MgF_2 and CaF_2 doped samples, respectively.

Chapter 7 deliberates an initiative towards the realization of conductor development using $NdFeAsO_{0.6}F_{0.4}$ found to exhibit the maximum J_C in bulk form (*Chapter 4*). The Powder in Tube (PIT) method was followed for mono-filamentary wire fabrication using $NdFeAsO_{0.6}F_{0.4}$ processed at 360 ºC for 5 h as the precursor. Initially, the compatibility of different sheath metals with the superconductor was investigated. The sheath metals such as Ag, Fe, Cu, Ni and SS were used and the metal sheathed Nd1111 wire samples were processed at different processing temperatures such as 850, 900 and 950 ºC. The sheath metals, Fe and Ag, were observed to be chemically compatible for Nd1111. Among these, the superconducting properties were found to be the best for Ag sheathed Nd1111 based wires processed at 900 ºC for 40 h. Specific metallic additives such as Sn, Pb and Mg were incorporated within the pnictide core in order to enhance the transport J_C of the wires. Among which only Sn addition was found to be favorable in supporting the existence of superconductivity while the others do not. Hence, the effect of varying Sn addition on the transport properties of both Fe sheathed Nd1111 tapes were also investigated. The summary and conclusions of the whole work and a few suggestions for future work are consolidated in Chapter 8.

List of Publications

List of publications in SCI journals

1. ***P. M. Aswathy***, J. B. Anooja, Neson Varghese, C. K. Chandrakanth, N. Devendra Kumar, A. Sundaresan and U. Syamaprasad, "Rare earth (RE – Ce, Gd) modified $Nd_{1-x}RE_xFeAsO_{0.7}F_{0.3}$ superconductor with enhanced magneto-transport properties," ***RSC Adv.*** 5, 41484 (**2015**).
2. ***P. M. Aswathy,*** J. B. Anooja, Neson Varghese and U. Syamaprasad, "The role of yttrium doping on the structural and superconducting properties of Sm1111 and its comparison with other (RE,Y)1111 (RE - La, Ce, and Nd) iron oxypnictides," ***J. Low Temp. Phys.*** 178, 285–294 (**2015**).
3. ***P. M. Aswathy***, J. B. Anooja, Neson Varghese, and U. Syamaprasad, "Influence of reactivity of sheath metals on the superconducting properties of $NdFeAsO_{0.6}F_{0.4}$ wires," ***Materials Science Forum-Trans Tech Publications*** 830, 557-560 (**2015**)
4. ***P. M. Aswathy***, J. B. Anooja, Neson Varghese, and U. Syamaprasad, "Enhanced transport and magnetic properties in gadolinium doped $NdFeAsO_{0.7}F_{0.3}$ superconductors," ***AIP Conference Proceedings*** 1665, 130047 (**2015**)
5. ***P. M. Aswathy,*** J. B. Anooja, Neson Varghese and U. Syamaprasad, "Microstructural refinement and enhanced transport properties in binary doped NdFeAsO superconductor," ***J. Appl. Phys.*** 115, 053903 (**2014**).
6. ***P. M. Aswathy,*** J. B. Anooja, Neson Varghese and U. Syamaprasad, "$NdFeAsO_{1-x}F_x$ Superconductor – Impact of Fluorine Variation on Microstructure and Transport Properties," ***J. Am. Ceram. Soc.*** 96, 1176–1180 (**2013**)
7. ***P. M. Aswathy,*** J. B. Anooja, P. M. Sarun and U. Syamaprasad, "An Overview on Iron based Superconductors," ***Supercond. Sci. Technol.*** 23, 073001 (**2010**). [**Topical Review, selected for Highlights of 2010**]
8. J. B. Anooja, ***P. M. Aswathy***, Neson Varghese, C. K. Chandrakanth, N. Devendra Kumar, A. Sundaresan and U. Syamaprasad, "Influence of rare earth doping on the structural and electro-magnetic properties of $SmFeAsO_{0.7}F_{0.3}$ iron pnictide," ***Inorg. Chem. Front.*** 2, 731-740 (**2015**).
9. J. B. Anooja, ***P. M. Aswathy,*** Neson Varghese, Manoj Raama Varma and U. Syamaprasad, "Structural and superconducting properties of BaF_2 Doped SmFeAsO," ***Materials Science Forum-Trans Tech Publications*** 830, 595-599 (**2015**)
10. J. B. Anooja, ***P. M. Aswathy,*** Neson Varghese, R. P. Aloysius and U. Syamaprasad, "SmFeAsO superconductor with preferred crystallographic orientation and enhanced critical current density," ***J. Am. Ceram. Soc.*** 97, 2099–2104 (**2014**).
11. J. B. Anooja, ***P. M. Aswathy***, Neson Varghese, R. P. Aloysius, and U. Syamaprasad, "Microstructure refinement and enhanced critical current density in binary doped SmFeAsO superconductor," ***AIP Conference Proceedings*** 1591, 1536 (**2014**).
12. J. B. Anooja, ***P. M. Aswathy***, Neson Varghese, K. Vinod, A. Bharati and U. Syamaprasad, "Transport and magnetic properties of yttrium doped NdFeAs(O,F) superconductor," ***J. Alloys and Compd.*** 566, 43–49 (**2013**).

13. J. B. Anooja, ***P. M. Aswathy***, P. M. Sarun, U. Syamaprasad, "A novel low temperature synthesis route for $SmFeAsO_{1-x}F_x$ bulk superconductor with improved transport properties," ***J. Alloys and Compd.*** 514, 1-5 (**2012**).
14. Neson Varghese, Devadas K. M., ***P. M. Aswathy***, J. B. Anooja, Manoj Raama Varma and U. Syamaprasad, "Enhanced transport current in MgB_2 superconducting wire through metallic Fe addition", ***Materials Science Forum-Trans Tech Publications*** 830, 595-599 (**2015**)
15. Neson Varghese, K. Vinod, S. Rahul, K. M. Devadas, Syju Thomas, "Lowering the sintering temperature of MgB_2/Fe wires with high transport current by nano cu doping," ***P. M. Aswathy***, S. Pradhan and U. Syamaprasad, ***AIP Conf. Proc.*** 1349, 891 (**2011**).
16. S. Vinu, P. M. Sarun, R. Shabna, ***P. M. Aswathy***, J. B. Anooja, U. Syamaprasad, "Suppression of flux-creep in (Bi,Pb)-2212 superconductor by holmium doping," ***Physica B*** 405, 4355 (**2010**).
17. P. M. Sarun, S. Vinu, R. Shabna, J. B. Anooja, ***P. M. Aswathy***, and U. Syamaprasad, "Structural and transport properties of $(Bi_{1.6}Pb_{0.5})(Sr_{2-x}Lu_x)Ca_{1.1}Cu_{2.1}O_{8+\delta}$ superconductor," ***IEEE transactions on applied superconductivity*** 20, 2 (**2010**).

⌗ *List of Conference Papers*

1. ***P. M. Aswathy***, J. B. Anooja, Neson Varghese, Manoj Raama Varma and U. Syamaprasad, "*Influence of Reactivity of Sheath Metals on the Superconducting Properties of $NdFeAsO_{0.6}F_{0.4}$ Wires*," Presented at the International Conference on Advanced Materials and Manufacturing Process for Strategic Sectors (ICAMPS 2015), held at Trivandrum, Kerala, during May 13-15, **2015**. (Published in Trans. Tech Publications) (**Best Poster Prize**)
2. ***P. M. Aswathy***, J. B. Anooja, Neson Varghese and U. Syamaprasad, "*Enhanced Transport and Magnetic Properties in Gadolinium doped $NdFeAsO_{0.7}F_{0.3}$ Superconductors*" Presented at the 59th DAE Solid State Physics Symposium (DAE SSPS 2014), held at Vellore Institute of Technology, Vellore, Tamil Nadu, during December 16-20, **2014**. (Published in AIP Conf. Proc.)
3. ***P. M. Aswathy,*** J. B. Anooja, Neson Varghese and U. Syamaprasad "*Enhanced Transport Properties In NdFeAsO Superconductor Through Microstructural Refinement By CaF_2 Doping*," Presented at the 2nd International Conference on Advanced Functional Materials (ICAFM) held at NIIST, Thiruvananthapuram on February 19-21, 2**014**.
4. ***P. M. Aswathy,*** J. B. Anooja, Neson Varghese and U. Syamaprasad, "*Impact of Fluorine Variation on the Structural and Superconducting Properties of $SmFeAsO_{1-x}F_x$,*" Presented at 25th Kerala Science Congress held at Technopark, Trivandrum on January 30, **2013**.
5. ***P. M. Aswathy***, J. B. Anooja, P. M. Sarun and U. Syamaprasad, "*Effect of Pre-Processing Technique on Phase Formation, Sintering Temperature and Superconducting Properties of $SmFeAsO_{1-x}F_x$,*" Presented at the Asian Conference on Applied Superconductivity and Cryogenics (ACASC) held at IUAC, New Delhi on November 16-18, **2011**.
6. J. B. Anooja, ***P. M. Aswathy,*** Neson Varghese, Manoj Raama Varma and U. Syamaprasad, "*Structural and Superconducting Properties of BaF_2 Doped SmFeAsO*," Presented at the International Conference on Advanced Materials and Manufacturing Process for Strategic Sectors

(ICAMPS 2015), held at Trivandrum, Kerala, during May 13-15, **2015**. (Published in Trans. Tech Publications)

7. J. B. Anooja, ***P. M. Aswathy,*** Neson Varghese and U. Syamaprasad, "*Magneto-Transport Properties of $SmFeAsO_{0.7}F_{0.3}$ Superconductor Upon Gd Doping at Sm Site*," Presented at the International Conference on Science, Technology and Applications of Rare Earths (STAR 2015), held at Trivandrum, Kerala, during April 23-25, **2015**.
8. J. B. Anooja, ***P. M. Aswathy***, Neson Varghese and U. Syamaprasad, "*Microstructure Refinement and Enhanced Critical Current Density in Binary Doped SmFeAsO Superconductor*" Presented at the 58th DAE Solid State Physics Symposium (DAE SSPS 2013), held at Thapar University, Patiala, Punjab during December 17-21, **2013**. (**Best Poster Prize**)
9. J. B. Anooja, ***P. M. Aswathy***, Neson Varghese and U. Syamaprasad, "*Enhanced Superconducting Properties in NdFeAs(O,F) Superconductor by Yttrium Doping*" Presented at 25th Kerala Science Congress held at Technopark, Trivandrum on January 30, **2013**.
10. Neson Varghese, K. M. Devadas, J. B. Anooja, ***P. M. Aswathy,*** Manoj Raama Varma and U. Syamaprasad, "*Enhanced Transport Current in MgB_2 Superconducting Wire Through Metallic Fe addition*," Presented at the International Conference on Advanced Materials and Manufacturing Process for Strategic Sectors (ICAMPS 2015), held at Trivandrum, Kerala, during May 13-15, **2015**. (Published in Trans. Tech Publications)
11. Neson Varghese, K. Vinod, S. Rahul, K. M. Devadas, Syju Thomas, ***P. M. Aswathy***, S. Pradhan and U. Syamaprasad, "Lowering the sintering temperature of MgB_2/Fe wires with high transport current by nano cu doping," Presented at the 55th DAE Solid State Physics Symposium (DAE SSPS 2010), held at Manipal on December 26-30, **2010**. (Published in AIP Conf. Proc.)
12. Neson Varghese, J. B. Anooja, ***P. M. Aswathy***, K. Vinod, S. B. Roy and U. Syamaprasad, "*Effect of Combined Addition of Nano SiC and TiC on Structural and Superconducting Properties of MgB_2*," Presented at the International Conference on Advanced Functional Materials (ICAFM) held at NIIST, Thiruvananthapuram on December 9-10, **2009**.

CHAPTER 1

SUPERCONDUCTIVITY - FUNDAMENTALS AND APPLICATIONS

1.1 Historical development of superconductivity

Superconductivity is a startling phenomenon in which a material cooled to very low temperatures exhibits a persistent frictionless flow of current as long as it is kept at low temperatures. The backbone of the superconductivity history is a series of spectacular and completely unexpected experimental discoveries leaving the then contemporary theoretical physics puzzled. The first one was the discovery of superconductivity in mercury by the famous Dutch Scientist Kammerlingh Onnes in 1911, at Leiden in the Netherlands. He was the first person who could ever reach very low temperatures and marked the beginning of a new field of science, the low temperature physics. One of his students who had been monitoring the variation of resistance in mercury wires at low temperatures noticed a precipitous drop in resistance within a very small temperature interval at around 4 K as shown in Figure 1.1 (Onnes *et al.* 1911).

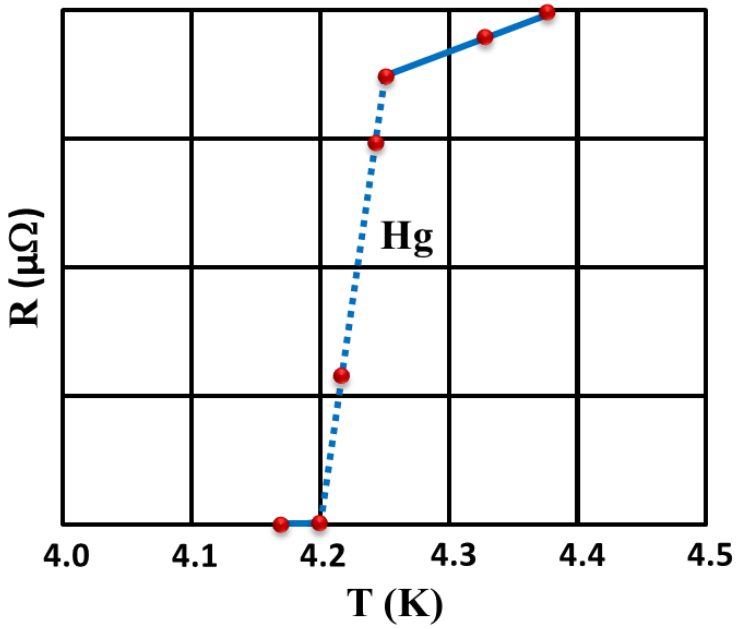

Figure 1.1: Illustration of Kamerlingh Onnes' discovery of superconductivity in 1911. At 4.2 K, the resistance of Hg drops abruptly to a value no greater than 10^{-5} Ω

Later, Walther Meissner and Robert Ochsenfeld discovered another striking phenomenon in 1933 known as Meissner effect in which a superconductor expels applied magnetic field on transition from normal to the superconducting state (Meissner *et al.* 1933). This superconducting phenomenon, demonstrating abrupt vanishing of resistance

and expulsion of the magnetic field, remained inexplicable until 1935. Then, Fritz London and Heinz London developed mathematical relationships with the help of Maxwell's equations which explained both the manifestations of a superconductor (London *et al.* 1935a; London *et al.* 1935b). Though the theory proposed by London and Heinz clarified the experimental observations, it could not provide any microscopic origin to the superconducting properties. As an extension of the London theory, the Ginzburg-Landau (GL) theory was established in 1950 introducing a complex valued superconducting order parameter varying smoothly in space (Ginzburg *et al.* 1950; Ginzburg *et al.* 2004). This macroscopic theory was found appropriate for any superconductor defining it as a charged Bose superfluid. The hypothesis was a strange idea that contradicted common knowledge at that time; however, Abrikosov proved the validity of GL theory by the theoretical prediction of quantized flux lines known as vortices (Abrikosov 1957a; Abrikosov 1957b). In 1950, Maxwell and Reynolds observed the Isotope effect in Hg according to which the critical temperature (T_C) of a superconductor is inversely proportional to the square root of its mass (Maxwell 1950; Reynolds *et al.* 1950). The observation also suggested that the electron-phonon coupling might be responsible for superconductivity. In 1957, the trio, John Bardeen, Leon Neil Cooper and Robert Schrieffer proposed the BCS theory, a microscopic quantum theory describing superconductivity as a microscopic effect caused by condensation of Cooper pairs into a boson-like state (Bardeen *et al.* 1957a; Bardeen *et al.* 1957b). In 1962, Josephson's tunneling theory was proposed to describe the tunneling of Cooper pairs through a barrier between two superconductors (Josephson 1962).

Since the discovery of superconductivity in Mercury, a series of other metals and alloys were checked for superconductivity. Twenty-seven of the metals turned out superconductors, in their usual crystallographic forms, at atmospheric pressure and very low temperatures. The metals found to be superconducting include aluminum, tin, lead, rhenium, lanthanum, and protactinium. While certain metals, semimetals, or semiconductors such as uranium, cerium, silicon, and selenium are superconductors only at high pressures. Bismuth and five other elements that are not superconducting in their usual crystallographic form, tend to be superconducting upon synthesizing them in a highly disordered form. However, superconductivity is not observed in any of the magnetic elements such as chromium, manganese, iron, cobalt, or nickel. The vast majority of the known metallic superconductors have T_C values between 1 and 10 K (Matthias *et al.* 1963, Eisenstein *et al.* 1954).

Among the metallic elements, tungsten has the lowest critical temperature, 0.015 K, and niobium the highest, 9.2 K. It was observed that though Nb superconducts at 9.2 K in its elemental form; it cannot carry significant bulk currents and was therefore limited to radio frequency and electronic applications such as SQUIDS for very sensitive current and magnetic field sensors. In order to increase the current carrying capacity of Nb, it was magnetically hardened by alloying and by introducing pinning centers for the magnetic flux. Further, an alloy of niobium and titanium, Nb-Ti flourished as a workhorse in superconductor magnet technology (Shen *et al.* 2001). As the usability of Nb-Ti is limited to low operating temperatures and magnetic fields up to 10 T, another Nb based superconductor, Nb_3Sn with a T_C of 18.3 K was used. Its superior superconducting properties are due to the specific crystal structure, A15 phase. Nb_3Sn was exclusively applied in magnetic fields between 10 and 20 T. As the intermetallic phase Nb_3Sn is very brittle, complicated manufacturing technologies are an essentiality. The potential applications of superconducting wires are in the electric power technology and in high magnetic field systems. Due to the need to cool Nb based superconductors down to the temperature of liquid helium (4.2 K), their use in power applications remained practically inert. Thus, the application field of Nb based superconducting wires is retained mainly in the generation of high magnetic fields in the key areas such as Magnetic Resonance Imaging (MRI) in medicine, Nuclear Magnetic Resonance Spectroscopy (NMR) in biology and chemistry, magnets for Nuclear Fusion power technology and magnets for particle accelerators in High Energy Physics.

By 1975, more than two thousand different superconductors including metals and alloys were unraveled with a maximum T_C of 22.3 K for Nb_3Ge in 1973 (Poole *et al.* 1995). For the next ten years, no further increase in critical temperature was observed. In the early 1980s, a worldwide effort was made by physicists in search of novel superconducting materials. In 1986, it was Georg Bednorz and Alex Muller who discovered superconductivity in Ba doped La_2CuO_4 at about 30 K marking the beginning of high temperature superconductivity (Bednorz *et al.* 1986). Many scientists believed that the mechanism in high temperature superconductors could not be explained using the BCS theory. In 1987, an American physicist P. W. Anderson and the Indian theoretical physicist Ganapathy Baskaran proposed a theoretical model called Resonating Valence Bond theory that tried to describe high temperature superconductivity especially that observed in cuprate compounds (Anderson 1987). During this period itself, superconductivity was observed at 90 K in a perovskite compound $YBa_2Cu_3O_7$ (Wu *et al.* 1987). This was

followed by an enthusiastic overnight symposium at Hilton hotel in New York which was called as a Woodstock of physics. Moreover, the discovery was significant since from that point forward it became possible to use cheap liquid nitrogen as a coolant. Later, scientists experimented with many different forms of perovskites. The critical temperatures as high as 112 K in a Bismuth based cuprate and 126 and 135 K in Thallium and Mercury based cuprates, respectively were reported further (Sheng et al. 1988; Parkin et al. 1988). It is to be noted that though these materials have complicated crystal structures and tedious processing techniques, the very high critical temperatures make them cheap and useful for high temperature applications. But the major drawback of these materials is the large anisotropy and degradation in current carrying capacity at higher applied fields.

In 2001, the Akimitsu group at Aoyama Gakuin University found that a simple intermetallic MgB_2 exhibited superconductivity at 39 K (Nagamatsu *et al.* 2001). This value of T_C is close to what has been considered the maximum possible by pairing caused due to electron-phonon interaction. It is still considered as a typical phonon type BCS superconductor with s-wave symmetry. The simpler composition, easy synthesis procedures, weak link free grain boundaries, lower anisotropy and high transport critical currents make it an excellent material suitable for electronic devices and persistent current magnets. The main disadvantage of early MgB_2 samples was their low critical magnetic field H_{C2}. But later H_{C2} was increased to more than 40 T in bulk and around 60 T in oriented thin films by carbon doping. Even though its critical temperature is below the boiling point of liquid nitrogen, the possibility of cooling with a cryocooler to 20 K and operation in the persistent-current mode raised the demand for MgB_2 wires for many practical applications.

Another breakthrough came with the discovery of superconductivity in an iron based superconductor $LaFeAsO_{1-x}F_x$ with a critical temperature of 26 K by a Japanese group led by Hideo Hosono in February 2008 (Kamihara *et al.* 2008). The critical temperatures of this class of materials were soon raised to as high as 56 K. A wide variety of pnictide and chalcogenide compounds belonging to the iron based family was discovered thereafter. The interesting features pertaining to these materials and other aspects will be discussed in detail in the next chapter.

1.2 Fundamental characteristics of superconductors

A superconductor is not merely a “perfect conductor”. Rather, it is a phenomenon characterized by both the complete absence of electrical resistance and the damping of the interior magnetic field. The vanishing of the electrical resistance and the observation of

ideal diamagnetism are characteristic fundamental properties of superconductors. The variation of resistivity (ρ) and susceptibility (χ) with respect to temperature in a superconductor is depicted in Figure 1.2.

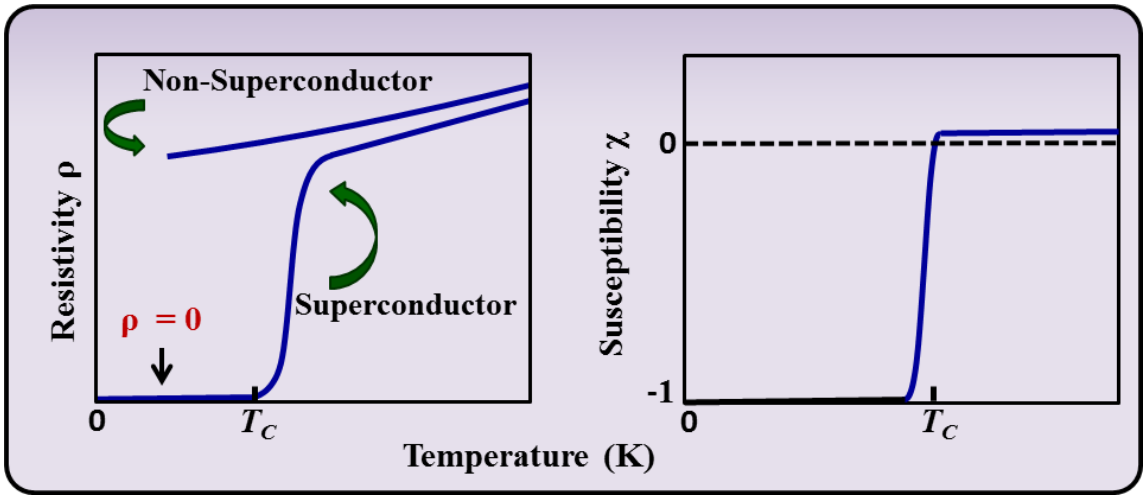

Figure 1.2: The variation of resistivity and susceptibility of a superconductor with temperature

1.2.1 Critical surface of a superconductor

While mentioning the details of superconductor, one should definitely have an idea of certain critical parameters related to it. A material remains to be a superconductor as long as it is kept below a particular,

a) temperature, known as ***Critical temperature*** **(T_C)**
b) field, known as ***Critical field*** **(H_C)** and
c) current, known as ***Critical current*** **(I_C)** or current density, ***Critical current density*** **(J_C)**.

These three parameters form a three dimensional boundary called the critical surface (shown in Figure 1.3) below which, the material is a superconductor and above it, the material turns out to be normal. Though the values of the critical parameters vary from one material to another, the basic aim of an experimentalist is to enhance these values so as to increase the superconducting critical surface or more specifically to widen the operating range of the material. Both T_C and H_C are intrinsic superconducting properties whereas J_C of a superconductor is somewhat extrinsic. Hence, for a particular superconductor, it is true that T_C and H_C cannot be altered much. But its J_C can be enhanced to an extent by appropriate doping or change in synthesis method.

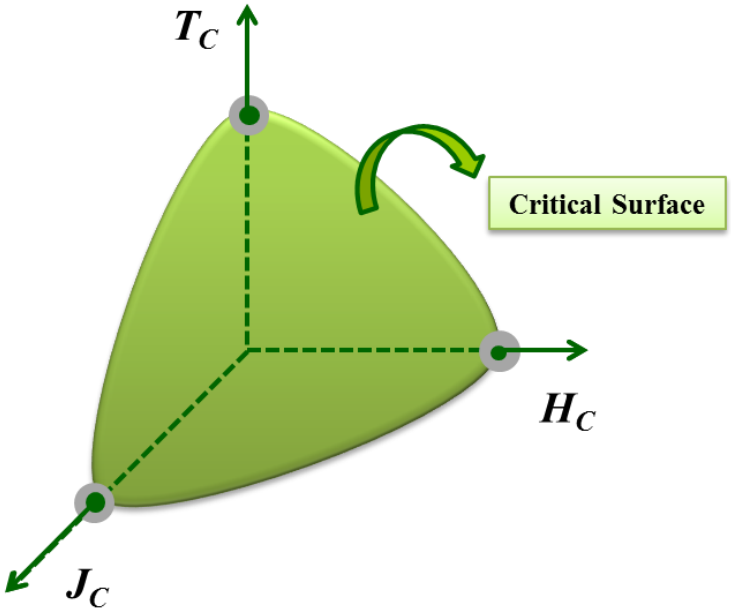

Figure 1.3: The critical surface encompassing the critical parameters of a superconductor

1.2.2 Classification of superconductors

Based on the critical temperature and behavior in an applied magnetic field, superconductors can be classified into two. Moreover, they can also be categorized on the basis of the superconducting mechanism obeyed. On the basis of

Critical temperature (T_C) –

a) **Low temperature superconductors (LTS)** : Materials having $T_C < 77$ K

b) **High temperature superconductors (HTS)** : Materials having $T_C > 77$ K

The method of classifying superconductors as HTS and LTS is based on whether their T_C is above or below the boiling point of Liquid Nitrogen (77 K). However, there exists another convention wherein all superconductors having a $T_C > 30$ K are generally categorized as HTS or relatively high T_C materials.

Behavior in applied magnetic fields –

a) **Type I superconductors** : Materials which are superconductors (in Meissner state) only below a lower critical field H_{C1}, above this field they are normal

b) **Type II superconductors** : Materials which are in Meissner state below H_{C1} and remain in an intermediate state with flux penetration up to an upper critical field H_{C2} and above this they are normal

Superconducting Mechanism –

a) **Conventional Superconductors** : Materials which obey BCS theory

b) **Unconventional Superconductors** : Materials which do not follow BCS mechanism instead have pairing symmetry other than s-wave

1.2.3 Basic features of superconductors

The superconducting transition is accompanied by abrupt changes in various physical properties as a part of a phase transition from the normal state to the superconducting state. The superconducting state further prevails depending upon the critical parameters such as the temperature at which it is maintained and the magnetic field being experienced. When a superconductor is placed in a weak external magnetic field H, the field penetrates down to a short distance λ from the surface of the superconductor, called the penetration depth, after which it decays rapidly to zero. Generally, superconductors have a penetration depth of the order of 100 nm. The expulsion of the magnetic field by the creation of super currents is called the Meissner effect. However, the Meissner effect is different from "perfect diamagnetism". According to Lenz's law, a changing magnetic field applied to a conductor will induce an electrical current in the conductor that creates an opposing magnetic field. In a perfect conductor, an arbitrarily large current can be induced, and the resulting magnetic field exactly cancels the applied field. The Meissner effect differs from perfect diamagnetism because a superconductor expels all magnetic fields, not just those that are changing as expected from Lenz's law. The expulsion of magnetic field in a superconductor at temperature below T_C is shown in Figure 1.4 (a). If a superconductor is cooled below T_C and a magnet is placed upon it, the superconductor will try to repel the magnet. This results in Magnetic levitation, which can be considered as a demonstration of the Meissner effect (shown in Figure 1.4 (b)).

The Meissner effect was explained by London who showed that the electromagnetic free energy in a superconductor is minimum and he provided the London equation which predicts that the magnetic field in a superconductor decays exponentially from the value it possesses at the surface. The Meissner effect is not followed when the applied magnetic field is too large. Superconductors can be divided into two classes according to their behavior in the presence of magnetic fields. In the Type I superconductors, superconductivity is abruptly destroyed when the strength of the applied field rises above a critical value H_C. In Type II superconductors, increasing the applied field above a critical value H_{C1} (lower critical field) leads to a mixed or vortex state in which an increasing amount of magnetic flux penetrates into the material, but there remains no resistance to block the electric current as long as the current is not too large. At

a field strength H_{C2} (upper critical field), superconductivity is completely destroyed. Most of the elemental superconductors are Type I whereas almost all of the alloys and compound superconductors are found to follow Type II behavior. The variation of internal magnetization with applied field for (a) Type I and (b) Type II superconductors is shown in Figure 1.5.

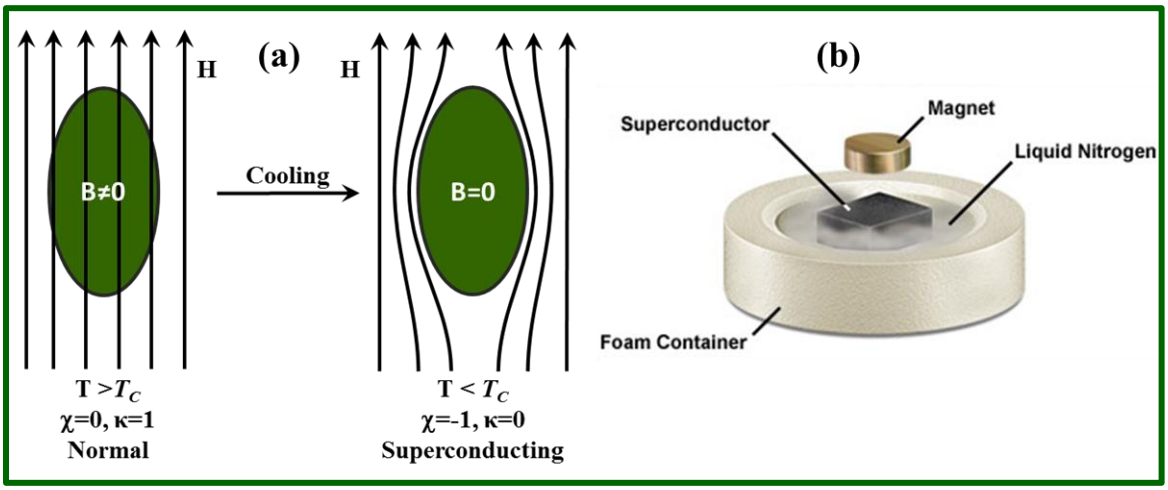

Figure 1.4: The Meissner effect in a superconductor (a) a schematic representation of Meissner effect and (b) an image of a magnet being repelled by a superconductor

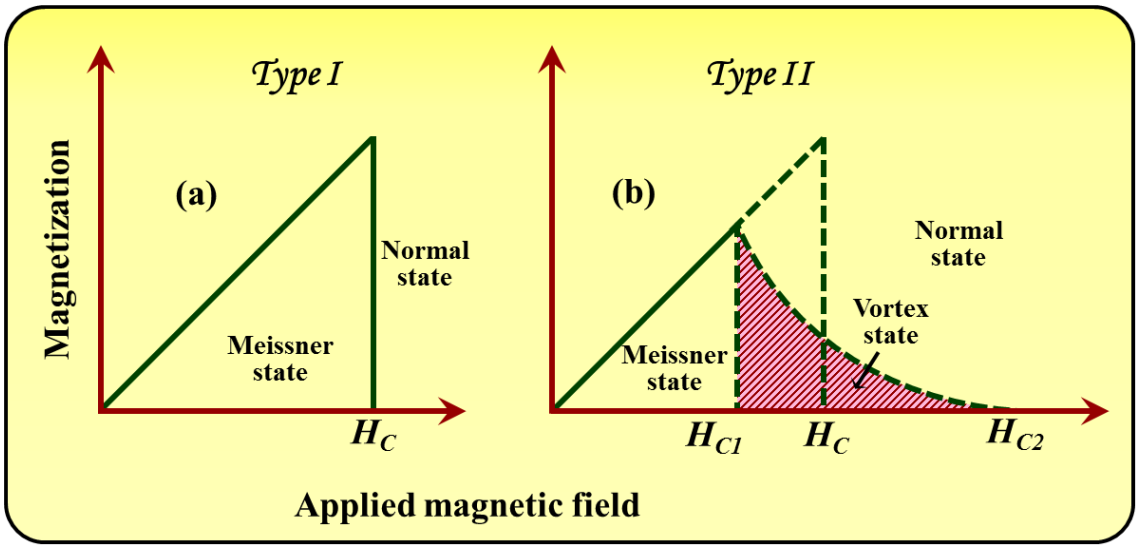

Figure 1.5: Variation of magnetization with applied field for (a) Type I and (b) Type II superconductors

The penetration of the magnetic field in the mixed state is actually caused by “vortices”. The vortices are often called as "fluxons" since the flux carried by these vortices is quantized. These quantized vortices are also known as Abrikosov vortices, named after the person who proposed the concept of vortices. The basis of Abrikosov’s model of the vortex state is the phenomenological GL theory, which simplifies the

theoretical treatment of a spatially varying order parameter in a Type II superconductor. Within the framework of the GL theory the structure of an Abrikosov vortex is characterized by two fundamental length scales: the magnetic penetration depth λ, and the coherence length ξ, where λ > ξ. The coherence length ξ is approximately the distance over which the pair potential (order parameter) Ψ(r) rises from zero at the center of a vortex (r = 0) to its asymptotic value Ψ_0 outside the vortex core. Its value can be determined experimentally from measurements of the upper critical field, $H_{C2} = \Phi_0/2\pi\xi^2$. Abrikosov differentiated Type I and Type II superconductors on the basis of the fact that surface energy of a boundary between a normal and superconducting region has a different sign (Abrikosov 2004). The surface energy is proportional to the difference (ξ-λ) and changes sign depending on the value of the GL parameter. The GL parameter 'K' is, essentially, a ratio of the fundamental length scales in GL i.e. K = λ/ξ. The classification is as a) *Type I superconductor: 0 < K < 1/√2 (positive surface energy)* and b) *Type II superconductor: K > 1/√2 (negative surface energy)*. The variation of the magnetic field and superconducting order parameter at a normal-superconducting interface of Type I and Type II superconductors is shown in Figure 1.6.

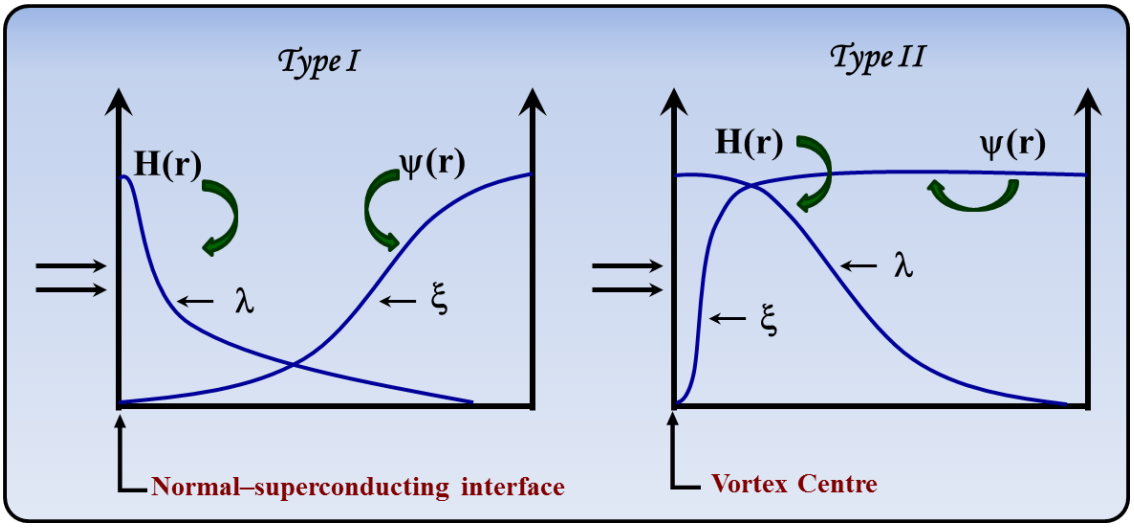

Figure 1.6: Variation of magnetic field and superconducting order parameter at a normal-superconducting interface of Type I and Type II superconductors

Each Abrikosov vortex has a normal core as a long thin normal cylinder along the field direction. The order parameter inside the core $|\psi|^2 = 0$. The radius of the normal core ~ ξ. Around the normal core, there exists a circulating super-current. The direction of circulation is such that the direction of the magnetic field created by this current coincides with the direction of external magnetic field (along the normal core). The size of the region where the super-current circulates is ~ λ. Each vortex carries one quantum of magnetic

flux. The penetration of the vortices in the superconductor takes place at H > H_{C1}. These vortices have the same direction of circulation and hence repel one another and minimize their free energy by forming a triangular lattice. Mixed state exist for H_{C1} < H < H_{C2}. As field increases from H_{C1} to H_{C2}, the density of vortices increases (lattice period decreases). At H_{C2}, the distance between vortices becomes ~ ξ, |ψ| → 0 and the second order phase transition to the normal state takes place. An illustration of flux vortices distributed in a superconductor with super-current formation around each vortex is shown in Figure 1.7 (a). Figure 1.7 (b) shows the status of flux lines in a superconductor according to the application of the magnetic field.

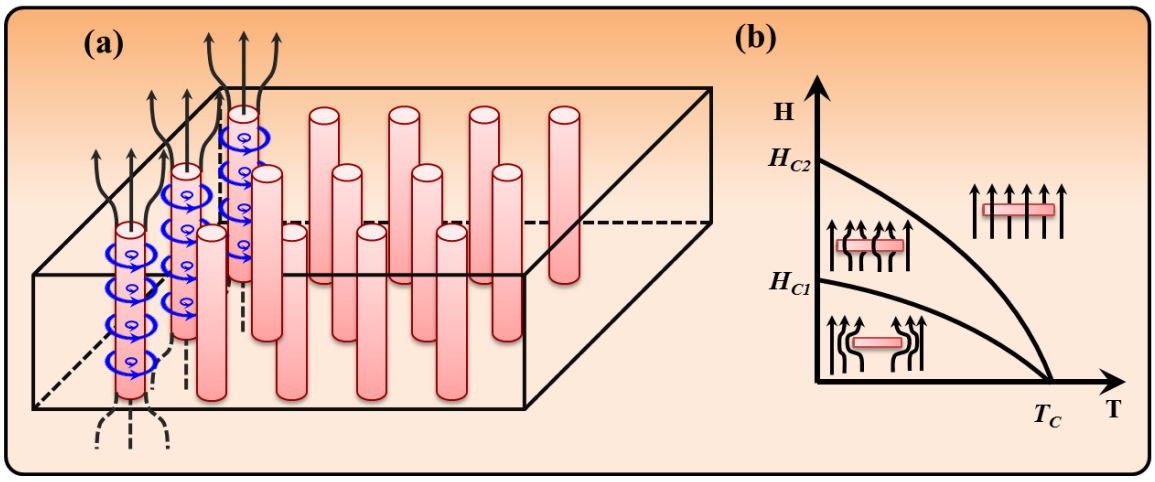

Figure 1.7: An illustration of (a) flux vortices in a Type II superconductor under an applied magnetic field and (b) its H-T phase diagram: Below H_{C1}, the superconductor expels magnetic field completely. Between H_{C1} and H_{C2}, the superconductor is in a mixed state with the presence of vortices

For carrying large currents without resistance, the mixed state of Type II superconductor with large values of H_{C2} plays major role. The transport current flowing in a superconductor from an external source, in the direction perpendicular to the vortices, exerts a Lorentz force on the vortices. If the superconductor is absolutely perfect and homogeneous (free of defects), an arbitrary small Lorentz force would cause vortex motion and dissipate energy. In addition to the two limiting parameters T_C and H_{C2}, which are intrinsic characteristics of a superconducting material, the zero resistance property of the superconducting state is also lost if the material carries a current density larger than a critical value J_C. The J_C of a superconductor is a structure-sensitive property and can vary by as much as several orders of magnitude as a result of thermal or mechanical treatment of the material. As current densities are raised higher than J_C the material does not go suddenly from the superconducting state to the normal resistive state, but develops a 'flux-flow resistivity' that rises with increasing current density (Chaddah *et al.* 2003). When

current is passed through a superconductor in its mixed state, a non-vanishing Curl H is required and this needs a gradient in the vortex density. The repulsive interaction with vortices on either side will no longer cancel out, since the density gradient implies unequal distances between vortices. Each vortex thus experiences a net force which is proportional to both the density of vortices and to its gradient, i.e. to both B and J. This driving force can be derived and is found to be F = H × Curl H = H × J. The force F on each vortex, which is equivalent to a Lorentz force, will cause the vortices to move. The vortex motion produces an electric field parallel to J, thus causing a resistance, and this is called the flux-flow resistance. This resistance is much smaller than the normal state resistance, but the material no longer has infinite conductivity. In an inhomogeneous Type II superconductor containing various types of defects (grain boundaries, dislocation walls, dislocation tangles, voids, or second-phase precipitates), the flux vortices can be pinned by the defects (Schmidt *et al.* 1997). These point-defects or line defects can provide optimum pinning when their dimensions are close to the coherence length of the Cooper pairs in the superconductor.

When a vortex passes through a normal impurity region in a superconductor, the total energy dissipated is lower than when the vortex lies just outside the impurity. This is because there are more Cooper pairs in the sample in the former case, while the condensation energy is absent both in the vortex and in the impurity in the latter case. The pinning force (F_P) on the entire system of vortices in the superconductor is then the resultant of various pinning forces between individual vortices and impurity sites, and the interaction between vortices themselves. It is obvious that the pinning force increases with rise in number of individual pinning (or impurity sites), but the pinning force is lowered due to the rigidity of the vortex lattice which hinders distortions necessary for the vortices to pass through the random pinning sites. The pinning force prevents the motion of vortices until the Lorentz force (J × H) exceeds the pinning force F_P. This defines a critical current density, $J_C = F_P \times H$ below which transport current is carried without any resistance, and above which flux-flow resistivity sets in. In short, F_P depends on various factors including the field H, and J_C and has an intricate field and temperature dependence. Thus, the zero resistance property of a superconductor exists within an operating volume in the field-temperature-current density space, enclosed by the J_C, H_{C2}, and T_C lines.

Apart from the basic features, the thermal properties of a superconductor are also interesting. The specific heat is a measure of how effectively heat can be introduced into a material and helps raising its temperature. A related quantity is the thermal conductivity

which is a measure of how easily heat flows through a material from a region at a high temperature to a region at a low temperature. The specific heat of electrons in a superconductor varies with absolute temperature both in the normal and superconducting state (Gregersen *et al.* 2011). The specific heat in the superconducting state is smaller than that in the normal state at low temperatures, but superconducting specific heat becomes larger than normal specific heat as T_C is approached. At T_C, the specific heat drops abruptly to normal specific heat for the classical superconductors while the curve has a cusp shape near T_C for HTS. Precise measurements indicate that at temperatures much below T_C, the logarithm of the electronic specific heat is inversely proportional to the temperature. This temperature dependence analyzed on the basis of statistical mechanics strongly suggests that there is a gap in the distribution of energy levels for the electrons in a superconductor, which requires a minimum energy for the excitation of an electron from a state below the gap to a state above it.

Thermal conductivity of a material involves the transport of entropy. However, superconducting electrons do not scatter phonons and hence they carry no entropy. Below T_C, the entropy of a superconductor drops continuously to zero so that the thermal conductivity can be expected to decrease toward zero also. For all superconductors, the thermal conductivity in the normal state approaches the thermal conductivity in the superconducting state as the temperature approaches T_C. This suggests that the energy gap (Δ) for each electron approaches zero near T_C. This justifies the fact that electronic specific heat in the superconducting state is higher than that in the normal state near T_C. As the temperature is raised towards the T_C, the energy gap in the superconducting state decreases, the number of thermally excited electrons increases, and this requires the absorption of heat. In unconventional superconductors, with decreasing temperature the electronic contribution of thermal conductivity vanishes much more slowly due to the relatively large number of quasiparticles present in HTS.

1.3 Theories proposed for conventional superconductivity

Superconductors are defined by the electrodynamic properties - ideal conduction and magnetic-field repulsion. Since the discovery of superconductivity, great efforts have been devoted to find out how and why it works. Thus, it was thought appropriate to describe the phenomenon within the formal framework of electrodynamics. Some of the conventional theories are discussed below.

1.3.1 London Theory

In 1935, Fritz London and Heinz London presented Meissner effect as an outcome of the minimization of the electromagnetic free energy carried by super-current (London *et al.* 1935). They developed a phenomenological theory to describe the specific electrodynamics of superconductors. It is based on a two-fluid picture wherein the electrons are classified into two sets, one from a normal fluid of concentration n_n and the other from a superfluid of concentration n_s, where $n_n+n_s = n$, the total electron density. They introduced the following constitutive relation complementary to the Maxwell equations:

$$E = \frac{\partial(\Lambda J)}{\partial t} \qquad (1.1)$$

where, $\Lambda = \frac{m}{(n_s e^2)}$ with 'm' the effective mass of the electrons and 'e' the electron charge. The London equation together with the Maxwell equations led to:

$$\nabla^2 H = \frac{H}{\lambda^2} \qquad (1.2)$$

where, $\lambda^2 = \frac{mc^2}{4\pi n_s e^2}$, c - the speed of light in vacuum. This implies that a magnetic field applied on a superconductor is exponentially screened from its interior over a distance 'λ', thus accounting for the Meissner effect. The London equation was further modified using the vector potential A as:

$$J = -\frac{A}{\Lambda c} \qquad (1.3)$$

The actual value of n_s is temperature dependent, starting from zero at $T = T_C$ and continuously increasing up to the total density of conduction electrons n when $T \rightarrow 0$. If this upper limit n is inserted in Eq. (1.3), the so-called London penetration depth is obtained:

$$\lambda_L(0) = \left(\frac{mc^2}{4\pi n_s e^2}\right)^{\frac{1}{2}}$$

Without giving a microscopic explanation of the superconducting mechanism itself, the London theory described the superconducting behavior of extreme Type II superconductors. However, the theory failed to provide accurate information about the superconducting state for non-extreme Type II superconductors. Later in the 1950s, theoretical condensed matter physicists arrived at a concrete understanding of 'conventional superconductivity', delivering two noteworthy and significant theories: the

phenomenological Ginzburg-Landau theory (1950) and the microscopic BCS theory (1957).

1.3.2 Ginzburg-Landau theory

Ginzburg and Landau proposed a generalization of the London theory, introducing a complex wave function Ψ(r) for superconducting electrons, (wherein $|\Psi(r)|^2 = n_s/2$). This wave function was called as a complex order parameter which is zero in the normal state and has a finite value in the superconducting state. This theory is based on the theory of second-order phase transitions developed by Landau, according to which a phase transition of second order occurs when the state of a body changes gradually while its symmetry changes discontinuously at T_C.

Minimizing the Gibb's free energy in an applied field with respect to Ψ and A, a set of coupled nonlinear differential equations known as Ginzburg-Landau equations were proposed (Ginzburg *et al.* 1950):

$$\alpha\Psi + \beta|\Psi|^2\Psi + \frac{1}{2m^*}\left(-i\hbar\nabla - \frac{2e}{c}A\right)^2 \Psi = 0$$

$$j = -\frac{i\hbar e}{m^*}(\Psi^*\nabla\Psi - \Psi\nabla\Psi^*) - \frac{4e^2}{mc^*}|\Psi|^2 A$$

These Ginzburg-Landau equations allow determining the spatial variation of the order parameter and the current distributions. The theory also introduces two important characteristic length scales: the coherence length 'ξ' and the penetration depth 'λ'. The coherence length 'ξ', indicates the length scale over which the order parameter is allowed to vary without generating pair breaking kinetic energy and can be obtained from the first GL equation as:

$$\xi = \left(\frac{\hbar^2}{2m^*\alpha(T)}\right)^{1/2}$$

where 'ξ' has the dimension of length. The temperature dependence of the coherence length is given as: $\xi(T) = \xi_0\left(1 - \frac{T}{T_c}\right)^{-1/2}$ where the length ξ_0 is $\left(\frac{\hbar}{2m^*\alpha_0}\right)^{1/2}$

The penetration depth λ, over which the magnetic field varies can be obtained from the second GL equation as: $\lambda(T) = \left(\frac{m^*c^2\beta}{16\pi\alpha(T)e^2}\right)^{1/2}$

The penetration depth also has the same temperature dependence as that of coherence length, i.e. $\lambda(T) \propto \left(1 - \frac{T}{T_c}\right)^{-1/2}$

The temperature dependence of ξ and λ depends on the purity of the materials, defined by the electron mean free path $l_{el.}$

In the case of a clean superconductor, i.e. $l_{el} >> \xi_0$, the GL theory is valid if $\xi(T)$, $\lambda(T) >> \xi_0$. The condition $\lambda(T) >> \xi_0$ expresses again that the temperature must be close to T_C. In dirty superconductors ($l_{el} << \xi_0$), the validity interval for the GL theory is much wider (Tinkham 1975). In this case, the characteristic scale of inhomogeneity is the mean free path and the GL theory can be applied if $\xi(T)$, $\lambda(T) >> l_{el}$. Although the GL theory has been derived only close to the transition region, it turns out that its validity range is much larger. Moreover, the GL theory was able to explain experimental results for superconducting samples with sizes smaller than the coherence length ξ (Geim *et al.* 1997).

1.3.3 The microscopic BCS theory

The microscopic mechanism of superconductivity was described by Bardeen, Cooper and Schrieffer in 1957 (Bardeen 1957). In a normal conductor, an electrical current can be considered as a fluid of electrons moving across a heavy ionic lattice. The electrons constantly collide with the ions in the lattice, and during each collision some of the energy is absorbed by the lattice and converted into heat, mainly the vibrational kinetic energy of the lattice ions. As a result, there is constant dissipation of the energy carried by the current which is termed as the "electrical resistance". BCS theory assumes that there is an attraction between electrons, which overcomes the Coulomb repulsion, and forms pairs of electrons called Cooper-pairs. The Cooper electrons indirectly attract each other in the following manner: one electron slightly disturbs the lattice in its neighborhood. The resulting phonon interacts with another electron taking advantage of the deformation and lowers its energy. The second electron emits a phonon by itself which interacts with the first electron and so on. The passing back and forth of phonons couples the two electrons together and brings them into a lower energy state. A schematic representation of electron-phonon interaction is shown in Figure 1.8. Electrons in a Cooper-pair are placed on the Fermi surface and have opposite momentum and opposite spin. These electrons form a cloud of Cooper-pairs which drift cooperatively through the crystal. In order to destroy a Cooper-pair, all Cooper-pairs in a macroscopic region of the superconductor need to be destroyed. It requires much energy and hence the probability of the process is very small.

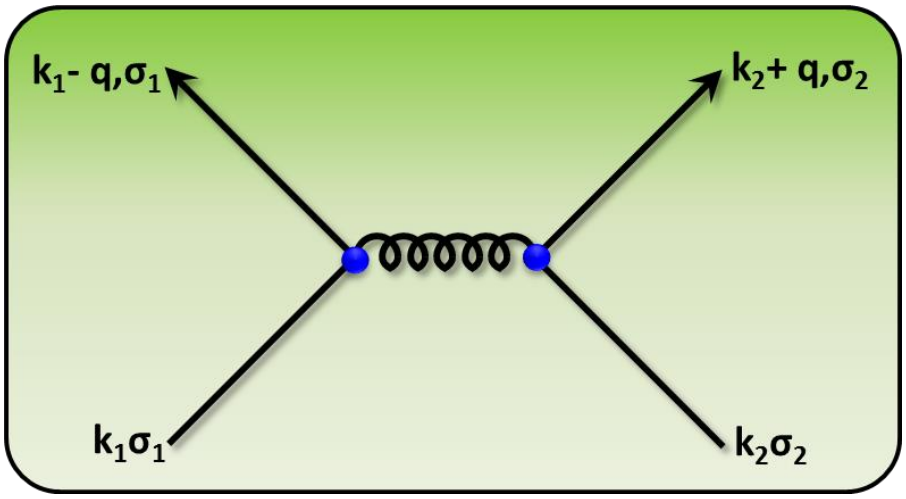

Figure 1.8: A schematic representation of electron-phonon interaction

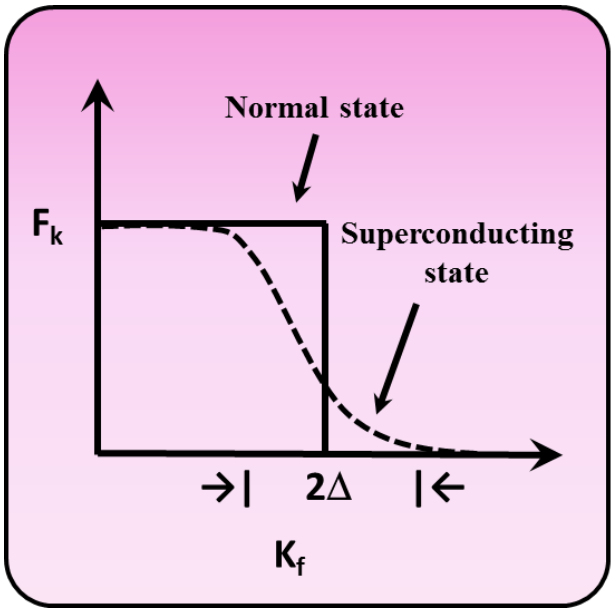

Figure 1.9: The Fermi function versus energy for a normal conductor and a superconductor and the energy gap between the two

Since the electrons of a Cooper-pair have a lower energy than two separate electrons, the Fermi energy of the superconducting state is supposed to be lower than that for the non-superconducting state. The lower state is separated from the normal state by an energy gap, E_g. The Fermi function versus energy for a normal conductor and a superconductor and the energy gap between the two are shown in Figure 1.9. If E_g is larger than the thermal energy of the lattice, the Cooper-pairs will not be scattered by the lattice and can flow without energy dissipation. Thus, the energy gap stabilizes the Cooper-pairs and prevents them from breaking apart, which causes zero resistance.

The BCS treatment of electron pairing defines the critical temperature as the temperature at which the gap is completely closed and the T_C is equated as

$$K_B T_c = 1.13\hbar\omega_D e^{-1/gN(0)},$$

where ω_D is the phonon frequency and gN(0) is the BCS coupling constant.

Thus, main results of the BCS theory summarize that it is possible to create bound states of electron pairs around the Fermi surface due to their interactions with lattice phonons. This attractive s-wave pairing gives rise to a modified energy spectrum of the conduction electrons, with a gap between the ground state and the first excited states corresponding to the minimal excitation energy of Bogoliubov's quasiparticles, which correlate electrons with opposite momenta and spins close to the Fermi level. This energy gap has definite temperature dependence, and the temperature at which it vanishes thereby restituting the original energy spectrum of non-paired electrons, gives the critical temperature for the superconducting transition. The BCS microscopic theory gives an excellent account of the data in those cases where the energy gap is constant in space.

In Type I superconductors, one has to consider spatial inhomogeneity at the interface where the superconducting state is joined into the normal state. This sort of spatial inhomogeneity becomes more prevalent in the mixed state of Type II superconductors. In such situations, the fully microscopic theory becomes very difficult, and much reliance is placed on the more macroscopic Ginzburg-Landau theory. Moreover, BCS theory suffers many drawbacks such as: a) it is a weak coupling theory ($\lambda << 1$), b) it neglects both electron-electron Coulomb interaction and electron-phonon retardation effects, and c) it lacks predictive power.

It is interesting to note that London theory is a limiting case of both GL theory and BCS theory. In 1959, after two years of BCS discovery, Gor'kov showed that the GL theory is valid near T_C and suitable to deal with spatially varying situations thus establishing the relationship between the various conventional theories of superconductivity (Gor'kov 1959).

1.4 Mechanisms proposed for unconventional superconductivity

Based on the BCS theory and its extensions, it was understood that superconductivity occurred only at temperatures around 23 K (Nb_3Ge) and was restricted to non-magnetic metallic elements and simple compounds. In 1979, when superconductivity was observed in various materials classes that differ from each other and from the typical LTS superconductors already known, the preconceived notions changed. Further, the T_C observed in most of the materials were rather high and superconductivity seemed unconventional. The discovery of high temperature superconducting (HTS)

materials again showed the limits of the BCS theory. An even more puzzling discovery was the announcement of superconductivity in MgB_2 at 39 K. The surprise was not the critical temperature itself but the fact that MgB_2 behaves as a Type II superconductor with two kinds of electrons, yet being a conventional superconductor. The mechanism of the new kind of superconductivity still remains one of the most enigmatic problems in the solid state physics. One of the perspectives of the term 'unconventional' refers to superconductors with order parameters having a lower rotational symmetry than the normal-state crystal. This broken rotational symmetry may occur in real space, or in both real space and spin space (Muzikar 1997). Conventional superconductors are well described by the s-wave order parameter which implies isotropic attractive forces between electrons in all spatial directions. But the order symmetry in unconventional superconductors appears to be much more complex. The high T_C superconductors have a d-wave order parameter, implying a strong directional dependence of their electron-electron interactions. However, unconventional superconductivity becomes a problem due to different issues such as complicated crystalline structures having high T_C, presence of a strong anisotropy, existence of non-adiabatic effects and strong electronic correlations instead of electron-phonon interaction (Askerzade 2012; Anderson 1997). Moreover, certain unconventional superconductors exhibit several phase transitions and mixed states such as the coexistence of superconductivity and ferromagnetism or vitreous spin state.

In high T_C cuprates, which possess not only very high values of T_C but also exhibit physical properties inexplicable by the classical BCS scheme; the key structural element is a CuO_2 plane. Here, charge carriers appear due to the doping of the CuO_2 planes of a parent antiferromagnetic insulator upon aliovalent substitution or by the creation of oxygen vacancies in charge reservoirs outside the conducting planes. The distance between CuO_2 planes in neighboring unit cells is large compared to the in-plane distance between neighboring copper atoms causing strong conductivity anisotropy at temperatures above T_C and the two-dimensional coherence of the superconducting state at temperatures below T_C. Strong electron correlations, unusual symmetry of the pseudo-gap and the superconducting order parameter in cuprates strongly suggest an electron based superconducting mechanism rather than a BCS phonon mechanism or Eliashberg theory (Yu *et al.* 2008). The Hubbard model and the related t-J model are some of these mechanisms. The two-dimensional Hubbard problem has no accurate solutions and approximate solutions given by numerical methods are often contradictory, which doubts about the credibility of this approach, since

the unusual isotopic effect in cuprates indicates a nontrivial role of phonons in pairing-interaction formation.

1.4.1 Hubbard model

Estimates of T_C made on the basis of phonon-exchange and the experimentally derived values of the Debye frequency, the electron-phonon coupling, and the normal-state density of states are much lower than the observed T_C in HTS. Also, BCS phonon interaction is flat in k-space, which favors an s-wave gap. An s-wave gap is inconsistent with nearly all experiments on the cuprates that are sensitive to the gap. It is observed that d-wave pairing in the cuprates is probable if there is an attractive interaction for momentum transfers q ≈ (π/a, π/a). The parent or undoped cuprates are found to be antiferromagnetic. A slight hole doping or a stronger electron doping helps in disturbing the antiferromagnetic order and upon larger doping, superconductivity emerges. However, further doping (the "over-doped" region) suppresses superconductivity again.

The two-dimensional single-band repulsive Hubbard model is thought to be the simplest model that captures the main physics of the cuprates. The Hubbard model can be considered as an upgrading over the tight-binding model, which includes the hopping term only (Hubbard 1963). For strong interactions, it proposes a qualitatively different behavior from the tight-binding model and properly predicts the existence of so-called Mott insulators. The Hamiltonian in real space for the Hubbard model is composed of two terms as follows,

$$H = -\sum t_{ij} c_{i\sigma}^{\dagger} c_{j\sigma} + U \sum c_{i\uparrow}^{\dagger} c_{i\uparrow} c_{i\downarrow} c_{i\downarrow}^{\dagger} \text{ , with U > 0}$$

Where, c and $c^{\dagger}$ are the creation and annihilation operators respectively, 'U' the on-site energy and 't' the kinetic energy.

Also, the undoped cuprate compounds have an odd number of electrons per unit cell. Thus for them the single band must be half-filled while for doped cuprates it is close to half filling. The lattice in real space is a two-dimensional square lattice with each site 'i' corresponding to a copper ion. In the Hubbard model, electrons move around in the two-dimensional space by hopping among discrete sites arranged in the square lattice and interact with each other whenever they are on top of each other at the same site. Mathematically, the Hubbard model is defined simply as a sum of the kinetic and the interaction energy term. For the kinetic energy or the hopping integral term, only the nearest-neighbor hopping is often considered for convenience:

$$H = -t \sum_{\langle i,j \rangle,\sigma} \left(c_{i\sigma}^{\dagger} c_{j\sigma} + c_{j\sigma}^{\dagger} c_{i\sigma} \right)$$

where <i,j> denotes that i and j are the nearest neighbor, and σ indicates the spin index, ↑ and ↓. For the interaction energy term, the on-site energy, U, is chosen to be either negative or positive depending on whether the interaction between electrons is attractive or repulsive:

$$H_U = U \sum_i n_{i\uparrow} n_{i\downarrow}$$

where $n_{i\sigma}$ is the number of electrons at site i with spin σ. Technically, $n_{i\sigma} = c^{\dagger}_{i\sigma} c_{i\sigma}$.

Attractive Hubbard model

The attractive Hubbard model is a natural model for superconductivity, where the BCS theory can be applied in the form of a mean-field theory. Then, the mean- field Hamiltonian becomes as follows:

$$H = -t \sum_{\langle i,j\rangle,\sigma} \left(c^{\dagger}_{i\sigma} c_{j\sigma} + c^{\dagger}_{j\sigma} c_{i\sigma}\right) + |U| \bar{O} \sum \left(c^{\dagger}_{i\uparrow} c^{\dagger}_{i\downarrow} + c_{i\downarrow} c_{i\uparrow}\right) + |U| \sum_i \bar{O}^2 - \mu \sum_{i,\sigma} c^{\dagger}_{i\sigma} c_{i\sigma},$$

where the fourth term is the chemical potential term, added to tune the electron density.

Repulsive Hubbard model

Since the discovery of high-temperature superconductivity, intensive attention has been given to the repulsive Hubbard model particularly in the strong coupling regime where U is much larger than t. This seems to be oxymoronic since pairing requires an attractive interaction, not repulsive. The central mystery of high-temperature superconductivity is the possibility of repulsive interaction to induce pairing.

1.4.2 t-J model

The t-J model was deduced from the Hubbard model by Jozef Spalek, in 1977 (Spalek 2007). It represents a very non-trivial model of strongly correlated fermions due to the following reasons:

1. It represents a system of strongly inter-correlated itinerant fermions which transform into an antiferromagnetic state of localized particles (the Mott-Hubbard insulator); the classic situation takes place at the half filling state, with n = 1. The half-filled state is an antiferromagnetic insulator modeled by the Anderson kinetic exchange.
2. The itinerant state is represented by particles called the correlated holes in the Mott-Hubbard insulator, which do not have the ordinary fermion properties. They cannot be represented by Landau quasi-particles since they do not represent almost-filled band states.

3. The magnetic interaction between the correlated itinerant particles i.e. the kinetic exchange is also regarded as the source of real-space pairing as it takes place between the nearest neighbors. Hence, antiferromagnetism and the newly paired state must be regarded on equal footing with the paired state (resonance valence bond state or superconducting state). This is particularly relevant in the context of high temperature superconductivity near the band filling, i.e. close to the Mott transition.
4. Due to the non-trivial character of the kinetic energy, it can become comparable or even smaller than the kinetic-exchange-energy part. Thus, magnetic polaron or phase-separated states or a new type of spin-paired states can be formed, parallel to the transition to a localized state for a small carrier concentration of holes.

Until 1987, the t-J model was regarded as a generic model for explaining the antiferromagnetism of Mott insulators and relatively rarely considered for n ≠ 1. Later, it was argued strongly that the p - d hybridization can be incorporated into an effective d-band Hubbard model. The t-J Hamiltonian is given as:

$$H = -t \sum_{\langle ij \rangle \sigma} \left(\bar{c}_{i\sigma}^{\dagger} \bar{c}_{j\sigma} + \bar{c}_{j\sigma}^{\dagger} \bar{c}_{i\sigma} \right) + J \sum_{\langle ij \rangle} (\bar{S}_i . \bar{S}_J - n_i n_j / 4)$$

Where c and $c^{\dagger}$ are the creation and annihilation operators, respectively, 'U' the on-site energy, 't' the kinetic energy, 'σ' the spin index and 'S' the spin operator.

1.4.3 Gutzwiller Approximation

Gutzwiller proposed the projected wave functions in 1963 to study the effect of correlations presumed to induce ferromagnetism in transition metal compounds (Gutzwiller 1963). Later, these wave functions were used to study the Mott-Hubbard metal insulator transition and for a description of liquid ^{3}He as an almost localized Fermi liquid (Brinkman *et al.* 1970). However, these early studies considered only a projected Fermi sea, in the Hubbard model, whereas Anderson proposed a projected BCS paired wave function for the t-J model. Gutzwiller formulated the approximation for describing electrons with strong local interactions in terms of the Gutzwiller wave function, composed of a many-electron wave function acted on by a correlation operator, Gutzwiller projection. Majority of the techniques used to analyze Gutzwiller projected wave functions address the calculation of single particle spectral features. The Gutzwiller projection operator projects out all doubly occupied sites. This is a projection in the mathematical sense since it lowers the dimensionality of the space of wave functions (a Hilbert space), which has the benefit of reducing the computational complexity of the problem. The Gutzwiller projector determined so as to minimize the ground state energy is given by:

$$P = \prod_i (1 - n_{i\downarrow}\, n_{i\uparrow})$$

The Gutzwiller Approximation is a straightforward method to handle Gutzwiller projected wave functions, which incorporate strong electron correlations by prohibiting doubly occupied sites. Within the approximation, the effects of projection are absorbed by statistical weight factors, which then allow for an analytical treatment of strongly correlated Gutzwiller wave functions. Gutzwiller projected wave functions have the advantage that they can be studied both analytically and numerically. These wave functions are used to study correlations such as pairing correlations and magnetic correlations, in a large Hubbard repulsive interaction. Gutzwiller-Resonating Valence Bond theory of superconductivity explains several key features of the HTSCs (Edegger *et al.* 2007). Moreover, it could be used to study a wide range of physical phenomena in the proximity of a Mott transition.

1.4.4 Resonating Valence Bond (RVB) theory

In 1972, even before the discovery of HTSC, Anderson considered alternative ground-state wave functions on the square lattice which can compete with the Neel antiferromagnet (Anderson 1973). Anderson was inspired by L. Pauling's work, who had successfully described the chemical structure of benzene molecules as quantum-mechanical superpositions of different valence-bond configurations and hence the name resonating-valence-bond (RVB) (Pauling 1949; 1953). Pauling had also applied these ideas to valence electrons in solids. Soon after the discovery of high T_C superconductivity, Anderson suggested the concept of an RVB state as relevant for the HTSCs. In RVB, the half-filled Hubbard model is a Mott insulator with one electron per site. The charged states, doublons and holons, form bound charge-neutral excitations in the Mott insulating state and lead to the vanishing of electrical conductivity. Equivalently, virtual hopping can cause a super-exchange interaction J between the electrons at the copper sites. Therefore, the half-filled systems can be regarded as Heisenberg antiferromagnets with a coupling constant J.

According to Anderson, upon doping, quantum fluctuations melt the antiferromagnetic Neel lattice and create a spin liquid ground state (called as the RVB state) in which the magnetic singlet pairs of the insulator become the charged superconducting pairs. The RVB theory provides a clear explanation for several important features of the high T_C materials such as the d-wave pairing symmetry, the shape of the superconducting dome, the existence of a pseudogap phase, the strong deviations from the

BCS ratio and the singular k-dependence of the one-particle self-energy when approaching half-filling.

Anderson's proposal to understand HTS as a doped spin liquid is very sophisticated and interesting. A wave function with resonating singlets and no translational symmetry breaking (termed spin liquid by Anderson) is represented as

$$|RVB\rangle = P_d \left[\sum_{i,j} \tilde{a}\,(r_i - r_j) b_{ij}^{\dagger}\right]^{N/2} |0\rangle = P_d \left[\sum_{i,j} \tilde{a}\,(r_i - r_j) c_{i\uparrow}^{\dagger} c_{j\downarrow}^{\dagger}\right]^{N/2} |0\rangle$$

The product produces states containing N/2 singlets. Those states which contain doubly occupied sites are then removed using the Gutzwiller projector. |RVB⟩ is a superposition of all singlet-product states with bond occupation probability a(r). The RVB wave function is a variational state for the t-J model. Indeed, it was found by Gros and Yokoyama et al. in 1988 that a BCS wave function with d-wave gap symmetry is a favored variational state of the t-J model for a large range of doping. The energy gain of this state is mainly due to the spin-exchange term as we expect from Anderson's arguments. It took many years until the experimental technique of angle-resolved photoemission spectroscopy (ARPES) was accurate enough to confirm the d-wave gap symmetry in the superconducting phase of the cuprates.

1.4.5 Spin fluctuation models

While the RVB theory approaches the problem from the strong coupling limit, i.e. large on-site electron repulsion U, spin fluctuation models start from the weak coupling (small U) limit (Edegger 2007). The model extends the Hartree-Fock random phase approximation and leads to a pairing state with d-wave symmetry. Within this model, superconductivity is mediated by the exchange of antiferromagnetic spin fluctuations. In unconventional superconductors, superconductivity is often found in the vicinity of antiferromagnetism and it rarely coexists with the magnetic order. It is true for most of the iron pnictides and heavy-fermion superconductors. The vicinity of a magnetically ordered phase makes itself felt by strong magnetic fluctuations and strong but short-range, spin correlations, observed as enhanced spin susceptibility. During magnetic second-order phase transition, the static spin susceptibility χ_q diverges at q = Q, where Q is the ordering vector. It is Q = 0 for ferromagnetic order and Q = (π/a, π/a) for checkerboard (Neel) order on a square lattice. Even at a distance from the transition or at non-zero frequencies, the susceptibility tends to have a maximum close to Q. Beyond the magnetic phase or at high frequencies the remnant magnetic order becomes small. It can be concluded that the

exchange of spin fluctuations could provide the attractive interaction needed for Cooper pairing (Timm 2012).

1.5 Technological applications of superconductors

The superconducting technology integrates various technologies by considering its research history, present status, future prospects, and the application in energy, transportation, and communications. Even after celebrating the 100th anniversary of the discovery of superconductivity, the applications of superconductivity are still limited to specific purposes that require ultimate performance. The major reason lies in the cooling penalty. However, superconductivity is a unique phenomenon involving a persistent current, perfect diamagnetism, and the Josephson Effect, which cannot be imitated. Lance Cooley, who is based at the Fermi National Accelerator Laboratory, says: "Superconductivity has been meeting some great challenges over the past 50 years. The Large Hadron Collider, mankind's largest machine, would not exist without superconductivity…..new materials and technologies enable researchers and entrepreneurs to be more versatile and apply superconductivity in other ways that contribute to our everyday lives, such as innovations to benefit our environment".

A majority of the current extensions of technology still rely on the low temperature superconductors. Applications of high T_C superconductors include magnetic shielding devices, medical imaging systems, superconducting quantum interference devices (SQUIDS), infrared sensors, analog signal processing devices, and microwave devices. With the flight of time in understanding of the properties of different superconducting materials, applications such as power transmission, superconducting magnets in generators, energy storage devices, particle accelerators, levitated vehicle transportation, rotating machinery, and magnetic separators will become more practical. However, this is also closely related to the development of analytical equipment and technologies depending on progress in comprehensive technologies beyond superconductivity technologies.

The most promising application of superconductors is strong magnets that exploit their zero resistance. The first commercial application of superconductivity in large scale was magnetic resonance imaging (MRI). It is a non-intrusive medical imaging technique that creates a two-dimensional picture of tumors and other abnormalities within the body or brain. This requires the patient to be placed inside a large and uniform electromagnet having a high magnetic field. The normal electromagnets have issues such as higher dissipation of heat and requirement of large amount of power; owing to their resistive nature. Superconducting magnets, instead, need power only to maintain the cool

environment. Once current starts flowing in the superconducting wire, the power supply can be switched off as the wires remain superconducting in persistent mode as long as the temperature is kept below the T_C of the superconductor.

Nuclear magnetic resonance (NMR) spectroscopy, a standard technique for determining protein structures that provides extremely precise information on the structure of molecules around the atom in interest, is also making use of superconductors. NMR systems with normal magnets are now being replaced by systems using superconducting magnets as cutting-edge analytical systems in universities and institutions so as to further increase its resolution. Researchers have also attempted to fabricate NMR magnets that produce magnetic fields above 20 T, by cooling high-temperature superconducting magnets to liquid helium temperature (Kitazawa 2012).

Table 1.1: A tabular comprehension of some superconductivity applications

Application	Being used currently	Emerging areas
Medical	**Magnetic Resonance Imaging**	**Biotechnical Engineering**
Electronics	**Squids** **Particle Accelerators** **Sensors**	**Transistors** **Josephson junction Devices** **Circuitry Connections**
Industrial	**Separation** **Magnets**	**Sensors and Transducers** **Magnetic Shielding**
Power Generation		**Motors** **Generators** **Energy Storage** **Transmission** **Fusion** **Transformers and Inductors**
Transportation		**Magnetically Levitated Vehicles** **Marine Propulsion**

One of the other remarkable applications of superconducting magnets is motors for ship propulsion. Motors for automobiles are the candidates standing next to it. In both cases, stronger magnetic fields having rotating rotors will be available, the torque at low speeds increases, energy efficiency can be improved, and the motor size can be reduced. This will help saving space, reducing noise, and improving steering performance. On a small scale, the industrial application of superconducting magnets has also been launched. A few examples of industrial applications include recycling of resources, separation of minerals, the magnetic treatment of waste water, single crystal growth furnaces and accelerators for particle radiation cancer therapy (Kitazawa 2012).

The applications of superconductivity using its coherent electron properties, such as diamagnetism and the Josephson Effect are still very limited. Typical applications of these properties include preamplifier devices used in radio astronomy observatories and superconducting quantum interference devices (SQUIDs) used in magneto-encephalography and magneto-cardiography for studying the functions of the brain and heart. SQUIDs are so sensitive to small magnetic fields that it can detect the magnetic fields from the heart (10^{-10} T) and even the brain (10^{-13} T). For comparison, the Earth's magnetic field is about 10^{-4} Tesla. As a result, SQUIDs are used in non-intrusive medical diagnostics on the brain. They are also used to detect and safely recover unexploded ordinances (UXOs). Thousands of UXOs are discovered each year around Europe, especially in areas that were heavily bombed during the Second World War. A complete network of SQUIDs speckled around the globe could also aid the detection of solar bursts which send magnetic particles hurtling towards Earth. A similar network could also help detect the specific magnetic signature of earthquakes before they strike (Kitazawa 2012).

The superconductors are traditionally used in scientific research where high magnetic field electromagnets are required. The cost of keeping the superconductor cool is much smaller than the cost of operating normal electromagnets, which dissipate heat and have high power requirements. One such application of powerful electromagnets is in high energy physics where beams of protons and other particles are accelerated to almost light speeds and collided with each other so that more fundamental particles are produced. It is expected that this research will answer basic questions such as those about the origin of the mass of particles that make up the universe. In fact, all high-energy accelerators built since the 1980s make use of superconducting acceleration cavities and/or magnets. The LHC, the latest stage in this evolution, has 1250 superconducting dipoles operating at 8.33 T, 400 superconducting quadrupoles producing gradients of 223 Tm^{-1} and thousands of other superconducting magnets for correcting multipole errors, steering the beams and increasing luminosity in collision (Lebrun 2000).

Large and powerful superconducting electromagnets will possibly turn up as future energy source known as nuclear fusion. Nuclear fusion results in the release of large amounts of energy without any harmful waste. Two isotopes of hydrogen, deuterium and tritium, will fuse to release clean nuclear energy and helium. For this reaction to occur, the deuterium and tritium gases must be heated to millions of degrees so that they become fully ionized. For this, they must be confined in space so that they do not escape while being heated. Powerful and large electromagnets made from superconductors are capable

of confining these energetic ions. An international fusion energy project, known as the International Thermonuclear Experimental Reactor (ITER) uses large superconducting magnets and is due for completion in 2017 (Koizumi 2013).

Another area that is already progressing with the help of superconducting technology is high-speed rail travel. Magnetically Levitating (Maglev) trains, whereby the carriage is levitated by magnets and has no contact with the track, have already been deployed in Germany, China, Japan and Brazil. Japan Railways (JR) is carrying out a unique project of a superconducting magnetically levitated train (JR-Maglev), which is levitated using persistent-current-mode superconducting magnets and runs at a high speed without coming into contact with the rails (Kitazawa 2012). JR-Maglev does not require power supply via a pantograph because onboard superconducting magnets operate in persistent current mode. The absence of pantographs avoids the delay of trains due to power failure making JR-Maglev highly advantageous. Moreover, in JR-Maglev the levitation method uses the same coils for both levitation and guidance for midway from the left and right sidewalls. The levitation-guide coils are not connected to any external power source, and both ends of each individual coil remain just closed. Upon the approach of onboard magnets, a faradaic current is induced in the levitation-guide coils to repel the magnets.

Another promising application of superconductors is in power transmission cables. Overcoming technological difficulties in the development of superconducting materials, the target performance of high-temperature superconducting wires was finally achieved in 2005, two decades after the discovery of the high-temperature superconductivity. An electric current flow that is 10 to 100 fold larger than that through Cu cables with the same cross-sectional area is now possible. Currently, so-called ‘‘smart grids’’ are attracting attention, and various countries are planning their power supply strategies by considering that a superconducting core network will ultimately form the backbone of the power transmission system. Similarly, the size and power consumption of conventional power generators set up at the top of tall towers for wind power generation are also expected to be downsized by replacing those with superconducting power generators. The increased torque at low speeds will make gears unnecessary and will be highly advantageous for the use of superconducting generators in large wind power plants at sea (Kitazawa 2012).

The list of applications and areas befitting the superconducting technology is limitless as we go on unraveling the possibilities and outreach of this fascinating

phenomenon. However, now it is under the spotlight and the scientific community will undoubtedly make advantage of it.

CHAPTER 2

FEATURES OF IRON BASED SUPERCONDUCTORS

2.1 High T_C in iron pnictides - a new era of superconductivity

The fortuitous discovery of superconductivity in an iron based compound LaFePO, while looking for device application of transparent oxide semiconductors, prompted the Japanese group led by Hideo Hosono to replace the pnictogen, phosphorous with arsenic and to substitute oxygen with fluorine thereby observing a T_C of 26 K in $LaFeAsO_{1-x}F_x$ (Kamihara *et al.* 2006; Kamihara *et al.* 2008). This was reported as a two-page paper in *J. Am. Chem. Soc.* in 2008 followed by record breaking publications in arXiv (Ishida *et al.* 2009; Ren(a) *et al.* 2009). The T_C values were raised above 50 K within no time and this broke the monopoly of cuprates as high temperature superconductors. The condensed matter physicists were tantalized by the discovery especially the Chinese groups as one of the science magazine title says "New Superconductors Propel Chinese Physicists to Forefront" and sooner this class of superconductors witnessed considerable progress in materials synthesis, measurements on physical properties and theoretical understandings. Thus, fundamental and applied research in iron pnictides turned out to be a new problem for material scientists in addition to the time-honored problem of cuprates.

Iron based layered pnictide oxides have sparked immense interest in the chemistry and physics communities reminiscent of the superconductivity in high T_C cuprates during 1980s. Pnictide oxides popularly known as 'oxypnictides', are a unique class of compounds. Group 15 elements (excluding nitrogen) are called 'pnictogens' or 'pnicogens', and their anionic forms or compounds containing anionic pnictogens are called 'pnictides' (Ozawa *et al.* 2008). Pnictide ions are often found in compounds without oxygen in their components. Usually, pnictogen and oxygen co-exists as 'pnictates' where pnictogens are cations due to the high electronegativity of the coexisting oxygen. In contrast to pnictate compounds, 'oxypnictides' accommodate both pnictogen and oxygen as anions. This unique anionic environment of oxypnictides tends to have characteristic structures that are seldom observed in simple oxides. The iron based superconductors could be broadly divided into two classes. The first class is iron pnictide materials, including REFeAsO (1111 system) (where RE is a rare earth) with ZrCuSiAs-type structure, $BaFe_2As_2$ (122 system) with $ThCr_2Si_2$-type structure, and LiFeAs (111 system) with PbFCl-type structure. Another class is the iron chalcogenides: FeCh (Ch-

chalcogenides) compounds (11 type) and recently discovered new $A_xFe_2Se_2$ (A=alkaline earth metals) systems formed by introducing charge reservoir layers between FeCh sheets. Many more iron based compounds with different and novel structures were found and thus a whole class of iron based superconductors was established in a short time. The characteristic features such as layered structure, antiferromagnetic metallic parent compound, relatively smaller anisotropy, different order symmetry, less sensitive conductive layer allowing any site substitution are the fascinating factors of iron pnictides to mention a few. The superconducting properties of these materials such as relatively high T_C, moderate J_C and upper critical fields as high as 300 T are also captivating. Though the factors such as highly reactive ingredients (rare earth and alkaline earth metals), toxicity and volatility of arsenic and trickier chemistry of the compounds are major hurdles; the discovery of superconductivity in iron pnictides has begun a new era by opening up a number of research avenues both in understanding the superconducting mechanism and molding of promising candidates suitable for technological applications.

2.2 Crystal, electronic and magnetic structure of RE1111 system

As for any functional material, the structure-property correlation has a significant role in superconductors also. Every superconductor discovery is followed by a series of experiments and theoretical predictions probing the crystal, electronic and magnetic structure of the material and its association with the occurrence of superconductivity.

2.2.1 Crystal structure

Among the pnictide oxides, those with a ZrCuSiAs-type (tetragonal, P4/nmm) structure have been under intense scrutiny since the recent discovery of superconductivity in LaFeOP (Kamihara *et al.* 2006). These equiatomic quaternary pnictide oxides LnMPnO (Ln = Y, lanthanide, actinide; M = d-metal; Pn = pnictogen) with the ZrCuSiAs-type structure is the largest family of layered d-metal pnictide oxides. The crystal structure of ZrCuSiAs-type pnictide oxides is shown in Figure 2.1. This structure consists of alternating fluorite-type $[M_2Pn_2]$ layers and anti-fluorite type $[Ln_2O_2]$ layers. The fluorite-type $[M_2Pn_2]$ layer consists of square nets of M capped with Pn alternately above and below the net centers. In this layer, M is tetrahedrally coordinated by four Pn, and Pn is coordinated by four M to form square-pyramids. The anti-fluorite-type $[Ln_2O_2]$ layer also has the same configuration of atoms, but it is in the reverse manner: O is tetrahedrally coordinated by four Ln, and Ln is coordinated by four O to form square-pyramids. This multi-layer architecture of pnictides with tetrahedral network of FeAs layers correspond to

the featured planar CuO_2 plane in cuprates and honey-comb 2D lattice of boron in diborides, underline the relevance of lattice effects for high-temperature superconductivity. In other words, the structure of the iron pnictide superconductors is a practical realization of a 'heterostructure at the atomic limit' that was described to be the essential material architecture for the emergence of HTS.

Hopping between Fe atoms with mediating As ions is expected to give the major contribution to the kinetic energy and to the exchange interaction leading to the emergence of superconductivity. Here, the dependence of the electronic properties on the crystal structure i.e. the distortion of the As tetrahedron formed by the Fe-As bonds is quite interesting (Calderón *et al.* 2009). This dependence is of importance for both weak coupling models based on nesting properties and strong coupling models based on super-exchange interaction, aimed at explaining the properties of these systems. For each family of iron pnictides, the As tetrahedron exhibits different distortions. It is almost regular in the 122 family with the four As-Fe-As angles close to the ideal value, 109.47° while it is elongated in LiFeAs (the As^{top}-Fe-As^{top} angle is 102.8°). Here, As^{top} refers to an As atom placed above the Fe plane. In the 1111 family, the tetrahedron is squashed and the As^{top}-Fe-As^{top} angle depends on the specific composition, being equal to 113.7° in LaFeAsO and 120.6° in LaFePO. Differences in the electronic properties of these compounds have been attributed to the different distortion of the tetrahedral. The As-Fe-As angle is also sensitive to doping and can be deeply modified under pressure. At optimal doping concentration the tetrahedron in $Ba_{1-x}K_xFe_2As_2$ changes from squashed (in underdoped) to elongated (in overdoped) and under high pressures the tetrahedron in $CaFe_2As_2$ collapses. A possible correlation between the critical temperature and the As-Fe-As angle suggests that, within a class of iron pnictides, deviations from the regular tetrahedron turns detrimental for superconductivity (Calderon *et al.* 2008; Singh *et al.* 2008; Ganguli *et al.* 2011). It is also argued that there is a correlation between stronger interaction and higher critical temperature in iron pnictides due to a narrower bandwidth for the regular tetrahedron. This argument seems to be supported by the lower critical temperatures and lack of structural distortion and magnetism in LiFeAs and LaFePO. An unusually large sensitivity of the iron moment and the band structure to the separation of the As atoms with respect to the plane has also been found in density functional theory calculations.

It has been found that the Fe-As bond length hardly shows any change, suggesting the strongly covalent nature of this bond, while the Fe-Fe and Fe-RE bond lengths decrease with decreasing rare-earth size. In support of the important role played by the local

structure, transmission electron microscopy (TEM) images of 1111 compounds show complex structural transitions in both crystalline symmetry and local microstructural features. The structural instability due to the proximity to a structural phase transition is accompanied by a magnetic instability. In SmOFeAs, NdOFeAs and PrOFeAs the tetragonal–orthorhombic phase transition is found on cooling below 135, 136 and 150 K, respectively. This transition precedes magnetic ordering in the parent 1111 compounds, whereas both transitions occur simultaneously in 122 systems.

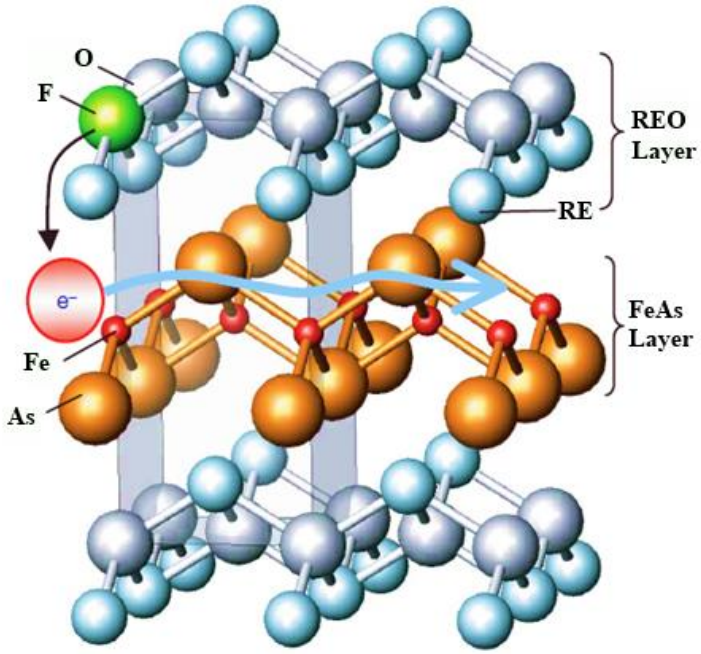

Figure 2.1: The crystal structure of $REFeAsO_{1-x}F_x$ based superconductors

There have been some dozens of iron based superconductors discovered so far, classified into many groups. The superconducting transition temperature T_C scatters from 10 K to 55 K, somewhat depending on the structural parameters such as the bond angle of As-Fe-As and the height of As with respect to the Fe plane. In fact, the maximum T_C also depends on the type of doping since doping brings about structural modifications which in turn decides the T_C variation.

2.2.2 Electronic structure

Within the Fermi liquid theory for conventional metals, charge-carriers are described as travelling waves or Bloch states whose ensemble of allowed wave-vectors describes a three dimensional surface in reciprocal space called the Fermi-surface. From the geometry of this Fermi surface one can infer fundamental properties of any given metal such as the tendency towards an itinerant magnetic instability, associated strength of spin-

fluctuations, and the compatible symmetries for a superconducting gap. Band-structure calculations along with density of states and the Fermi surface topology could provide the first glimpse of electronic structure in the iron based superconductors (Singh *et al.* 2008). A typical plot showing the band structure calculations and total density of states for LaFeAsO is given in Figure 2.2 (a) (Singh *et al.* 2008). Unlike the cuprates, the parent compounds of iron pnictides are metals, instead of insulators. The first-principle calculations showed that the energy bands near the Fermi surface are mainly contributed by the Fe '3d' orbitals, together with some contribution from As 'p' orbitals, within several eV of the Fermi level. In the FeAs layer, the Fe atoms form a square lattice and an Fe atom is coordinated by four As atoms in a tetrahedron. In fact, there are two Fe atoms in each unit cell due to the staggered arrangement of the As ions above and below the square palette of Fe. Due to the direct Fe-Fe bonds and the hybridization with the As '4p' orbitals, the Fe '3d' orbitals form a complex band structure. But, according to Mazin, it is in fact relatively simple to unfold the band structure to the extended Brillouin zone (BZ) corresponding to the one Fe unit cell (Mazin *et al.* 2008). Thus, several simplified tight-binding models have been proposed, ranging from the simplest two-orbital models including only the 'd_{xz}' and 'd_{yz}' orbitals of the Fe atom, the three-orbital models by including the 'd_{xy}' orbital into the two-orbital models, to the more sophisticated five-orbital model including all the five '3d' orbitals of the Fe atom (Li(d) *et al.* 2013).

Further, different experiments such as neutron magnetic scattering, quantum oscillation measurements and angular magneto-resistance measurements were also done to probe the Fermi surface (FS) of iron pnictides. The calculated density functional theory (DFT) Fermi surfaces (Ren(a) *et al.* 2009) for undoped LaFeAsO consist of two small electron cylinders around the tetragonal M point and two hole cylinders, plus a heavy 3D hole pocket around Γ as shown in Figure 2.2 (b). The high symmetry points are defined as Γ(0, 0, 0); X(0.5, 0, 0); S(0.5, 0.5, 0); Y(0, 0.5, 0) and Z(0, 0, 0.5), in terms of reciprocal lattice vectors. To be specific, the Fermi surface has five sheets including two high velocity electron cylinders around the zone edge M-A line, two lower velocity hole cylinders around the zone center, and an additional heavy 3D hole pocket, which intersects and anti-crosses with the hole cylinders, and is centered at Z. The heavy 3D pocket is derived from Fe 'd_z' states, which hybridize sufficiently with As 'p' and La orbitals to yield a 3D pocket. The electron cylinders are associated with in-plane Fe 'd' orbitals and have higher velocity and make larger contribution to the in-plane electrical conductivity. The electronic structures and Fermi surfaces of the 122 and 111 phases were also investigated with the

density functional calculations. The Fermi surfaces of 122 are similar to those in LaFeAsO, but the hole Fermi surface at the Z point is flattened out, suggesting a more three-dimensional character than that in the 1111 and 111 structures.

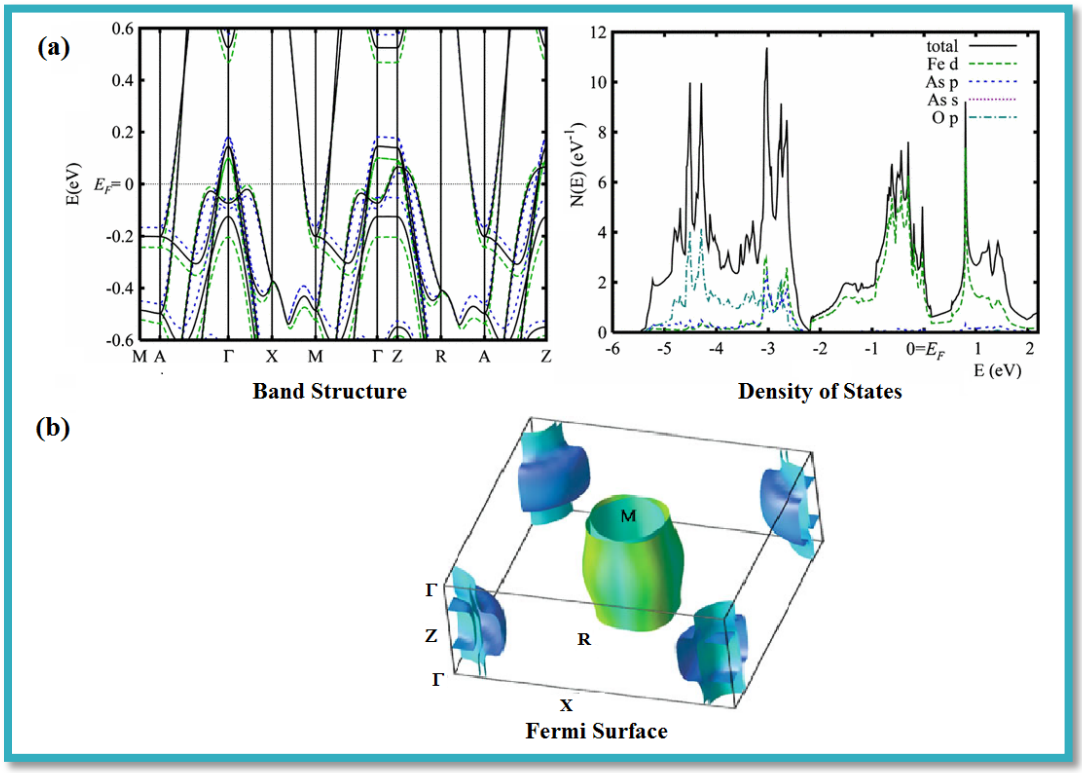

Figure 2.2: (a) Band structure and density of states (DOS) and (b) Fermi surface of LaFeAsO

The observed Fermi surface was further supported by angle-resolved photoemission spectroscopy (ARPES) measurements from various groups. It proved that the low-lying electronic structures of iron based superconductors are characterized by multi-band and multi-orbital nature. The Hund's rule coupling and the fluctuating collinear spin order is responsible for the large electronic structure reconstruction, spin density wave and structural transition in iron pnictides. It was also found that early reports on local density approximation (LDA) calculations support the formation of spin density wave (SDW) instability in undoped systems due to Fermi surface nesting between the hole-like Fermi surface at Γ and the electron-like Fermi surface at X. Doping plays a key role in the Fe based compounds by suppressing the long range magnetic ordering and structural transition. Electron doping reduces density of states, which would lower pairing strength by reducing the phase space, and at the same time strongly suppresses ferromagnetic fluctuations, which are strongly pair breaking for singlet superconductivity. The main effect of doping is suggested to be a reduction in the degree of nesting of the Fermi

surfaces, which seems consistent with the experimental fact that the phase diagram is approximately symmetric against hole and electron doping. Upon doping, the superconductivity is enhanced by the Fermi surface nesting between d_{xz}/d_{yz} orbitals while diminishes quickly after the central d_{xz}/d_{yz} hole Fermi surfaces sink below E_F.

In short, the fermiology found in doped LaFeAsO gives rise to strong but broad antiferromagnetic spin fluctuations near the M point in the Brillouin zone, while the tendency to magnetism existing at zero doping is suppressed. These fluctuations are instrumental in creating a superconducting state with order parameters of opposite signs on the electron and hole pockets i.e. the superconducting gap of iron pnictides can be described ubiquitously under the s-wave pairing symmetry.

2.2.3 Magnetic structure

Shortly after the discovery of superconductivity in $LaFeAsO_{1-x}F_x$, calculations indicated that conventional electron-phonon coupling was insufficient to explain the high transition temperatures, which was later verified experimentally. It was understood that a ubiquitous magnetically ordered state is present indicating magnetism in close proximity to superconductivity leading one to naturally consider the interplay between magnetism and superconductivity in these materials. It is interesting that Fe which is detrimental to superconductivity remains as one of the main ingredient in iron oxypnictides and governs the magnetism of these materials. Besides the FeAs layers of the pnictide, the magnetic structure is also modified by the presence of other elements such as for instance a magnetic rare earth. This is specifically the case for the 1111 system presently holding the record of the highest critical temperatures. The interplay of the rare-earth magnetism with that of Fe ions and their combined effect on superconductivity is of primary interest. A further common, extrinsic source of magnetism is due to small fractions of impurity phases containing Fe such as Fe_xAs_y phases.

The magnetic structure of the oxypnictides within the *ab* plane consists of chains of parallel Fe spins that are coupled antiferromagnetically in the orthogonal direction (Figure 2.3 (b)), with an ordered moment substantially less than one Bohr magneton. Hence, these are itinerant electron magnets, with a spin structure that is consistent with Fermi-surface nesting along with possible strong electron correlation effects (Lumsden *et al.* 2010). In addition to this Fermi surface nesting scenario, it has been proposed that near-neighbor and next-near-neighbor interactions between local Fe moments are both antiferromagnetic and of comparable strength leading to magnetic frustration (Yildrim 2008). This also provides an explanation for the structural phase transition as the lattice distortion relieves the

magnetic frustration. These frustration effects have also been used to explain the small ordered moment. It is already believed that the magnetic order is mainly driven by either Fermi surface nesting or local moment super-exchange interactions (Ma(b) *et al.* 2009); but an alternate approach concludes that though the moments are largely local in nature, the interactions are relatively long-ranged itinerant interactions as opposed to super-exchange (Johannes *et al.* 2009). It was later proposed that both the magnetic and structural transitions are driven by orbital physics and that the structural transition is, in fact, a ferro-orbital ordering transition. This model explains the coupling of the structural and magnetic transitions and is consistent with the rather large ordering temperature (Lee(a*) et al.* 2009).

Changes of the ordered magnetic structure with different rare earth elements (REFeAsO) was extensively studied with neutron diffraction as well as local probe methods (Wei 2013). The ordering wavevector of (½, ½, ½) observed for RE = La is also observed for RE = Nd (de la Cruz *et al.* 2008; Chen(e) *et al.* 2008). However, for RE = Ce and Pr the ordering is described by the wavevector (½, ½, 0) suggesting ferromagnetic coupling between planes (Zhao *et al.* 2008a; Zhao *et al.* 2008b). This suggests rather weak interplanar coupling which is strongly influenced by the rare earth ion and the associated induced structural changes. Unfortunately, for the case of RE = Sm, the high absorption cross-section for Sm makes neutron scattering measurements very difficult (Ryan *et al.* 2009). Neutron scattering measurements on SmFeAsO were performed but could only explore the low temperature ordering of the Sm moments. The size of the ordered moment as a function of RE has been a topic of considerable interest. Neutron scattering on RE = Pr indicates a moment of 0.34 μB identical to that observed for RE = La (moment = 0.48 μB measured below the Pr ordering temperature) (Kimber *et al.* 2008). The moment for RE = Nd appears smaller and initially, Fe ordering was not observed, but later measurements clearly indicated Fe ordering with an ordered moment of 0.25 μB, the smallest of any of the rare earths. For RE = Ce, a much larger magnetic moment of 0.8 μB more than twice the size of any other rare earth. Thus, on the basis of these neutron diffraction results, the Fe moment size varies considerably with rare earth element. However, a contradictory picture is obtained from ^{57}Fe Mossbauer measurements. The Mossbauer measurements yield an ordered Fe moment μB of 0.34, 0.35, .34 and 0.33 for RE = La, Nd, Ce, and Pr, respectively (McGuire *et al.* 2008, McGuire *et al.* 2009, Sanchez *et al.* 2009). This suggests an ordered Fe moment size which is independent of rare earth ion, in apparent contradiction to the neutron diffraction results.

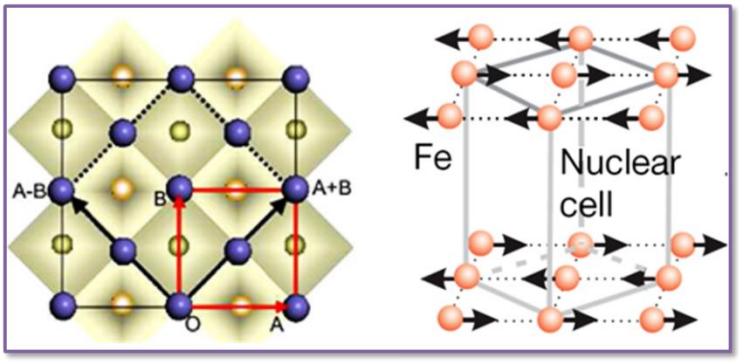

Figure 2.3: (a) Lattice of FeAs layer with dark and light shaded areas indicating As atoms below and above Fe square lattice, respectively (b) Spin orientation of Fe atoms in the Fe lattice

The first evidence of the interplay between magnetism and superconductivity in the Fe based superconductors was the presence of magnetism in the concentration dependent phase diagrams. In summary, the parent compounds exhibit a magnetically ordered state which is suppressed with doping and superconductivity appears at higher concentrations. While this general behavior is common for different materials, the behavior near the boundary between superconductivity and magnetism is material specific as shown in Figure 2.4. The magnetically ordered state of some materials vanish abruptly with the appearance of superconductivity, in others superconductivity emerges precisely as the magnetic order is destroyed, and still others exhibit coexistence between the magnetically ordered and superconducting states. The interactions in the magnetically ordered parent compounds have been determined to be anisotropic 3D interactions. With doping, the correlations along the c axis appear get quickly suppressed so that in optimally doped samples the spin excitations appear to be 2D in character much as in the normal state of the parent compounds.

The magnetic phase diagrams of the Fe-based materials indicate that the paramagnetic state of the parent compounds appears to be the same paramagnetic state out of which superconductivity develops in the optimally doped materials. In the superconducting materials, spin fluctuations near (½, ½, 0) have been found in all cases investigated. Since the development of the BCS theory, it has been of interest to see whether the effective interaction responsible for the superconducting pairing could be mediated by excitations other than phonons. In early investigations itself, the first-principle calculations have proved that the electron–phonon coupling is not sufficient to explain the superconductivity in iron based superconductors. On the other hand, the experiments have shown that the superconducting state is proximity to the AFM spin-density-wave state. It is strongly argued that the AFM spin fluctuations in iron based superconductors could lead to

a superconducting state with a gap which has the opposite sign on the electron and hole pockets (Li(d) *et al.* 2013). In brief, below T_C, the development of a spin resonance demonstrates a direct interplay between magnetism and superconductivity which appears to support sign reversal s-wave symmetry.

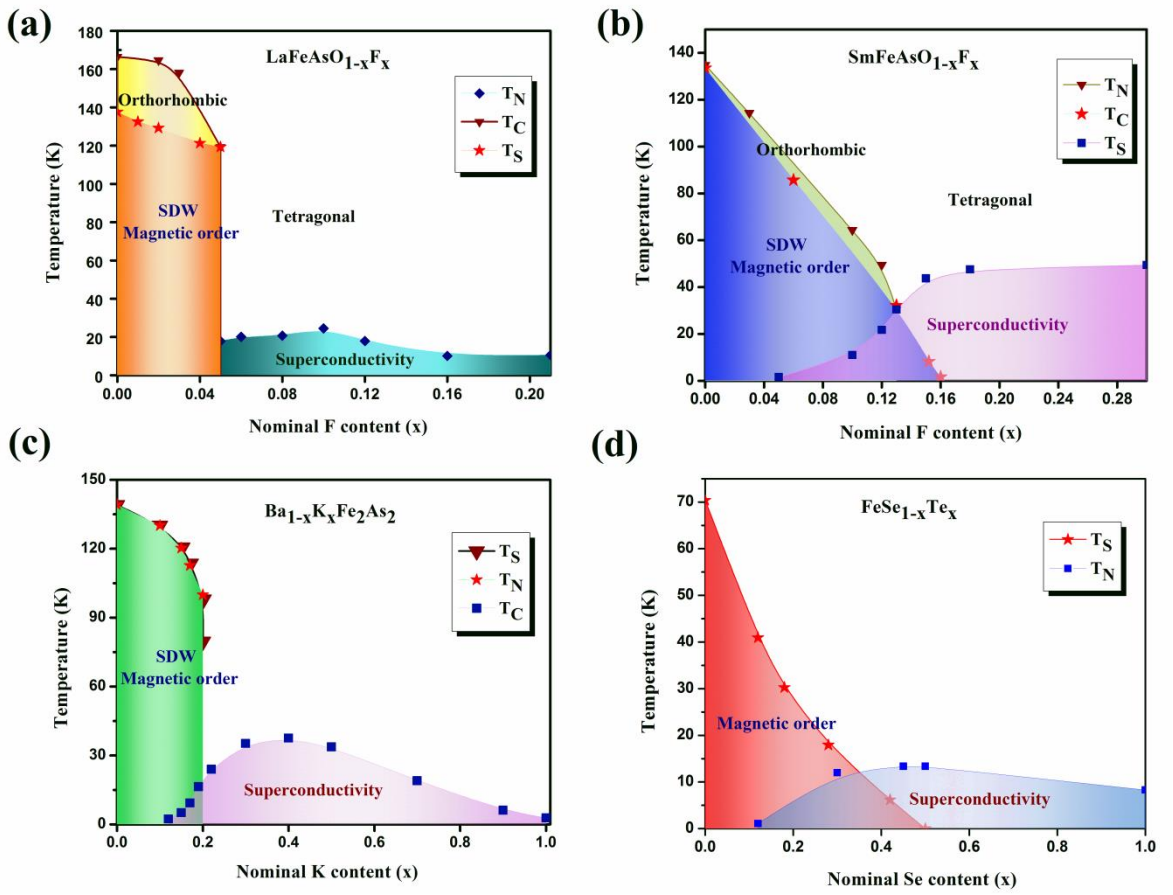

Figure 2.4: Phase diagrams of (a) La1111 (b) Sm1111 (c) Ba122 and (d) Fe(Se,Te) systems

2.3 Iron based superconductors: A bridge between MgB_2 and cuprates

Iron based superconductors share several characteristics with high temperature superconductors, such as the layered structure, the coexistence of different orderings, the occurrence of superconductivity upon doping, the small coherence length, and unconventional pairing (Norman 2008; Yamamoto *et al.* 2011). Some of these aspects have shown to be unsuitable for practical application. On the other hand they exhibit several advantages namely, they are metallic in the parent compounds, smaller anisotropy and not strongly dependent on the level of doping, the supposed order parameter symmetry seems to be different, and in principle not so detrimental to current transmission across grain boundaries, impurities do not significantly affect T_C. Moreover, they are extremely versatile in terms of chemical composition, as they belong to a

comprehensive class of materials, where many chemical substitutions are possible and their layered structure allows designing new iron pnictides with composite structures or even artificial multilayers. This versatility could enable the superconducting properties to be tailored for commercial technologies. High temperature superconductivity emerges in cuprates and iron pnictides through the suppression of magnetism in the undoped materials, 'parents', which are in a Mott-insulating and a semi-metallic spin-density wave form, respectively. They also share characteristics with the more conventional MgB_2. The most remarkable one is the multiband nature that has offered unprecedented tools in MgB_2 to tune and improve the superconducting properties. But all attempts to raise T_C by atomic substitutions have not succeeded in MgB_2 (Vinod *et al.* 2007).

But many unusual features of iron pnictides set them apart from the more conventional two-band s-wave superconductor MgB_2 and make them closer to cuprates, in short, iron pnictides form a bridge between the more conventional MgB_2 and highly unconventional cuprate superconductors. Table 2.1 gives a comparison of the properties of different classes of superconductors. Regarding the superconducting mechanism followed, iron pnictides are not conventional like MgB_2 in which the high T_C is caused by strong intra-band pairing and weak inter-band pairing mediated by phonons whereas iron pnictides are governed by an unconventional superconducting mechanism. Superconductivity in iron pnictides occurs on the FeAs planes. Given that magnetic ions suppress the traditional singlet s-wave electron-phonon superconductivity, the fact that superconductivity in iron pnictides originate from the quintessential magnetic Fe ion makes it rather unconventional. Similar to the cuprates, iron pnictides become superconducting on doping parent antiferromagnetic (AF) compounds. Unlike the cuprates in which superconductivity occurs upon doping an AF Mott insulator, iron pnictides turn superconducting on doping a parent AF semi-metal with the Neel temperature T_N = 150 K (Paglione *et al.* 2010, Johnston 2010). Iron pnictides are multiband superconductors with several disconnected electron and hole sheets of the Fermi surface formed by hybridized d-orbitals of Fe. Cooper pairing in iron pnictides has been attributed to AF or orbital excitations, resulting in strong inter-band interaction between different sheets of the FS and unconventional pairing symmetry: either the s± pairing with a sign change in the s-wave order parameters on different FS sheets or mixed s-wave and d-wave symmetry (Kemper *et al.* 2010, Kontani *et al.* 2010; Mazin *et al.* 2009). The degree of electron correlation in iron pnictides was not clear at first, but it is generally believed that pnictides lie somewhere between the strongly correlated cuprates

and the weakly-correlated conventional superconductors. However, similar to cuprates, the mechanism that leads to high T_C superconductivity in these materials is still far from being well understood.

Table 2.1: A comparison of properties observed in different classes of superconductors

Property	Conventional superconductors	MgB_2	Iron based superconductors	Cuprates
T_C (max)	***30 K***	***39 K***	***56 K***	***134 K***
Relationship to magnetism	***No magnetism***	***No magnetism***	***Parent compounds are magnetic metals***	***Parent compounds are magnetic insulators***
Pairing Interaction	***Electron-phonon***	***Electron-phonon***	***Presumably magnetic***	***Probably magnetic***
Order Parameter	***One band, same sign s-wave***	***Two band same sign s-wave***	***Two band, sign reversal s-wave***	***One band sign reversal d-wave***
Dimensionality	***Three dimensional***	***Three dimensional***	***Variable***	***Two dimensional***
Correlation effects	***None (nearly free electrons)***	***None (nearly free electrons)***	***Long range (non-local magnetic correlations)***	***Strong local electronic interactions***

Most iron pnictides are in the clean limit in which the mean free path due to elastic scattering on impurities is longer than $\xi \sim$ 1-2 nm. Thus, impurities do not increase H_{C2} of these materials as effectively as they do in conventional superconductors such as Nb-Ti or Nb_3Sn (Shapira *et al.* 1965; Orlando *et al.* 1979). Instead, the behavior of H_{C2} in iron pnictides can be tuned by doping which expand or shrink some of the Fermi surface pockets (Gurevich 2010). As far as vortex dynamics and pinning are concerned, some members of the iron pnictide families behave like conventional low-T_C superconductors for which the role of thermal fluctuations of vortices is inessential (Yuan *et al.* 2009). However, RE1111 systems such as Nd1111 or Sm1111 have many similarities with the cuprates (such as $YBa_2Cu_3O_{7-x}$), including reduced vortex melting field, thermally activated vortex flow and creep resulting from thermal fluctuations of vortex matter (Jaroszynski *et al.* 2008a). Similar to the cuprates, iron pnictides are extreme-type II superconductors with the Ginzburg-Landau (GL) parameter K $\sim$ 102 and the lower critical field $H_{C1}(0) \sim$ 10 mT and $H_{C2}(0) \sim$ 100-300 T (Putti *et al.* 2010, Hunte *et al.* 2008). The London penetration depth in iron pnictides extracted from magnetization, nuclear magnetic resonance and muon spin relaxation measurements gave the

characteristic values $\lambda_0 \sim$ 150-300 nm not very different from those for the cuprates (Johnston 2010, Gurevich 2011).

The Ginzburg number $G_i \sim 10^{-10}$-10^{-6} are characteristic of conventional BCS low-T_C superconductors for which fluctuations are negligible. The region of $G_i \sim 10^{-5}$-10^{-3} corresponds to 'intermediate-T_C' superconductors in which fluctuation effects are present but not severe enough to affect the mean-field BCS relations and vortex properties (Larkin *et al.* 2007). For instance, MgB_2 has a $G_i \sim 10^{-4}$ (Putti *et al.* 2010). In the cuprates, G_i $\sim 10^{-3}$-1 static and dynamic properties of vortex structures are strongly affected by thermal fluctuations, so that the least anisotropic $YBa_2Cu_3O_{7-x}$, has $G_i \sim 10^{-2}$, while the very anisotropic layered Bi-2212 and Bi-2223 cuprates have $G_i \sim 1$ (Tsuei *et al.* 2000). The G_i values ranging from $G_i \leq 10^{-4}$ to $G_i \sim 10^{-2}$ are characteristic of iron pnictides in which different phases of vortex matter, from the conventional Abrikosov lattices to the vortex glass/liquid phases first discovered in the cuprates can exist (Blatter *et al.* 1994).

The difference between H_{irr}(T) and H_{C2}(T) curves are more pronounced for Nd1111 while Ba122 behaves more like a conventional low-T_C superconductor, consistent with the values of G for these materials (Hunte *et al.* 2008). However, the resistance curve R(T,H) for Nd1111 not only shifts but also broaden as H increases. In this case thermal fluctuations of vortices are essential, resulting in thermally activated vortex dynamics which is very similar to cuprates. Different members of the same iron pnictides can exhibit both thermally activated and non-activated vortex dynamics: for example, Nd1111 with $T_C \approx 55$ K behaves qualitatively similar to YBCO, whereas La1111 with $T_C \approx 26$ K behaves more like MgB_2 (Jaroszynski *et al.* 2008, Gordon *et al.* 2010). Such a difference between these two materials results from the two-fold difference in T_C, which significantly enhances thermal fluctuations.

The maximum elementary pinning force occurs as the size of non-superconducting defects such as second phase precipitates approximately equal to the diameter of the vortex core $2\xi \sim$ 4-10 nm (Brandt *et al.* 1995). As a result, vortices in iron pnictides can be pinned even by 'natural' crystalline disorder such as dislocations and grain boundaries. They are also similar to cuprates as the vortices in iron pnictides can be pinned by oxygen vacancies. However, as in cuprates, they suffer from poor grain connectivity which can drastically reduce J_C in polycrystalline materials. Strong vortex pinning and high H_{irr} are not yet sufficient for applications which also require long polycrystalline wires. One of the main issues for the cuprates is that grain boundaries between misoriented crystallites impede current flow. Recent experiments revealed similar weak linked grain boundaries in

Ba122 and La1111 (Lee(e) *et al.* 2009; Haindl *et al.* 2010). The grain boundary problem in the cuprates and iron pnictides may be caused by the same materials features which contribute to high values of T_C and H_{C2}, such as low carrier densities, short coherence lengths, unconventional pairing symmetry, large screening lengths and competing antiferromagnetic states; characteristic of both cuprates and iron pnictides. In the cuprates, local non-stoichiometry, charge and strains around dislocation cores, impurity segregation and precipitation of non-superconducting and magnetic secondary phases at grain boundaries can also inhibit grain connectivity (Song *et al.* 2005). It is unclear to what extent all these factors contribute to the weak-link behavior of grain boundaries in iron pnictides as compared with conventional superconductors or even the two-band MgB_2 in which grain boundaries are not weak links (Larbalestier *et al.* 2001b). However, the high upper critical fields and the irreversibility fields of iron pnictides suggest good prospects for magnet applications. Anyhow, just like the cuprates, the high H_{C2} and T_C in iron pnictides are not enough to assure applications at higher temperatures. Making them useful may require complex and expensive technologies, regardless of the values of T_C and H_{C2}. The lower values of $T_C < 55$ K limit applications of iron pnictides to temperatures 20-30 K where the use of effective cryocoolers as in the case of MgB_2 is possible and can take advantage of very high upper critical fields and irreversibility fields which are much better than cuprates. As far as pinning is concerned, thin film and single crystal of iron pnictides can carry high J_Cs ~ 10^8 A/cm^2 at 4.2 K, making them competitive with conventional superconductors and indicate good possibilities for magnet applications.

2.4 Status of superconducting properties in RE1111 system

Iron based superconductors are well known for the variety of classes within the family with different crystal structures having layered nature as a common feature. The superconducting properties such as T_C, J_C, and H_C exhibited in iron pnictides varied from class to class. While all attempts to raise T_C of MgB_2 by atomic substitutions were not successful, the substitutional chemistry of iron pnictides eventually revealed numerous new Fe-based superconductors with higher T_C. As a result, not only has T_C been increased up to 56 K in RE1111 by substituting La with other rare earths RE = Ce, Pr, Sm, Nd in the RE1111 family, but many new families, most notably, $Ba_{1-x}K_xAs_2Fe_2$ with T_C = 38 K; LiFeAs with T_C = 18 K and arsenic-free chalcogenides $FeSe_{1-x}Te_x$ with T_C = 15 K were discovered (Aswathy *et al.* 2010).

As discussed earlier, in RE1111 family, the fluorine free parental compound REFeAsO is not a superconductor. Superconductivity is achieved by fluorine doping at oxygen site, creation of oxygen vacancies, cobalt/nickel doping at Fe site and hetero/isovalent ion substitution at rare earth site. The modified RE1111 compounds show a wide range of T_C variation as shown in Figure 2.5. The first reported compound $LaFeAsO_{1-x}F_x$ showed a T_C of 26 K which was soon increased to a maximum of 43 K by applying external pressure. Further, La was replaced by other isovalent rare earths of smaller diameter such as Pr, Nd and Sm, pushing the T_C to a maximum of 56 K. It was already proposed that the maximum T_C possible in RE1111 compounds is in the 50s K and the initial lower values were attributed to non-optimal synthesis. The variation of T_C with respect to pressure (P) as well as doping concentration (x) was studied on almost all RE1111 superconductors. Both dT_C/dP and dT_C/dx gave the same sign, indicating the same suppression effect on the spin density wave state (Takabayashi *et al.* 2008; Chu *et al.* 2008). Doping brings structural modifications such as a reduction in cell volume, a decrease in distance between layers, an increase in distance between RE^{3+} and F^- which enhances spin and charge density fluctuations.

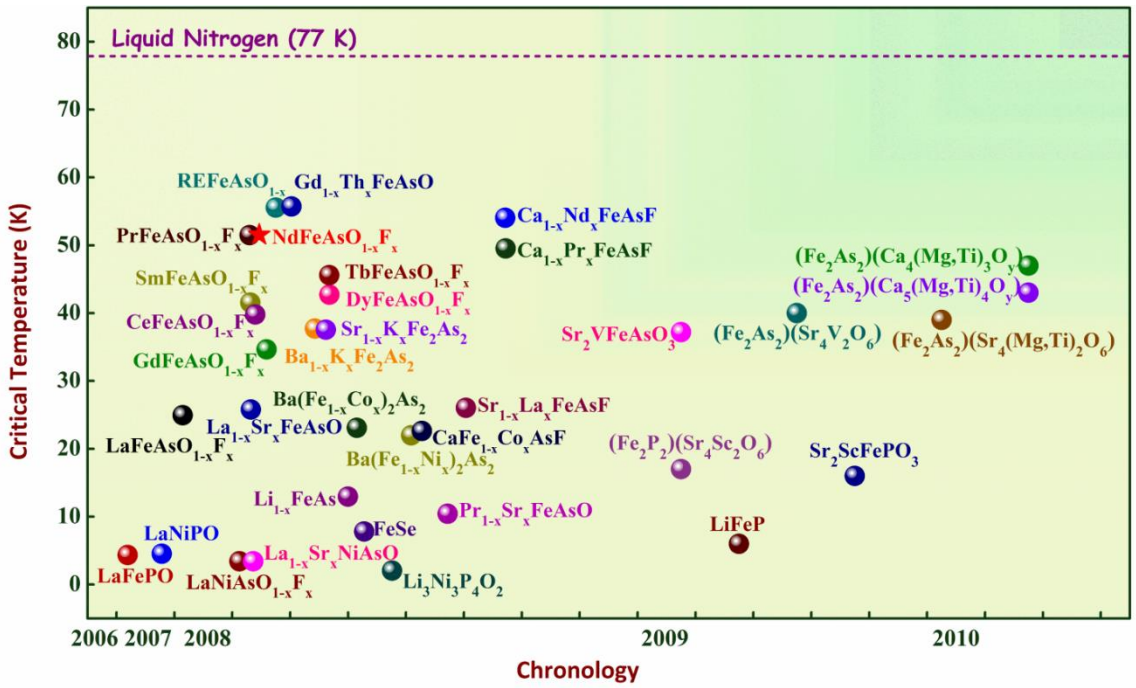

Figure 2.5: The plot shows the wide range of T_C displayed by iron pnictides

Hole doping was first tried using Ca^{2+} ions in LaFeAsO at the lanthanide site and did not show superconductivity. Wen *et al.* reported superconductivity in $La_{1-x}Sr_xFeAsO$ (T_C = 25 K) even in the absence of F doping (Wen *et al.* 2008). Apart from bivalent ion, thorium ion, another heterovalent ion was also substituted at the rare earth site in order to

achieve a higher T_C. $Gd_{1-x}Th_xFeAsO$ displayed a T_C of 56 K, which was much higher than the F doped $GdFeAsO_{1-x}F_x$ sample (Wang(b) *et al.* 2008). Later, partial substitution of Tb^{3+} by Th^{4+} in TbFeASO, exhibited superconductivity with a T_C of 52 K (Li(a) *et al.* 2008). Next is Fe site doping wherein cobalt is the widely used candidate for electron doping. It was observed that substitution of Co atoms at the Fe site induced superconductivity in LaFeAsO (T_C = 13 K) and SmFeAsO (T_C = 15 K) (Matsuishi *et al.* 2008; Qi *et al.* 2008a). Besides the doping of cobalt in parental systems, it has also been doped simultaneously with fluorine; but resulted in the suppression of T_C. Dopants such as Rh, Ir, Pd, Ni, Ru and Mn at the Fe site were also tried to induce superconductivity and most of them led to insensitive suppression of T_C, which stood against the proposed s-wave pairing symmetry (Qi *et al.* 2009a; Li(a) *et al.* 2009; Ni *et al.* 2009; Han *et al.* 2009; Schnelle *et al.* 2009; Sato *et al.* 2010). Regarding the arsenic site, an arsenic deficient compound, $LaFeAs_{1-\delta}O_{0.9}F_{0.1}$ was reported by Fuchs et al. with a T_C = 28.5 K (Fuchs *et al.* 2008). Phosphorous doping at the arsenic site was also reported with a maximum T_C of 30 K in 122 compounds and below 11 K in the RE1111s (Ren(b) *et al.* 2009, Wang(b) *et al.* 2009). Both doping at the Fe site and the creation of As vacancies reveal the fact that iron based superconductors can tolerate in-plane disorder in the FeAs conducting layer to some extent.

A series of F free oxygen deficient samples ($REFeAsO_{1-x}$; RE = Gd, Sm, Nd, Pr, Ce, La) prepared by the high pressure synthesis technique was reported (Ren(a) *et al.* 2008a). Oxygen deficiency could produce more lattice shrinkage and charge carriers, thereby increasing the density of states (DOS). The onset T_C values of the $REFeAsO_{1-x}$ family (with RE = Ho, Y, Dy, Tb, Gd, Sm, Nd, Pr, Ce, and La) were found to be 50.3, 46.5, 52.2, 48.5, 53.5, 55, 53, 51.3, 46.5 and 31.2 K respectively (Ren(a) *et al.* 2008a; Yang(b) *et al.* 2008a, Yang(b) *et al.* 2008b; Ren(a) *et al.* 2008b; Lee(b) *et al.* 2008). The onset T_C in these compounds increased with the decrease in size of the RE atom and reached a maximum of 55 K for Sm (Ren(a) *et al.* 2008b). The crystal structure of $REFeAsO_{1-x}$ is modified compared with that of REFeAsO. The $FeAs_4$ coordination in $REFeAsO_{1-x}$ transforms into a regular tetrahedron with increasing oxygen deficiency accompanied by an increase in T_C, and T_C reaches a maximum when the $FeAs_4$ lattice forms a regular tetrahedron (Lee(b) *et al.* 2008). In addition to oxygen deficient samples, fluorine doped samples subjected to external pressure showed either suppression or enhancement of T_C. The pressure dependence of T_C i.e. dT_C/dP is found to be negative or positive, the sign changes from positive to negative at the quantum critical point (QCP). In

short, T_C in iron pnictides varies widely according to the dopant used, doping site, doping concentration and external pressure applied.

The upper critical field H_{C2}, and the critical current density J_C, are two important parameters to characterize superconductivity. H_{C2} is an intrinsic property of a type II superconducting material in which the resistive transition (ρ-T) width increases with increasing magnetic field, H. Usually, the H_{C2} of the sample can be measured from the resistive transition (ρ-T) analysis under different magnetic fields. According to the conventional BCS picture, H_{C2} is linear in T near T_C and saturates at the 0 K limit. This behavior may deviate on considering the presence of impurity scattering. The H_{C2}(0 K) can be calculated using the one band Werthamer-Helfand-Hohenberg (WHH) formula, $H_{C2}\,(0) = -0.693 T_C \left(\frac{dH_{C2}}{dT}\right)_{T_C}$, where $\frac{dH_{C2}}{dT}$ is obtained from the slope of the graph H_{C2} versus T at T_C. Rather high values of H_{C2} are obtained for the Fe based superconductors using this equation, i.e. 45, 185, 144, 150 and 304 T for La, Ce, Pr, Sm and Nd based 1111 systems (Gordon *et al.* 2010; Shahbazi *et al.* 2010; Bhoi *et al.* 2009; Senatore *et al.* 2008; Jia *et al.* 2008a), all are well above that of Nb_3Sn (H_{C2}(0) = 30 T) (He *et al.* 2010). However, these H_{C2} values are extrapolated from measurements at low magnetic field and high temperature using the one band WHH model, which is not valid for the low temperature range.

Table 2.2: Status of superconducting properties of iron pnictides compared to other superconductors

Properties	**Nb-Ti**	**Nb_3Sn**	**MgB_2**	**1111**	**122**	**111**	**11**	**YBCO**	**Cuprates**
T_C (K)	9	18	39	**56**	38	18	16	90	135
H_{C2}(0) (T)	10	20	30-40	**>300**	>100	15-30	>40	50	100
γ	-	-	3-5	**5**	2	2	2	5-7	50-200
ξ (nm)	4-5	3	3.7-12	**2.3**	2.1	4.8	2.6	2	1.5
J_C (A/cm^2) (at 4.2 K)	10^6	10^6	10^6	**10^6**	10^6	10^6	10^6	10^6	10^7

High magnetic field measurements up to 60 T conducted on the single crystals of $NdFeAsO_{0.7}F_{0.3}$ show a spin dependent positive magneto-resistance for $H||c$ due to the presence of some paramagnetic phase of Nd^{3+} ions (Jaroszynski *et al.* 2008a). They introduce several pairing scenarios in order to explain the H_{C2} versus T curve and the best fit is obtained by considering the paramagnetic effect. The paramagnetic effect on H_{C2}(T) in oxypnictides significantly reduces H_{C2}(0) as compared to that based on extrapolations of H_{C2}(T) near T_C down to low temperatures. The extrapolation of H_{C2} near T_C to low

temperatures following the GL theory neglects the essential paramagnetic limitations and could overestimate the actual $H_{C2}(0)$ (Jo *et al.* 2009). The extrapolated H_{C2} values are two or three times higher than the weak coupling Pauli-limited field, the field at which the free energy in the normal state becomes equal to the condensation energy of the superconductor, which may indicate a considerable enhancement of the Pauli-limited field by the strong coupling effect. The highest reported upper critical field for RE1111 system is observed in the single crystals of Nd1111 system i.e. around 300 T with a relatively small mass anisotropy parameter $\gamma = m_a/m_c \leq 5$, where m_a and m_c are the effective masses along the *ab* plane and the *c* axis, respectively. However, the above studies were performed in magnetic fields not exceeding 9 T, where most of the multiband effects would not manifest themselves in the H_{C2}(T) curves. The very high magnetic fields make them promising for high field applications as wires. Although the cuprate superconductors exhibit much higher T_C and similar high H_{C2} as compared to iron pnictides, the small degree of electromagnetic anisotropy between the *c* axis and *ab* plane directions confirmed in 11, 122 and 1111 systems encouraged the development of more versatile conductors. Soon after, iron pnictide wires were fabricated using the RE1111 compounds following the powder-in-tube (PIT) method. Table 2.2 shows a status of superconducting parameters of different iron pnictides compared to other potentially established superconductors.

Though iron pnictides have gathered enough attention in terms of their relatively high T_C and very high H_{C2}, the status of transport J_C was not much promising in the early stages of discovery. But, the dependence of J_C on the magnetic field was confirmed to be small and moderately high J_C values were found to be maintained up to very high fields. However, in the past two years, the transport J_C of iron pnictide wires has been rapidly increased (Ma(a) *et al.* 2012; Togano *et al.* 2011; Gao *et al.* 2011; Weiss *et al.* 2012; Gao *et al.* 2012). At 4.2 K, a wire with 122 compounds has achieved transport J_C of 10^5A/cm^2 in self-field and even 1.4 $\times 10^4$ A/cm^2 in a field of 14 T, respectively (Weiss *et al.* 2012; Gao *et al.* 2012). Compared with 122, the transport J_C of 1111 wires is still much lower of the order of 10^3 (Wang(a) *et al.* 2012). It is to be noted that two main difficulties limit the progress of RE1111 wire development (Fujioka *et al.* 2011a). The first one is the difficulty in achieving exact composition in RE1111 by maintaining the fluorine content since fluorine is highly unstable during sintering. This in turn affects the phase purity; a large amount of detrimental impurities such as FeAs, REOF etc. interrupt grain-to-grain super-current flow. The second issue lies in the compatibility of different sheath materials with the highly reactive ingredients. These problems severely limit the transport J_C of RE1111

wires. Therefore, it is essential to overcome these difficulties to make a breakthrough. Several methods such as sheath metal variation and addition of materials with lower conductivity were tried further to increase the critical current density of RE1111 wires (Ma(a) *et al.* 2011, Wang(a) *et al.* 2013).

It is said that the cuprates needed more than fifteen years to realize industrial products, by expending enormous research funds and continuing strenuous efforts from researchers all over the world. Hence, the effort and funding spend during the past five years for understanding superconducting properties of iron based superconductors is much less when compared to cuprate superconductors. Understanding the determining factors for J_C and the introduction of effective pinning centers are believed to be essential for the development of superconducting technologies versatile enough to generate high fields.

2.5 Objectives of the present work

For technological applications, such as magnets and cables, superconductors in the form of flexible wires or tapes have to be developed. In addition, the behavior of transport critical current density of these conductors in high fields also must be observed. Iron pnictides are extreme type-II superconductors with very high H_{C2}(T) which often extrapolate to $H_{C2}(0) \sim$ 100-300 T. Large values of H_{C2} in semi-metallic iron pnictides result from their short coherence lengths due to relatively high T_C and low Fermi velocities revealed by band structure calculations and angular-resolved photoemission spectroscopy. Vortex matter in iron pnictides exhibits a variety of different behaviors and glass phases controlled by pinning and thermal fluctuations. Several transport and heat-capacity studies on Nd1111 revealed an upper critical field of $H_{C2}||ab$ = 304 T and $H_{C2}||c$ = 62-70 T extrapolated from the WHH formula. It has also been observed that Nd1111 could provide irreversibility fields up to 40-50 T at 20 K. The high H_{C2} and irreversibility fields suggest good prospects for magnet applications. Moreover, the relatively high $T_C \sim$ 55 K makes them suitable for applications around 30 K where the use of effective cryocooler can take advantage of their very high upper critical fields and irreversibility fields. Superconducting iron based wires fabricated by the powder-in-tube (PIT) method has been reported globally only by very few groups. Both *in situ* and *ex situ* PIT fabrication processes have been reported. The former employs starting materials, whereas the latter employs a powder of synthesized superconducting material. A disadvantage of the *ex situ* fabrication of the RE1111 wire is that the fluorine content in the system decreases during the heat treatment after rolling. However, it is really a challenge to fabricate wires of $REFeAsO_{1-x}F_x$, since these materials are mechanically hard and brittle and therefore not easy to draw into the

desired wire geometry. On the other hand, the use of proper metal cladding is another critical issue because of the strong chemical reactivity of these materials at high processing temperatures. Hence, the proposed work focuses on surpassing the existing hurdles and developing Nd based iron pnictide wires suitable for magnet applications. Before stepping into wire development, it is necessary to optimize the processing parameters such as temperature and duration to synthesize bulk Nd1111 with enhanced electromagnetic properties. The effect of various dopants at different sites also should be examined and the best dopants for enhancement of T_C, J_C and H_{C2} must be identified. Further, the compatibility of Nd1111 with different sheath materials needs to be studied. After choosing the appropriate sheath material both in terms of chemical compatibility and mechanical workability, the fabrication of wires using PIT method will be taken up.

In short, the main motives of the present thesis work are as follows:

Objectives:

- *Preparation of good quality polycrystalline Nd1111 bulk samples at relatively low temperatures and ambient pressures.*
- *Enhancement of superconducting properties such as T_C, $J_C(H)$ and H_{C2} by incorporation of suitable dopants.*
- *Studies on the development of metal sheathed Nd1111 superconducting wires/tapes for magnet application.*

CHAPTER 3

PREPARATION AND CHARACTERIZATION OF IRON PNICTIDES

3.1 Preparation techniques for iron pnictides

The discovery of superconductivity in iron pnictides by Hosono's group spurred the whole family of condensed matter scientists captivating both the theorists and experimenters. Though the Japanese and Chinese groups published papers at a rate of 2.5 per day in arXiv and synthesized almost all doped versions of iron pnictides especially the 1111 class, a close survey would reveal that only a few groups could prepare these trickier compounds successfully. Meanwhile, physicists around the world conducted different measurements on the compounds borrowed from these groups. It was observed that either the quality or size of the samples or both remained insufficient to discriminate among the various theoretical ideas proposed (Day C. 2009). The reasons for the fewer groups indulging in the development of iron pnictides and the problems of achieving samples with high quality and large quantity can be discussed in detail. Iron pnictide superconductors are having a variety of classes ranging from different multilayer structures to the simple two element 11 system. The ingredients, processing conditions and techniques differ according to each class. All these superconductors can be developed in different forms such as bulk/polycrystalline, single crystals, thin films, wires and tapes. Though conventional solid state route is the basis for polycrystalline samples, the preparation technique chosen varies according to the type of superconductor.

3.1.1 Polycrystalline samples

For the synthesis of polycrystalline samples mainly two techniques are adopted:

a) Solid state synthesis (at ambient conditions)

b) High pressure synthesis

3.1.1.1 Solid state synthesis

The conventional solid state synthesis method is the easiest way to make desired compounds through direct reaction of the starting materials at high temperatures wherein powder reactants of almost similar particle size are mixed, ground, pressed into pellets and heat treated at high temperatures. The synthesis of iron oxypnictides using solid state method can either be done by one single step or two-step. For the REFeAsO (RE1111) compound, earlier almost every group followed the two-step synthesis technique wherein

the first step comprises of the synthesis of certain binary compounds followed by a second step allowing the reaction of these binaries with the remaining raw materials to form the final compound (Kamihara *et al.* 2008; Sefat *et al.* 2008; Shekhar *et al.* 2008; Chen(b) *et al.* 2008; Lorenz *et al.* 2008). This route was frequently adopted due to the simple reasons such as volatility and toxicity of arsenic and high oxygen/moisture affinity of rare earth metals. The high volatility of arsenic creates enormous vapor pressures at sintering temperatures above 600 °C. The presence of fluoride compounds causes volatile loss of fluorine and this exacerbates the situation. Hence, the two-step method helped in forming polycrystalline samples by reacting stable binaries in evacuated quartz tubes at relatively high temperatures avoiding the risks of explosion. However, then comes the question of quality or phase purity of the samples thus obtained. We know that Fe is more prone to react with As to form a stable covalent compound FeAs, while RE tends to form a stable ionic compound with the O element, RE_2O_3. The melting points of RE_2O_3 compounds are very high. As a result, the reaction between the two stable compounds FeAs and RE_2O_3 becomes difficult and this leaves small amounts of RE_2O_3 and FeAs as impurities in the RE1111 compound (Fang *et al.* 2010). One-step synthesis method has also been tried wherein all ingredients are taken stoichiometrically and reacted in inert atmospheres, but the samples so formed also lack purity (Awana *et al.* 2008; Qi *et al.* 2008b).

The amount of impurities can be controlled both by the choice of starting materials and by suitable modification of processing techniques. For RE1111 system, the starting materials include pure rare earth metals, As, Fe, Fe_2O_3/RE_2O_3 and FeF_2/REF_3. The rare earth metals are expensive and very sensitive to oxygen and humidity. They need to be handled carefully in a well-conditioned glove box having high purity inert atmosphere. The toxicity and volatility of arsenic should be taken care of by taking appropriate safety measures for proper usage and disposal after use. Now, in the early reports it was seen that RE_2O_3 was used as the oxygen source. But, later it was observed that for improved reaction Fe_2O_3 is a better source since RE_2O_3 is comparatively more stable and hard to dissociate (Chen(b) *et al.* 2008a). Further, it was seen that FeO is much better than Fe_2O_3 (Wang(a) *et al.* 2012). Finally, in solid state synthesis one has the freedom to choose the starting materials according to their reaction characteristics so as to obtain a particular compound with a desired stoichiometry. However, regarding stoichiometry, one of the hurdles with fluorine doped RE1111 system lies in the large disparity between the nominal F content needed and the actual content in the sample formed (Malavasi *et al.* 2010). Thus, several precautions are taken in solid state method itself such as optimization of processing

temperatures, use of expensive materials such titanium as wrappers for samples heat treated in quartz tubes, use of excess ingredients to compensate the loss and so on. Still, the control on fluorine content and its estimation in the final compound remains a concern.

3.1.1.2 High pressure synthesis

In search of other options to control the volatile loss of fluorine, it was observed that iron pnictides can be prepared using high pressures also (Ren(a) *et al.* 2009). The high pressure method differs from the two-step solid state method in the second step. The ingredients are pelletized and prepared pellets are sealed in boron nitride (BN) crucibles, then placed inside a graphite heating tube and mounted into a six-anvil high-pressure sintering machine. A high pressure of 6 GPa, a pressure enough to squeeze out the air, was applied to the sample which was then heated at 1250 °C for two hours while maintaining the pressure, and then cooled before the pressure was released. This high pressure method has proven to be more effective for F doping (Yang(b) *et al.* 2009). The reason is that the press-sealing of the BN cell is much better at keeping the fluorine from being lost. In addition, fluorine can react with the quartz tube, sometimes even causing breakage of the tube when the sample mass is too high. Another advantage is that high pressure synthesis can produce a very dense and high quality sample that is more suitable for physical property measurements. However, the samples synthesized through high pressure method are restricted to smaller sizes.

High pressure sintering was found to be very effective in synthesizing a new series of oxygen deficient $REFeAsO_{1-x}$ superconductors without F doping, similar to the adjustment of oxygen content in cuprates (Ren(a) *et al.* 2008c; Ren(a) *et al.* 2008d). The synthesis of the O deficient samples is similar to that explained above, only with different starting chemicals according to the chemical formula. Since one vacancy can release two electrons into the lattice, whereas an F atom only releases one, the O deficient method proved to be more effective and advantageous than F doping by eliminating the reactive F. However, until now, this $REFeAsO_{1-x}$ superconductor has not been obtained by methods other than high pressure synthesis. The reason is that the O vacancy is not stable in these compounds (Ren(a) *et al.* 2009). Moreover, this technique could also induce superconductivity in heavy rare earth based RE1111 systems which were not superconducting when prepared at ambient pressures. In terms of properties, high pressure synthesized samples display higher T_C, smaller lattice parameters and unit cell volume. Nevertheless, iron oxypnictides are now being synthesized in either ways depending on the starting materials and requirements.

3.1.2 Single crystals and thin films

Extensive work has been carried out to synthesize high purity polycrystalline materials and to grow sizeable single crystals of iron based superconductors in order to explore the intrinsic as well as anisotropic physical properties and superconducting mechanism. The availability of millimeter-sized high quality single crystals enables various structural and physical property studies to be conducted by different techniques. The successful growth of centimeter sized single crystals of 122 systems has enabled significant understanding of these iron pnictides and elucidated the important structural, magnetic, thermodynamic, and transport features of these novel superconductors (Canfield *et al.* 2010). In contrast, the growth of RE1111 has been found to present several challenges showing serious difficulty in synthesis protocol. There are no reports available on the multicomponent phase diagram and the melting/solidification mode of REFeAsO compounds, which would facilitate design and optimization of growth processes. Moreover, the high vapor pressure at relatively low temperatures and toxic nature of arsenic require special precautions during the crystal growth. Single crystals of RE1111 were initially grown out of NaCl flux under ambient or high pressure. The low solubility of the starting materials in NaCl flux demands high temperatures and high pressure for larger crystals (Fang(b) *et al.* 2009; Martin *et al.* 2009; Lee(d) *et al.* 2009).

The first report based on single crystal growth using flux method was from Jia et al. (Jia *et al.* 2008a). They synthesized single phase samples of $NdFeAsO_{0.82}F_{0.18}$ with plate like crystals of size ranging from 5 to 50 nm. In the preparation process, NaCl/KCl was used as the flux, with a mass ratio NaCl:Nd1111 = 10:1, and sealed in an evacuated quartz tube, and heat treated at 1050 °C for 10 days. This method is efficient in lowering the processing temperature, and growing high quality single crystals, even though the growth time is longer. However, the separation of crystals from flux by washing and cleaning processes generates a large amount of hazardous waste water containing sodium arsenate hydrate (Yan *et al.* 2011). This motivated the search for the criteria in looking for new, environmentally benign fluxes for the growth of RE1111 compounds and this led to NaAs. Later, it was identified that NaAs can be a suitable flux for the growth of plate-like LaFeAsO single crystals with typical dimensions of $3 \times 4 \times (0.05–0.3)$ mm^3. This growth protocol was then applied to other RE1111 compounds with magnetic rare earth ions. The ability to extract RE1111 crystals from this NaAs flux suggests that NaAs has significant oxygen solubility, possibly due to the formation of the ternary compound $NaAsO_2$, and enough oxygen diffusivity to transport solute to the growth front. Oxygen solubility and

diffusivity are two important factors in searching for an alternative environmentally benign flux for the growth of RE1111 superconductors.

High quality epitaxial thin films are very helpful to explore the intrinsic properties of superconductors, especially when it is difficult to prepare sizable single crystals. Successful fabrication of thin films is essential for the development of electronic devices such as the Josephson device and SQUIDs. Actually, it is a tough task to obtain even polycrystalline films because of the difficulties associated with the excitation laser source and the preferential deposition of non-metallic impurity phases present in iron oxypnictides. Some groups have succeeded in the fabrication of epitaxial thin films by Pulsed Laser Deposition (PLD) (Hiramatsu *et al.* 2008; Choi *et al.* 2009; Backen *et al.* 2008; Kidszun *et al.* 2010). The first report is on deposition of codoped $SrFe_2As_2$ on (*100*)-oriented mixed perovskite (La, Sr)(Al, Ta)O_3 single crystal substrates using a second harmonic Nd:YAG laser. Thereafter, the thin film forms of La1111 on (*001*)-oriented $LaAlO_3$ and MgO were developed by a group in Germany (Backen *et al.* 2008). Recently the growth of epitaxial thin films of RE1111 by molecular beam epitaxy (MBE) has been reported (Kawaguchi *et al.* 2010, Ueda *et al.* 2011). The growth of superconducting Sm1111 films by F diffusion using MBE was also reported. The growth conditions and the properties of resultant films were compared for CaF_2 and $LaAlO_3$ substrates. The F diffusion approach is powerful to grow plain superconducting RE1111 films, but it has a problem with the existence of an undesired layer of SmOF and/or SmF_3 on the surface of films, which is not suitable for fabricating multi-layer Josephson junctions (Takeda *et al.* 2012).

3.1.3 Wires and tapes

From the application point of view, iron based superconductors are attractive due to their relatively high T_C and high critical fields. All the early reports showed that iron based superconductors exhibited extremely high H_{C2}, very low anisotropy, and rather large J_C values with field independency at low temperatures, indicating good possibilities for magnet applications at 20-30 K, where the niobium-based superconductors cannot play a role owing to their lower T_Cs. Shortly after the discovery of oxypnictide superconductors, the first trial fabrication of pnictide wire was reported for La1111, Sm1111, and (Sr, K)Fe_2As_2 superconductors (Gao *et al.* 2008a; Gao *et al.* 2008b; Gao *et al.* 2009b). Initially, the critical current density (J_C) was estimated only from magnetization measurements and not from I-V measurements. To observe J_C in the I-V measurement, the good connections between a sheath and the superconducting phases are absolutely necessary. As we know,

wires for bulk applications are always based on polycrystalline materials, however, the global J_C observed in polycrystalline samples is just in the orders of 10^3 A/cm^2 at 4 K in self-field (Yamamoto *et al.* 2008; Wang(a) *et al.* 2009; Putti *et al.* 2010). It was reported that strong granularity of these compounds restricted global J_C values to very low ones (Gao *et al.* 2008b). Microstructural studies emphasized cracks, low density, grain boundary-wetting FeAs phase, and phase inhomogeneities which cause local suppression of the order parameter at grain boundaries as responsible factors for current blocking in polycrystalline materials. Moreover, iron pnictides have relatively tough and hard phases, and thus cannot be plastically deformed. Therefore, the most common approach for developing wires from such brittle superconductors i. e. the powder-in-tube (PIT) process was followed, in which powders are packed in a metal tube, mechanically processed into a wire or tape form, and finally heat treated for reaction. The PIT process is attractive from the aspect of applications, taking advantage of the low material costs and the relatively simple deformation techniques. Actually, the PIT process was being used for making electrical conductors from brittle superconductors such as Nb_3Sn, MgB_2, and cuprates (Kunzler *et al.* 1961; Flukiger *et al.* 2003; Hikata *et al.* 1989).

Generally, the PIT pnictide wire is fabricated by packing stoichiometric amounts of 11, 122 or 1111 powder particles into a metal tube under Ar atmosphere and sealed to form a billet. The billet is then swaged and drawn to wire composites and finally given a heat treatment under Ar. In order to get a tape form, the final wire sample is again flat rolled. Furthermore, the PIT technique is usually classified into two different processes: *in situ* and *ex situ*. In the former case, a mixture of the starting materials is packed into a metal tube and the reaction is performed within the final wire or tape after deformation, whereas the latter employs a precursor of synthesized superconducting material before filling into the metal tube.

In the early stage of pnictide wire development, one of the main challenges encountered in fabricating wires or tapes by the PIT process is the hardness and brittleness of the compound pnictide. On the other hand, the use of proper metal cladding is another critical issue because of the strong chemical reactivity of the pnictide at the high heat treatment temperatures of 900-1200 °C for tens of hours (Ma(a) *et al.* 2012). Thus, the choice of the metallic sheath has been reduced to those elements or metals showing little or no reaction with pnictide at this temperature range. However, early efforts suffered from the reaction layer problem. Zhang et al. systematically studied the effect of various sheath materials on the microstructure and superconducting properties of Sm1111 wires

(Zhang(b) *et al.* 2010). By means of the elemental maps and EDX spectra measurements, indeed all the sheaths such as Nb, Ta and Fe/Ti showed a markedly high reaction with the pnictide due to the diffusion of As into the sheath, the interfacial reaction layer ranges from 60-200 μm thick. These results demonstrated that such a thick reaction layer formed between the core and the sheath would act as a big barrier for obtaining the transport J_C values in the wire samples. In 2009, Wang et al. fabricated $Sr_{0.6}K_{0.4}Fe_2As_2$ wires and tapes wherein a composite sheath material Ag-Fe was used (Wang(a) *et al.* 2010). This led to the first success in measuring the transport critical current in the 122 type wires, a breakthrough in iron pnictide wire development. Later, Fujioka et al. claimed that Cu could work as a good sheath material, but they did not provide a critical current data for their wires (Fujioka *et al.* 2011b). Future studies may focus on the methods of texturing and element-doping in order to minimize weak-link problems at grain boundaries and to improve the inter-granular current density of polycrystalline 1111 superconducting wires.

3.2 Processing technique followed in the present work

The overall analysis of processing techniques adopted by different internationally accredited groups and the discussions on the merits and demerits of these techniques prompted us to develop a novel route taking consideration of all aspects concerning the 1111 class of iron pnictides. The processing technique followed both for polycrystalline/bulk and wire samples and details regarding the technique chosen are dealt in the succeeding sections. The processing technique discussed in this section has been followed throughout the thesis work.

3.2.1 Processing technique for bulk samples

The bulk samples of RE1111 were synthesized by conventional solid state route at ambient pressures. The synthesis method is essentially a single step process, i.e. all the ingredients are processed together. However, the heat treatment was done in two stages. In short, the synthesis of bulk superconductors is done using a single step two stage method involving a novel pre-processing technique developed by our own group (Anooja *et al.* 2012).

Samples with nominal compositions of $REFeAsO_{1-x}F_x$ were synthesized in the following manner. Stoichiometric amounts of RE, Fe, As, Fe_2O_3 and FeF_2 powders (M/s Alfa Aesar, purity 99.9%) were used as starting materials. Since rare earth is highly oxygen sensitive, the storage and use of rare earth is a problem. A well-conditioned glove box with high purity argon atmosphere was exclusively used for the work to resolve this

issue. The glove box has two chambers: a main chamber and ante chamber. The pressure inside both the chambers is monitored using Pirani gauges and displayed by digital and analogue meters. The minimum pressure reached in the ante chamber is 10^{-3} milli bar. The highly reactive rare earth rods and the volatile arsenic are stored in the ante chamber. Inside the glove box, we have placed a weighing machine, a set of sieves and files and also have fixed a vice so as to clamp the rare earth rod for filing. This rod is then subjected to filing under inert atmosphere and the rare earth powder thus obtained is sieved to particles of size around 75 μm. All the ingredients are then weighed, mixed and ground into a homogenous mixture within the glove box. The homogenous mixtures of each stoichiometry was then compacted into rectangular pellets with dimensions of 15 mm × 5 mm × 2 mm, under a pressure of 500 MPa using a hydraulic press (Herzog TP 20P). The pellets were barely placed in one end closed quartz tubes, evacuated with argon partial pressure and sealed. The sealed tubes were then subjected to heat treatment in a programmable muffle furnace having stability and accuracy better than ±1 °C controlled using Eurotherm-2404 temperature controller. The exhaust gases from the furnaces, if any, were allowed to flush through an outlet and driven above the building height. The pellets in the evacuated quartz tubes were pre-processed at an optimized condition of 360 °C for 5 h. The optimally pre-processed samples, were again ground, repelletized and sealed in an evacuated quartz tube for the final sintering at 1000 °C for 50 h. This is the preparation procedure generally followed for all the bulk samples and it is schematically represented in Figure 3.1. Depending upon the dopants or starting materials used the final sintering temperature is altered.

3.2.2 Processing technique for wires

The rapidly growing literature dealing with the preparation of iron pnictide compounds demands that the feasibility of fabricating powder-in-tube (PIT) processed pnictide wires needs to be explored in detail. The PIT process takes advantage of the low material costs and the deformation techniques employed are relatively simple. The choice of the metallic sheath has been reduced to those elements or alloys showing little or no reaction with pnictides at high temperatures. Generally, RE1111 based iron pnictides are synthesized at temperatures as high as 1150–1250 °C. On the other hand, low temperature fabrication process is required from the point of view of the sheath reactivity and the processing cost. The PIT processing routes reported so far either follow the *in situ* method wherein the starting materials are directly filled in the tubes, then rolled and heat treated or the *ex situ* method where the reacted samples are filled and further processed.

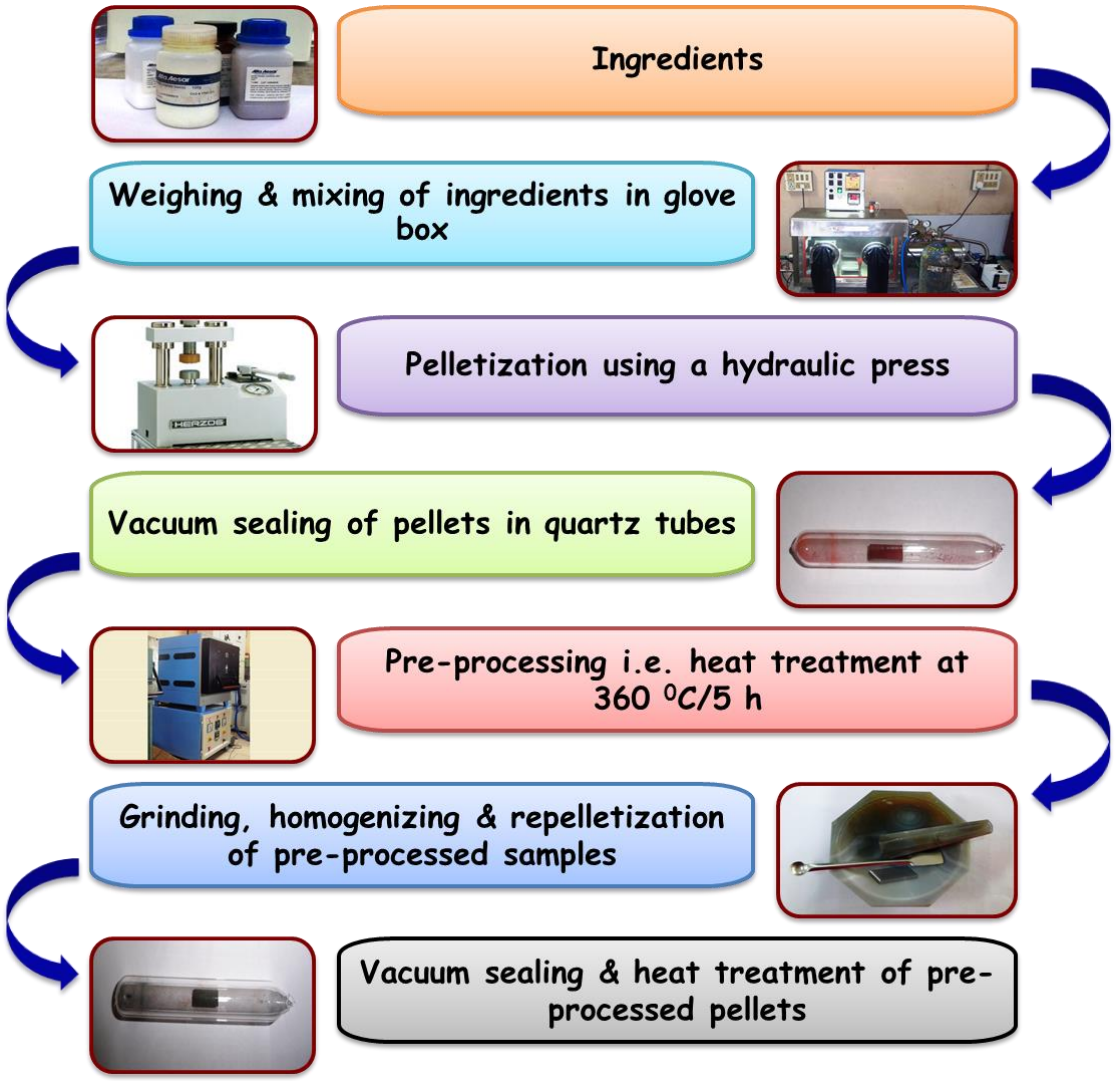

Figure 3.1: A schematic representation of the preparation procedure for bulk superconductors

In the present work, we prepared RE1111 based wires using the precursor developed by the pre-processing technique as described in the previous section followed by the PIT method. A schematic diagram displaying the steps for preparation of metal sheathed RE1111 wires is shown in Figure 3.2. Initially, the ingredients such as freshly made RE filings, Fe powder, Fe_2O_3 powder, As lumps and FeF_2 powder, with a stoichiometry $REFeAsO_{1-x}F_x$ were well ground in Ar atmosphere. The homogenous powder was then pre-processed at a temperature of 360 °C for 5 h. This precursor powder was further placed in metal tubes (OD/ID: 6/4 mm). The filled tube was end sealed and then groove rolled down to desired dimensions. Short samples were cut from the as-drawn wires for sintering. For tape preparation, the wires were further flat rolled. The wires/tapes were then sintered at temperatures of 800-950 °C for 30-50 h in Ar atmosphere.

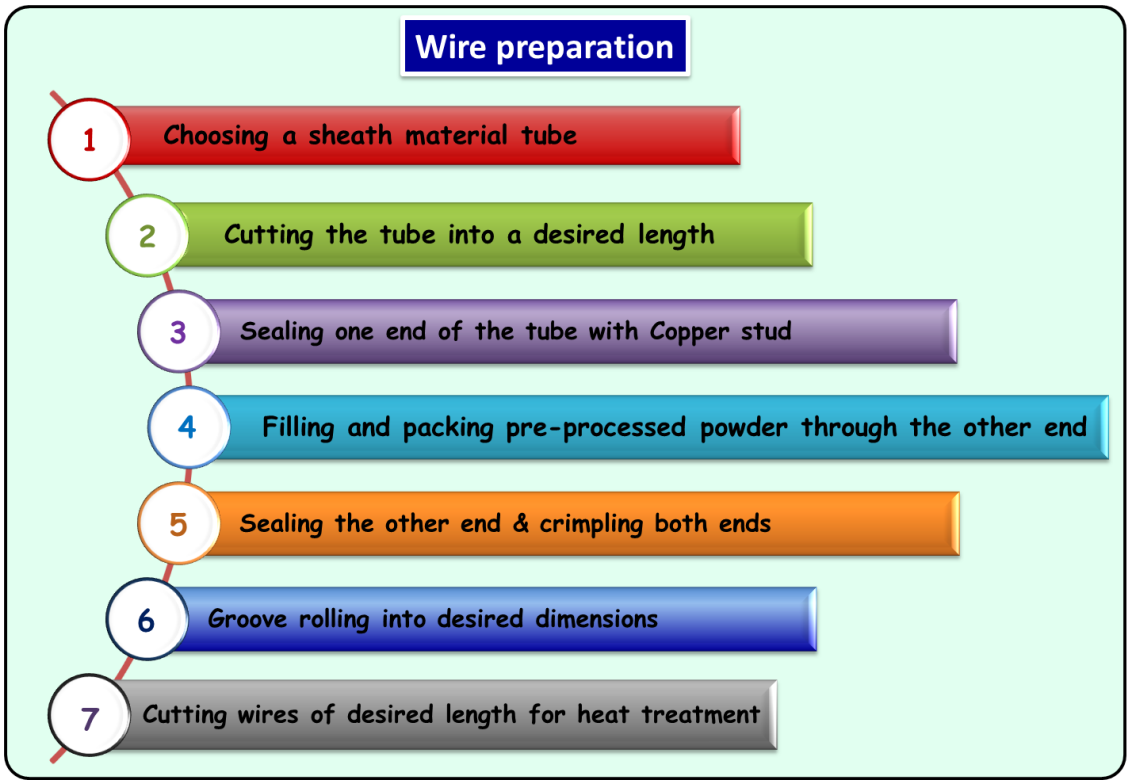

Figure 3.2: A schematic representation of the preparation procedure for superconducting wires

3.3 Characterization techniques adopted

Understanding the relationships between processing, structure, properties, and performance is of at most importance in the development process of new and advanced materials. The superconducting bulks as well as wire/tape samples prepared for the present work were, hence, subjected to both structural and superconducting characterizations. This section gives a detailed description regarding the characterization techniques adopted and the instrumental specifications.

3.3.1 Structural and microstructural characterization

Structural characterization of materials involves the understanding of the elemental composition, the crystal and local structures, and the types of defects present in the material. Microstructural analysis gives a deeper insight of the overall homogeneity, sample density and grain morphology of the materials at micro level. The samples prepared for the present study were subjected to different characterizations such as x-ray diffraction, optical imaging, scanning electron microscopy and energy dispersive x-ray analysis.

3.3.1.1 X-ray diffraction (XRD) analysis

X-ray powder diffraction is a rapid analytical technique primarily used for phase identification of crystalline materials and determination of unit cell dimensions. The

principle behind this technique is that materials can be probed to different extents with electromagnetic radiations of suitable wavelengths. To yield useful information about the structure of the analyzed material, x-rays having wavelength of the same order of magnitude as the interatomic spacing in the crystal structure is highly essential. In 1912, Max Von Laue discovered that crystalline substances act as three dimensional gratings for x-ray wavelength to the spacing of planes in a crystal lattice. A crystal is a complex but orderly arrangement of atoms, and all atoms in the path of an x-ray beam scatter the incident x-rays simultaneously. In general, the scattered x-rays interfere, essentially canceling each other out. In certain specific directions, where the scattered x-rays are "in-phase", the x-rays scatter cooperatively to form a new wave. This process of constructive interference is diffraction. W.L. Bragg developed an equation for diffraction, equivalent to the simultaneous solution of the three Laue equations by monochromatic radiation, which allows diffraction to be treated mathematically as reflection from the diffracting planes. He pointed out that, for any crystal, one can draw a set of equidistant parallel planes that pass through all of the atoms in the crystal, and that there are many different sets of such "Bragg" planes. The planes are labeled with a set of integers (*hkl*), called the Miller indices, which are identified as the reciprocals of the fractional intercepts which the plane of interest makes with the crystal axes. Consider a beam of parallel x-rays penetrating a stack of planes of spacing d, at a glancing angle of incidence, θ as shown in Figure 3.3. Each plane is pictured as reflecting a portion of the incident beam. The "reflected" rays combine to form a diffracted beam if they differ in phase by a whole number of wavelength, that is, if the path difference = nλ where n is an integer.

The diffractometer unit used for the x-ray analysis of samples for the present study is PANalytical X'pert Pro (Model: PW 3040/60) x-ray diffractometer with CuKα radiation employing a proprietary detector, X'Celerator and a monochromator at the diffracted beam side. A mechanical assembly called goniometer holds and moves the x-ray source on one arm and the detector on the other as shown in Figure 3.4. The system has 'θ-θ' Bragg-Brentano geometry (both source and detector make an angle θ with the sample surface) with fully automated operation and data acquisition. Programmable slits are used to limit the x-ray beam to the specified sample area. Most of the scans are performed under a tube voltage and current of 40 KV (λ = 1.540566 Å) and 30 mA, respectively. The sample to be analyzed was finely powdered, filled in standard holders and the XRD data were recorded at room temperature. For less amount of powder (especially from small wires/tapes) a

standard zero back ground holder was used. Usually, the samples were scanned for 2θ in the range from 20 to 70° with a step size of < 0.02°.

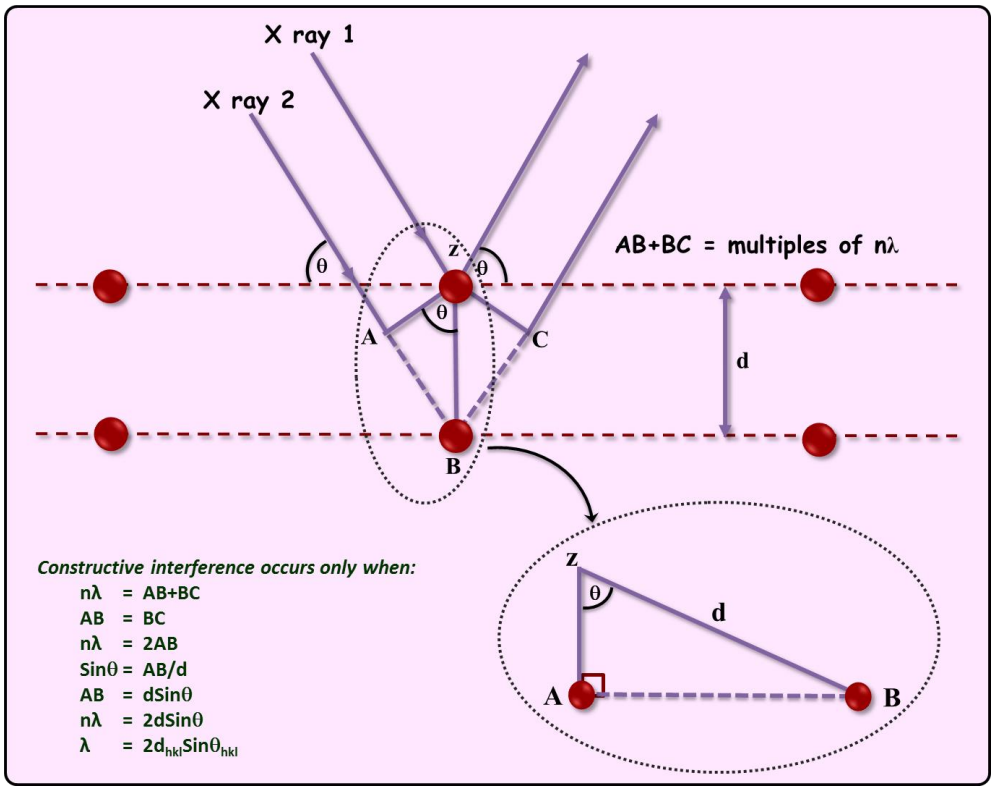

Figure 3.3: Bragg's representation treating x-ray diffraction as reflection from parallel planes

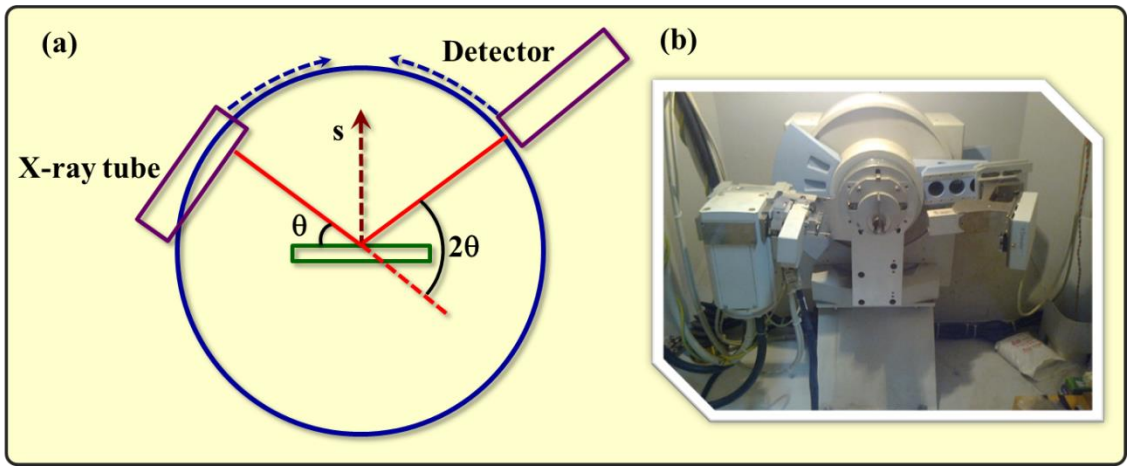

Figure 3.4: (a) Schematic representation of powder x-ray diffraction technique and (b) Photograph showing the source, sample holder and detector held by goniometer

The uses of x-ray diffraction mainly include phase identification, unit cell lattice parameter refinement, and estimation of crystallite size and microstrain of the sample. The diffraction pattern for every phase is as unique as a fingerprint. The position and relative intensity of a series of peaks of the experimental data can be matched to the reference

patterns in the database to identify a particular phase. Using X'Pert Highscore software, phase identification of the samples can be performed with support of the ICDD-PDF-2 database. The volume percentages of different phases in the samples can be assessed semi-quantitatively, from the integrated x-ray peak intensities, using the relation

$$\text{Vol.\,\% of phase X} = \left(\frac{\Sigma(Integrated\ peak\ intensities\ of\ phase\ X)}{\Sigma(Integrated\ peak\ intensities\ of\ all\ phases)}\right)$$

By accurately measuring peak positions and corresponding d values over a long range of 2θ, one can also determine the unit cell lattice parameters. Crystallites smaller than ~120 nm create broadening of diffraction peaks. This peak broadening can be used to quantify the average crystallite size of nanoparticle using the Scherer equation. Microstrain may also create peak broadening. Analyzing the peak widths, Full width at half maximum (FWHM) over a range of 2θ can be estimated and using a Williamson-Hall plot ($FWHM \times Cos\theta$ *versus* $Sin\theta$) one can separate microstrain and crystallite size (Williamson *et al.* 1953). In the present work, XRD analysis has been used for phase identification, phase quantification, lattice parameter and FWHM calculation.

3.3.1.2 Optical imaging

The optical microscopes use visible light and a system of lenses to magnify images of small samples. The image from an optical microscope can be captured by normal light-sensitive cameras to generate a micrograph. Developments in technology like complementary metal-oxide semiconductors (CMOS) and charge-coupled device (CCD) based cameras allow the capture of digital images. Purely digital microscopes use a CCD camera to examine a sample and the resulting image directly displayed on a computer screen. A Leica EZ4 HD stereo microscope with magnification up to 35X was used for the close examination of the samples prepared for the present work. Leica EZ4 HD stereo microscope offers high quality 4.4:1 zoom. The 7 LEDs in this model provide transmitted, incident and oblique light for high quality illumination and contrast. The integrated High Definition digital camera offers a fast live image on a computer screen or high definition display transforming a stereomicroscope into a USB microscope. It captures 3 Mega pixel color images directly onto SD card or Windows or Mac computer. The intuitive Imaging software allows for easy fine tuning, capture, and archiving of images. The Leica LAS EZ software also allows for basic annotation and measurements such as exact estimation of core and sheath cross sectional areas of wires/tapes. In the present study, optical microscopy is used to analyze the cross section of the wire or tape samples. Samples of size around 5 mm were cut from long conductors, polished mechanically and placed under

the microscope in suitable holders for taking images at different magnifications. The cross sectional analysis provides the details regarding estimation of core area, homogeneity of the filaments, final geometry and the interfacial reaction between core and sheath of the conductors.

3.3.1.3 Scanning electron microscopy (SEM)

While using visible light as a source of electromagnetic radiation one can probe only the superficial appearance of a material, alternatively the use of a focused beam of electrons for scanning a material can yield finer details and this is called as Scanning Electron Microscopy. The scanning electron microscope (SEM) uses a focused beam of high-energy electrons to generate a variety of signals at the surface of solid specimens. The signals that derive from electron sample interactions reveal information about the sample including external morphology (texture), chemical composition, and crystalline structure and orientation of materials making up the sample. In most applications, data are collected over a selected area of the surface of the sample, and a two dimensional image is generated that displays spatial variations in these properties. The electron beam is generally scanned in a raster scan pattern, and the beam's position is combined with the detected signal to produce an image. Specimens must be electrically conductive, at least at the surface, and electrically grounded to prevent the accumulation of electrostatic charge at the surface. Specimens can be observed in high vacuum, low vacuum and in environmental SEM specimens can be observed in wet condition. The types of signals produced in SEM include secondary electrons (SE), back-scattered electrons (BSE), characteristic x-rays, light (cathodoluminescence) (CL), specimen current and transmitted electrons. In the most common or standard detection mode, secondary electron imaging (SEI), the SEM can produce very high-resolution images of a sample surface, revealing details less than 1 nm in size. The spatial resolution of the SEM depends on the size of the electron spot, which in turn depends on the wavelength of the electrons the electron-optical system that produces the scanning beam. The resolution is also limited by the size of the interaction volume.

In the present study, the microstructural analysis was done using a JEOL JSM 5600LV scanning electron microscope equipped with an energy dispersive x-ray spectrometer (Phoenix) used in SEI mode. Freshly fractured surfaces of the bulk samples are mounted on brass studs using adhesive carbon tapes or conducting silver paste. Since the iron pnictide samples are electrically conducting, gold coating is not required. The brass studs with the mounted samples are loaded on the sample holder of the microscope. In the case of wires/tapes, the cross sectional surface of the conductor is polished and then

erected on brass studs for SEM. SEM images were taken for a magnification up to 5000 times. The SEM analysis of the samples prepared for the present work has helped in analyzing the sample homogeneity, density, grain morphology and connectivity.

3.3.1.4 Energy dispersive x-ray spectroscopy (EDX/EDS)

Energy dispersive x-ray spectroscopy is an analytical technique that qualitatively and quantitatively identifies the elemental composition of materials analyzed in SEM. EDS analyzes the top two microns thickness of the sample with a spatial resolution of one micron. Beryllium windowed EDS detect all elements with atomic numbers greater than oxygen at concentrations greater than 0.1%. When the electron beam of the SEM is scanned across the sample, it generates x-rays from the atoms. To return the ionized atom to its ground state, an electron from a higher energy outer shell fills the vacant inner shell and, in the process, releases an amount of energy equal to the potential energy difference between the two shells. This excess energy, which is unique for every atomic transition, will be emitted by the atom either as an x-ray photon or will be self-absorbed and emitted as an Auger electron. The energy of each x-ray photon is characteristic of the atom from which it escapes. The EDS system collects the x-rays, sorts them by energy and displays the intensity versus their energy. This qualitative EDS spectrum can then be further analyzed to produce either an area elemental analysis (displayed as a dot map) or a linear elemental analysis (displayed as a line scan) showing the distribution of a particular element on the surface of the sample. The EDS data can be compared to either known standard materials or computer-generated theoretical standards to produce either a full "quantitative" or a "semi-quantitative" analysis. The location of the peaks identifies the elements.

In the present study, an EDS (Phoenix) attached with SEM was used for elemental analysis. Quantitative analysis requires much more effort and care, but with proper settings, an accuracy of ± 2% of the wt % is obtained (example, for 10 wt% the accuracy is ± 0.2 wt %). Each spectral data is taken after an exposure time of 60 seconds. Once the spectrum is collected, the background is removed by digital filtering algorithm. The obtained profile is compared with the standard materials of known homogeneous compositions at the microscopic level.

3.3.2 Superconducting characterization techniques

As we know, the phenomenon of superconductivity is realized by the zero resistance behavior exhibited by a material at very low temperatures. This implies that a

material can be checked for superconductivity only if it is cooled from room temperatures to very low temperatures with simultaneous monitoring of resistivity. Another approach uses the magnetic behavior of a superconductor. Superconductors show perfect diamagnetism once they are kept below the critical temperatures. Hence, susceptibility measurement with varying temperature is also an important superconducting characterization technique. Apart from the basic check for superconductivity, the samples proved to be superconductors can also be subjected to many other measurements such as current versus voltage measurement, critical current density versus applied field measurement and so on, to understand and compare their performance level with the existing ones.

3.3.2.1 Resistivity versus temperature (R-T) measurement

Resistivity depends upon the nature of the material. The resistivity is calculated by measuring resistance R and the dimension of the sample (length, width, thickness). The resistance is determined by voltage/current value. When a current of known value is fed to the sample, then a potential difference is produced across the sample. From these measurements, the resistivity is calculated as, $\rho = \left(\frac{R \times A}{l}\right)$.

There are various methods of resistivity measurements such as two-probe and four-probe methods. In two probe method only one pair of leads runs to the sample from the instrument, in which case the voltmeter and current source share the same pair of leads. In this case, we cannot get the exact resistance. The advantage of for four probe method over two probe method is that it minimizes the other contributions. i.e., lead resistance, contact resistance, etc. to the resistance measurement, which results an accurate measurement of sample resistance. In this method four equally spaced probes are in contact with a material of unknown resistance. The outer two probes are used for sourcing the current and two inner probers are used for measuring the resulting voltage drop across the surface of the sample. In this case, the voltage, $V = (I-I_1)R - I(2R_{contact}+2R_{lead})$ as observed from Figure 3.5 (a). Since the resistance or voltage across the voltmeter measuring the sample voltage is typically much larger than other resistance in the circuit, $I_1 <<< I$. So, $V = IR$, exactly gives the sample voltage.

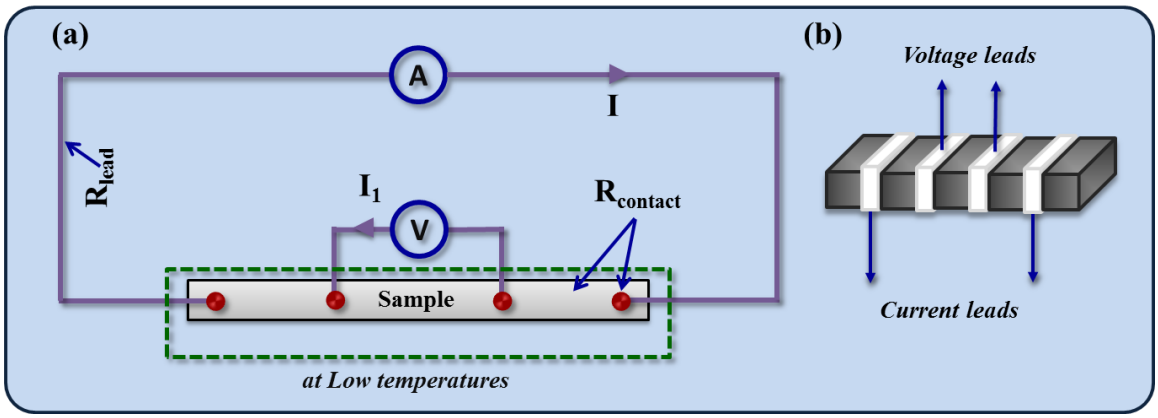

Figure 3.5: Schematic representation of (a) four-probe measurement and (b) a pellet with four probes

In the present study, we measured the resistance of the sample from 300 K down to 12 K a helium based cryocooler integrated cryostat with provision for four probe measurement. The cryocooler used is a Gifford-McMohan cooler manufactured by Sumitomo Heavy Industries Ltd (SRDK-408). A programmable milli-ampere source (***Keithley 220/6220***) was used as current source and a nano-voltmeter (***Keithley 181/2182A***) was used for voltage measurement. Lakeshore L332/L340 model temperature controllers were used for monitoring and controlling the sample temperatures. Oxygen free high conductivity (OFHC) copper wires of suitable gauges were used for both current and voltage leads. The as-prepared bulk pellets were grooved and wound with copper wires at four positions and pasted with air drying silver paint as shown in Figure 3.5 (b). Generally, a current of 100 mA was sourced through the outer end current leads and voltage was measured from the inner voltage taps. If the sample is a superconductor, the R-T plot exhibits a sudden transition or drop of resistance at a particular temperature, which is denoted as the critical temperature, T_C. The difference between the temperatures corresponding to the 90% and 10% of normal state resistivity just above T_C (i.e. $T_{Conset} - T_{Coffset}$) is defined as ΔT_C for the samples.

Apart from the R-T measurements at self-field (0 T), R-T measurements were also conducted under different fields ranging from 0-9 T using PPMS (Quantum design) so as to estimate the upper critical fields of selected samples. The field dependent ρ-T plots showed a broadening with respect to that at 0 T. The normal state resistivity value just above the superconducting transition (say 56 K) was taken as ρ_n. Then, H-T phase diagram was plotted using the field and T_C values obtained for 90% ρ_n values of ρ-T plot at each field. The slope of this H-T plot i.e. d(H_{C2})/dT at T_C was further used to estimate the H_{C2} WHH theory.

3.3.2.2 Current versus voltage (I-V) measurement

I-V measurement is very important to understand the current limitation of the superconductor and thereby to evaluate its status for practical applications. I-V measurements were carried out using four-probe method to determine the current carrying capacity i.e. critical current, I_C. During I-V measurements, a ramping current was passed for short durations (10-100 ms) with sufficient intervals of time for cooling. Here, the current source used is of 100 A capacity (***APLAB 9711P***). From the I-V characteristics, the current at which the voltage shows a sharp rise is usually considered as the transport I_C. Here, the standard 1 μV/cm criterion was used to determine the I_C. Ratio of I_C to the cross sectional area of the sample core is taken as the critical current density (J_C). Both the R-T and I-V measurements were automated and controlled by a PC, interfaced with the system through GPIB/LABVIEW.

3.3.2.3 Hall Effect measurement

Hall Effect is the creation of a potential difference within a sample in the transverse direction i.e. perpendicular to both the current flow and applied field. The Hall co-efficient estimated for a sample depends on whether it has only one type or two types of charge carriers and the temperature dependence of Hall co-efficient also varies depending on whether the material is single or multiband type. The Hall Effect measurement of selected samples at different selected temperatures was also done using the PPMS (Quantum Design). The voltage leads of the samples were fixed in such a way that the leads face each other vertically and are perpendicular to the current leads fixed on the ends along the longitude of the rectangular pieces of samples. The current flows from one end to the other end along an equipotential line and the transverse voltage was measured at different field values sweeping the field from -9 to 9 T. It is to be noted that the field direction was perpendicular to the plane of the sample. Thus, the measured voltage, current flow and applied magnetic field remained mutually perpendicular. Then, the Hall voltage was estimated by eliminating the longitudinal resistivity contribution i.e. the Hall voltage was calculated as:

$$V_H = \frac{V(+H) - V(-H)}{2}$$

Thereafter, the transverse resistivity (ρ_{xy}) was plotted against field which is found to be linear with negative slope; the slope of this plot i.e. ρ_{xy}/B gives the Hall coefficient, R_H. The charge carrier density was then estimated as n = 1/(eR_H).

3.3.2.4 Specific heat capacity measurement

Heat capacity (C) of selected samples was also measured to ensure the T_C and thereby the crystal quality using PPMS (Quantum Design). Initially, the heat capacity of the puck along with suitable amount of adhesive (for sample fixation) is measured with varying temperature and the data was saved as addendum data. The samples were then cut into small cubic pieces having mass less than 10 mg and were placed carefully on the adhesive. The heat capacity of the puck along with the adhered sample was then measured in the same temperature range as for the addenda. The heat capacity of the addenda was then subtracted from the total data, which gives the heat capacity of the sample. The specific heat capacity is directly given by the instrument on providing the mass of the sample, i.e. specific heat C_P = C/m.

3.3.2.5 AC susceptibility versus temperature (χ-T) measurement

The measurement of *ac* magnetic susceptibility as a function of temperature is a convenient and straightforward way to confirm superconductivity in a material. Besides providing a detailed characterization of compounds, *ac* susceptibility measurement is fast and does not require any electrical contact. That is probably the reason why this measuring technique is so widely used for studying superconductors. In *ac* magnetic measurements an *ac* field is applied to a sample and the resulting induced sample moment is time-dependent. *ac* measurements yield information about magnetization dynamics which are not obtained in *dc* measurements, wherein the sample moment is constant during the measurement time. The *ac* susceptibility has an in-phase, or real, component χ' and an out-of-phase, or imaginary, component χ". In the normal state (i.e. above the critical temperature), superconductors typically have a small susceptibility. In the fully superconducting state, the sample is a perfect diamagnet and so χ' = –1. The out-of-phase component of the susceptibility is nonzero for temperatures slightly below the transition temperature, where magnetic irreversibility occurs in the sample. In short, χ' demonstrates flux exclusion due to shielding currents, whereas χ" yields information about *ac* energy losses and relaxation processes. Careful examination of both components can reveal a granular microstructure and the presence of impurity phases, which determine the feasibility of the materials for practical applications. In addition, when varying the applied magnetic field amplitude and/or frequency, results generally allow more fundamental physical parameters, such as the thermal activation energy of flux lines or pinning length scales.

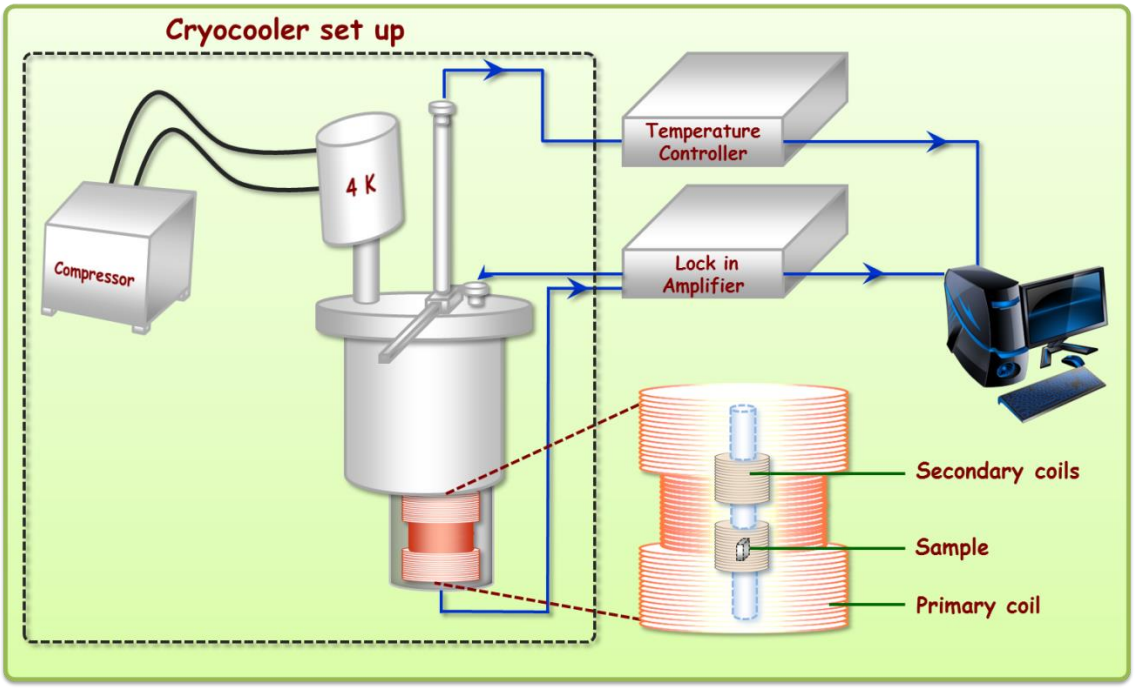

Figure 3.6: Schematic representation of a closed cycle *ac* susceptometer

The principle of *ac* susceptibility measurement is often based on a coaxial mutual inductance technique. A primary coil which generates an *ac* magnetic field and two secondary oppositely wound coils form the basic unit of the measuring circuitry. In the absence of a sample, the voltage measured across these two detection coils is ideally zero. Inserting a sample centered in one of the secondary coils will result in a non-zero signal in the secondary coil due to the electromotive force induced by the primary coil and this is directly proportional to the amplitude of *ac* susceptibility of the sample being measured. In the present study, the temperature dependence of ac susceptibility (χ-T) was measured using a closed-cycle ac susceptometer (ARS-CS202S-DMX-19 SCC, Advanced Research Systems, Macungie, PA) employing a lock in amplifier (SR850, Stanford Research Systems).

A schematic representation of the *ac* susceptibility system used for the present work is shown in Figure 3.6. The bulk samples were placed in the sample holder for susceptibility measurements. Measurements were taken from 300 K to 12 K with the help of lock in amplifier and lakeshore temperature controller and the data acquisition was automated using GPIB-LABVIEW. The χ-T measurement was mainly used for checking the material for superconductivity, determination of T_C and understanding the granularity of the sample. For this, measurements were conducted at a single frequency of ac signals (preferably, 208 Hz) with an *ac* field, H_{ac} = 0.49 mT. Multi-frequency measurements were

also conducted at different frequencies such as 208, 333, 533, 733 and 999 Hz at a fixed field.

3.3.2.6 Critical current density versus applied field measurement (J_C - H)

DC magnetization measurements were done using Physical Property Measurement System (PPMS), in collaboration with JNCASR (Jawaharlal Nehru Centre for Advanced Science and Research, Bangalore), Cambridge University, UK and also an in-house Vibrating Sample Magnetometer based Quantum Design Dynacool PPMS installed in May 2014 at CSIR-NIIST. The PPMS is an open-architecture, variable-temperature field system optimized to perform a variety of automated measurements for material properties such as specific heat, magnetic *ac* and *dc* susceptibility and both electrical and thermal transport properties. The base unit of the PPMS consists of a cryostat with a superconducting magnet coil. The different measurement options result from the use of different measurement inserts or sample holders and the call of the according software mode. It is well known that procuring and maintaining Liquid Helium is a task. This problem has now been solved by redesigning virtually cryogen-free systems with all the capabilities of the PPMS. These systems are integrated with a single, two-stage pulse tube cooler to cool both the superconducting magnet and the temperature control system, providing a low vibration environment for sample measurements. Only Helium-gas is needed for purging the sample chamber. The sample environment allows fields to a maximum of up to ± 16 T (depending on the magnet used) and standard temperature ranges of 1.9 - 400 K. To start the measurement one just needs to insert the sample in the PPMS and create or open a sequence. The system will automatically perform the measurement and start to collect significant data. The vibrating sample magnetometer (VSM) is a powerful measurement system to be used for magnetic sample characterization. The VSM option transforms your PPMS into a sensitive *dc* magnetometer for fast data acquisition. The sample is attached to the end of a sample rod that is driven sinusoidally. The movement of the sample is done by a special sample transport, which has a linear characteristic and thus is very precise and flexible. The basic measurement is accomplished by oscillating the sample near a detection (pickup) coil and synchronously detecting the voltage induced. The voltage induced in the pickup coil is amplified and lock-in detected as in ac susceptibility measurement. The major difference between ac susceptometer and VSM based dc magnetometer lies in the manner how flux variation is attained. Further options which extend the capability of the VSM include:

- Rapid and completely automated centering operation of the sample

- Sensitive *dc* magnetic moment measurement up to the maximum field of the magnet
- Possibility of sweeping the magnetic field or temperature while doing the measurement

For the present work, bulk samples cut into typical dimensions of 3 mm × 3 mm × 1.5 mm were used for magnetization measurements with magnetic field applied along the longest dimension of the samples. M-H (magnetization vs. field) hysteresis loops were measured at different temperatures up to the maximum field possible in the instrument used. Magnetic field dependence of the critical current density, $J_C(H)$ of the sample was estimated based on Bean critical state model (Bean *et al.* 1962) using the formula:

$$J_C(H) = \left(\frac{30 \times \Delta M}{\langle R \rangle}\right)$$

where, $\Delta M = M^+ - M^-$ (in emu/cm^3) is the width of the M-H loop and $\langle R \rangle$ is the average grain size in cm. The M-H measurements were conducted at different temperatures such as 5 K, 10 K, 20 K, 30 K, and 35 K. Flux pinning force (F_P) can be calculated using the formula, $F_P = J_C \times H$. $J_C(H)$ performance and flux pinning behavior of the samples were analyzed based on these measurements.

CHAPTER 4

PREPARATION OF $NdFeAsO_{1-x}F_x$ SUPERCONDUCTOR AND IMPACT OF FLUORINE VARIATION ON ITS STRUCTURAL AND SUPERCONDUCTING PROPERTIES

4.1 Introduction

Following the discovery of superconductivity in electron doped LaFeAsO (T_C ~ 26 K) (Kamihara *et al.* 2008), the T_Cs of these materials ramped up to 55 K by substitution of La^{3+} with other rare-earth elements of smaller ionic radii (Chen(c) *et al.* 2008; Ren(a) *et al.* 2008b; Liu(a) *et al.* 2008; Kito *et al.* 2008; Aswathy *et al.* 2010). The lanthanide substitution not only causes chemical pressure but also introduces additional spin degrees of freedom in the rare-earth oxide (REO) layer due to the unpaired RE 4f electrons. The presence of magnetic elements such as Fe and rare earths often questions the possible interplay of the local moment of the RE '4f' electrons and Fe '3d' electrons with superconductivity. The breakthrough also triggered an active debate regarding whether they resemble cuprates or conventional superconductors (Aswathy *et al.* 2010). Furthermore, the significant characteristic of this pnictide family is the versatile chemistry exhibiting superconductivity in various similar structures, allowing both electron and hole doping. Regarding the synthesis of iron pnictides, most of the groups adopt a two-step method wherein the binary compounds such as REAs, FeAs, or Fe_2As are prepared initially, to avoid the risk of As vapor pressure. The preparation of REAs itself is a two-stage process with processing temperatures in the range 500-600 °C (first stage) and 800-1000 °C (second stage) (Pissas *et al.* 2009; Ren(a) *et al.* 2008d; Zhao(b) *et al.* 2010; Tarantini *et al.* 2008). The final composition is often obtained on reacting the binaries with rest of the ingredients at high temperatures (1150-1350 °C) and/or high pressures (6 GPa) (Pissas *et al.* 2009; Ren(a) *et al.* 2008d; Zhao(b) *et al.* 2010; Tarantini *et al.* 2008; de la Cruz *et al.* 2008; Ding *et al.* 2011; Prozorov *et al.* 2009). Even though such high temperatures and pressures are preferred for the reaction to take place, the volatility of fluorine (F) often hampers the synthesis of iron pnictides with good transport properties. The synthesis route in which the pellets of homogenized ingredients including the binaries are vacuum sealed in quartz tubes for further heat treatment is referred as *ambient pressure synthesis* (APS) whereas *high pressure synthesis* (HPS) is carried out in in boron nitride crucibles under high pressures (up to ~ 6 GPa) and high temperatures (~ 1250 ºC) (Kito *et al.* 2008). The HPS method is mainly used to make fluorine free superconducting

oxypnictides and is restricted to small sized samples only. However, La/Ce/Sm1111 based systems are mainly synthesized using APS method but for Nd1111 samples HPS technique was found inevitable to circumvent the fluorine loss in common quartz tube method. Though rousing improvement has been observed in the superconducting properties of iron pnictides, efforts are still going on to optimize the processing parameters so as to minimize the processing temperatures and pressures with minimum fluorine loss and to reduce the reaction between the reactants and the container.

Among the different classes of iron based superconductors, $REFeAsO_{1-x}F_x$ (RE1111) compounds stand out in terms of relatively high T_C, moderate J_C and very high H_{C2}. These compounds crystallize in the ZrCuSiAs tetragonal structure of P4/nmm space group having two formula units per unit cell. The crystal structure consists of alternatively stacked REO and FeAs layers along the *c* axis. The parental phase REFeAsO is non-superconducting and shows structural as well as magnetic transition around 150 K. It is observed that either fluorine doping at oxygen site or creation of oxygen vacancies is inevitable for superconductivity to occur. Amongst the RE1111 compounds, the very high upper critical fields around 300 T make $NdFeAsO_{1-x}F_x$ one of the most promising candidates. Nevertheless, the impact of varying fluorine content on the electromagnetic properties of this superconductor has not been addressed so far. It is important to have a clear direction on how to optimize transport properties of polycrystalline materials and also to understand the intrinsic nature of their grain boundaries. Here, we discuss the influence of fluorine variation on the transport properties of Nd1111 superconductor samples synthesized at a relatively low temperature and ambient pressure. The correlation of the observed transport and magnetic properties of the samples with their microstructure is also discussed.

4.2 Precautionary steps taken for the synthesis of $NdFeAsO_{1-x}F_x$ compounds

The initial effort towards any synthesis procedure begins with the procurement of essential starting materials. In the present case since the ingredient, rare earth is extremely oxidizing in ambient conditions, the storage and processing of the ingredients in inert atmosphere demanded a glove box. A custom made glove box was procured and suitably modified. All the preparation procedures such as filing of rare earth metal rods/ingots into powders, weighing of ingredients and mixing was done after repeated (30-40 times) evacuation and filling of ultra-high purity Argon gas in the main chamber. For $NdFeAsO_{1-x}F_x$ based compounds, the ingredients include high purity chemicals such as Nd, Fe, As, Fe_2O_3, FeF_2 and other dopants for the doped variants. Among these ingredients, rare earth

and their compounds are highly expensive. Even if we preserve powders of pure rare earths in high vacuum or inert conditions, they get degraded with time. So the rare earth metals were procured in the form of rods and powdered by filing them in the glove box as and when required. The suppliers (M/s Alfa Aesar) provide pure rare earth rods which are packaged in Mylar under argon and hence can be safely stored in inert chambers. The rod to be used is fixed on a vice which is permanently fixed in the glove box. The rod is then filed using a suitable filing tool, in inert atmosphere. On obtaining enough powder the remaining rod is smeared with mineral oil and again stored in inert chamber. Here, the loss suffered due to degradation is limited to the surface layers only. The rare earth filings thus obtained are further ground to smaller grains and mixed with rest of the ingredients using an agate mortar and pestle kept inside the glove box. For arsenic, only required amount of arsenic lumps were ground and the rest were stored in vacuum sealed condition. For oxygen and fluorine sources, Fe based compounds: Fe_2O_3 and FeF_2 were chosen; since rare earth based compounds were not only expensive but also very stable and hence less reactive. The homogenized powders of starting materials were pelletized and the pellets were then vacuum sealed in quartz tubes. The sealed quartz tubes were heat treated in a programmable muffle furnace with special provisions for disposal of waste gases if any.

4.3 Preparation of $NdFeAsO_{1-x}F_x$ superconductor using a pre-processing technique

Samples with nominal compositions of $NdFeAsO_{1-x}F_x$ (x = 0, 0.1, 0.2, 0.3, and 0.4) hereafter referred as Nd0, Nd1, Nd2, Nd3, and Nd4 were synthesized by a one-step solid-state method using a pre-processing technique developed by our group (Anooja *et al.* 2012) (detailed discussion is given in *Chapter 3*). Stoichiometric amounts of Nd, Fe, As, Fe_2O_3, and FeF_2 powders (M/s Alfa Aesar, purity 99.9%) were used for the synthesis. The F source (FeF_2) was added 20% higher than the nominal compositions to compensate the volatile loss and reaction of F with quartz glass at elevated temperatures (Jaroszynski *et al.* 2008b; Chen(d) *et al.* 2010a). The corresponding excess of Fe was deducted from the free Fe added into the system. The starting materials were weighed, mixed, and ground to form a homogenous mixture, inside a glove box with ultra-high purity argon atmosphere. These samples were compacted into rectangular pellets with dimensions of $12 \times 2 \times 2$ mm^3, under a pressure of 500 MPa. The pellets were barely placed in evacuated sealed quartz tubes. The sealed tubes were subjected to a preprocessing at 370 °C for 5 h in a programmable muffle furnace. The preprocessed samples were again ground, pelletized, and sealed in

evacuated quartz tubes and sintered at 850 °C for 20 h and 1000 °C for 30 h in a single step.

The phase identification of the samples was performed using an x-ray diffractometer (PANalytical X'Pert Pro, the Netherlands) with CuKα radiation employing a proprietary high-speed detector and a monochromator at the diffracted beam side. Microstructural examination was done using a scanning electron microscope (JEOL-JSM-5600LV, Japan). Superconducting transport measurements such as resistivity versus temperature (ρ-T) and current versus voltage (I-V) were carried out using a closed-cycle cryocooler integrated cryocooler (Janis Research Co., SHI SRDK-408 SW, USA) by DC four-probe technique. The temperature dependence of *ac* susceptibility (χ-T) was measured using a closed-cycle *ac* susceptometer (ARS-CS202S-DMX-19 SCC, USA). The temperature of the sample was precisely controlled and monitored using two temperature controllers (Lakeshore-340 & 332, USA). DC magnetic measurements were done on a Physical Property Measurement System (Quantum Design, USA).

4.4 Impact of fluorine variation on the properties of the superconductor

4.4.1 Structural properties

Figure 4.1 shows the x-ray diffraction (XRD) patterns of Nd1111 samples with varying F levels. The diffraction patterns can be well indexed on the basis of the tetragonal ZrCuSiAs type structure. Small fraction of FeAs phase is found in all samples and its relative intensity is almost constant regardless of the F content. In F doped samples, NdOF phase is observed which increases on increasing the F content. The lattice parameters obtained from the XRD for the undoped and the F doped samples are included in Table 4.1. Compared with the undoped sample, the lattice parameters of the F doped samples are found to decrease systematically with increase in F content, indicating the increase in internal chemical pressure favoring the enhancement of T_C, as discussed in the succeeding section. But for the sample with x = 0.4, the *a* and *c* values increase which is reflected in the T_C reduction of that sample. The variation of lattice parameters with fluorine content is graphically represented in Figure 4.2 (a). A shift in the XRD peaks towards right is a direct indication of the shrinkage in lattice parameters. An enlarged view of the main peaks (*102*) of the XRD patterns is shown in Figure 4.2 (b). It is clearly seen that with the increase in F content there is a slight shift of XRD patterns towards the right, compared to that of the parental compound Nd0.

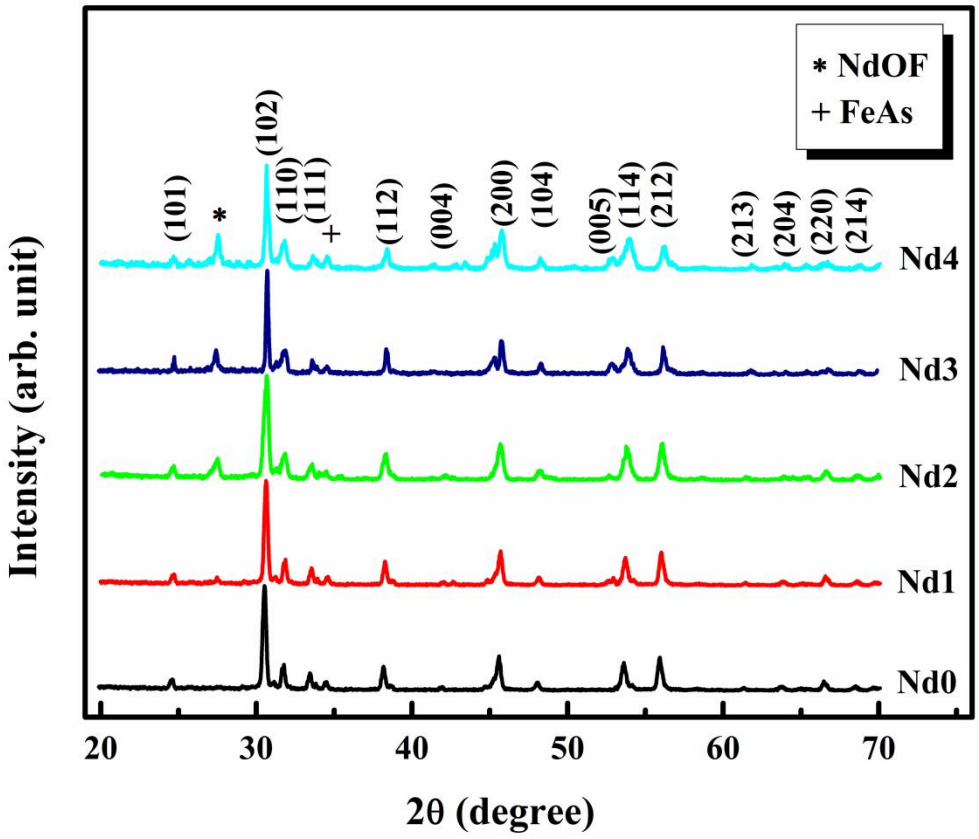

Figure 4.1: The XRD patterns of undoped and F doped Nd1111 samples

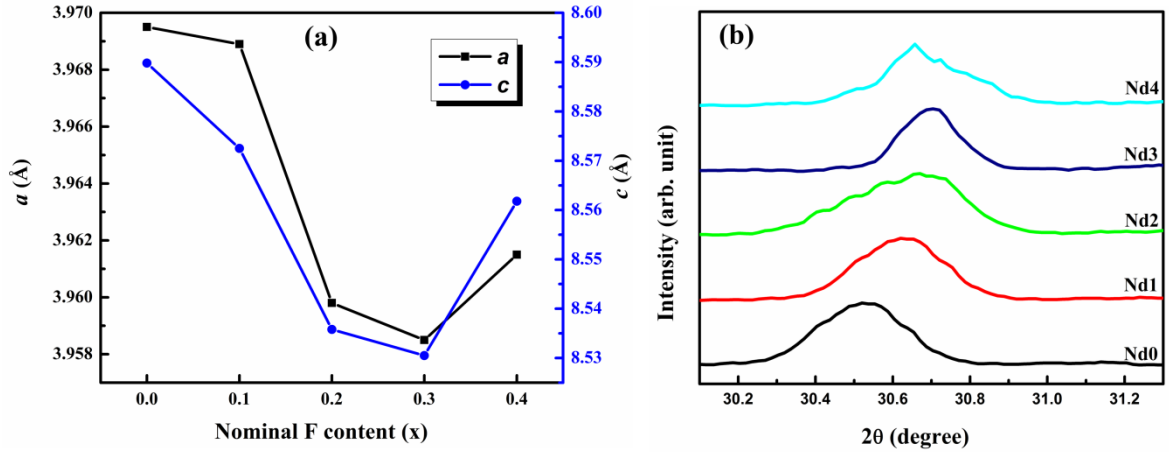

Figure 4.2: (a) Variation of lattice parameters with fluorine content and (b) Enlarged view of the (*102*) peaks showing a shift towards right due to lattice contraction

Figure 4.3 shows the Williamson-Hall plots of the (*102*), (*112*) and (*114*) planes for undoped and F doped Nd1111 samples and the dashed lines show the linear fits given to the data. It is observed that the slope of the linear plots increase with the increase in fluorine content. Since slope of the Williamson-Hall plots represent the strain in the lattice of the system, the increase in slope is an indication of the strain developed in the system

due to fluorine doping at oxygen site. However, the strain induced due to fluorine doping is found to saturate at a doping level of x = 0.4.

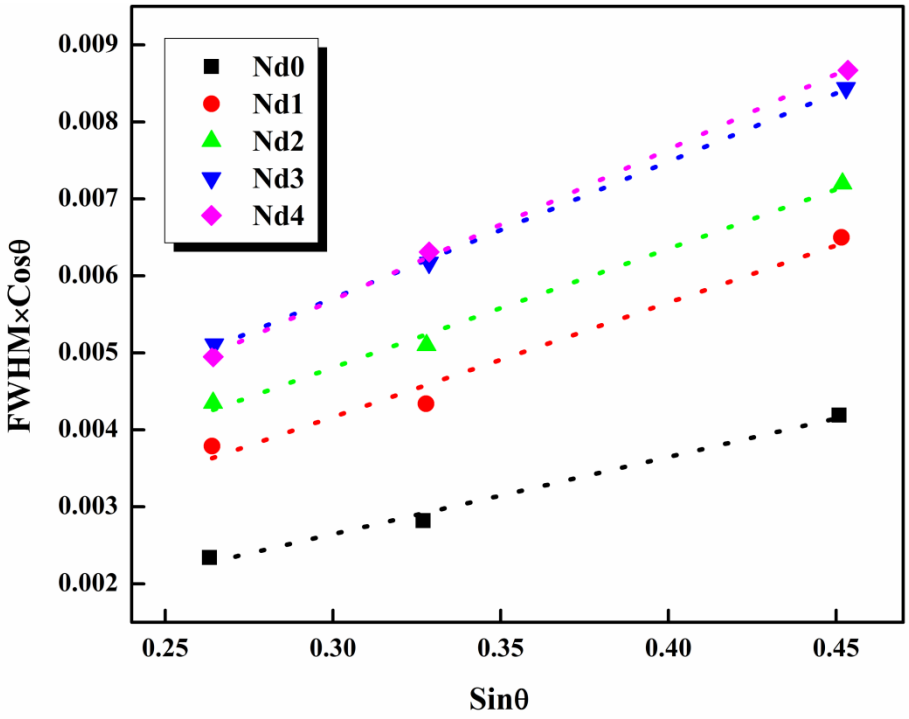

Figure 4.3: Williamson-Hall plots of the (102), (112) and (114) planes for all samples and the dashed lines represent the linear fits to the data points

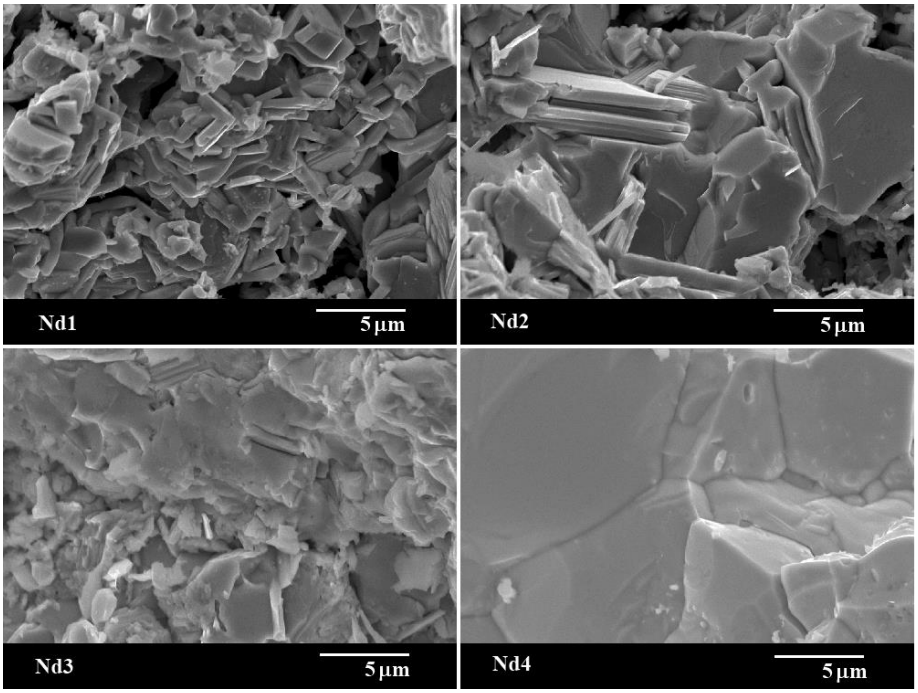

Figure 4.4: SEM images of Nd1111 samples with varying F content

Figure 4.4 shows the SEM images of the freshly fractured surfaces of F doped Nd1111 samples. The microstructure generally depicts flaky grains with good

homogeneity. But, there is a regular change in microstructure especially in terms of porosity and grain size as we move on from Nd1 to Nd4. The microstructure of Nd1 is more porous than all the other samples with small flaky grains. In Nd2, the porosity decreases and shows larger flaky grains. Porosity almost disappears in Nd3 and the grains seem to fuse into one another without clear boundaries. The microstructure of Nd4 is entirely different from all other samples exhibiting well-connected and very large grains. The improvement in density, grain connectivity, and grain size is expected to enhance the transport properties of these samples.

4.4.2 Superconducting properties

A detailed investigation has been carried out to understand the transport properties of Nd1111 superconducting samples with varying F content and to investigate the intrinsic limitations of iron pnictides while entering into practical applications. The superconducting properties have been analyzed employing both transport and magnetic measurements. The transport measurements include resistivity dependence on temperature and current-voltage characteristics; and magnetic measurements include temperature and frequency dependence of *ac* susceptibility and *dc* magnetic measurements at different applied fields.

Figure 4.5 shows the temperature dependence of resistivity (ρ-T) of pure and F doped Nd1111 samples and the inset shows an enlarged view around the superconducting transition region. The T_C, ΔT_C, normal state resistivity (ρ_{300}), and residual resistivity ratio (RRR) values obtained from the plots are tabulated in Table 4.1. As observed in all the parental compounds of RE1111 superconductors, the pure sample shows an anomaly around 130 K, usually called as the structural transition temperature (T_S), which is an indication of the structural as well as spin density wave instability (Zhao(b) *et al.* 2010). Fluorine doping at oxygen site shifts this anomaly to lower temperatures with an onset of superconductivity at x = 0.1. On further doping, T_C increases up to a maximum of 52.0 K for x = 0.3 and then decreases drastically to 47.6 K for x = 0.4. All the superconducting samples show a metallic behavior before the transition region. The ΔT_C values measured display broad transition widths except for x = 0.4. Furthermore, the residual resistivity ratio defined as the ratio of the normal state resistivity at room temperature (ρ_{300}) to the normal state resistivity close to the superconducting transition (here at 60 K, i.e. RRR = ρ_{300}/ρ_{60}) were also calculated for the F doped Nd1111 sample. RRR value is a common indicator of overall sample purity. Here, RRR values are found to be higher than other magnetic RE1111 pnictides processed at high temperatures but very less than La1111 (Ma(a) *et al.* 2011; Sefat *et al.* 2008). The values also exhibit a systematic increase up to the sample

with maximum T_C (Nd3) and then decreases. It is to be noted that the sample with the maximum T_C, has the lowest normal state resistivity and the highest RRR value.

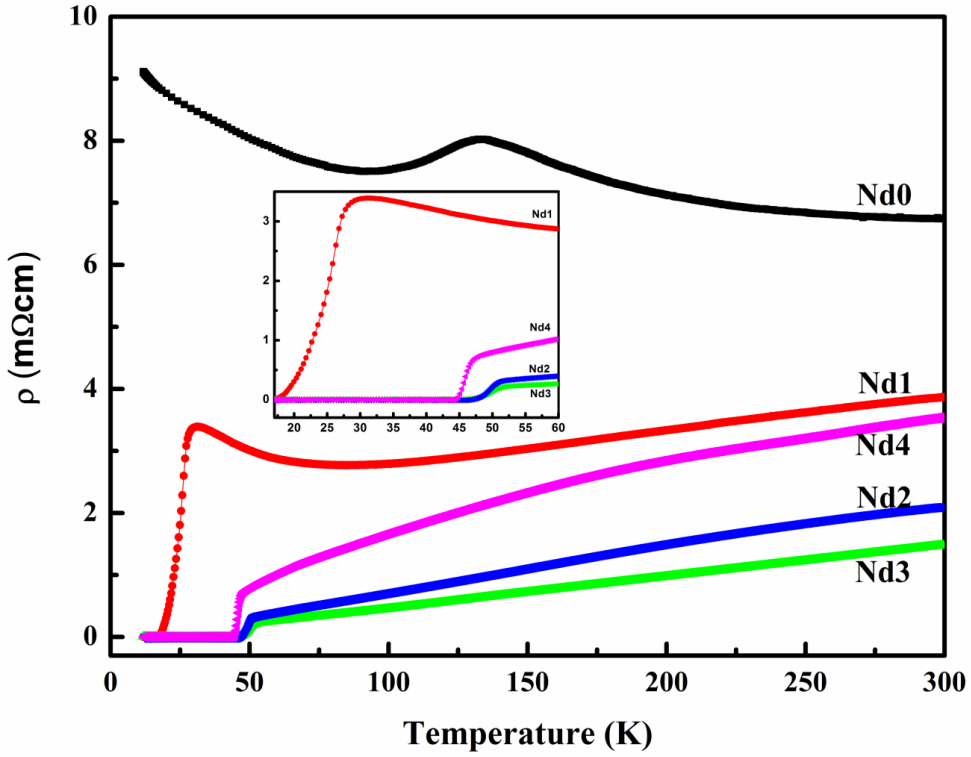

Figure 4.5: ρ-T plots of undoped and F doped Nd1111 samples with varying F content. Inset shows the enlarged view around transition

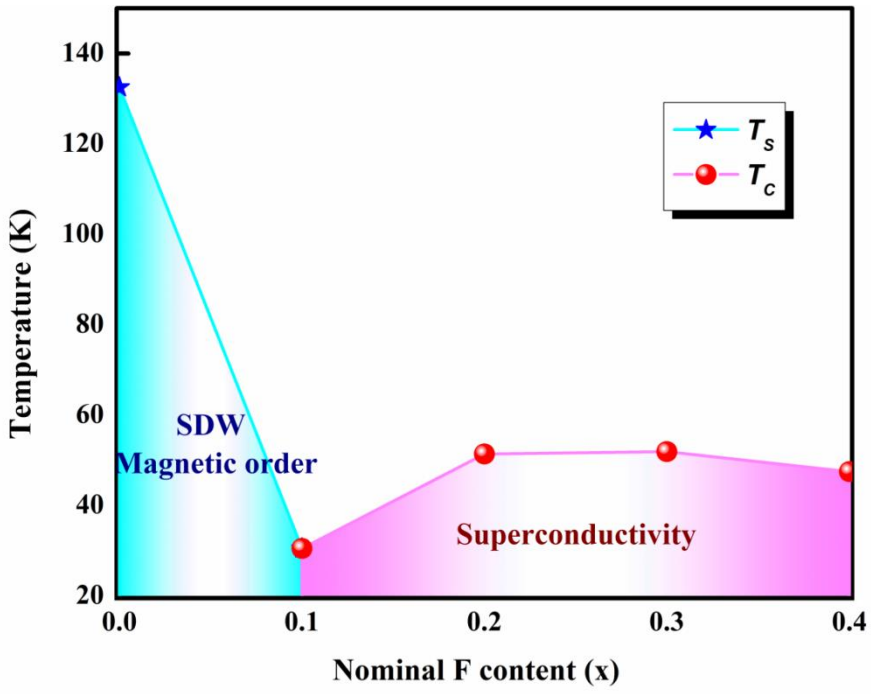

Figure 4.6: Phase diagram of Nd1111 system as a function of F content

The results obtained from the ρ-T plot are used to construct a phase diagram as a function of the F (electron) doping and this is shown in Figure 4.6. With increasing F-doping, the T_S for Nd1111 system (x = 0) is driven down, the superconducting state emerges at x = 0.1, and a maximum T_C of 52.0 K is attained at x = 0.3. On further increasing the F content i.e., at x = 0.4, the T_C decreases to 47.6 K. The solubility limit of F seems to reach at x = 0.3 itself and hence further addition of F results in T_C reduction. Figure 4.7 displays the I-V plots of the F doped Nd1111 samples measured at 12 K. The transport I_C values of all the samples, estimated using the standard 1 μV/cm criterion, and corresponding J_C values have been included in Table 4.1. The observed I_C values show a steady increase with F doping and attains a maximum of 42 A for Nd4 with a corresponding J_C of 1050 A/cm^2. The I_C variation observed can be well correlated with the microstructure of the corresponding samples. Obviously, the sample with x = 0.5 (Nd5) has to be measured to check whether there is any further increase in I_C, on increasing the F content. Although Nd5 was also prepared, it was highly fragile and hence could not be measured.

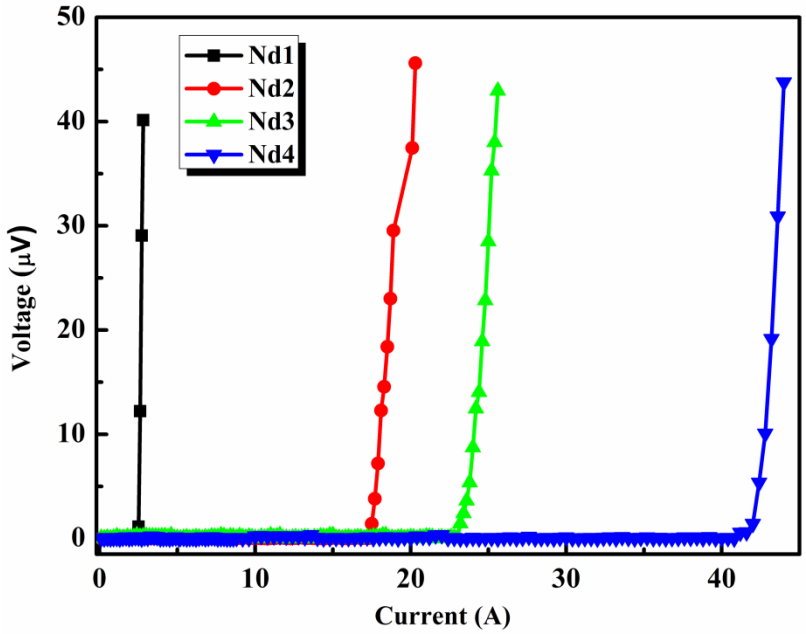

Figure 4.7: I-V plots of Nd1111 samples with varying F content measured at 12 K

The superconducting characteristics due to granularity have been often studied using the *ac* susceptibility measurements, a sensitive tool for the study of the currents flowing in granular materials. Macroscopically, polycrystalline samples of RE1111 samples exhibit an electromagnetic behavior typical of the granular systems, analogous to the intrinsic behavior of high T_C cuprates. Figure 4.8 shows the temperature dependence of *ac* susceptibility (χ-T) for all the superconducting samples measured at frequency, f = 208

Hz and *ac* field, $H_{ac} = 4.94 \times 10^{-4}$ T. The T_C values observed from the χ-T plots are in good agreement (within 0.5 K) with those obtained from the ρ-T. The real and imaginary parts of the fundamental *ac* susceptibility ($\chi = \chi' + i\chi''$) represent two complementary aspects of flux dynamics below T_C, a sharp decrease in the real part χ' represents the energy stored by the sample due to the diamagnetic response of the screening current induced in the superconductor by the external magnetic field, whereas the imaginary part is proportional to the energy or ac losses due to the vortex motion. In polycrystalline high T_C superconductors, a typical feature observed in χ-T plot is a two-step in χ' accompanied by two peaks in χ'' which arises due to the combined response of the superconducting grains and the inter-granular weakly coupled region. It is to be noted that our samples are also polycrystalline-sintered pellets composed of a conglomerate of grains with superconducting connectivity. Hence, a screening current may flow among the grains (inter-grain current), and at the same time, a screening current flows inside the single grains (intra-grain current). In *ac* susceptibility measurement, the overlap of these two signals can be detected, one coming from the inter-grain current and the other from the intra-grain current.

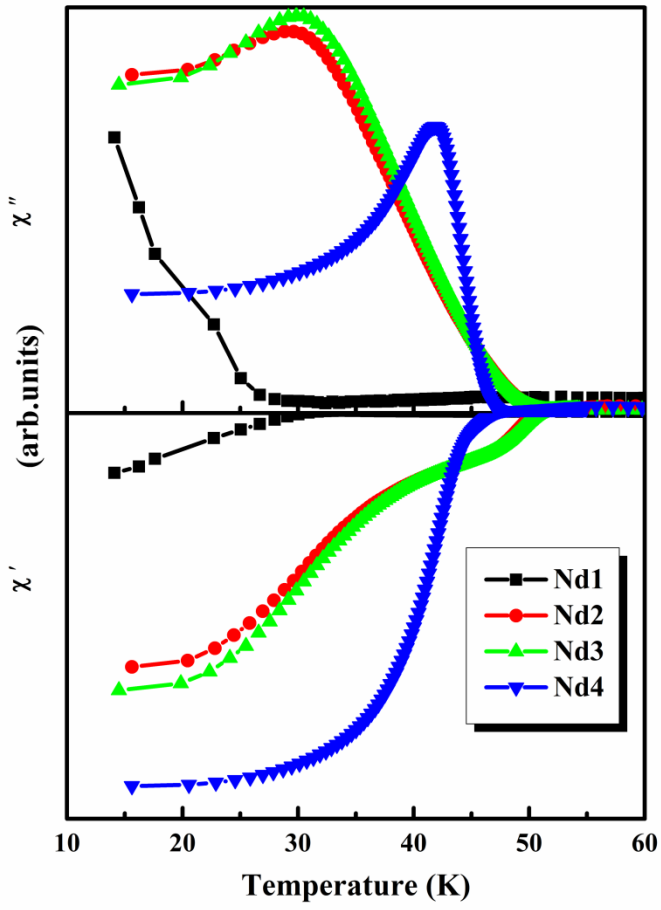

Figure 4.8: χ-T plots of Nd1111 samples with varying F content

Table 4.1: Structural and superconducting parameters of F doped Nd1111 samples

Sample Name	Lattice parameters (Å)		T_C (K)		ΔT_C (K)	$\rho_{300\ K}$ (mΩcm)	RRR	I_C (A) (at 12 K)	J_C (A/cm^2) (at 12 K)
	a	*c*	ρ-T	χ-T					
Nd0	3.9695	8.5898	-	-	-	-	-	-	
Nd1	3.9689	8.5725	30.5	30.1	13.4	3.89	1.36	2.5	62.5
Nd2	3.9598	8.5358	51.4	51.0	4.1	2.16	5.27	17.5	437.5
Nd3	3.9585	8.5305	52.0	51.5	5	1.47	5.65	23.0	575
Nd4	3.9615	8.5618	47.6	47.5	3.1	3.52	3.42	42.0	1050

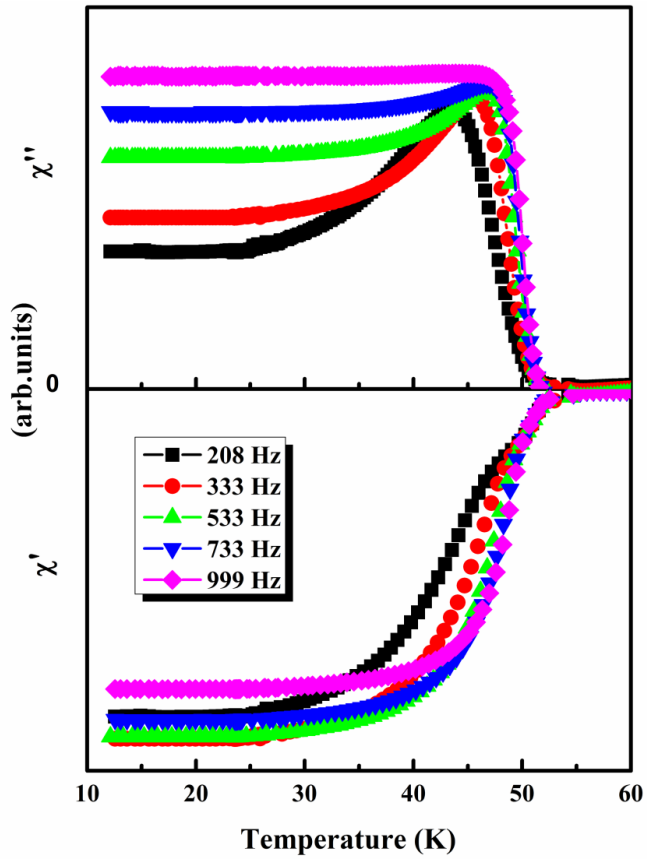

Figure 4.9: χ-T plots of Nd4 at different frequencies of *ac* signals

The diamagnetic transitions observed here, i.e., the real part χ′, has a double stepping nature for Nd2 and Nd3 with a peak in χ″ corresponding to the second step (lower T); while this step like behavior disappears in Nd4 and the peak in its χ″ shifts toward the first step (near T_C). The bumpy nature in the real part along with analogous peaks in the imaginary part can be attributed to the inter-granular and intra-granular current flow in the sample (Zhang(a) *et al.* 2010). Iron based superconducting samples exhibit this behavior

due to the inherent electromagnetic granularity and/or inhomogeneity, as mentioned earlier (Bonsignore *et al.* 2011; Polichetti *et al.* 2008). The suppression of this double stepping in x = 0.4 shows the reduced effect of granularity. It can be inferred that the sample Nd4 has well coupled grains which in turn justifies the enhanced J_C in Nd4. Besides this, the depth of the diamagnetic signal also increases with increase in F content from Nd1 to Nd4.

AC susceptibility measurements also help in investigating inter-granular as well as intra-granular vortex dynamics of a superconductor. In type II superconductors, there are various loss mechanisms such as flux flow or viscous losses, bulk pinning hysteretic losses, and flux line cutting losses. Bulk pinning losses are independent of frequency but dependent on the field, whereas flux flow losses depend on the frequency and not on the field (Celebi *et al.* 1998; Clemm *et al.* 1991). Experimentally, both field and frequency dependencies can be observed simultaneously (Emmen *et al.* 1990). In the low magnetic field amplitude range, the imaginary part of *ac* susceptibility in granular high T_C superconductors represents the inter-granular bulk pinning loss (Celebi *et al.* 1997). However, when the applied *ac* field amplitude is high enough, intra-granular loss peak can also appear (Lee(c) *et al.* 1996). Nikolo et al. have employed the Anderson flux creep model in their studies showing that *ac* loss peak shift with frequency in terms of activation energy for vortex de-pinning (Nikolo *et al.* 1989; Anderson P. W. 1962). Muller et. al. have shown that adding a flux creep term to the current density term in the critical state equation causes a change of inter-granular magnetic field variation such that the *ac* loss peak shifts to higher temperature with increasing frequency (Muller *et al.* 1991).

The frequency of the applied *ac* field plays an important role on determining the intrinsic *ac* magnetic properties of granular iron based superconducting samples also (Polichetti *et al.* 2010). In granular superconducting systems, inter-granular closed loops of current flow throughout the sample from one grain to the next one through the weak links between them and thereby create a critical state in the system (Chen(a) *et al.* 2005). Each weak link is characterized by a field and temperature dependent critical current density, the lowest of which represents the critical current density of an entire closed path formed by a given number of grains linked together. For temperatures and magnetic fields lower than their respective critical value, these current loops produce a partial shielding against the penetration of external magnetic field. So, if these closed current loops are present, the linked grains are subjected to a field which is reduced with respect to the applied one, and consequently the grains react to this reduced field. When the *ac* field of given frequency is applied, an electrical field proportional to that frequency acts on the sample, thus creating

currents again proportional to it. At a given temperature, if the frequency increases, the generated current can be sufficiently high to overcome some inter-grain critical current and can therefore break the closed loop around which the superconducting current flows. In these conditions, the closed paths around which the inter-granular current flows break, and the grains appear to behave as if they are not connected electrically, reproducing the effect of an increased *ac* field.

Figure 4.9 represents the real (χ') and imaginary (χ'') components of *ac* susceptibility as a function of temperature obtained at the frequencies f = 208, 333, 533, 733 and 999 Hz at an *ac* field of 0.49 mT for the sample Nd4. The overall behavior of *ac* susceptibility with respect to temperature resembles that of the single frequency measurement given in Figure 4.8. The onset T_C of the sample is found to be independent of the variation in *ac* frequency. However, there is noticeable frequency dependence in the imaginary part. The whole profile for the imaginary part resembles that of thermally activated flux creep phenomena predicted in the framework of the linear Kim-Anderson creep model (Kim *et al.* 1962; Anderson P. W. 1962). Here, we can observe an increase in peak height with the increase in *ac* frequency. Also, the peak in the imaginary part shifts to higher temperatures with the increase in *ac* frequency. With the increase in *ac* frequency, the inter-grain peak of the bulk sample moves to higher temperatures due to the presence of flux dynamic processes with characteristic times longer than 1/*f*. The temperature corresponding to the inter-grain peak is hereafter referred as T_P. When the frequency is increased, the inter-granular vortices have less and less time available to penetrate into the superconductor during each cycle. In order to reach full flux penetration, a weaker inter-granular pinning force density is required to compensate for less efficient magnetic relaxation or creep. Since the pinning force density weakens with increasing temperature, T_P must increase with increasing frequency.

The activation energy U, for the vortex creep can be obtained using the frequency *f*, dependence of the peak temperature T_P, expressed as an Arrhenius rate equation (salamati *et al.* 2004):

$$\text{i.e. } f = f_0 exp(-U/K_B T_P) \ ,$$

Where f_0 is a characteristic or attempt frequency and K_B is the Boltzmann constant.

Figure 4.10 represents $1/T_P$ dependence on ln(*f*) wherein we can see an exponential decrease in $1/T_P$ with respect to frequency instead of a linear behavior. However, the shift in peak temperature is relatively small. This is analogous to the frequency dependence of peak temperature observed in YBCO superconductors.

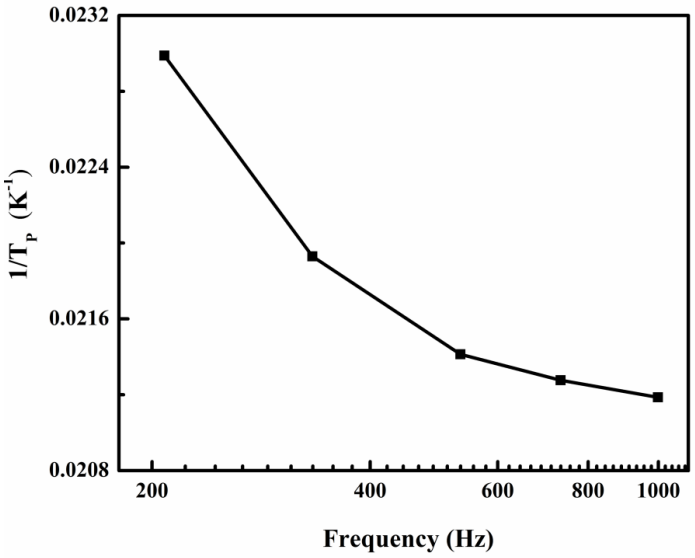

Figure 4.10: $1/T_P$ versus frequency profile for the sample Nd4

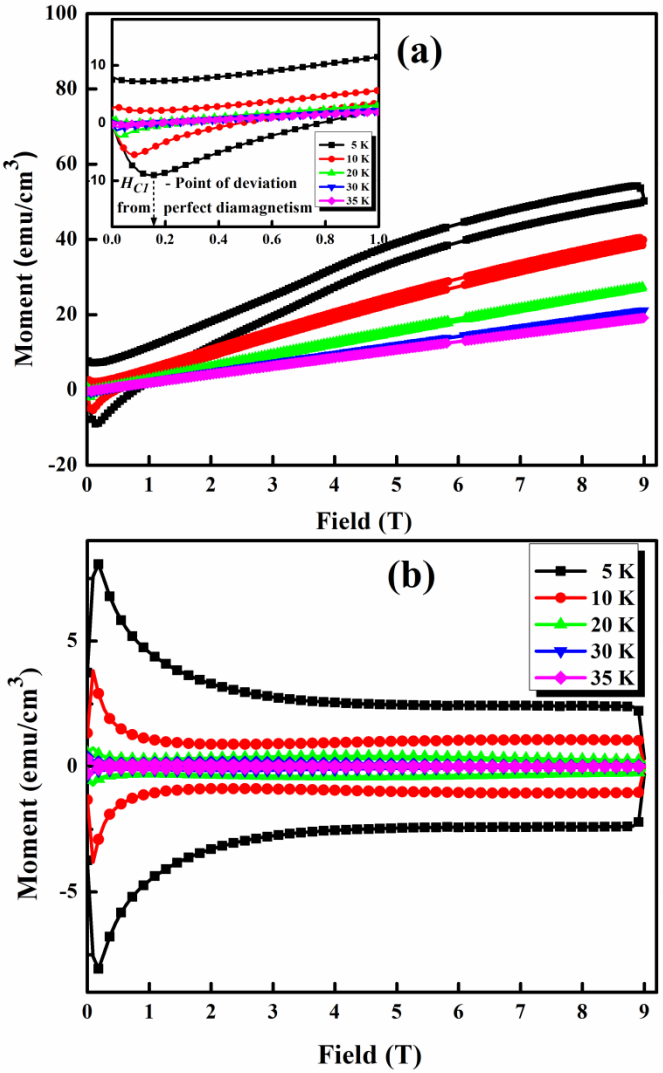

Figure 4.11: (a) The magnetic hysteresis loops i.e. M versus H plots of Nd4 measured at different temperatures 5, 10, 20, 30 and 35 K. Inset shows the enlarged view of MHLs at low fields and determination of H_{C1} and (b) shows the paramagnetic background subtracted MHLs

The critical current density J_C was also estimated using magnetic measurements i.e. magnetization versus magnetic field. This measurement is devoid of electrical contacts and can be performed on even small sized samples. Hence, measurement of the irreversible behavior in magnetization is one of the standard methods to determine J_C and its dependence on applied field H in a superconducting sample. During magnetic measurements, the voltage generated in the detection coil can probe the whole volume of the sample and this provides volume average of the sample's magnetic response (Nikolo *et al.* 1995). However, in order to employ this technique to determine the critical current density, a suitable critical state model must be invoked. Flux pinning centers present in a type II superconductor cause a non-uniform distribution of the penetrated flux and this also depends on the magnetic history of the specimen. In 1962, Bean introduced the critical state model to describe this behavior, which is now being applied extensively to study high temperature superconductors (Bean C. P. 1962). In this model, one assumes that the local current density, which by Ampere's law is associated with the non-uniform flux distribution, has a certain magnitude of J_C which is again dependent on the magnetic induction B. Thus, J_C is proportional to the vertical width of the magnetization hysteresis loop, ΔM. The magnetization hysteresis incorporates contributions from both inter-granular and intra-granular current flow. Besides, the electromagnetic behavior of RE1111 system is known to be influenced by the magnetic rare earth ions and inherent granularity. Thus, the effect of magnetic rare earth ions is directly observed in the magnetic hysteresis loop (MHL) of the sample.

The sample which exhibited the highest transport J_C among the series of samples subjected to I-V, i.e. Nd4 having a typical dimension of $3 \times 3 \times 1.5$ mm^3 was subjected to magnetization measurement up to a maximum field of 9 T. Figure 4.11 shows the magnetic hysteresis loops of Nd4, measured at 5, 10, 20, 30, and 35 K. A cursory look (Figure 4.11 (a)) itself gives an idea that the hysteresis loops are not symmetric and the peaks observed in the even quadrants deviate more from the y axis and get broadened at lower measurement temperatures. The MHLs measured at different temperatures also have a cross over at 0.4 - 0.6 T field. On increasing the applied field, the magnetic moment of the superconductor remains to be negative up to a particular field and thereafter the moment increases, approaches zero and increases further to much higher values. The overall behavior is a sum up of the irreversible superconducting hysteresis and paramagnetic background due to the presence of paramagnetic Nd^{3+} ions present in the sample (Prozorov *et al.* 2009). The hysteresis loops become thinner at higher fields and temperatures closer

to T_C; whereas at lower fields and low measurement temperatures the loops broaden. The lower critical field H_{C1}, the field above which flux penetration into the sample starts also can be estimated from the MHLs. The inset of Figure 4.11 (a) shows an enlarged view of the MHLs at low fields. On increasing the applied field, initially the magnetic moment of the sample becomes negative and at a particular field there is a reversal from the maximum negative moment i.e. a point of departure from linearity, the field corresponding to this point is taken as the H_{C1}. It is observed that for this sample H_{C1} is around 0.12 T at 5 K. All the measurements above 5 K give still smaller H_{C1} values closer to zero.

In order to further understand the pinning characteristics of the sample, the magnetic field dependence of critical current density (J_C) was estimated from magnetization curves using Bean's critical state model and the same has been represented in Figure 4.12. Since the Nd^{3+} ions present in the system $NdFeAsO_{0.6}F_{0.4}$ and the impurity phase (NdOF) are paramagnetic in nature, ΔM should be calculated after separating the paramagnetic background from the measured magnetic moment. Hence, the paramagnetic background was estimated as a mean of the upper and lower hysteresis branch (i.e. $M_P = (M^+ + M^-)/2$) for each loop and was deducted from the experimentally obtained MHLs. Then, the volume magnetization was estimated by dividing the obtained magnetic moment with the volume of the sample. Figure 4.11 (b) shows the paramagnetic background subtracted MHLs for Nd4 measured at different temperatures 5, 10, 20, 30 and 35 K. The width of the background subtracted magnetic hysteresis loop is maximum at the lowest measurement temperature (5 K) and goes on thinning as the measurement temperature nears the T_C of the sample. The width of the loop, ΔM is then calculated as $M^+ - M^-$. As already discussed the critical current flowing inside a superconductor can be categorized as intra-granular or local current and global current. Both local J_C and global J_C can be estimated using Bean model. It can be understood that the local J_C will be definitely higher than the global J_C especially when the superconductor is granular and has weak link problem (Wang(a) *et al.* 2009). Whereas if the superconductor is devoid of weak links and has good grain to grain connectivity, local and global J_C will be comparable (Larbalestier *et al.* 2001a). Chemical doping can increase the global J_C only if it refines the microstructure, improves the sample density and creates pinning centres at inter-granular paths thereby reducing the current limiting factors. However, improvement in local J_C can occur only if the dopant creates structural modification or lattice defects which act as effective vortex pinning centres within the grains.

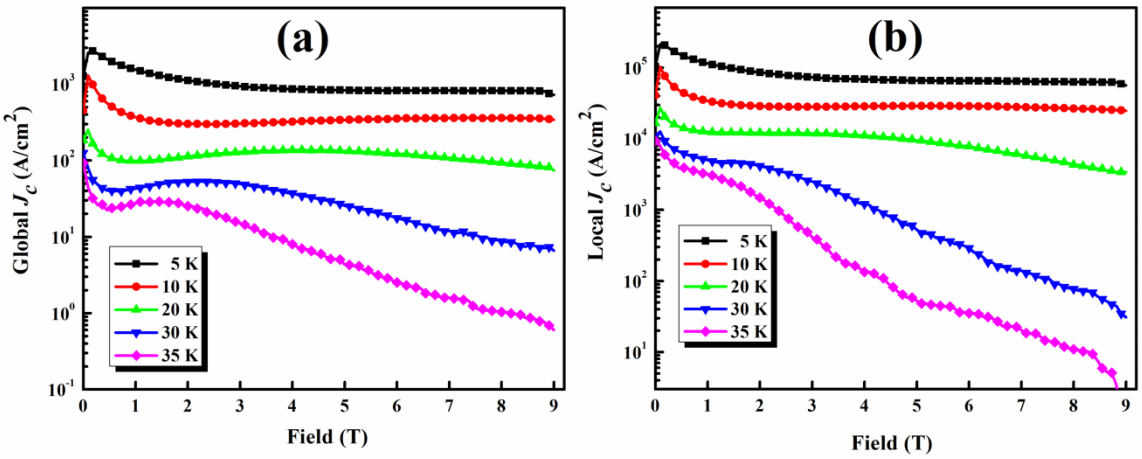

Figure 4.12: The critical current density of Nd4 estimated from Bean critical state model using MHLs measured at different temperatures 5, 10, 20, 30 and 35 K. (a) Global J_C and (b) Local J_C

The global critical current density, global J_C, which refers to the current flowing throughout the whole sample can be derived from the hysteresis loop width based on the extended Bean model as $Global\, J_C = 20[\Delta M/a(1 - \frac{a}{3b})]$, where ΔM is measured in emu/cm^3, 'a' and 'b' are the dimensions of the samples with a < b in cm and J_C in A/cm^2. It can be seen that the maximum global J_C observed for the sample is 2.5 × 10^3 A/cm^2 at 5 K. The studies on size-dependence of J_C indicate that the contribution of global currents to the hysteretic magnetization is less than that produced by the locally circulating currents. Moreover, there are reports showing that the electromagnetic granularity and presence of wet phases such as FeAs limit the global J_C of iron pnictides in the order of 10^3 (Wang(a) *et al.* 2009; Yamamoto *et al.* 2011). The overall $J_C(H)$ behavior observed in Figure 4.12 (a) shows that at low fields, around the H_{C1}, a maximum of J_C is observed for all the measurements at different temperatures. As the applied field increases, the J_C has a sudden decrease up to around 1 T and thereafter it remains relatively constant up to the maximum field applied. However, at higher measurement temperatures (30 and 35 K), the J_C goes on degrading with the field.

Further, the local J_C i.e. J_C within the grains was also estimated using Bean model. For this, the bulk sample was powdered and subjected to M-H measurement. Since the particles in the powdered sample are electrically isolated from each other, it is presumed that the magnetization of the powder sample comes from the superconducting current within each particle. Then, ΔM was calculated, as discussed earlier, for the powdered sample and the intra-grain J_C was estimated on the basis of Local $J_C = \left(\frac{30\Delta M}{\langle d \rangle}\right)$, where ΔM is measured in emu/cm^3 and '⟨d⟩' is the average grain size in cm. Both global J_C and local J_C are represented in Figure 4.12 (a) and (b), respectively. Obviously, the field dependence

of local J_C resembles that of global J_C with the former attaining a maximum of 2×10^5 A/cm^2 at 5 K. It is observed that there is a difference of about two orders of magnitude between local J_C and global J_C. Though the sample Nd4 shows the highest transport J_C of 1050 A/cm^2 among the series of samples studied, the transport J_C observed remains far from the local J_C estimated from magnetization measurements. The inherent electromagnetic granularity of this class of materials and the presence of weak links due to impurity phases are the possible reasons for this wide difference. For Nd4, the lattice modifications due to fluorine doping at oxygen site favors the pinning mechanism within the grains and thereby the local J_C whereas the presence of secondary phases as observed from XRD presumably hinders the global current.

Studies on the influence of F doping and the substitution range of F at O site are essential for the synthesis of iron pnictide superconductors with improved superconducting properties and also for the understanding of unconventional superconductivity. The phase diagrams reported for RE1111 compounds often show an anomalous behavior in the T_C versus F content plots at higher levels of F. In this region, the T_C maintains either a plateau-like trend or it reduces as in high T_C superconductors (Malavasi *et al.* 2010). In the present work, the variation in T_C shows a decreasing trend at x = 0.4. The replacement of O^{2-} by F^- ion results in the increase of charge carrier concentration to an optimum value at x = 0.3, leading to the maximum T_C. As the dopant concentration increases further (i.e., x = 0.4), the charge carrier concentration of the system goes to an overdoped region resulting in lowering of T_C. The variation observed in lattice parameters as well as electronic properties due to F doping conclude that the maximum T_C is achieved at an optimum value of x = 0.3. But, the effect of T_C reduction is not reflected in the observed J_C of the sample with x = 0.4 (Nd4). Instead, Nd4 exhibits the maximum transport J_C among all the samples because of the better microstructural properties. However, the global J_C and local J_C estimated from magnetization measurements are much higher. As already known, the Nd1111 system is a potential candidate for magnet applications, but the superconducting properties reported so far demand a high pressure/high temperature synthesis or vapor pressure controlled binary preparation. The synthesis method developed by our group and used here reduces the complexities such as initial binary preparation, wrapping with expensive materials or usage of high pressure capsules. Nevertheless, the highlight is that the electromagnetic properties obtained are competitive to the existing reports (Ding *et al.* 2011; Sun *et al.* 2011). Besides, the correlation of the observed transport properties with corresponding structural and microstructural aspects is remarkable. The suppression of

granularity as seen in χ'-T plot and the enhancement of transport J_C displayed by the sample with x = 0.4 (Nd4), are evidently reflected in the microstructure of the sample which exhibits well-connected and exceptionally large grains. The observations conclude that it is possible to obtain good quality samples even at relatively low processing temperatures, provided that higher content of F is used.

4.5 Conclusions

The structural and transport properties of the $NdFeAsO_{1-x}F_x$ with (x = 0, 0.1, 0.2, 0.3, and 0.4) samples have been investigated on samples prepared by a simple route. The correlation of the observed superconducting transport properties with their structural and microstructural aspects, on increasing the F content, is commendable. The achievement of an onset T_C of 52.0 K in Nd3 and transport J_C of 1050 A/cm^2 (at 12 K) in Nd4 processed at a temperature of 1000 °C is worthy enough for Nd-based iron pnictides which are usually processed at temperatures above 1150 °C or pressures of 6 GPa. A global J_C of 5.4×10^3 and a local J_C of 4.3×10^5 A/cm^2 (both at 5 K) were observed in magnetization measurements. The transport properties observed for the Nd1111 samples synthesized at such relatively low temperatures make these materials promising in the application point of view. However, there exists enough scope for efforts to minimize grain connectivity issues and reduce the large gap between the transport J_C and the magnetic J_C.

CHAPTER 5

THE STRUCTURAL AND SUPERCONDUCTING PROPERTIES OF RARE EARTH MODIFIED $NdFeAsO_{0.7}F_{0.3}$ SUPERCONDUCTORS

5.1 Introduction

With the discovery of iron based superconductors by Hosono's group, the world of superconductivity witnessed the unraveling of a series of other iron based compounds having different crystal structures and interesting superconducting as well as magnetic properties (Kamihara *et al.* 2008; Aswathy *et al.* 2010; Ren(a) *et al.* 2009). Presently, the focus is to enhance the transport current and to utilize the very high upper critical field in iron pnictides for practical applications. Apart from the explorations on application point of view, basic research through chemical doping is also being carried out at various sites of REFeAsO iron pnictides (Ren(a) *et al.* 2008b; Raghu *et al.* 2008; Wang(b) *et al.* 2009b; Li(e) *et al.* 2010). The REFeAsO system (abbreviated as RE1111 - RE refers to rare earth) shows a tetragonal to orthorhombic structural phase transition in between 100-200 K accompanied by a spin-density-wave (SDW) type antiferromagnetic long-range ordering (Liu(a) *et al.* 2008). The suppression of these structural and magnetic phase transitions is a major hurdle to induce superconductivity in this class of iron pnictides. Doping in the charge reservoir block (RE_2O_2 layer) and application of external pressure are effective methods to cause structural modification or balance in charge carrier concentration, which in turn induces superconductivity into the system (Aswathy *et al.* 2010; Ren(a) *et al.* 2009). Generally, fluorine substitution at oxygen site suppresses the SDW instability and retains the tetragonal structure below 100 K leading to superconductivity. Further, it also causes lattice contraction especially along the *c*-axis. Application of external pressure induces superconductivity as an aftereffect of the increase in charge transfer between the charge reservoir layer ($RE_2(O/F)_2$) and conducting FeAs layer due to the mechanically forced lattice contraction. In short, the RE1111 compounds show signs of superconductivity or enhancement in critical temperature (T_C) if lattice contraction is induced by internal chemical pressure or external pressure (Yang(a) *et al.* 2010; Takahashi *et al.* 2008; Zhao(b) *et al.* 2010).

In RE1111, instead of fluorine doping at oxygen site, the substitution of RE with either an isovalent or aliovalent ion in the former enhances internal chemical pressure for a dopant of smaller ionic radius and the latter produces superconductivity by the variation in

charge carrier concentration (Yang(a) *et al.* 2010; Takahashi *et al.* 2008; Zhao(b) *et al.* 2010; Wen *et al.* 2008). For isovalent doping, fixed fluorine to oxygen ratio or oxygen vacancy is essential. Here, we can expect a T_C enhancement in rare-earth doped sample when compared to the solo fluorine doped RE1111 compound (Prakash *et al.* 2009). In aliovalent doping, fluorine doping is not mandatory and the solo substitution of a bivalent or tetravalent ion at RE site in REFeAsO can give rise to superconductivity despite having a low T_C (Wen *et al.* 2008). Cobalt or nickel doping at iron site and phosphorous doping at arsenic site have also been carried out to establish the relationship between the magnetic moments of Fe/Ln and superconductivity (Wang(b) *et al.* 2009b; Li(e) *et al.* 2010; Li(c) *et al.* 2009).

The present chapter is a detailed investigation on the structural and superconducting properties of rare earth modified $NdFeAsO_{1-x}F_x$ superconductors. The rare earths chosen include yttrium (Y), cerium (Ce) and gadolinium (Gd) wherein Y is a non-4f non-lanthanide rare earth element while Ce and Gd are lanthanides similar to Nd positioned on either side in the periodic table with ionic radius of Ce being larger than Nd and that of Gd is smaller.

5.2 Influence of yttrium doping on the electromagnetic properties of $NdFeAsO_{0.7}F_{0.3}$

The $NdFeAsO_{1-x}F_x$ (Nd1111) system, which is renowned for its very high upper critical field and almost constant critical current density at high fields, was initially reported to be superconducting under high pressure synthesis conditions (Ren(a) *et al.* 2008d; Wang(c) *et al.* 2009). Later, electron and hole doped samples of Nd1111 processed at ambient pressures were also reported to be superconducting (Wen *et al.* 2008; Malavasi *et al.* 2009). A lot of investigations were carried out to demonstrate the symmetry of electron and hole doping in iron pnictides. Often chemical doping is done with an aim to enhance the existing status of superconducting properties. For this, the dopants are chosen based on certain pre-requisites such as ionic-size-match and valency; not to mention the existence of sporadic reports contradictory to this requirement. The choice of the second element also depends on the possible effects it can create in the crystal and electronic structure of the host material in enhancing any/all of its superconducting properties. So far, there have been studies of different rare earths getting substituted at lanthanide site; but yttrium, being a non-4f element, has been the most popular option for T_C enhancement (Prakash *et al.* 2009; Tropeano *et al.* 2009; Shirage *et al.* 2008; Ganguli *et al.* 2010; Lai *et*

al. 2012; Chen(d) *et al.* 2010b). The T_C of $LaFeAsO_{0.6}$ has been enhanced from 20 K to 43.1 K on replacing La^{3+} by smaller Y^{3+} (Tropeano *et al.* 2009). Also, optimum Y doping in $Ce_{1-x}Y_xO_{0.8}F_{0.2}FeAs$ significantly increases both T_C and H_{C2} to 48.6 K and 90 T respectively as compared to the Y free $CeO_{0.8}F_{0.2}FeAs$ (T_C = 42.7 K, H_{C2} = 43 T) (Prakash *et al.* 2009; Ganguli *et al.* 2010). In SmFeAs(O,F) system, contradictory results showing both T_C enhancement and reduction have been observed (Lai *et al.* 2012; Chen(d) *et al.* 2010b). However, no work has been reported on the effect of yttrium substitution in Nd based systems. Hence, in the following section, we discuss the synthesis of $Nd_{1-x}Y_xFeAsO_{0.7}F_{0.3}$ by simultaneous substitution of Y at Nd and F at O sites and the analysis of its superconducting properties in detail.

5.2.1 Experimental

Samples with nominal compositions of $Nd_{1-x}Y_xFeAsO_{0.7}F_{0.3}$ with x = 0, 0.1, 0.2, 0.3 and 0.4 labeled as NdY0, NdY1, NdY2, NdY3 and NdY4 respectively, were synthesized by a one-step solid state method (Anooja *et al.* 2012). Stoichiometric amounts of Nd, Fe, As, Fe_2O_3, FeF_2 and Y powders were weighed, mixed and ground, inside a glove box with high purity argon atmosphere, to form a homogenous mixture. These samples were compacted into rectangular pellets with dimensions of $12 \times 2 \times 2$ mm^3, under a pressure of 500 MPa. The pellets were placed in evacuated sealed quartz tubes. The sealed tubes were subjected to heat treatment at 360 ºC for 5 h in a programmable muffle furnace having stability and accuracy better than ± 1 ºC controlled using Eurotherm-2404 temperature controller. The samples were subsequently ground, repelletized and sealed in evacuated quartz tubes and then sintered at 1000 ºC for 50 h.

The facilities used for phase identification, microstructural examination, superconducting transport measurements, *ac* susceptibility measurements and *dc* magnetic measurements have been described in *Chapter 3*.

5.2.2 Results and discussions

The x-ray diffraction (XRD) patterns of all the samples are shown in Figure 5.1. The peaks are indexed on the basis of the tetragonal ZrCuSiAs type structure with the space group P4/nmm. The expected NdFeAsO was formed as the main phase for all the samples. FeAs and NdOF phases are also detected in all the samples and their relative intensity is almost constant irrespective of yttrium content. Minor amount of YOF phase is found in the Y doped samples up to NdY3. In NdY4, the YOF content is found to be relatively higher. Since, Nd is more reactive than Y; the formation of NdOF is preferred to

that of YOF. So the increase in YOF content at higher dopant levels (x = 0.2, 0.3 and 0.4) can be due to excess of yttrium than the nominal amount required to be substituted at Nd site. The lattice parameters were accurately obtained from Rietveld refinements on the XRD data employing the Fullprof program. The variation of lattice parameters as a function of Y content is shown in Figure 5.2 (a). Both *a* and *c* values are found to decrease on Y doping, resulting in a net reduction of cell volume. The lattice parameters *a* = 3.9591 Å and *c* = 8.6052 Å for NdY0 reduce to *a* = 3.9511 Å, *c* = 8.5616 Å for NdY3 sample. But for NdY4, the *a* and *c* values are found to remain almost stagnant which indicates that x = 0.3 is an optimum level for Y doping in Nd1111 system. For all doped samples, except NdY4, both NdOF and YOF impurity fractions do not change significantly with Y substitution. Hence, it can be surmised that the lattice parameter changes (shown in Figure 5.2 (a)) arise mainly from Y substitution and not from changes in F content of the superconducting phase. The lattice contraction due to the combined effect of yttrium and fluorine doping is also reflected in the shift of the XRD patterns towards higher angles as observed in the enlarged view (Figure 5.2 (b)) of the main peak (*102*).

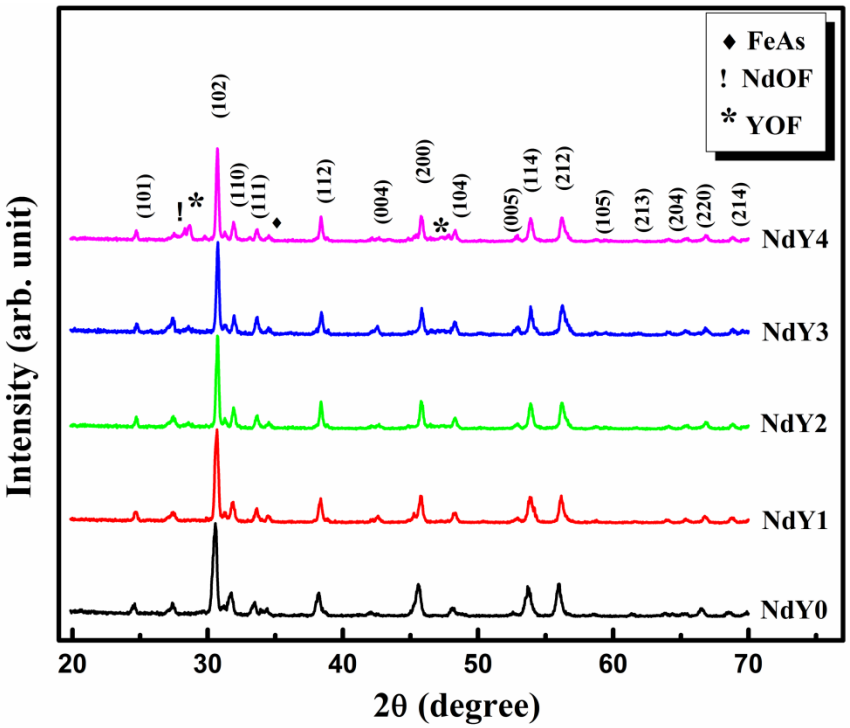

Figure 5.1: The XRD patterns of undoped and Y doped Nd1111 samples

The morphology of the pristine and Y doped samples was analyzed using the SEM images of freshly fractured surfaces of NdY0, NdY1, NdY2, NdY3 and NdY4 pellets which are shown in Figure 5.3. The images show that there is a systematic and gradual

change in morphology on going through samples from NdY0 to NdY3. The yttrium free sample shows clean flaky grains characteristic of RE1111 superconductors. But, the flaky nature of the grains changes on yttrium doping. In NdY3, the flaky nature of the grains completely disappears and transforms into cuboidal shape with rounded edges, where the secondary phases detected by XRD are also seen. For NdY4, the microstructure is found to be more porous and inhomogeneous. Due to this high porosity and fragility, NdY4 could not be used for further measurements.

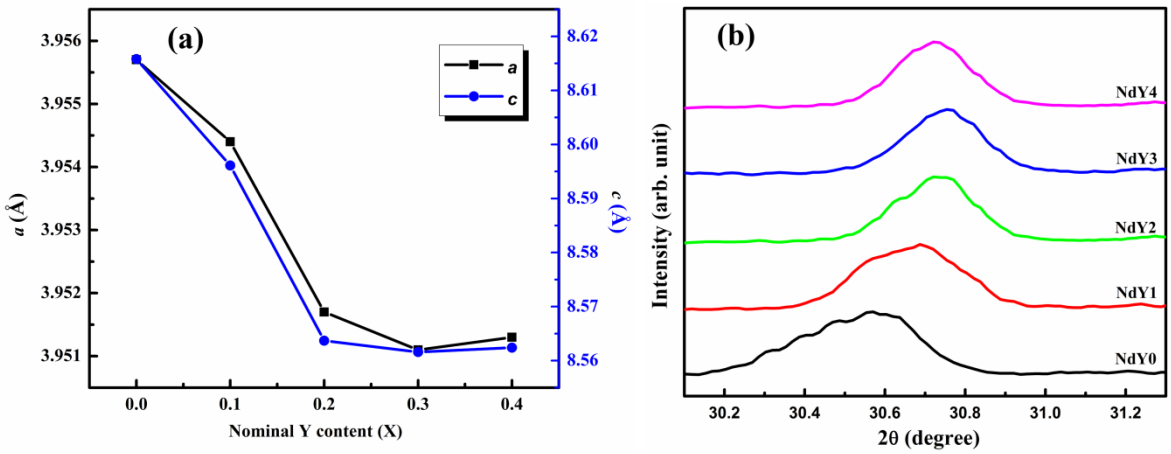

Figure 5.2: (a) Variation of lattice parameters with yttrium content and (b) Enlarged view of the (*102*) peaks showing a shift towards right due to lattice contraction

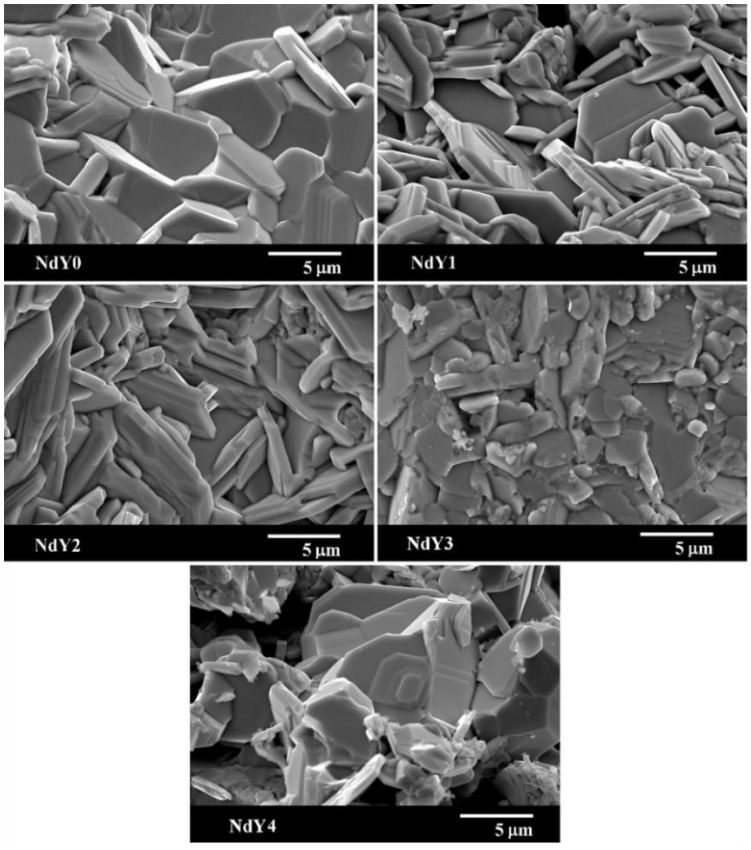

Figure 5.3: SEM images of the undoped and Y doped Nd1111 samples

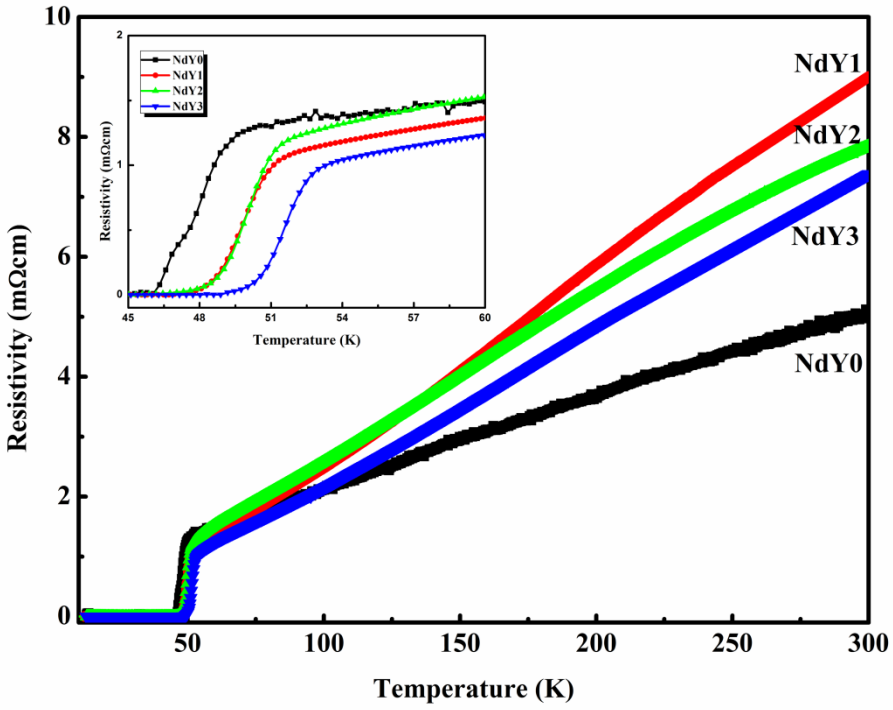

Figure 5.4: ρ-T plots of undoped and Y doped Nd1111 samples. Inset shows the zoomed region around the transition

The resistivity of the samples as a function of temperature is shown in Figure 5.4. In all the samples, the electrical resistivity gradually decreases on cooling and then drops drastically at T_C. Interestingly, the T_C increases for all Y doped samples and it is the maximum for NdY3 as shown in the inset (top-left) of Figure 5.4. For the yttrium free sample the superconducting transition temperature is observed to be 49.6 K which increases up to 53.3 K for the x = 0.3 composition (Table 5.1). For the x = 0.1 composition, the T_C is observed at 51.5 K which slightly increases to 51.7 K for the x = 0.2 composition. Moreover, the transition width ΔT_C, defined as ($T_{Conset} - T_{Coffset}$), for the sample NdY0 is 3.5 K which increases to 4.1 K on yttrium doping, regardless of the change in doping concentration. A linear temperature dependence of the resistivity persists from high temperatures to a characteristic temperature (T_S = 200 K), at which the resistivity deviates from linear behavior and shows a slight decreasing trend with decrease in temperature especially for NdY1. Below T_S, the resistivity again decreases rapidly leading to superconducting transitions. These features in the ρ-T plot can be the consequence of the spin density wave instability and also an indication of the pseudo gap regime existing in the samples (Liu(a) *et al.* 2008; Solovjov *et al.* 2010). The residual resistivity ratio RRR = ρ_{300K}/ρ_{55K} estimated for all the samples is also included in Table 5.1 and it is found that the RRR values of all the Y doped samples are comparatively higher

(5.76 - 7.38) than that of NdY0 (3.59). The presence of non-superconducting phases, as observed from XRD, and defects induced due to substitution are found to be the reasons for the increase in normal state resistivity (given in Table 5.1) and hence the increase in RRR value also.

In order to examine the effect of yttrium doping on the crystal structure and to understand the reason behind T_C enhancement, the lattice parameter variation of all the samples was analyzed. The six coordinate ionic radius of Y^{3+} ion (90 pm) is relatively small compared to that of Nd^{3+} ion (98.3 pm), which obviously leads to a contraction of lattice parameters. The shrinkage of lattice parameters observed along *a*-axis is 0.20% and that along the *c*-axis is 0.63%. This shrinkage causes a reduction in the cell volume which induces an additional chemical pressure into the system. Therefore, the T_C enhancement mechanism involved in the system is similar to that in the other oxypnictide superconductors i.e. 'lanthanide contraction' due to the substitution of a relatively smaller ion Y^{3+} in the place of Nd^{3+} (Prakash *et al.* 2009; Tropeano *et al.* 2009; Shirage *et al.* 2008; Ganguli *et al.* 2010). Replacement of La^{3+} by Y^{3+} in La1111 system is found to produce 1.8% and 1.7% reduction of *a* and *c* values, correspondingly T_C increases by ~ 17 K (Tropeano *et al.* 2009). While in the case of Y^{3+} in Ce^{3+}, *a* and *c* reductions are about 0.81% and 0.89%, respectively which cause a T_C increase of ~6 K (Prakash *et al.* 2009). On comparing Ce^{3+} and La^{3+} ions, the difference in ionic radii of Nd^{3+} and Y^{3+} is relatively small. Doping Y^{3+} in Nd^{3+} resulted in a total volume reduction of only 1.03%. Hence, the T_C gain of 3.9 K in yttrium doped Nd1111 system is reasonable. Apart from the ionic radii difference, the ionization energy difference between Y and Nd also prefers the formation of Y-O bond which is stronger and shorter than Nd-O bond, causing lattice contraction.

Figure 5.5 shows the *ac* magnetic susceptibility plots of the samples as a function of temperature which provides an insight into the granular behavior of the samples. In granular samples usually two types of screening currents exist: inter-grain and intra-grain currents. The real part of *ac* magnetic susceptibility is associated with the energy stored in the sample due to the diamagnetic response of these screening currents induced in the superconductor, whereas the imaginary part is proportional to the energy converted into heat during one cycle of the *ac* field. The onset of diamagnetic transition detected by *ac* susceptibility for all the samples is included in Table 5.1. The T_C values determined are comparable but slightly lower than those determined from the resistivity data. The yttrium free sample shows two step transitions in the real part and a peak corresponding to the inter-grain current in the imaginary part. Such double step transitions are already reported

in polycrystalline samples of iron based oxypnictides and this is attributed to the presence of electromagnetic granularity (Polichetti *et al.* 2008; Bonsignore *et al.* 2011). In the yttrium doped samples, the second step is found to get suppressed and completely vanishes from NdY2 onwards. The step near T_C is ascribed to the intra-grain shielding and that at lower temperature is due to the inter-grain shielding (Polichetti *et al.* 2008).

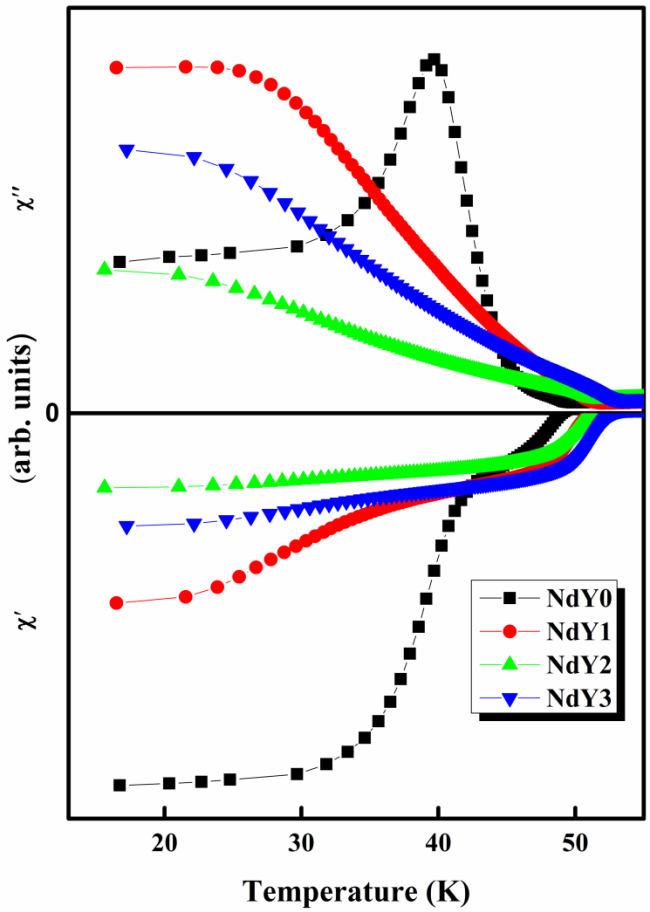

Figure 5.5: χ-T plots of the undoped and Y doped Nd1111 samples

Inhomogeneous/multiphase samples can also exhibit double step transitions (Zhang(a) *et al.* 2010). But from XRD and SEM analysis, it is clear that yttrium doping does not improve the homogeneity or alter the superconducting phase of the Nd1111 system. Hence, it is inferred that the suppression of the low temperature step occurs due to the absence of signals corresponding to inter-grain current flow. This is due to the inhibition of super-current flow between the grains because of non-superconducting secondary phases formed between the superconducting grains by yttrium doping. The inhibition of inter-grain current observed in the Y doped samples gives enough evidence for the degradation of transport current in these samples. Moreover, the peak height of χ'' and depth of diamagnetic signal in χ' of Y doped samples seem to be non-monotonous.

But, a noticeable shift and broadening of peaks exist in the doped samples. Usually, this behavior is observed while measuring χ''-T at different magnetic field amplitudes. The peak of χ'' shifts to lower temperatures and broadens more when the field amplitude H_{ac} is increased. This is due to the necessity of larger screening currents for higher applied fields (Saleh *et al.* 2003). Similar features such as decrease in peak height and peak broadening have been reported for YBCO samples also (Li(b) *et al.* 1997).

Table 5.1: Superconducting parameters of undoped and Y doped Nd1111 samples

Sample Name	T_C (K)		ΔT_C (K)	$\rho_{300\,K}$ (mΩcm)	RRR
	ρ-T	χ-T			
NdY0	49.6	49.2	3.5	5.06	3.59
NdY1	51.5	50.9	4.1	9.00	7.38
NdY2	51.7	51.5	4.1	7.84	5.76
NdY3	53.3	53.0	4.1	7.38	6.63

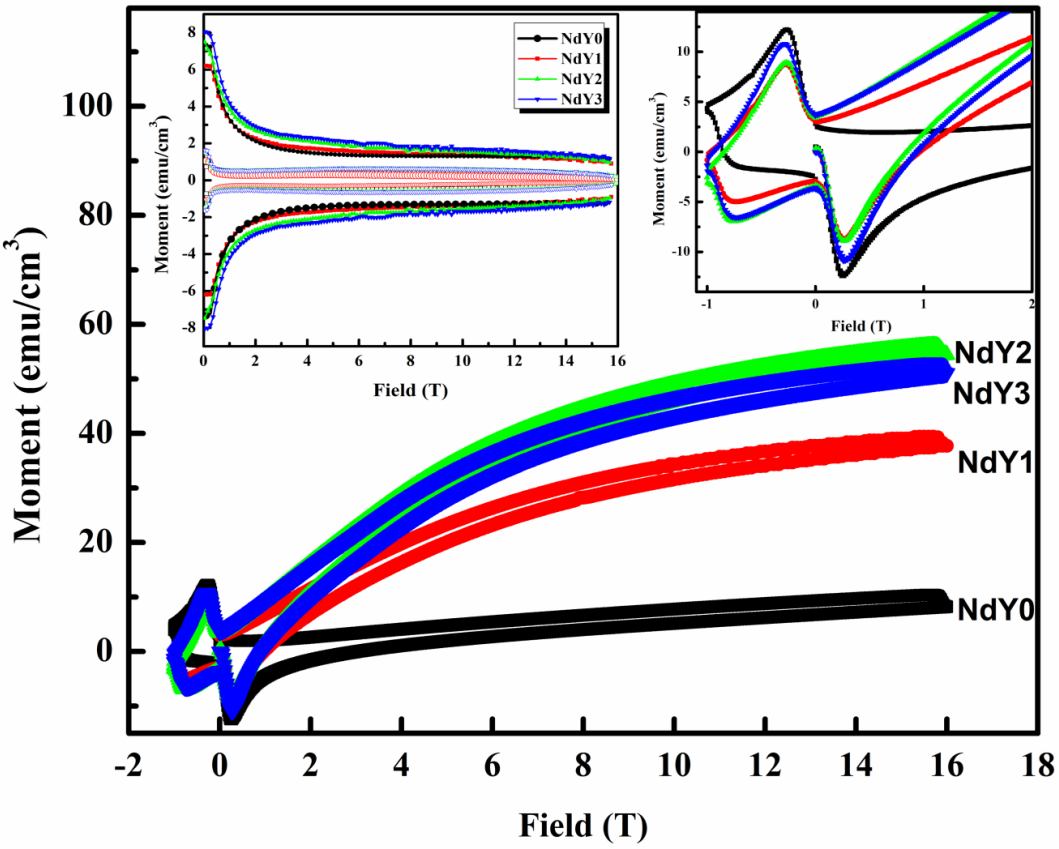

Figure 5.6: M-H loop of the samples at 4 K. Inset (top-right) shows enlarged plots at low fields. Inset (top-left) shows paramagnetic background subtracted M-H loop for all samples at 4 and 20 K

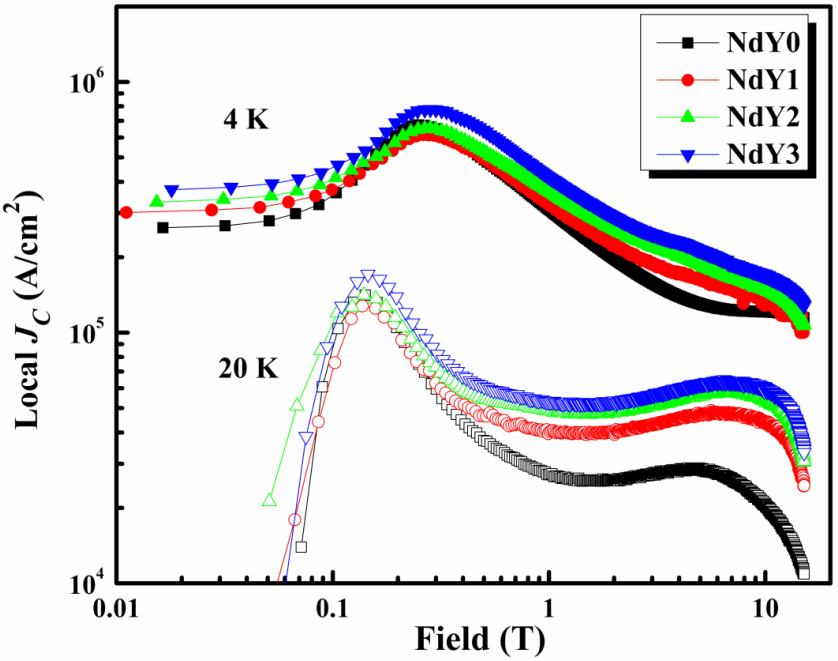

Figure 5.7: $J_C(H)$ plots of the undoped and Y doped samples at 4 K and 20 K

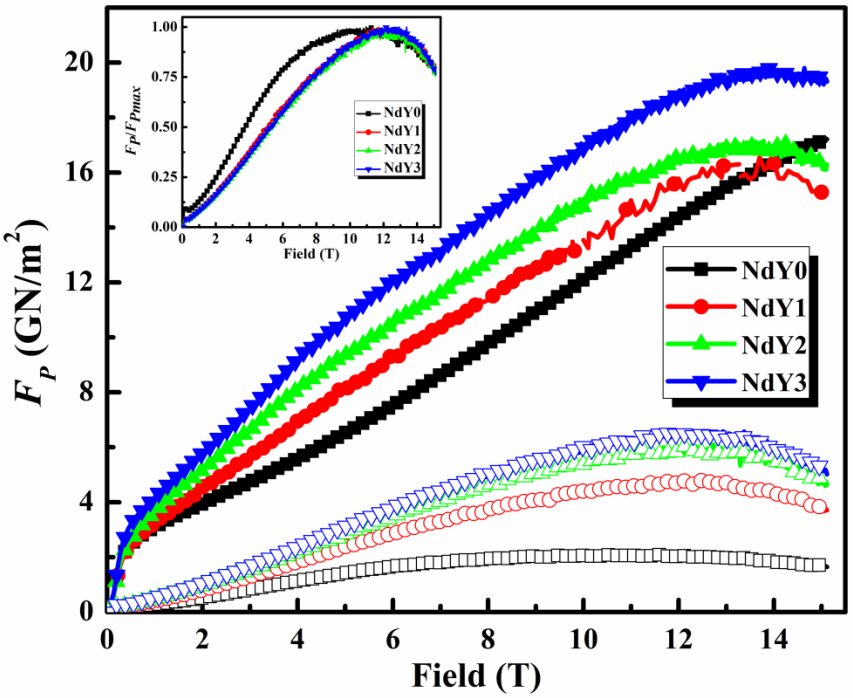

Figure 5.8: $F_P(H)$ plots of the samples at 4 and 20 K. Inset shows normalized F_P versus H plots at 20 K

The experimentally measured magnetic hysteresis (M-H) curves for the samples up to 16 T, measured at 4 K are shown in the Figure 5.6. The M-H loops appear as a combination of the irreversible superconducting hysteresis loop and a paramagnetic background. The observed M-H behavior is in accordance with the published reports of Nd1111 and is attributed to the paramagnetic nature of the Nd^{3+} ions (Prozorov *et al.*

2009). The impurity phase NdOF is paramagnetic at low temperatures and hence it can be assumed that the observed paramagnetic moment arises from the Nd^{3+} ions existing both in the superconducting phase and in NdOF. The top-right inset of Figure 5.6 shows enlarged view of M-H curve at low fields. The M-H curves are asymmetric with respect to the field axis. The field decreasing branch shows almost linear behavior and, moment tends to zero as H approaches zero. This indicates that the Bean-Livingston (BL) surface barrier dominates the flux entry and exit at the surface (Bean *et al.* 1964; Yeshurun *et al.* 1996). The paramagnetic background was estimated as a mean of the upper and lower hysteresis branch (i.e. $M_P = (M^+ + M^-)/2$) for each loop and was deducted from the experimentally obtained M-H curves. The top-left inset of Figure 5.6 shows the paramagnetic background subtracted M-H curves of undoped and Y doped $NdFeAsO_{0.7}F_{0.3}$ samples measured at 4 K and 20 K. At both measurement temperatures, the width of the hysteresis loop, ΔM (where $\Delta M = M^+ - M^-$) of Y doped samples show a systematic increase corresponding to Y content, due to vortex pinning.

The critical current density (J_C) of the superconducting samples is extracted from M-H curve using the Bean critical state model (Bean C. P. 1962), $J_C = 30\Delta M/\langle d\rangle$ (Chen(d) *et al.* 2008). Here, ΔM (emu/cm^3) is the width of the M-H curve and $\langle d\rangle$ is the average grain size in cm. An average grain size of 5 μm is used for the $J_C(H)$ calculations. From the *ac* susceptibility data, it is evident that Y doping causes the formation of non-superconducting phases which exacerbates the inter-grain connectivity in the samples. Hence, we considered the bulk samples as decoupled grains and calculated their intra-grain J_C using the above equation. Figure 5.7 shows the $J_C(H)$ characteristics of Y free and Y doped samples measured at 4 and 20 K with field values in the range of 0 - 16 T. It is clear from the figure that for higher fields, the J_C of Y doped samples is higher as compared to that in the undoped sample for both 4 K and 20 K. At 4 T and 4 K, the J_C of the doped sample NdY3 is 2.3×10^5 A/cm^2, ~ 60% higher as compared to the undoped sample (1.4×10^5 A/cm^2). At 20 K and 4 T, the J_C of NdY3 is 5.9×10^4 A/cm^2, which is enhanced by a factor of more than two when compared to that of the undoped sample (2.8×10^4 A/cm^2). Though the high intra-grain J_C values are promising, the considerable difference with transport J_C makes it clear that iron oxypnictide samples still face severe connectivity issues (Wang(a) *et al.* 2009; Moore *et al.* 2008). At 20 K, a broad hump similar to fish-tail effect (second magnetization peak) is observed in the 4 - 12 T regime in all the samples, but it is not as pronounced as in cuprates or in Ru/K doped Ba122 (Bharathi *et al.* 2010; Sharma *et al.* 2013). The fish-tail like feature is not prominent at 4 K, up to 16 T.

The flux pinning force density $F_P = J_C(H) \times H$ was calculated from the magnetic J_C data and the dependence of the pinning force on applied magnetic field is shown in Figure 5.8. As compared to the undoped sample, all the doped samples show enhanced pinning force at both 4 K and 20 K. F_P values as high as 19.8 and 6.5 GN/m^3 at 4 K and 20 K respectively are achieved, for the yttrium doped sample NdY3. The variation of normalized pinning force (F_P/F_{Pmax}) as a function of applied magnetic field measured at 20 K is also shown as an inset in Figure 5.8. It is observed that the field at which normalized F_P becomes maximum is shifted to higher values for the doped samples. The absolute values of F_{Pmax} and the field at which F_P becomes maximum are much higher implying that yttrium doping has caused considerable improvement in flux pinning. In short, besides the fluorine substitution at oxygen site, the substitution of Nd^{3+} with a relatively smaller ion Y^{3+} creates lattice defects in $NdFeAsO_{0.7}F_{0.3}$ and thereby improves the flux pinning capability of the system. An overall analysis on magnetic J_C and transport J_C shows that defects induced due to yttrium doping enhances the inherent vortex pinning and thereby the intra-grain J_C but transport J_C solely depends on the connections across grain boundaries which is poor in the present case. It is to be noted that weak link behavior and low inter-grain J_C are characteristic features observed in iron pnictides similar to cuprates (Yamamoto *et al.* 2011). But proper texturing of these samples can reduce the wide difference between the observed magnetic and transport J_C.

5.2.3 Conclusions

The magnetic and transport properties of yttrium doped $NdFeAsO_{0.7}F_{0.3}$ superconductor have been investigated. Yttrium doping causes an increase in T_C of Nd1111 system by around 4 K, with a maximum T_C of 53.3 K for the sample with x = 0.3. The shrinkage of lattice parameters and the consequent increase in inner chemical pressure are the reasons for the T_C enhancement. Also, the magnetic J_C measurements show that there is substantial enhancement in bulk flux pinning due to the creation of lattice defects; thereby enhancing the $J_C(H)$ performance in the yttrium doped samples as compared to the undoped sample.

5.3 Influence of Cerium and Gadolinium doping on the electromagnetic properties of $NdFeAsO_{0.7}F_{0.3}$

In the previous *Section 5.1*, the effect of a non-4f rare earth element ‘yttrium’ on the structural and superconducting properties of Nd1111 was investigated. Hence, in the present study, we have chosen two 4f rare earth elements i.e. Ce and Gd for partial

substitution of Nd in $NdFeAsO_{0.7}F_{0.3}$. Cerium is a magnetic rare earth with 4f electrons and variable valency (3 and 4). It is also known that cerium changes its valency upon cooling to very low temperatures and the oxidation state in the presence of other ions also varies. So the involvement of the valence electrons and their contribution to the total density of states in the Ce doped system remains intricate. Since the ionic size of Ce is larger than Nd, Ce substitution in Nd1111 is not expected to bring in a lattice contraction. However, the addition of Ce ions to the vacancies deliberately created at Nd site will definitely modulate the superconductivity observed in Nd1111 system. Whereas the dopant, Gd, is an isovalent ion for Nd and the ionic size of Gd is smaller than that of Nd. Thus, with respect to Nd, Ce is a larger ion and Gd is a smaller isovalent ion. In this study, we present a detailed investigation of the effects of Ce and Gd doping at Nd site on the structural and superconducting properties of $NdFeAsO_{0.7}F_{0.3}$ superconductor.

5.3.1 Experimental

Polycrystalline samples of $Nd_{1-x}Ce_xFeAsO_{0.7}F_{0.3}$ (x = 0, 0.1, 0.2 and 0.3), named as NdCe0, NdCe1, NdCe2 and NdCe3, and $Nd_{1-x}Gd_xFeAsO_{0.7}F_{0.3}$ (x = 0.1, 0.15 and 0.2) named as NdGd1, NdGd15 and NdGd2 were synthesized using the solid state method based on the pre-processing technique already reported by our group (Anooja *et al.* 2012). Stoichiometrically weighed powders of Nd, Ce, Gd, Fe, As, Fe_2O_3 and FeF_2 were mixed and ground using an agate mortar and pestle. All the samples were weighed, mixed and ground inside a glove box under high purity argon atmosphere. The samples were compacted into rectangular pellets by applying pressure of 500 MPa using a hydraulic press. These pellets were then sealed in evacuated quartz tubes and heat treated in a muffle furnace under identical conditions. The samples followed a heat treatment procedure of 360 °C/5h + 850 °C/30h + 1000 °C/20h with intermediate grinding and re-pelletizing. The clean, dense, rectangular pellets thus obtained were then subjected to structural and superconducting analysis.

5.3.2 Results and discussions

Figure 5.9 (a) and (b) show the X-ray diffraction (XRD) patterns of the finely powdered samples of $NdFeAsO_{0.7}F_{0.3}$ (Nd3) and Ce and Gd doped $NdFeAsO_{0.7}F_{0.3}$ (NdCe1, NdCe2, NdCe3, NdGd1, NdGd15 and NdGd2). The phase identification of all these samples confirmed that the major phase is NdFeAsO which resembles the ZrCuSiAs type structure of P4/nmm space group. Small amounts of impurity phases such as NdOF and FeAs are also present in all the samples. However, phases of Ce and Gd or their derivatives have not been detected in any of the Ce and Gd doped Nd1111 samples. Moreover, the

superconducting volume fraction is found to be more than 90% for all the samples. Figure 5.10 (a) and (b) show the enlarged view of the XRD patterns around the main peak (*102*) for Ce and Gd doped samples keeping Nd3 as a reference pattern. It is observed that the main peak of Ce doped samples shift towards the left with respect to that of Nd3 while in Gd doped samples the peak shifts towards the right. However, in Ce and Gd doped samples, the shift of the peaks is almost saturated for NdCe3 and NdGd2 samples, respectively.

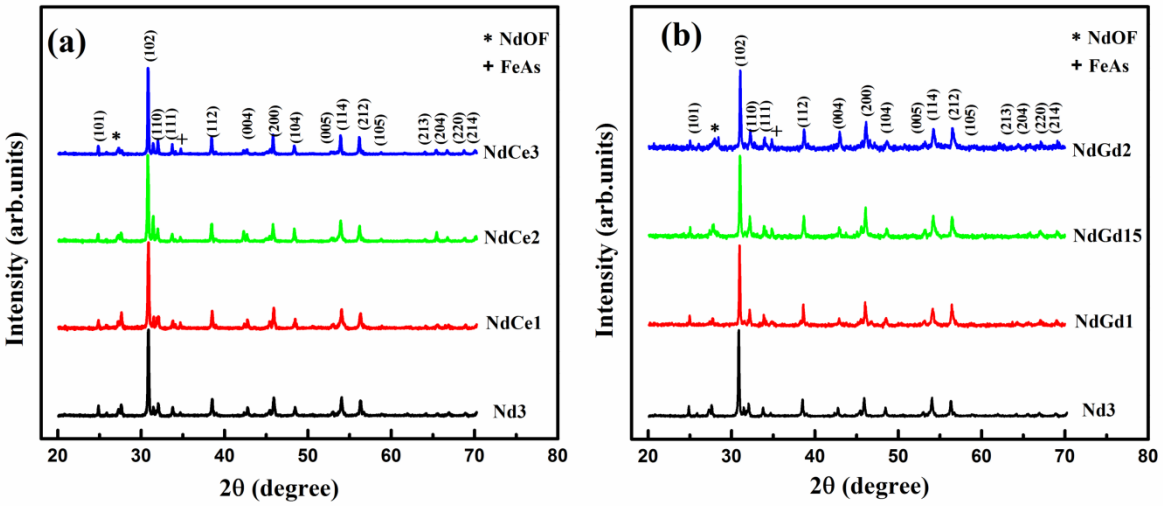

Figure 5.9: XRD patterns of (a) pure (Nd3) and Ce doped Nd1111 samples and (b) pure (Nd3) and Gd doped Nd1111 samples

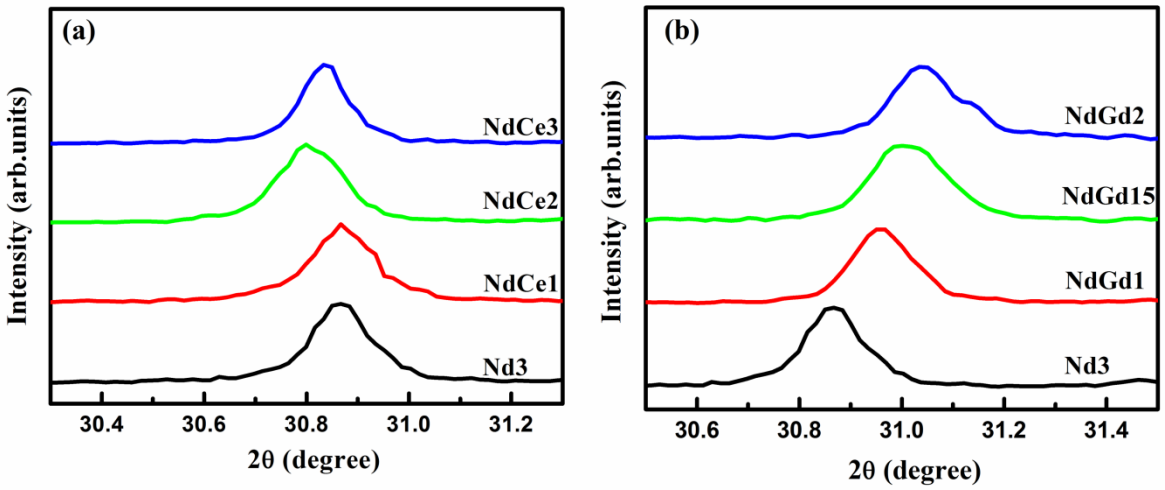

Figure 5.10: Enlarged view of the main peak (102) in (a) Ce doped Nd1111 samples and (b) that of the Gd doped samples

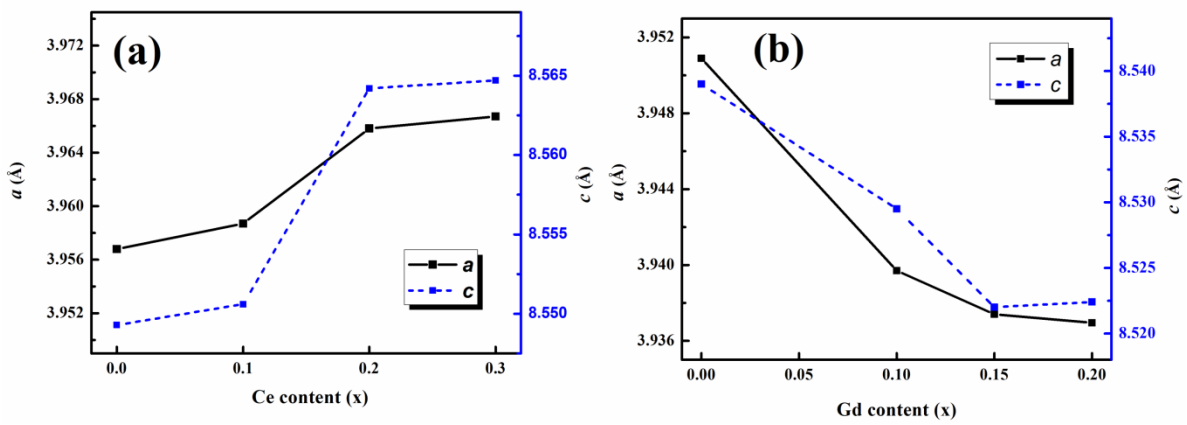

Figure 5.11: Lattice parameter variation in (a) Ce doped and (b) Gd doped Nd1111 samples

In order to understand the effect of Ce and Gd substitution on the crystal lattice of Nd1111 system, the lattice parameters of all the samples were calculated using the Rietveld refined XRD data. The variation in lattice parameters with respect to the varying Ce and Gd content is graphically represented in Figure 5.11(a) and (b), respectively. The lattice parameters *a* and *c* of the Ce doped samples are found to increase with an increase in Ce content and the values remain almost constant for x = 0.2 and 0.3. For Gd doped samples, the lattice parameters were found to decrease with Gd doping with no significant change above x = 0.15. On comparing the ionic radii of Ce^{3+} (1.01 Å) and Gd^{3+} (0.935 Å) with that of Nd^{3+} (0.983 Å), the influence of lanthanide contraction is expected to occur only for Gd doping since it is relatively smaller in ionic radius as compared to Nd. The observed lattice parameter variation confirms the fact that the crystal lattice of Gd doped Nd1111 samples experience an internal chemical pressure due to doping of smaller ions at Nd site and undergo lattice compression. Whereas in Ce doped Nd1111 samples increase in lattice parameter occurs due to the substitution of relatively larger ions at Nd site.

Figure 5.12 shows the SEM images of freshly fractured surfaces of undoped (Nd3), Ce doped (NdCe1 and NdCe3) and Gd doped (NdGd15 and NdGd2) samples. The morphology of samples varies from layered flaky grains with well-defined edges similar to that observed in cuprate superconductors (Vinu *et al.* 2010) to fused layered structures while using Ce and Gd as dopants, respectively. Ce and Gd doping cause minor but notable changes in the microstructure of Nd1111. In the Ce doped sample NdCe1, it is seen that the flaky nature of the grains is sustained with enhanced grain connectivity, well-defined edges and density in general. As the concentration of Ce doping is increased from NdCe1 to NdCe3, the porosity of the sample increases and the microstructure appears as conglomerated grains. The microstructure of Gd doped samples show densely packed grains fused together. The grain morphology remains unaffected while varying Gd

concentration from NdGd15 to NdGd2. The layered nature of undoped Nd1111 system changes into a partially fused grain morphology when Gd is used as dopant.

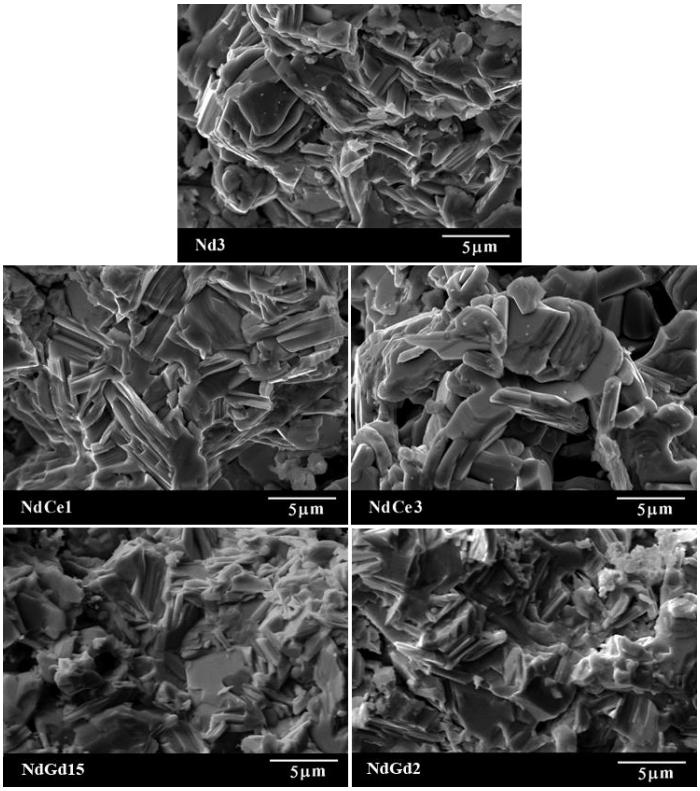

Figure 5.12: SEM images of freshly fractured surfaces of undoped (Nd3), Ce doped (NdCe1 and NdCe3) and Gd doped (NdGd15 and NdGd2) samples

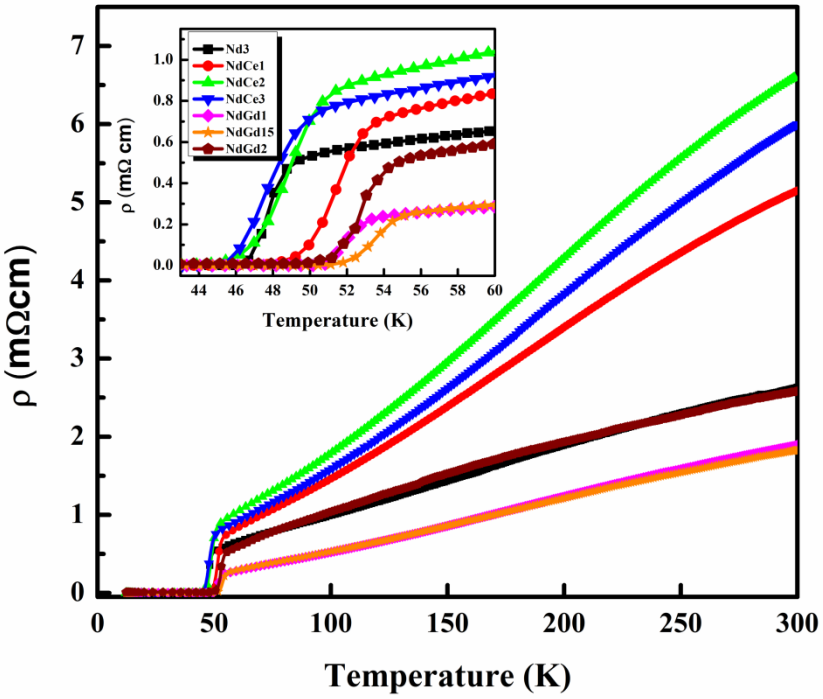

Figure 5.13: ρ-T plots of undoped (Nd3), Ce doped (NdCe1, NdCe2 and NdCe3) and Gd doped (NdGd1, NdGd15 and NdGd2) samples. Inset shows an enlarged view around the transition

Figure 5.13 shows the temperature dependent resistivity of undoped (Nd3), Ce doped (NdCe1, NdCe2 and NdCe3) and Gd doped (NdGd1, NdGd15 and NdGd2) samples and the inset shows an enlarged view around the transition. The undoped sample, $NdFeAsO_{0.7}F_{0.3}$ shows metallic behavior down to the superconducting transition with a T_C around 48.8 K. There were several attempts to increase the T_C of Nd1111 system following its first report on high pressure synthesis with a T_C of 51.9 K. The systems $CeFeAsO_{1-x}F_x$ and $GdFeAsO_{1-x}F_x$ synthesized at ambient pressure exhibit T_Cs of 41 K and 40.1 K, respectively and the mixed rare earth system $Ce_{1-x}Gd_xFeAsO_{0.84}F_{0.16}$ shows a maximum T_C of 47.5 K for x = 0.4 (Liu(a) *et al.* 2008; Chen(b) *et al.* 2008b; Cui *et al.* 2010). Here, it is interesting to observe that both Ce and Gd doping in $NdFeAsO_{0.7}F_{0.3}$ enhance the T_C of the system and the T_C values for all the samples are included in Table 5.2. All the samples remain metallic from room temperature down to their respective transition temperatures. The maximum T_C values attained due to Ce and Gd doping are 53.6 K (x = 0.1) and 55.1 K (x = 0.15), respectively. The normal state resistivity at room temperature (ρ_{300}) and residual resistivity ratio (RRR = ρ_{300}/ρ_{60}) are given in Table 5.2. Both ρ_{300} and RRR values are found to be higher for Ce doped samples compared to Nd3 whereas the values are comparable to that of Nd3 for Gd doped samples. Generally, lanthanides such as La, Nd, Sm and Gd exist as trivalent ions, but Ce changes its valency or oxidation state between 3 or 4, according to the compound in which it exists (Tang *et al.* 1999). Since the 4f electrons in Ce are not fully localized, the charge density in the conducting block of Ce doped Nd1111 is unpredictable. However, in the present case, the increase in T_C of the samples with Ce doping confirms the enhancement in charge transfer between the charge reservoir and conducting layers favoring T_C enhancement. It is believed that elemental Ce doped in Nd1111 has a valency of 3 since modern purification methods yield trivalent Ce. However, at low temperatures a larger ion doping is not expected to cause T_C enhancement, but a change in valency can modulate the charge carrier density. Hence, it is presumed that the mixed valency nature exhibited by Ce at high pressures/low temperatures or change in local chemistry has helped in achieving an optimum charge density upon reaching the doping level of x = 0.1 (Salamati *et al.* 2004). But the lattice mismatch caused by Ce substitution is found to increase the normal state resistivity and the RRR values are found to be relatively high. For Gd doping, lattice parameter reduction due to smaller isovalent ion substitution facilitates effective charge transfer. Thus, substitution of both smaller and larger ion at Nd site shows that lattice contraction due to smaller

isovalent ions favors T_C enhancement in Gd doped system while in Ce doped system the condition is similar to the doping of aliovalent larger ions.

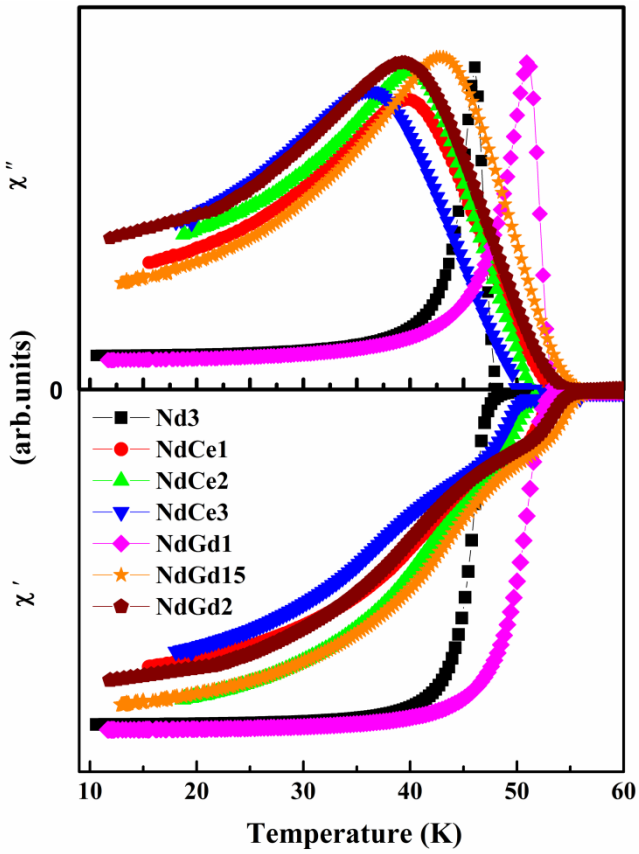

Figure 5.14: Normalized χ-T plots of undoped (Nd3), Ce doped (NdCe1, NdCe2 and NdCe3) and Gd doped (NdGd1, NdGd15 and NdGd2) samples

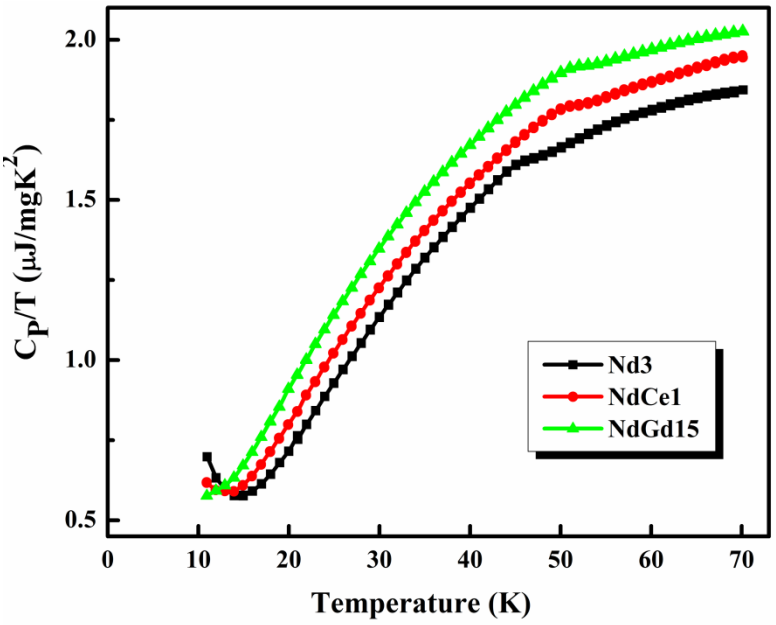

Figure 5.15: C_P/T versus T plots of undoped (Nd3), Ce doped (NdCe1) and Gd doped (NdGd15) samples

Figure 5.14 shows the temperature dependent *ac* susceptibility plots of undoped (Nd3), Ce doped (NdCe1, NdCe2 and NdCe3) and Gd doped (NdGd1, NdGd15 and NdGd2) samples measured at 0.49 mT *ac* field and 208 Hz signal frequency. The T_C values obtained through *ac* susceptibility measurement are in good agreement with the resistivity data (Table 5.2). The *ac* susceptibility plots represent both the real (χ') and imaginary (χ'') parts with respect to temperature. The real part χ' evolves as a step like diamagnetic transition on reaching a temperature corresponding to the T_C of the respective sample i.e. transition from near-perfect screening to complete penetration of external ac magnetic field into the sample; while χ'' forms a peak corresponding to this transition temperature and gives a measure of the dissipation in the sample (Zhang(a) *et al.* 2010). In some cases, instead of single step sharp transition the real part exhibits a double step or hump like behavior at a lower temperature. The two steps are attributed to the contributions from two types of current flowing in the sample: the intra-grain and inter-grain currents. The step near T_C represents intra-grain current and the step at a lower temperature represents inter-grain current. Often superconductors having electromagnetic granularity and mixed phases exhibit such double step transitions (Zhang(a) *et al.* 2010; Polichetti *et al.* 2008). It is observed that almost all of the doped samples in the present study show double step transitions in χ' and a peak corresponding to the lower step in χ''. The inherent electromagnetic granularity of iron pnictides and the presence of similar phases at lower doping levels including the impurity phases are the reasons for this double stepping nature.

Apart from ρ-T and χ-T measurements, the samples were also subjected to calorimetric measurements so as to confirm the bulk superconductivity existing in the samples. At lower temperatures the average thermal energy available to each particle degree of freedom is smaller, and thermal energy storage becomes limited. Hence, as the temperature falls towards absolute zero, so does the heat capacity of a material. The specific heat capacity, i.e. heat capacity per unit mass, is an intensive bulk property that analyses the low energy electronic excitations at the Fermi level thereby enabling it to provide information on the density of states, the nature of the superconducting gap or unconventional gap states. Specific heat capacity of a material has temperature dependent contributions both from electrons and phonons. Thus, the temperature dependent behavior of specific heat capacity gives an idea on the phase transitions, thermal fluctuations and anisotropy within the sample. In the present case, Figure 5.15 shows the temperature dependent heat capacity (C_P/T versus T) plots of Nd3, NdCe1 and NdGd15 at 0 T. It is observed that specific heat decreases linearly for all the samples down to their respective

superconducting transition temperatures. Small step like humps are observed near T_C and thereafter the specific heat values decrease rapidly. The onset T_C i.e. the temperatures at which the slight increase in C_P occur are found to be around 47, 53, and 54 K for Nd3, NdCe1 and NdGd15, respectively. These transitions are not as distinct as in the case of ρ-T and χ-T plots. Moreover, the humps in C_P are found to be smaller as compared to that observed in the Nd1111 single crystal reported elsewhere (Welp *et al.* 2008). The doped samples display a relatively higher specific heat value and their ΔC_P near T_C is also relatively larger as compared to the undoped sample, Nd3. At very low temperatures i.e. around 10 K, an upturn is observed in the specific heat which is an indicator of the Schottky anomaly due to the paramagnetic ions present in the sample (Welp *et al.* 2009).

Table 5.2: Superconducting parameters of undoped, Ce and Gd doped Nd1111 samples

Sample Name	T_C (K)		$\rho_{300\ K}$ (mΩcm)	RRR
	ρ–T	χ–T		
Nd3	48.8	48.2	3.5	2.6
NdCe1	53.6	53.4	5.1	6.1
NdCe2	51.4	51.5	6.6	6.4
NdCe3	50.6	50.3	5.9	6.5
NdGd1	53.3	52.9	2.8	1.9
NdGd15	55.1	55	3.3	1.8
NdGd2	54.8	54.5	4.3	2.6

In order to understand the role of charge carrier density in the enhancement of T_C in the doped samples NdCe1 and NdGd15 as compared to Nd3, Hall Effect measurements were carried out on rectangular pieces of the samples. The voltage leads were connected perpendicular to the current leads, across an approximate equipotential line in the center keeping the applied field perpendicular to the plane of the sample. The Hall voltage (V_H) was estimated after measuring the transverse voltage by sweeping the magnetic field from 9 to -9 T, and thus subtracting out the resistive contribution. The variation of transverse resistivity (ρ_{xy}) with respect to the applied field measured at 100 K is given in Figure 5.16. The transverse resistivity is found to be negative and exhibits a linear dependence on the applied field for both undoped and doped samples. On taking the slope of the linear curves for all the samples, we get the Hall co-efficient i.e. $R_H = \rho_{xy}/\mu_0 H$ (Cheng *et al.* 2008). It is observed that the linear curves for the doped samples NdCe1 and NdGd15 are closer and their respective values of Hall co-efficient are smaller compared to that of Nd3. The R_H values for these samples are -5.6×10^{-9} m^3/C, -4.8×10^{-9} m^3/C and -4.6×10^{-9} m^3/C for

Nd3, NdCe1 and NdGd15, respectively. The negative R_H values indicate that the majority charge carriers are electrons. On the basis of single band model, the carrier density can be estimated as $n_e = 1/(eR_H)$ and the approximate carrier densities calculated for Nd3, NdCe1 and NdGd15 are $1.1 \times 10^{27}/m^3$, $1.3 \times 10^{27}/m^3$ and $1.35 \times 10^{27}/m^3$, respectively. It is clear that the charge carrier density of the doped samples is relatively higher than the undoped sample, Nd3 at optimum levels of x = 0.1 and 0.15 for Ce and Gd doping, respectively.

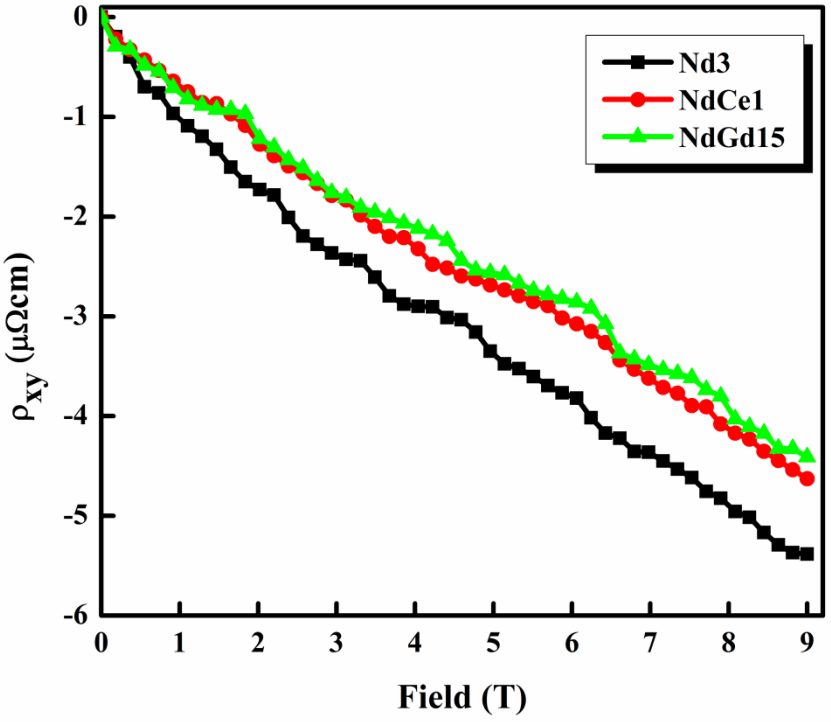

Figure 5.16: ρ_{xy} versus field plots of undoped (Nd3), Ce doped (NdCe1) and Gd doped (NdGd15) samples measured at 100 K

Figure 5.17 shows the magnetic hysteresis loops (MHLs) of undoped (Nd3), Ce doped (NdCe1) and Gd doped (NdGd15) Nd1111 samples measured at 5 and 20 K up to a field of 6 T. The hysteresis loops are not symmetric and the width of the loops thins down at high temperature and high field. With the increase in the applied field, the magnetic moment of the samples remains to be negative up to a particular field and thereafter the moment increases, approaches zero and increases further. This point of deviation from linearity gives lower critical field H_{C1} of the samples. Here, the H_{C1} values are 0.12, 0.18, and 0.2 T at 5 K for Nd3, NdGd15 and NdCe1 samples, respectively. It is clearly seen that the hysteresis loops obtained for these samples are superimposition of a superconducting hysteresis loops on top of strong paramagnetic, field dependent background due to the presence of paramagnetic Nd^{3+} ions present in the sample (Prozorov *et al.* 2009; Tarantini *et al.* 2008). Taking the mean value of the two branches as the paramagnetic

magnetization, $M_P = (M^+ + M^-)/2$, added to the small reversible magnetization of the vortex lattice and subtracting it from the total moment gives the background subtracted magnetization of the samples as shown in insets of Figure 5.17 (a) and 5.17 (b). At low fields, the widths are broader and they thin down with field penetration. However, the width of MHLs in the doped samples (NdCe1 and NdGd15) is larger than that in the undoped sample (Nd3) at both 5 and 20 K measurements. Among the doped samples, the width of MHLs is larger for NdCe1 as compared to NdGd15. This gives a direct inference that vortex pinning is higher in Ce doped samples.

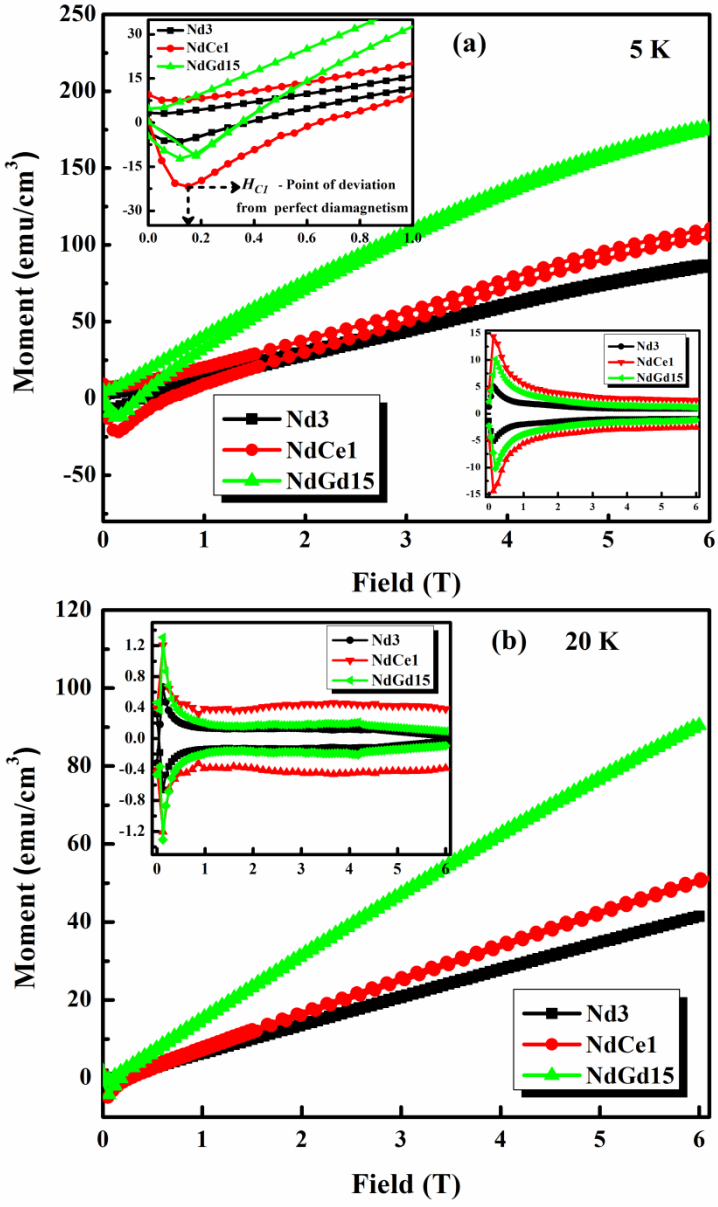

Figure 5.17: The magnetic hysteresis loops (MHLs) of undoped (Nd3), Ce doped (NdCe1) and Gd doped (NdGd15) Nd1111 samples measured at (a) 5 K and (b) 20 K up to a field of 6 T. Insets show the paramagnetic background subtracted MHLs at respective temperatures

Further, the magnetization width (ΔM) due to the critical state of pinned vortices can be estimated as $\Delta M = M^{+} - M^{-}$. Using the extended Bean model and taking the sample dimensions as length scales of magnetization current loops, the global critical current density J_C can be estimated as $Global\, J_C = 20[\Delta M/a(1 - \frac{a}{3b})]$ where ΔM is measured in emu/cm^3, 'a' and 'b' are the dimensions of the samples with a < b in cm and J_C in A/cm^2 (Bean C. P. 1962). The field dependent J_C of undoped (Nd3), Ce doped (NdCe1) and Gd doped (NdGd15) Nd1111 samples measured at 5 and 20 K up to a field of 6 T are given in Figure 5.18. The J_C of all the samples increases up to H_{C1} and further there is an abrupt decrease in J_C up to an applied field of 1 T. Thereafter, an almost constant J_C is observed for all the samples up to the maximum applied field. The doped samples show competitively better $J_C(H)$ performance in comparison to the pristine sample Nd3. The maximum global J_C observed for Nd3 is 1.8×10^3 A/cm^2 at 5 K, while for NdCe1 and NdGd15, the J_C is found to be 3.4×10^3 A/cm^2 at 5 K which is almost double to that of Nd3. Both NdCe1 and NdGd15 trail similar $J_C(H)$ behavior up to 2 T with NdCe1 excelling NdGd15 at higher fields up to 6 T, as expected from the M-H data. At 20 K, the sample Nd3 shows degradation in J_C at higher fields, particularly at 20 K, whereas the doped samples still exhibit enhanced J_C with weak field dependence.

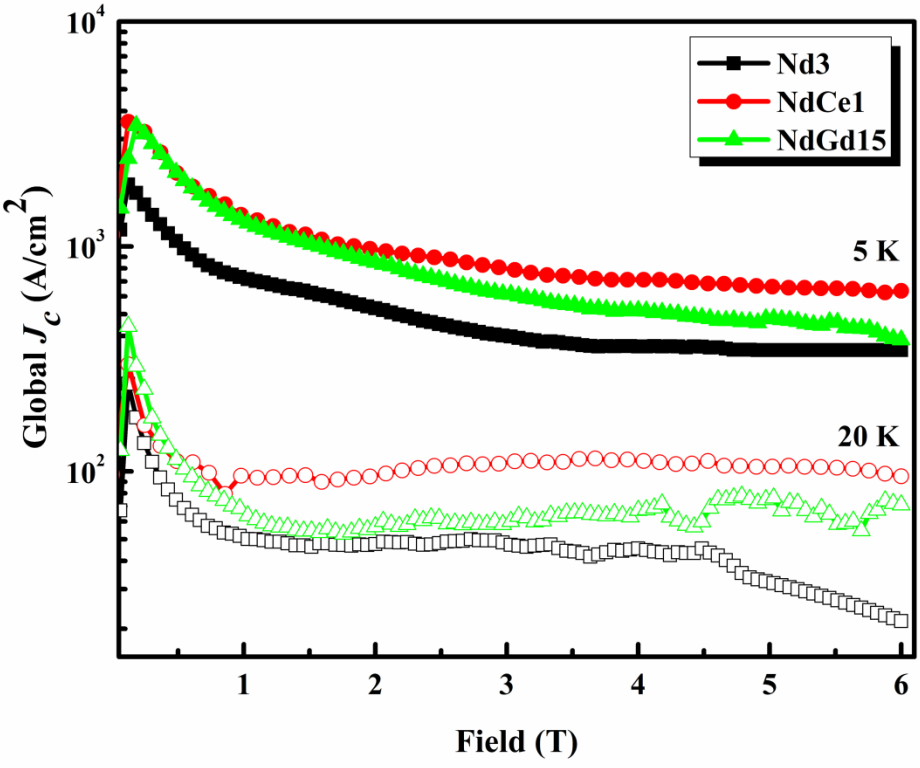

Figure 5.18: $J_C(H)$ plots of undoped (Nd3), Ce doped (NdCe1) and Gd doped (NdGd15) samples measured at 5 K (closed symbols) and 20 K (open symbols) up to a field of 6 T

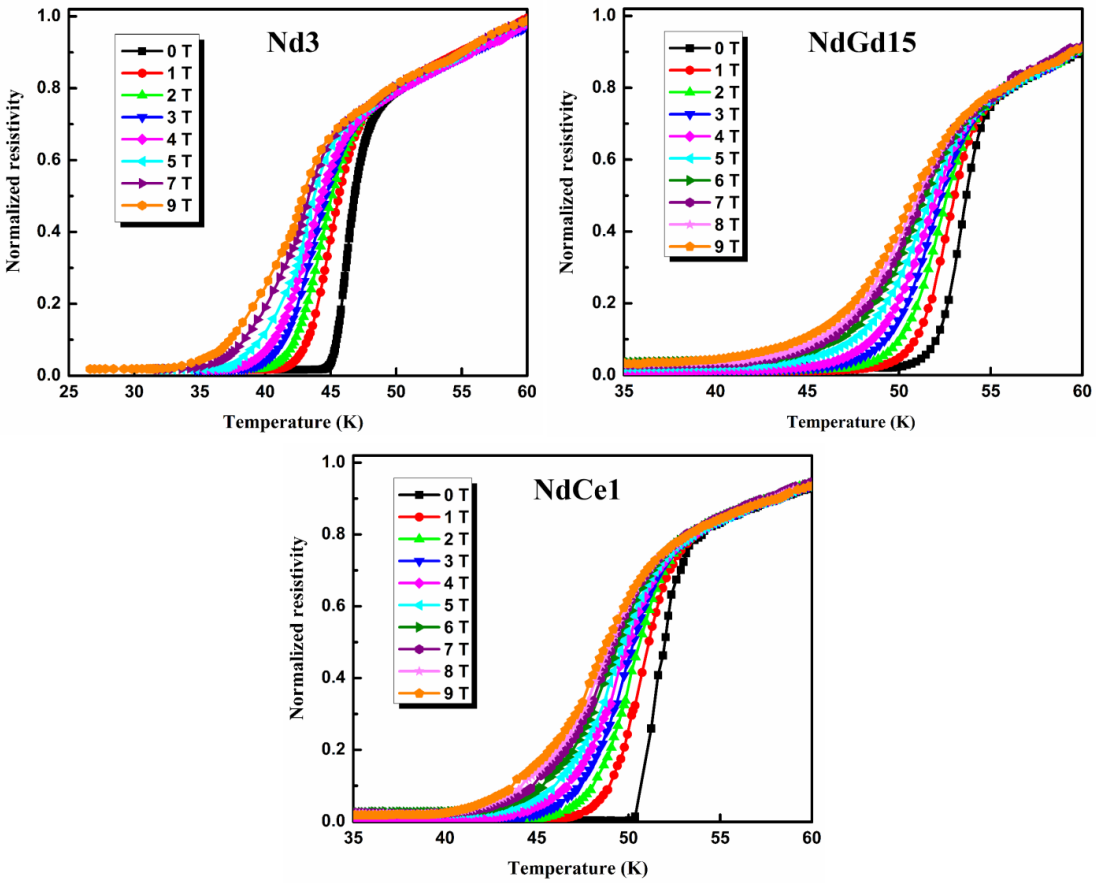

Figure 5.19: ρ-T plots of Nd3, Gd doped (NdGd15) and Ce doped (NdCe1) sample measured at fields 0-9 T

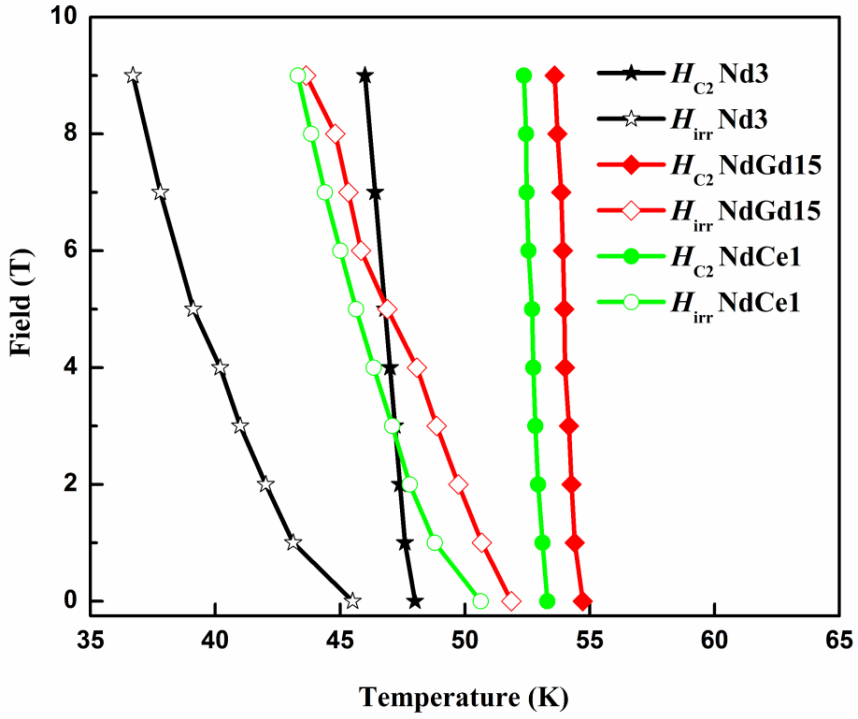

Figure 5.20: H-T phase diagram of undoped (Nd3), Gd doped (NdGd15) and Ce doped (NdCe1) samples measured at fields 0-9 T

The improvement of $J_C(H)$ performance of a superconductor is mainly controlled by the flux pinning centres in it. Often substitution of appropriate dopants creates lattice defects or point pinning centres and sometimes secondary phases or precipitates act as flux pinners (Neson *et al.* 2010). In the present case, both Ce and Gd substitution at Nd site creates lattice defects which help in pinning the flux lines on the defects thereby enhancing the current density at applied fields but at higher fields NdCe1 outdo NdGd15. This leads to an inference that lattice defects created due to the substitution of Nd^{3+} with a relatively larger ion Ce^{3+} acts as a stronger flux pinner compared to that due to Gd^{3+}. However, the contribution of secondary phases towards flux pinning is presumed to be minimal since no such secondary phases due to Ce or Gd substitution have been detected in XRD. In the undoped sample Nd3 itself, the pinning of flux lines is accomplished by the defects due to fluorine doping at oxygen site. Moreover, $J_C(H)$ measurements and flux pinning studies on single crystals of different RE1111 systems have already shown that spatial fluctuations of the critical current density do exist on the macroscopic scale and the major contribution comes from collective pinning of vortex lines by microscopic defects by the mean-free-path fluctuation (δK) mechanism (Van der beek *et al.* 2010). However, substitution of fluorine at oxygen site is also found to create local phase variations, indicating a strong possibility for δT_C pinning mechanism (Shlyk *et al.* 2014). In the present study, apart from fluorine substitution, the major contribution to vortex pinning is from the substitutional defects due to rare earth doping at Nd site in Nd1111.

To obtain information about the upper critical field (H_{C2}) and flux pinning properties, the temperature dependence of resistivity was measured by applying magnetic fields ranging from 0 to 9 T as shown in Figure 5.19. The method of estimating H_{C2} using four-probe resistivity measurement under varying magnetic field provides more accurate values, advantageous over calorimetric measurements which are influenced by the strong paramagnetism of Nd^{3+} ions at high fields (Welp *et al.* 2008; Jaroszynski *et al.* 2008b). Similar to the layered cuprate superconductors, the iron pnictide systems are also reported to have very high critical field and the ρ-T plots under magnetic field variation exhibit a fan-shaped behavior (Hunte *et al.* 2008; Jia *et al.* 2008b). On increasing the field, onset T_C slightly decreases, while the zero resistance temperature or offset T_C largely decreases apparently due to the broadening of the resistivity transition. At the field of 1 T, there is a sudden change in onset T_C. However, the rate of broadening decreases at higher fields. Since the transition temperature does not shift much towards low temperatures, a very high value of $H_{C2}(0)$ (H_{C2} at zero temperature) is ensured.

The upper critical field H_{C2} and irreversibility field H_{irr} were determined from the 90% and 10% values of the normal state resistivity. In Figure 5.20, a graph is plotted with temperatures (T) corresponding to $0.90\rho_n$ (ρ_n - resistivity taken at 56 K) along x-axis and the respective fields (H) around y-axis. The significant upward curvature of the plots have been already observed in polycrystalline and single crystals of Nd1111 proving it to be an intrinsic feature of oxypnictides rather than a manifestation of the vortex lattice melting or granularity (Jaroszynski *et al.* 2008b). The slope of this H-T phase diagram i.e. $d(H_{C2})/dT$ at T_C is used to estimate the H_{C2} on the basis of Werthammer-Helfand-Hohenberg (WHH) theory which is -4.8 T/K, -8.8 T/K and 9.7 T/K for Nd3, NdGd15, and NdCe1, respectively (Werthammer *et al.* 1966). Accordingly, $H_{C2}(0) = -0.693T_C[d(H_{C2})/dT]$ has been calculated as 162 T for the undoped sample, Nd3; 335 T for the Gd doped sample, NdGd15; and 360 T for the Ce doped sample NdCe1. The estimated values of H_{irr} for Nd3, NdGd15 and NdCe1, are 34.8 T, 42.4 T and 47.5 T, respectively. Earlier studies on single crystal forms of Nd1111 samples have shown a maximum H_{C2} of 304 T using WHH theory (Jia *et al.* 2008a). Even though the WHH and Ginzburg-Landau equations seem to be less valid for the low temperature range, the H_{C2} values estimated using both equations are usually far below the real experimental data; indicating that the real H_{C2} in the samples should be higher than what is estimated from the WHH theory. Thus, it is evident that lattice defects due to rare earth doping, especially Ce doping at Nd site, has been effective in increasing the pinning properties and H_{C2} of pristine Nd1111 thereby making it an ideal candidate for high field applications.

5.3.3 Conclusion

Polycrystalline samples of $NdFeAsO_{0.7}F_{0.3}$ and the doped variants $Nd_{1-x}Ce_xFeAsO_{0.7}F_{0.3}$ and $Nd_{1-x}Gd_xFeAsO_{0.7}F_{0.3}$ were synthesized at ambient pressure to investigate the substitutional effects of relatively larger (Ce^{3+}) and smaller (Gd^{3+}) ions at Nd^{3+} site on the structural and superconducting properties of $NdFeAsO_{0.7}F_{0.3}$. Maximum T_Cs of 53.6 K and 55.1 K was obtained through Ce and Gd doping at x = 0.1 and x = 0.15, respectively. At self-field and up to the field of 2 T, both Ce and Gd doped Nd1111 samples exhibit a similar $J_C(H)$ performance with a magnitude double to that of Nd3. However, at higher fields, the $J_C(H)$ behavior of Ce doped Nd1111 sample is competitive to that of the Gd doped sample. In summary, the smaller ionic size of Gd^{3+} is found to enhance the T_C of Nd1111 through lanthanide contraction while the lattice defects created

due to the relatively larger Ce^{3+} ion is found to enhance the $J_C(H)$ performance at high fields.

5.4 Summary

Rare earth modified $Nd_{1-x}RE_xFeAsO_{0.7}F_{0.3}$ (RE = Y, Ce and Gd) samples were found to exhibit enhanced magnetic and superconducting properties as compared to the solo fluorine doped $NdFeAsO_{0.7}F_{0.3}$. The transition temperatures were enhanced to a maximum of 55.1 K with Gd doping. Yttrium and Gadolinium doping were found to enhance T_C through lattice contraction or inner chemical pressure by virtue of their smaller ionic size compared to Nd^{3+} ion; whereas Cerium doping also helped T_C enhancement due to its multivalent nature at low temperatures. Very high upper critical fields of around 360 T and superior $J_C(H)$ performance were also exhibited by the rare earth modified samples. The lattice defects due to substitution at Nd^{3+} site were found to create additional pinning centres which enhanced the flux pinning capability of these samples even at higher magnetic fields.

CHAPTER 6

STUDIES ON BINARY DOPING IN NdFeAsO SUPERCONDUCTOR USING DIVALENT FLUORIDES

6.1 Introduction

Superconductivity in REFeAsO (RE1111, RE - Rare earth) systems could be achieved either through hole or electron doping, isovalent substitution, application of pressure or chemical intercalations (Kamihara *et al.* 2008; Wen *et al.* 2008; Lu *et al.* 2008; Yang(a) *et al.* 2010). As already discussed iron pnictides especially the RE1111 compounds have four different sites for appropriate chemical substitution or doping or creation of vacancies. Initially, the charge reservoir layer i.e. RE_2O_2 layer was mainly modulated, both to induce superconductivity and to enhance the existing properties, instead of the conducting block layer i.e. Fe_2As_2 layer which is relatively tolerant and robust as compared to the CuO_2 layer in cuprates. Fluorine doping at oxygen site or creation of oxygen vacancies was found to be essential to induce superconductivity in the RE1111 compounds (Aswathy *et al.* 2010; Zhao(b) *et al.* 2010). Substitution of trivalent rare earths having smaller ionic radii was then found to increase the T_C of F doped RE1111 compounds due to lanthanide contraction (Lu *et al.* 2008; Wei *et al.* 2008). Doping at RE site with bivalent or univalent ions is also considered as another way of inducing superconductivity by donating holes to the system (Wen *et al.* 2008; Rotter *et al.* 2008). However, the T_C obtained for the hole doped systems was relatively lower than the electron doped ones.

It becomes more interesting when both holes and electrons are introduced into the RE1111 compounds using a single source, an alkaline earth metal fluoride. Apart from the variation in nature and density of charge carriers, the dopant ions play a major role in modifying the electronic structure through structural modifications such as lattice parameter variations and Fe-As-Fe bond angles which indirectly affect the FeAs layer. NdFeAsO based superconductors are well known for their very high upper critical field and field independent $J_C(H)$ performance (Jia *et al.* 2008a; Jaroszynski *et al.* 2008a). But the transport properties of binary doped NdFeAsO superconductors have not been addressed so far. In this chapter, two different alkaline earth metal fluorides such as CaF_2 and MgF_2 have been chosen to introduce both holes and electrons simultaneously into NdFeAsO system. The influence of this binary doping or codoping at Nd^{3+} and O^{2-} sites with Ca^{2+}/Ba^{2+} and F^-, respectively on the structural, microstructural, transport and

magnetic properties of Nd1111 has been investigated in detail and discussed in this chapter.

6.2 Experimental

Polycrystalline samples with nominal compositions of NdFeAsO, $NdFeAsO_{1-x}F_x$ (x = 0.3 and 0.4) and $Nd_{1-x}A_xFeAsO_{1-2x}F_{2x}$ (A= Ca and Mg & x = 0.15, and 0.2) were synthesized by solid state method (Anooja *et al.* 2012). The ingredients Nd, Fe, As, Fe_2O_3, FeF_2 and CaF_2/BaF_2 were stoichiometrically weighed and mixed. The samples NdFeAsO, $NdFeAsO_{0.7}F_{0.3}$, $NdFeAsO_{0.6}F_{0.4,}$ $Nd_{0.85}Ca_{0.15}FeAsO_{0.7}F_{0.3}$, $Nd_{0.80}Ca_{0.2}FeAsO_{0.6}F_{0.4}$, $Nd_{0.85}Mg_{0.15}FeAsO_{0.7}F_{0.3}$ and $Nd_{0.85}Mg_{0.2}FeAsO_{0.6}F_{0.4}$ are labeled as Nd0, Nd3, Nd4, NdCa15, NdCa2, NdMg15 and NdMg2, respectively. Here, Nd3 and Nd4 are the samples doped with fluorine only using FeF_2 as fluorine source. While the binary doped samples NdMg15/Ca15 and NdMg2/Ca2 have stoichiometrically similar fluorine content as in Nd3 and Nd4, respectively; the fluorine source used is CaF_2/MgF_2. The weighing and mixing of starting materials were performed in a glove box filled with high purity argon gas. Following this, the homogenous mixtures were compacted into rectangular pellets having dimensions 5 × 5 × 15 mm^3 and sealed in evacuated quartz tubes. The sealed quartz tubes were then heat treated at 360 °C for 5 h. The pre-processed samples were ground, re-pelletized and again sealed in evacuated quartz tubes. The samples were then heat treated at 850 °C/30 h + 1150 °C/20 h. The furnace was then cooled with a slow ramp rate of 1 °C/min to avoid the breaking of quartz tubes.

6.3 Influence of CaF_2 doping in NdFeAsO superconductor

6.3.1 Structural and transport properties of CaF_2 doped NdFeAsO

The powder x-ray diffraction patterns of the samples are shown in Figure 6.1. The major phase in all the samples was identified as that of NdFeAsO. The pure sample Nd0 contains phases of FeAs which are present in other samples also. In all the doped samples, apart from FeAs, NdOF phase is also present. The peaks corresponding to CaF_2 or its derivatives are not present in any of the binary doped samples. Thus, it can be inferred that the Ca^{2+} ions have been incorporated into the system appropriately. On comparing with the main peak (*102*) of pure sample Nd0, the corresponding peak of the F doped samples Nd3 and Nd4 show a right-shift and that of the binary doped samples NdCa15 and NdCa2 show a left-shift (shown in Figure 6.2 (a)). The right-shift observed in the samples Nd3 and Nd4 is an indication of *c*-axis contraction caused due to fluorine (or electron) doping which is relatively more in Nd4. Whereas, the left-shift in the binary doped samples indicates that,

though both holes and electrons are doped in the system, hole doping dominates electron doping. The most interesting feature in the XRD patterns of binary doped samples is the relatively high intense peaks corresponding to the (*00l*) planes. Among the binary doped samples, NdCa2 exhibits the maximum alignment of the (*00l*) plane as compared to NdCa15. This demonstrates the feasibility of achieving preferred orientation of the crystallites along the *c*-axis in NdFeAsO based iron pnictides.

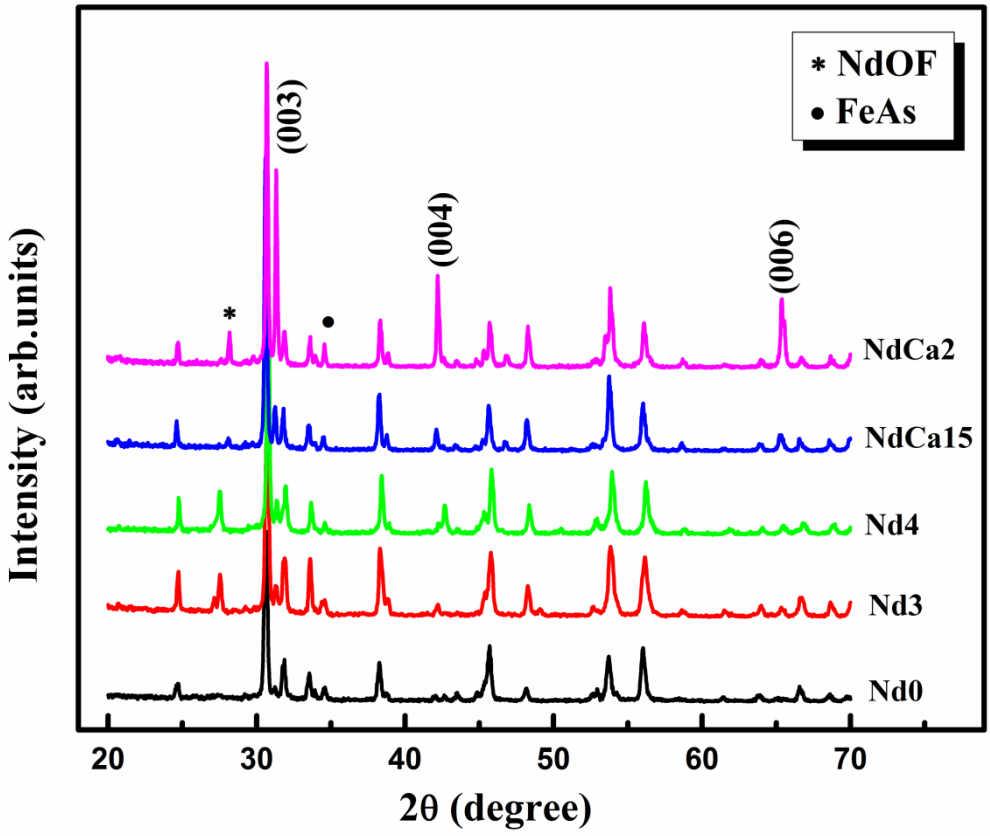

Figure 6.1: XRD patterns of the undoped (Nd0), F doped (Nd3 and Nd4) and binary doped (NdCa15 and NdCa2) samples

In order to correlate the shift in peaks observed with the structural modifications in these samples, the lattice parameter calculations were also done (Table 6.1). The lattice parameters *a* and *c* of Nd3 and Nd4 are smaller than that observed for the parental compound Nd0. Since fluorine doping at oxygen site in RE1111 system causes lattice shrinkage, particularly along the *c*-axis, the decrease in lattice parameter values can be considered as an aftereffect of the electron doping. In the case of binary doped samples, both the lattice parameter values are higher compared to that of Nd0, Nd3 and Nd4. The increase in lattice parameters is a reflection of the left-shift observed in the binary doped samples due to the dominance of hole doping. However, both the *a* and *c* values are found to be higher for NdCa15 compared to NdCa2 i.e. increase in binary doping beyond an

optimum value brings a lattice contraction especially along the *c*-axis. The increase in doping content reduces the interlayer distance between the charge reservoir layer (NdO) and conducting bn layer (FeAs) due to chemical pressure. The dominance of hole doping seems to decrease on reaching a stoichiometry of x = 0.2. From the XRD patterns, the full-width at half maximum (FWHM) values of (*101*), (*102*), (*112*), and (*114*) peaks of undoped, F doped and binary doped samples are estimated and are displayed in Figure 6.2 (b). The FWHM of polycrystalline samples depends on both the crystallite size and lattice strain. It decreases with increase in crystallite size and decrease in lattice strain. It can be seen that the FWHM values decrease for binary doped samples compared to the corresponding F doped samples and the undoped sample.

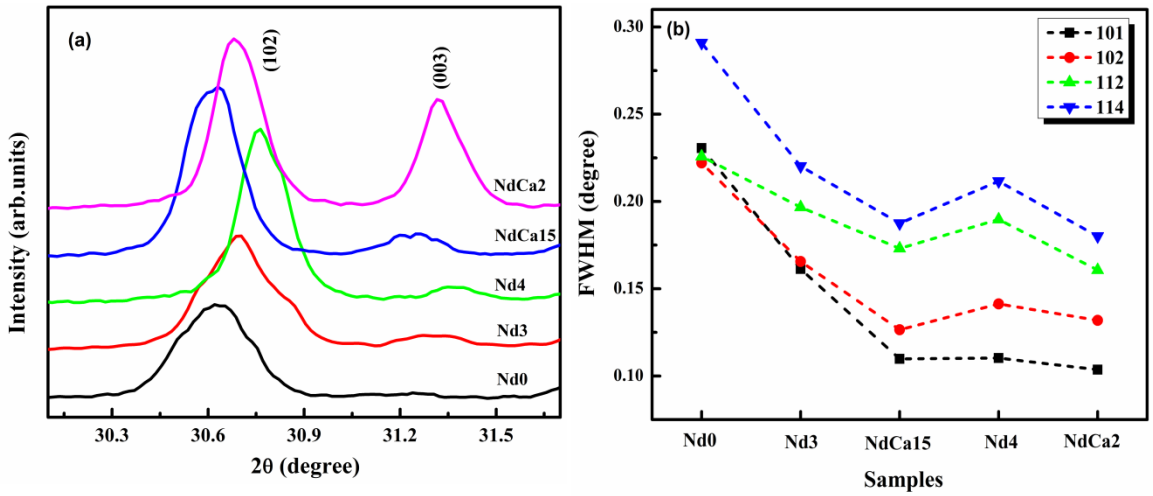

Figure 6.2: (a) Enlarged view of the (*102*) peaks showing the shift and (*003*) peaks showing the large intensity variation due to binary doping (b) FWHM of all the samples for (*101*), (*102*), (*112*), and (*114*) peaks

The SEM images of freshly fractured surfaces of the samples are shown in Figure 6.3. It is seen that there is distinct change in the morphology and grain size of the samples on moving from Nd0 to NdCa2. The grains of the pure (Nd0) and F doped (Nd3 and Nd4) samples are much smaller when compared to the binary doped samples (NdCa15 and NdCa2). The pure sample Nd0 is porous in nature and its grains appear to be fused. On fluorine doping, the grains become more sharp and clear, but the porosity still remains. The microstructure of Nd4 is much superior to that of Nd3 both in terms of grain size and grain connectivity. The observation is in agreement with the reported result that microstructure improves with the increase in fluorine doping level (Aswathy *et al.* 2013). In binary doped samples, a remarkable change is observed both in grain connectivity and grain size. The preferred orientation of crystallites along *c*-axis as found from the XRD analysis and the observed decrease in FWHM of the binary doped samples, especially in NdCa2, are clearly

reflected in the corresponding SEM images. The lowering of FWHM in the binary doped samples supports the increase in grain size in these samples. The porosity is almost absent and the grain size has increased much in the binary doped samples. The enhanced grain growth with preferential orientation in NdCa15 and NdCa2 could be a consequence of the binary doping with CaF_2. Calcium and calcium compounds are found to promote abnormal grain growth (AGG) in different oxide ceramics such as Al_2O_3 (Altay *et al.* 2003), α-SiAlON (Shuba *et al.* 2002), and Ca_2CoO_3 (Tani *et al.* 2007) etc. Here, it is to be noted that, though the grains are layered and larger in size, they are randomly oriented. So, in order to completely exploit the merit of microstructure to enhance the critical current density of conductors these grains need to be properly aligned using methods such as powder-in-tube technique as done in the case of Bi-based cuprates.

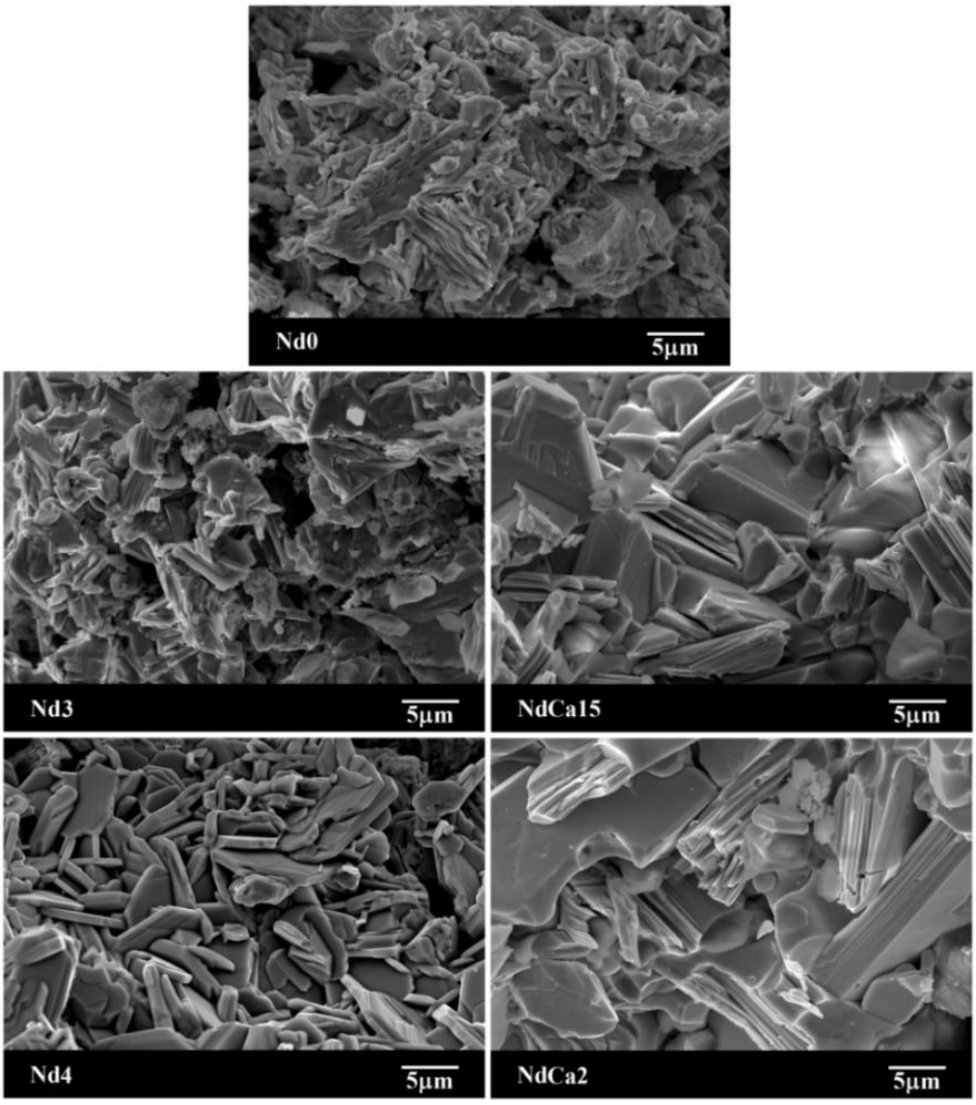

Figure 6.3: SEM images of undoped (Nd0), F doped (Nd3 and Nd4) and binary doped (NdCa15 and NdCa2) samples

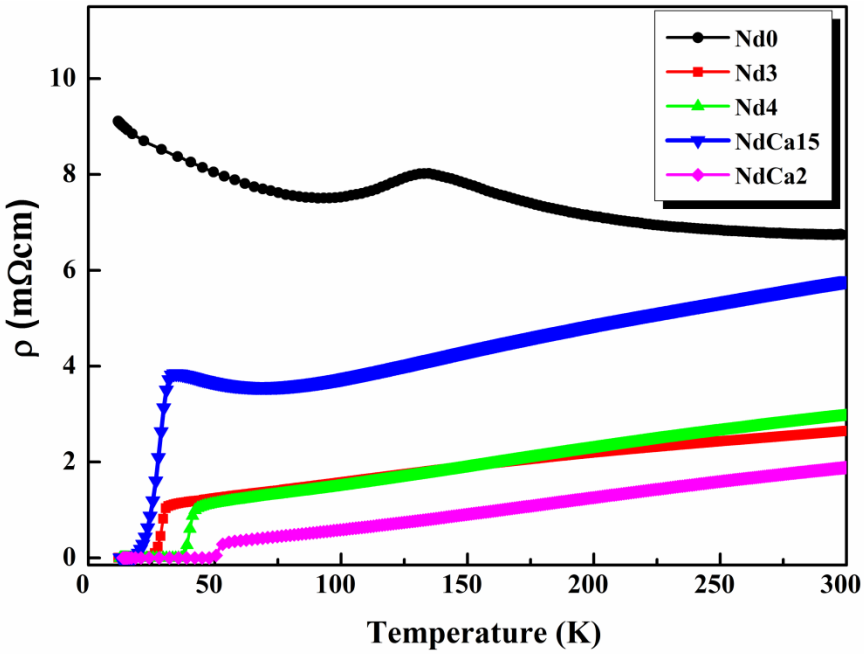

Figure 6.4: ρ-T plots of undoped (Nd0), F doped (Nd3 and Nd4) and binary doped (NdCa15 and NdCa2) samples

The effect of binary doping in NdFeAsO system on the critical temperature T_C and other transport properties was studied through temperature dependent resistivity (ρ-T) measurements and the plots are shown in Figure 6.4. All the data obtained related to structural and superconducting properties of the samples are given in Table 6.1. The pure sample Nd0 is not a superconductor and it displays a resistivity behavior as expected for a parental compound of RE1111 system. The F doped and binary doped samples exhibit a metallic nature above the superconducting transition region. For NdCa15, there is a kink near the transition region depicting an underdoped condition. This is a consequence of inadequate fluorine doping or under-doping due to volatile loss of fluorine supplied by nominal content of CaF_2 for the x = 0.15 stoichiometry. The normal state resistivity of this sample is comparatively higher, but the T_C (32.8 K) is higher than the F doped sample, Nd3 (30.6 K). Even though the sample NdCa15 shows signs of under-doping, the difference in carrier concentration of both holes and electrons is the reason behind the higher T_C observed in NdCa15 when compared to the corresponding F doped sample Nd3. In Nd4, the T_C is found to be 42.2 K which is higher due to the higher content of fluorine compared to that of Nd3. For NdCa2, the normal state resistivity is lower than those of Nd3, Nd4 and NdCa15, and the T_C has increased to a maximum of 52.3 K. Thus, simultaneous doping of 20 % calcium at Nd site and 40 % fluorine at oxygen site has enhanced the T_C as compared to the corresponding F doped sample. The residual-resistivity-ratio (RRR = $\rho_{300/}\rho_{55}$) is a measure of sample purity and homogeneity. It is

observed that RRR is lower for NdCa15 and higher for NdCa2 as compared to the F doped samples Nd3 and Nd4. In NdCa2, the higher RRR and lower normal state resistivity (ρ_{300}) values indicate a much better sample homogeneity than the other samples. The ΔT_C (T_{Conset} – $T_{Coffset}$) is also found to be lower for NdCa2 compared to all other samples. Hence, on considering all the parameters such as RRR, ΔT_C, and T_C, the sample NdCa2 is found to be superior to all other samples. Since all the samples were processed under identical conditions, the higher T_C values observed in binary doped samples compared to their corresponding F doped samples is presumed to be due to the combined effect of hole and electron charge carriers provided by the binary dopant CaF_2.

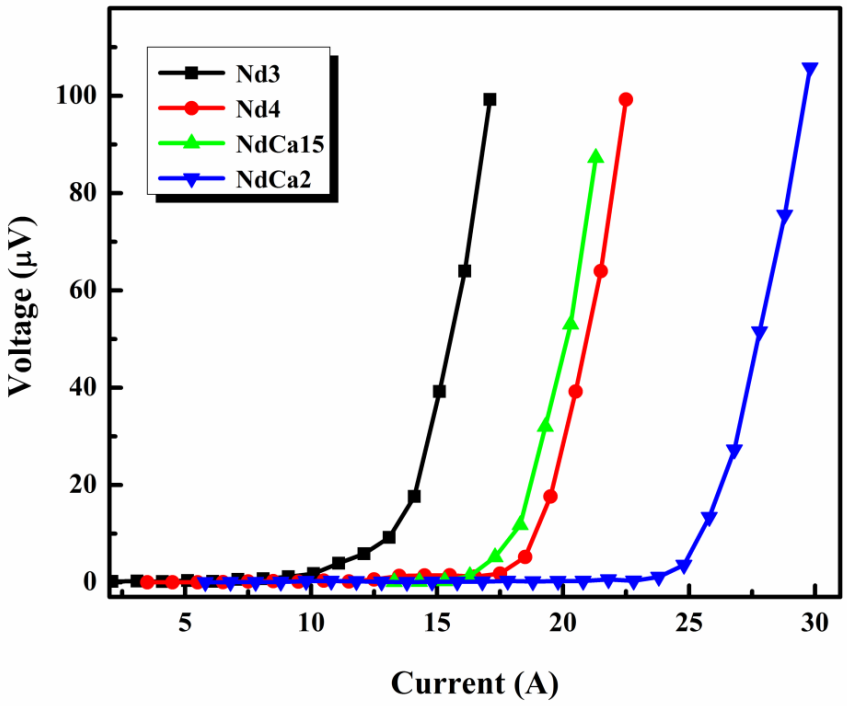

Figure 6.5: I-V plots of F doped (Nd3 and Nd4) and binary doped (NdCa15 and NdCa2) at 12 K

The transport current versus voltage (I-V) measurements were conducted on all the doped samples at 12 K and self-field. The I-V plots of measurements done on samples with a cross section of about 2 × 1 mm^2 are shown in Figure 6.5. It is observed that the transport I_C and corresponding J_C values are higher for the binary doped samples as compared to the corresponding F doped samples. The added advantage of T_C enhancement and the refinement in microstructure collectively enhance the transport I_C of NdCa2. A maximum I_C of 24.8 A and J_C of 1240 A/cm^2 are achieved in this sample. This shows that adequate binary doping can improve the microstructure of the sample and also enhance the transport critical current density significantly higher than by solo fluorine doping.

Table 6.1: Structural and superconducting parameters of pure (Nd0), F doped (Nd3 and Nd4) and binary doped (NdCa15 and NdCa2) samples

Sample Name	Fluorine source	Lattice parameters (Å)		T_C (K)		ρ_{300K} (mΩcm)	RRR	Transport J_C (A/cm^2)
		a	*c*	ρ-T	χ-T			
Nd0	-	3.9815	8.5818	-	-	6.75	-	-
Nd3	FeF_2	3.9675	8.5709	30.6	30.2	2.65	2.07	505
NdCa15	CaF_2	3.9770	8.5864	32.8	32.5	5.78	1.60	815
Nd4	FeF_2	3.9624	8.5573	42.2	41.8	2.96	2.51	875
NdCa2	CaF_2	3.9717	8.5717	52.3	51.9	1.89	5.92	1240

Figure 6.6 shows the *ac* magnetic susceptibility of the F doped (Nd3 and Nd4) and binary doped (NdCa15 and NdCa2) samples with varying temperature measured at *ac* frequency 208 Hz and *ac* field 0.49 mT. The *ac* susceptibility curves (both real, χ' and imaginary, χ'') of the samples have been normalized and scaled between 0 and 1 by dividing with χ'_{max} and χ_p'' so that the effect of binary doping can be understood clearly. The in-phase component, χ', represents the magnetization induced in the sample in-phase with the applied field. For a superconducting sample, it should be negative as expected for a perfect diamagnetic material. Apart from the normal step like transition, the presence of a double stepping nature in the diamagnetic transition is an evidence of the inherent electromagnetic granularity prevailing in iron pnictides. But, in the present case it is to be noted that the binary doped samples do not exhibit such a double step. This may be due to the improvement in grain connectivity and grain size which alleviates the granularity in these samples. The microstructure and transport current measurements of these samples also support the suppression or absence of granularity. While χ' refers the in-phase component, χ'' is referred as the imaginary part which is proportional to $\pi/2$ out of phase or quadrature component of the magnetization. This imaginary component has a positive or nonzero value for temperatures below T_C. It shows two distinct peaks wherein the higher temperature peak corresponds to the individual superconducting grains i.e. intra-granular superconductivity whereas the lower temperatures peak corresponds to the inter-granular coupling (Bonsignore *et al.* 2011).

The flux creep dynamics in the sample NdCa2 was studied by monitoring the *ac* susceptibility at different frequencies for varying temperatures at a fixed *ac* field. Figure 6.7 shows the temperature dependencies of χ' and χ'' for H_{ac} = 0.49 mT at frequencies f = 208, 333, 533, 733 and 999 Hz. The frequency dependence of *ac* susceptibility is observed

distinctly. The diamagnetic onset transition temperature in real part of *ac* susceptibility (χ') remains the same irrespective of the frequency. The inter-granular peak in the imaginary part (χ'') shifts towards higher temperatures with increase in frequency. The flux creep model proposes that the shift in peaks with the increase in frequency is due to the insufficient time for inter-granular vortices to relax and penetrate into the superconductor during each cycle (Muller *et al.* 1990). For complete penetration of flux lines, the pinning force density between the grains is to be weakened. This is possible only when the temperature increases and hence the peak temperature, T_P, increases with increase in frequency. The maximum of $\chi''(T)$, i.e. χ_p'' is at a frequency given by the equation:

$f = f_0 \exp(-U/k_B T)$, where f_0 is an attempt frequency and U is the activation energy for flux creep. In a superconductor, the activation energy or the pinning energy depends on both temperature and applied magnetic field.

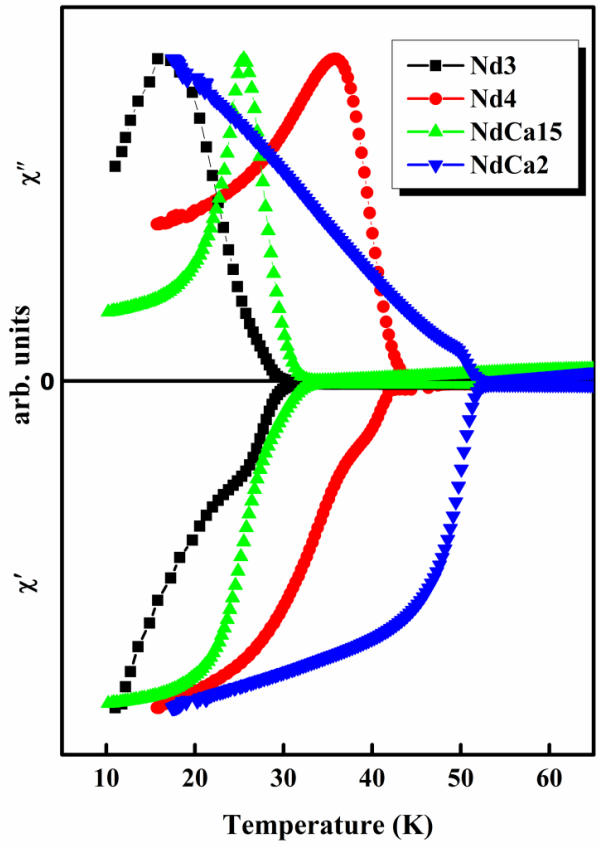

Figure 6.6: Normalized χ-T plots of F doped (Nd3 and Nd4) and binary doped (NdCa15 and NdCa2) samples

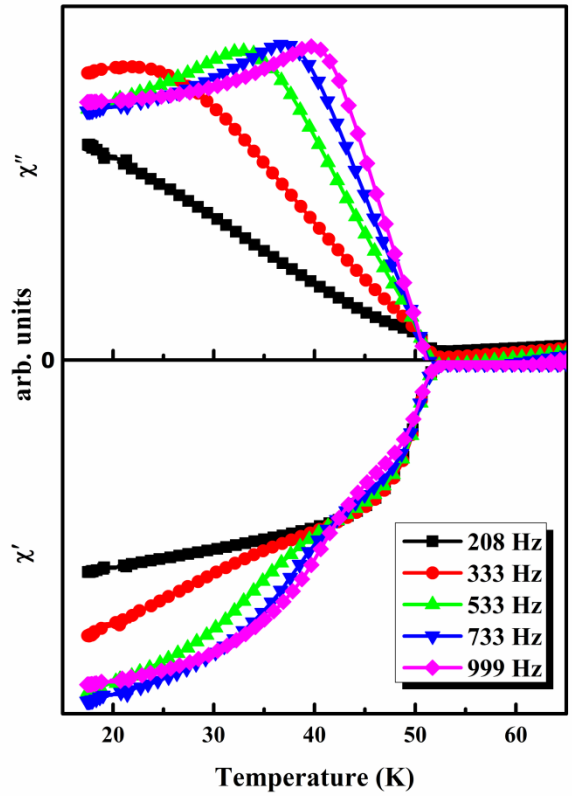

Figure 6.7: χ-T plots of binary doped sample NdCa2 at different frequencies of *ac* signals

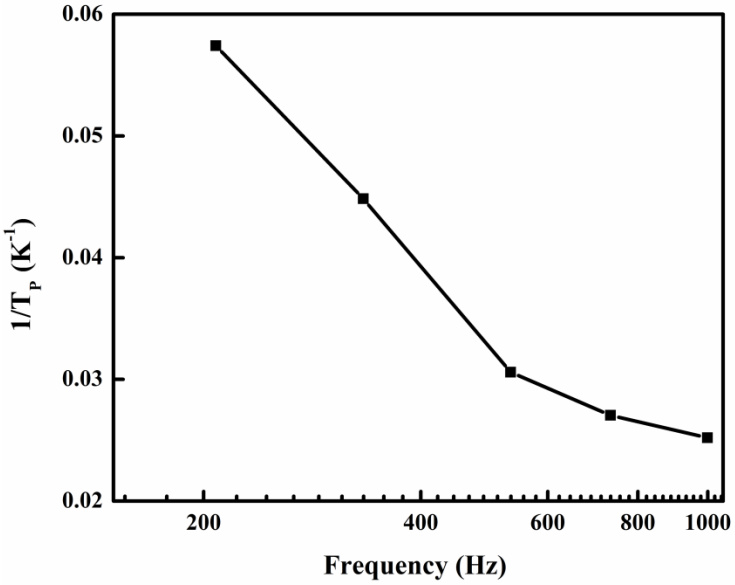

Figure 6.8: $1/T_P$ versus frequency for the binary doped sample NdCa2

Figure 6.8 shows an exponential dependence of $1/T_P$ versus frequency. The above mentioned Arrhenius-like equation can be used to calculate the pinning energy or activation energy for particular field amplitude H_{ac}. The dependence of peak temperature on frequency follows the same trend of exponential decrease as observed in YBCO superconductors (Liu *et al.* 2005; Salamati *et al.* 2004). But, in the present case, the shift in peak temperature with respect to frequency is comparatively larger. Moreover, we can see

that with the increase in frequency, the real part of *ac* susceptibility shows the double stepping nature which is clearly observed at a frequency of 999 Hz (Figure 6.7). These observations conclude that for the binary doped sample NdCa2, the inherent granularity of iron pnictides becomes pronounced only at higher frequencies of *ac* signal. Thus, the coupling between the grains is relatively stronger at lower frequencies.

It is true that the enhancement in T_C and J_C values of a superconductor definitely makes it superior. Different techniques of chemical doping and addition can be used to enhance the transport properties of a bulk superconductor. Both *in situ* and *ex situ* development of iron pnictide wires were attempted soon after its discovery, but the transport J_C reported in RE1111 wires (of the order of 10^3) is even lower than that of other iron pnictide counterparts i.e. 122 system (of the order of 10^5). But there is hardly any report on transport J_C in polycrystalline bulk samples of NdFeAsO based systems. In the present work, the simultaneous doping of Ca^{2+} ions at Nd^{3+} site and F^- ions at O^{2-} site has increased the T_C and J_C of the binary doped samples compared to the corresponding F doped samples. This is a result of the combined effect of both holes and electrons in NdCa2 by binary doping. The observation of *c*-axis alignment and the refinement of microstructure in the samples doped using CaF_2 as the fluorine source are noteworthy. Though preferential orientation gives great scope for further improvement in transport J_C; in the present case, the grain size enhancement caused by binary doping is the major reason for enhanced transport J_C observed.

6.3.2 Conclusions

We could successfully synthesize polycrystalline samples of NdFeAsO based superconductors with simultaneous doping of holes and electrons at Nd^{3+} and O^{2-} site with Ca^{2+} and F^- respectively using CaF_2 as a binary dopant. The sample $Nd_{1-x}Ca_xFeAsO_{1-2x}F_{2x}$ with x = 0.2 exhibited a maximum T_C of 52.3 K and a maximum transport J_C of 1240 A/cm^2 at 12 K. The refinement of microstructure with highly enhanced grain size and preferential orientation of (*00l*) planes achieved in the binary doped sample is mainly the reason for enhanced transport properties. Since iron-pnictides do share the problems of weak links and anisotropy as observed in cuprates, alignment of the preferentially oriented grains along a single axis is expected to further improve the transport properties significantly. Hence, the observations in the present work conclude that the orientation of crystallites in bulk samples can be mechanically worked out to yield tapes having preferentially aligned grains along a single axis, to achieve iron pnictide superconductors of technological significance.

6.4 Influence of MgF_2 doping in NdFeAsO system

6.4.1 Structural and transport properties of MgF_2 doped NdFeAsO

The x-ray diffraction (XRD) patterns of the undoped (parent) compound, the fluorine alone doped compounds Nd3 and Nd4 and the binary doped compounds NdMg15 and NdMg2 are shown in Figure 6.9. All the peaks of the XRD patterns are indexed and the major phase is found to be that of NdFeAsO. Apart from the usual impurity phases such as NdOF and FeAs, the doped samples show no other phases corresponding to Mg or its derivatives, confirming the incorporation of Mg^{2+} ions into the $NdFeAsO_{1-x}F_x$ system.

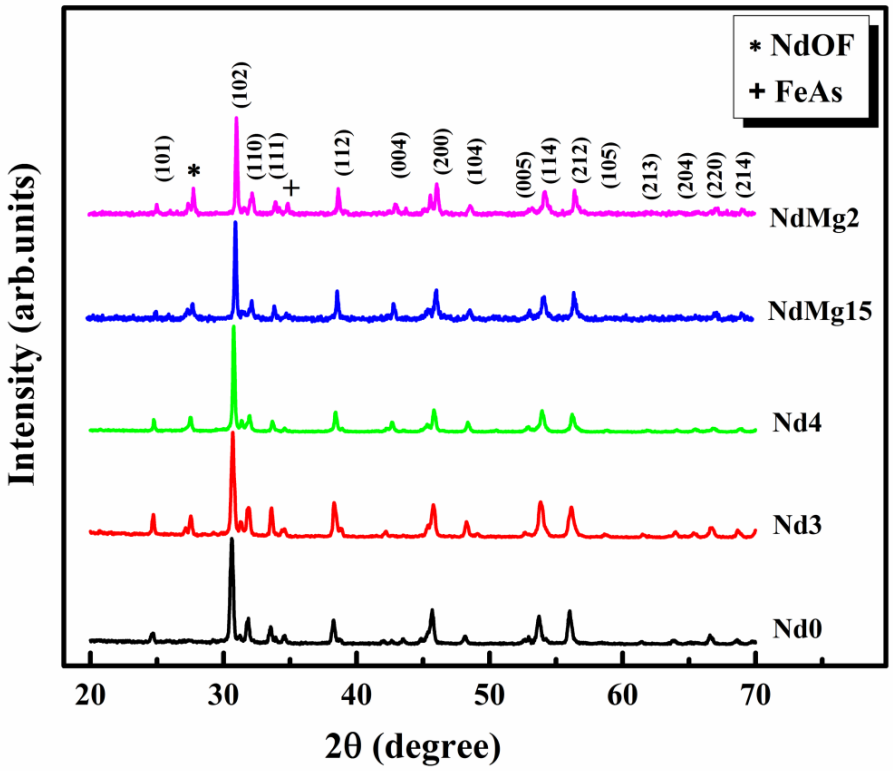

Figure 6.9: XRD patterns of the undoped (Nd0), F doped (Nd3 and Nd4) and binary doped (NdMg15 and NdMg2) samples

An enlarged view of the main peak (*102*) of all the XRD peaks is shown in Figure 6.10 (a). It has already been discussed that doping with fluorine at oxygen site always leads to shift in XRD patterns towards the higher angles. Substitution of Nd^{3+} site with a smaller rare earth ion Gd^{3+} was also found to replicate the same. However, larger ions such as Ce^{3+} and Ca^{2+} caused a shift towards the lower angles as compared to the F doped samples. In the present case, Mg^{2+} ions are smaller than Nd^{3+} and hence the peak shift towards right with respect to both undoped and F doped samples is reasonable. The lattice parameters of these samples were also calculated using the XRD patterns and are included in Table 6.2. Both the lattice parameters *a* and *c* were found to decrease in the binary doped samples

compared to that of F doped and undoped samples. The decrease in lattice parameters i.e. contraction of lattice structure supports the creation of inner chemical pressure due to the relatively smaller Mg^{2+} ion doping at Nd^{3+} site. The full-width at half maximum (FWHM) values of (*101*), (*102*), (*112*), and (*114*) peaks of undoped, F doped and binary doped samples were also estimated and are displayed in Figure 6.10 (b). The FWHM values of the binary doped samples were found to be lower than that of the F doped and undoped samples similar to that observed in the CaF_2 doped samples.

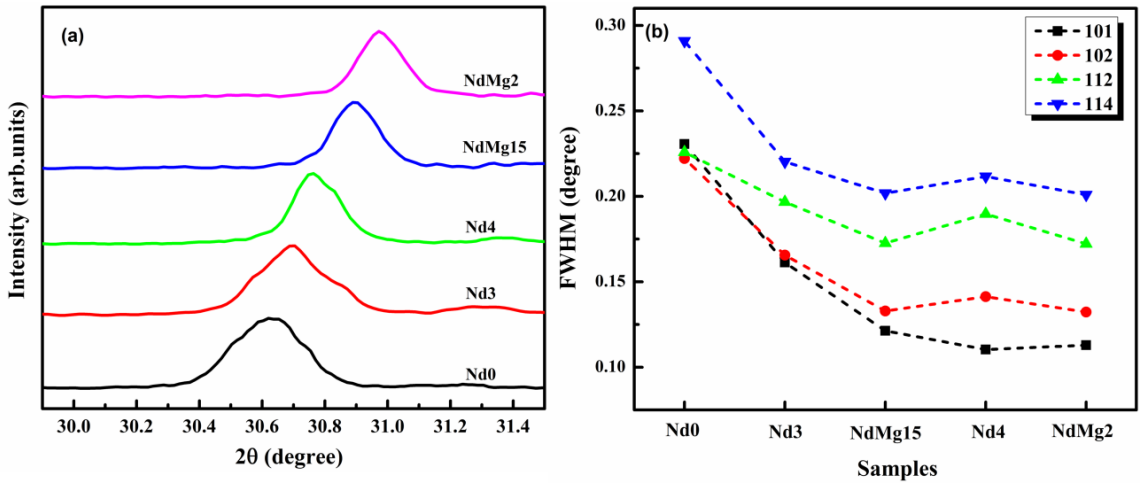

Figure 6.10: (a) Enlarged view of the (*102*) peaks showing the shift in the peaks with respect to the undoped sample (b) FWHM of all samples for the (*101*), (*102*), (*112*), and (*114*) peaks

Table 6.2: Structural and superconducting parameters of pure (Nd0), F doped (Nd3 and Nd4) and binary doped (NdMg15 and NdMg2) samples

Sample Name	Fluorine source	Lattice parameters (Å)		T_C (K)		ρ_{300K} (mΩcm)	RRR	Transport J_C (A/cm^2)
		a	*c*	ρ-T	χ-T			
Nd0	-	3.9815	8.5818	-	-	6.75	-	-
Nd3	FeF_2	3.9675	8.5709	30.6	30.2	2.65	2.07	505
NdMg15	MgF_2	3.9523	8.5273	44.7	44.6	9.01	2.98	850
Nd4	FeF_2	3.9624	8.5573	42.2	41.8	2.96	2.51	875
NdMg2	MgF_2	3.9458	8.5098	54.7	54.5	5.42	6.06	1150

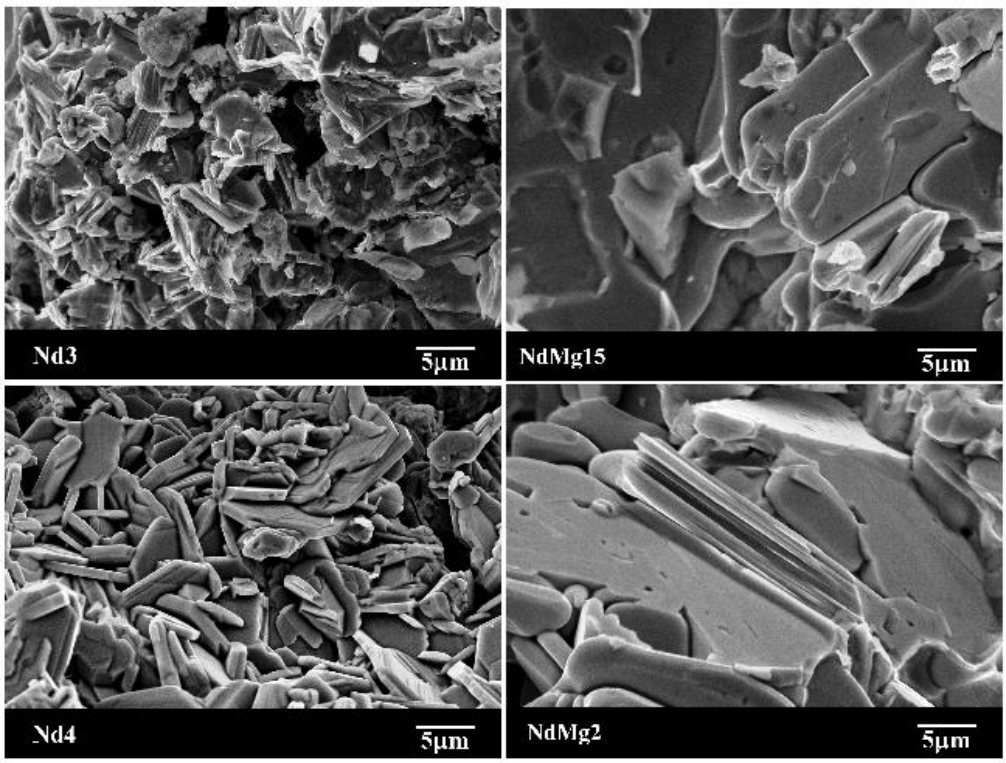

Figure 6.11: SEM images of F doped (Nd3 and Nd4) and binary doped (NdMg15 and NdMg2) samples

The microstructural analyses of these samples were also carried out and Figure 6.11 shows the SEM images of the fractured surfaces of the F doped samples Nd3 and Nd4 along with the corresponding binary doped samples NdMg15 and NdMg2, respectively. The morphology of all the samples shows the characteristic flaky and layered nature of iron pnictides. The microstructure is also homogenous and dense, in general. However, there is notable and dramatic change in morphology of the samples upon binary doping as compared to the corresponding F alone doped samples. In particular, both grain size and grain connectivity are enhanced in the binary doped samples similar to the CaF_2 doped samples. Moreover, the porosity in the F doped samples is also found to decrease tremendously upon binary doping. Since crystallite size effectively contributes to the broadening of the XRD peaks, the increased grain size observed in binary doped samples can be well correlated with the decreased FWHM values obtained for these samples. It is to be noted that binary doping using both MgF_2 and CaF_2 as dopants has brought about significant microstructural refinement. Conversely, the preferential alignment observed in CaF_2 doped samples is not observed in MgF_2 doped samples. So the inference is that alkaline earth metal fluorides used as fluorine source generally refine the microstructure while preferential orientation of crystallites is mainly promoted by the characteristic nature of calcium and calcium based compounds.

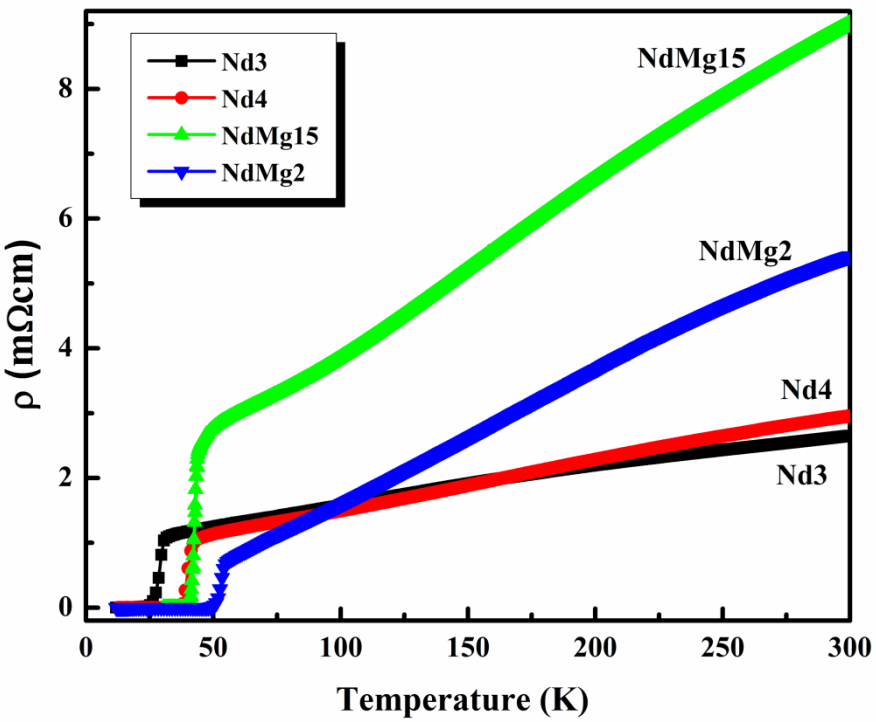

Figure 6.12: ρ-T plots of F doped (Nd3 and Nd4) and binary doped (NdMg15 and NdMg2) samples

Figure 6.12 shows the temperature dependent resistivity of F doped (Nd3 and Nd4) and corresponding binary doped (NdCa15 and NdCa2) samples. All the samples show metallic nature with an abrupt decrease in resistivity especially below a characteristic temperature T_s, around 150 K up to their superconducting transitions. The presence of slope-change in the resistivity curves from 300 K up to superconducting transitions is an indication of the inherent pseudo gap behavior of RE1111 systems. The onset T_C values of all the samples are given in Table 6.2. It is interesting to observe that the T_C values of the binary doped samples are higher than the corresponding F doped samples. A maximum T_C of 54.7 K is obtained for the sample NdMg2, i.e. $Nd_{1-x}Mg_xFeAsO_{1-2x}F_{2x}$ with x = 0.2 stoichiometry. Regarding the binary doped sample $Nd_{1-x}Mg_xFeAsO_{1-2x}F_{2x}$ with x = 0.15 stoichiometry, the T_C value is only 44.7 K, but the superconducting transition is sharp and doesn't show any sign of under-doping as observed in NdCa15. Apart from the modulation in charge carrier density due to binary doping, the smaller ionic size of Mg^{2+} has a major role in increasing the inner chemical pressure of the system that enhances the charge transfer between the charge reservoir layers and conducting block layers. Thus, the structural modification due to the relatively smaller Mg^{2+} ion and the effective contribution of the charge carriers (both electrons and holes) together enhance the T_C of the system.

Figure 6.13 shows transport I-V measurements of the superconducting samples Nd3, Nd4, NdMg15 and NdMg2 at 12 K. The critical current I_C of all the samples was estimated following the standard 1 μV/cm criterion and is given in Table 6.2. The I_C values

of the binary doped samples are found to be substantially higher as compared to the F doped ones. The maximum I_C of 23 A is obtained for NdMg2 which corresponds to a transport J_C of 1150 A/cm^2. The improved microstructure especially the increased grain connectivity is the main reason behind the enhanced transport J_C. The relatively high T_C also supports the sample to maintain such a high J_C.

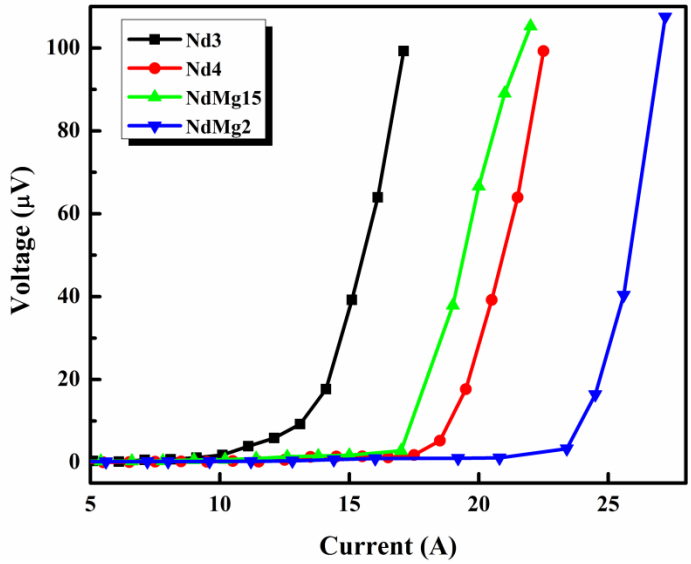

Figure 6.13: I-V plots of F doped (Nd3 and Nd4) and binary doped (NdMg15 and NdMg2) at 12 K

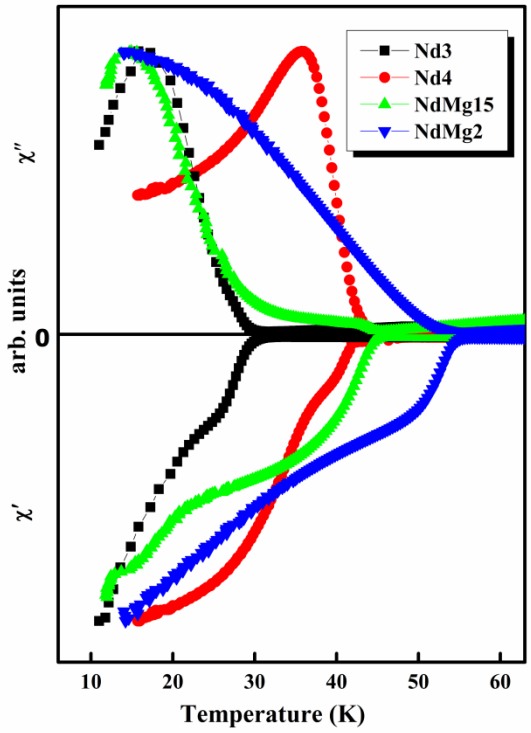

Figure 6.14: Normalized χ-T plots of F doped (Nd3 and Nd4) and binary doped (NdMg15 and NdMg2) samples

Figure 6.14 shows the temperature dependent normalized *ac* susceptibility curves of Nd3, Nd4, NdMg15 and NdMg2 measured at 208 Hz and *ac* field 0.49 mT. As discussed earlier, the real part of the *ac* susceptibility curve χ' gives diamagnetic response due to the screening currents created on the surface of the samples. The T_C values of the samples have been estimated on the basis of the diamagnetic transitions and the data is in agreement with the T_C values obtained through resistivity measurements. It is also observed that all the samples show double stepping nature in the diamagnetic transitions. The samples also show a peak in the imaginary part χ'', corresponding to the transitions in χ', indicating the amount of loss suffered by the system to shield itself from the applied field of the *ac* signal.

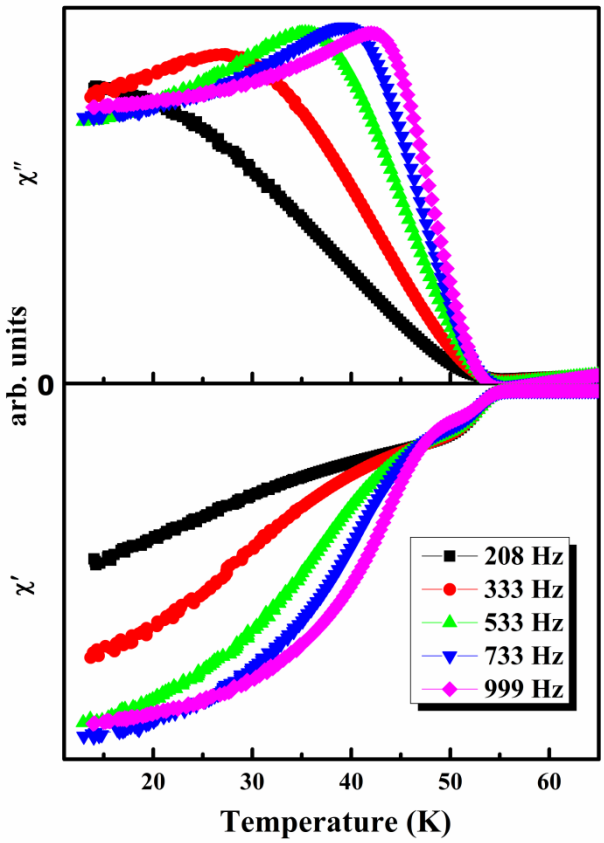

Figure 6.15: χ-T plots of binary doped sample NdMg2 at different frequencies of *ac* signals

Figure 6.15 shows χ-T plots of binary doped sample NdCa2 measured at different frequencies of *ac* signals. In the present case, the depth of the diamagnetic transitions is found to increase with increasing frequency. However, frequency variation has no pronounced effect on the transition temperatures of the real part irrespective of the superconducting system being analyzed. In the imaginary part, the peak height is found to increase and the peak temperature (T_P) shifts to higher temperatures with respect to increase in frequency similar to that observed in YBCO. For MgF_2 doped samples, the shift

in peak is relatively larger than the shift in CaF_2 doped samples and much larger than that in YBCO. The extent of shift and the increase in peak height depend on the flux dynamics of the system which is presented in the succeeding section. Moreover, the shifts in peaks of χ'' with increasing *ac* field frequency can help in estimating the flux pinning energy in superconductors. The frequency dependence of T_P can be attributed to the inter-granular flux creep or magnetic relaxation in the superconductor. The shift in T_P with respect to frequency represented as $1/T_P$ vs. frequency in Figure 6.16 follows an exponential curve as observed for CaF_2 doped sample. However, the slope of the Arrhenius curve is directly related to the activation energy of the system as mentioned earlier. It is clear that the effect of inherent granularity and wet phases in this system becomes detrimental making the flux creep easier and becomes more pronounced at higher frequencies.

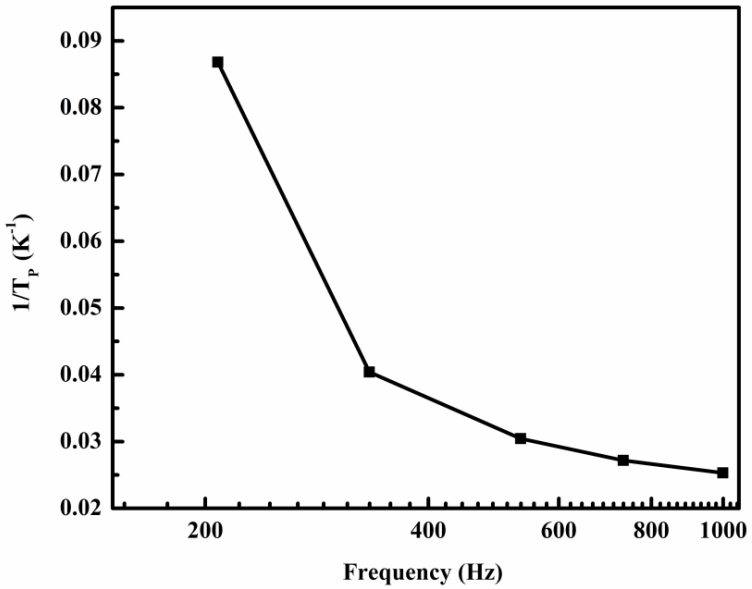

Figure 6.16: $1/T_P$ versus frequency for the binary doped sample NdMg2

6.4.2 Conclusions

It is observed that T_C enhancement in MgF_2 doped system is assisted by the smaller ionic size of Mg^{2+} ions apart from the contribution of charge carriers as a result of binary doping. Though the use of MgF_2 as fluorine source does not cause any preferential orientation of crystallites, it does refine the microstructure of the samples remarkably both in terms of grain size and grain connectivity which in turn favors the enhancement of transport current. Thus, the overall analysis of structural and transport properties of MgF_2 doped NdFeAsO samples conclude that MgF_2 helps in enhancing the T_C and transport J_C of the system as observed in CaF_2 doped samples.

6.5 Magnetic properties of CaF_2 and MgF_2 doped NdFeAsO superconductors

In addition to the structural and transport characterizations, selected samples i.e. the F doped sample (Nd4) and corresponding binary doped samples (NdCa2 and NdMg2) which gave the best transport J_C were subjected to magnetic measurements such as magnetization versus field (M-H) and resistivity versus temperature (ρ-T) at different fields. These measurements have given a lot of information on the J_C behavior of the samples under applied magnetic field and their upper critical fields.

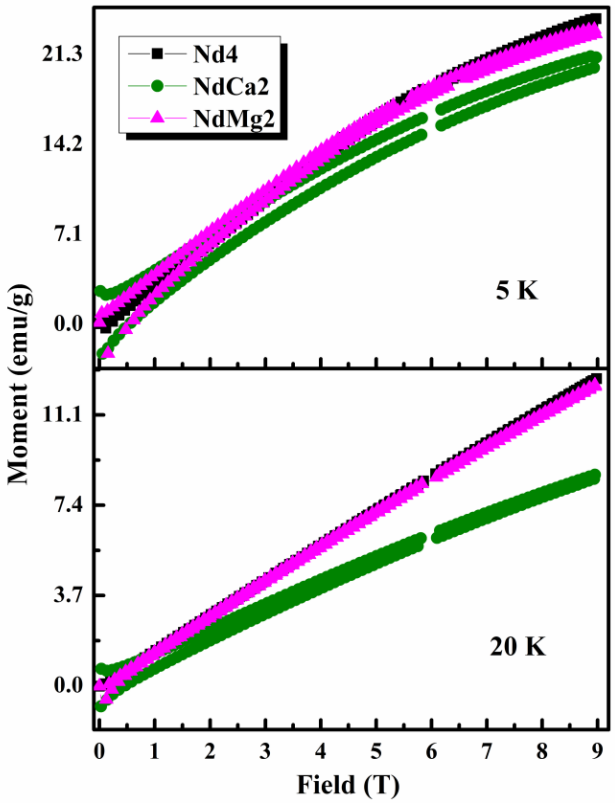

Figure 6.17: Magnetic hysteresis loops of Nd4, NdCa2 and NdMg2 measured at 5 and 20 K up to 9 T

Figure 6.17 shows the magnetic hysteresis loops (MHLs) of Nd4, NdCa2 and NdMg2 measured at 5 and 20 K up to a field of 9 T. Here, the powder samples were subjected to measurement and the moment obtained is normalized using the weight of the samples in grams. The observed high magnetization of all the samples is the contribution of the superconductor vortex pinning along with the paramagnetic moment due to Nd^{3+} ions. At 5 K, the width of the MHLs of the binary doped samples is found to be broader than that of the F doped sample. However, the width of all these samples becomes narrow at a higher measurement temperature i.e. at 20 K. At higher measurement temperature the contribution due to vortex pinning decreases. Similarly, the width also narrows down on increasing the applied field up to 9 T since vortex pinning is also weakened on the

application of higher magnetic fields. It is also observed that the contribution due to paramagnetic moment seems to be higher for MgF_2 doped samples as compared to the CaF_2 doped samples. However, Nd4 shows the highest moment since there is no substitution at Nd^{3+} site as compared to the binary doped samples and hence all the Nd^{3+} ions contribute to the paramagnetic counterpart of the magnetization.

The magnetic moment measured for the samples with increasing field shows that all the samples give a negative moment or remain diamagnetic up to a certain lower critical field, H_{C1} above which the moment increases. In Figure 6.18, it is observed that the CaF_2 doped sample does not show a significant increase in H_{C1} (~ 0.07 T) as compared to Nd4 (H_{C1} ~ 0.05 T). However, the MgF_2 doped sample NdMg2 shows an H_{C1} of 0.16 T which is more than three times the H_{C1} of Nd4. Even though the width of MHL i.e. the overall vortex pinning is larger for NdCa2, lower critical field is found to be higher for NdMg2.

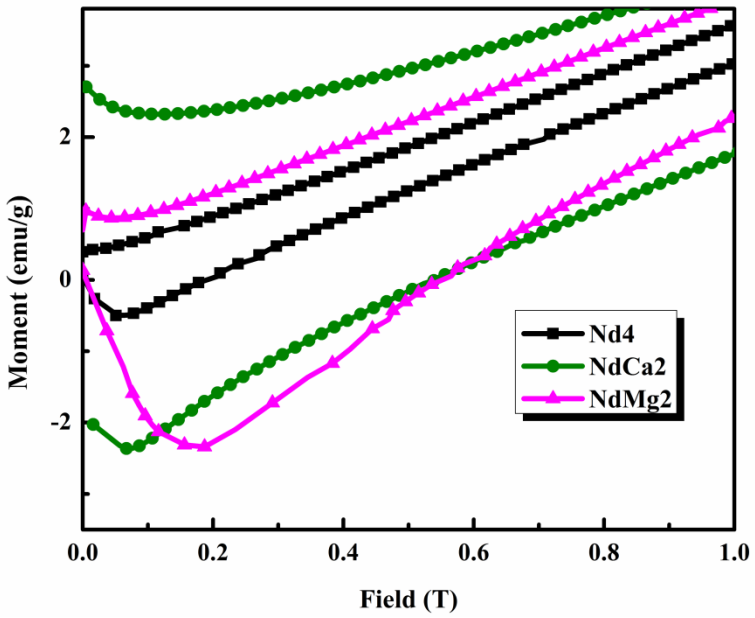

Figure 6.18: Enlarged view of the MHLs of Nd4, NdCa2 and NdMg2 measured at 5 K up to 1 T

In order to deduce the magnetization due to superconductor vortex pinning alone, the contribution due to paramagnetic moment (i.e. $M_P = (M^+ + M^-)/2$) has to be estimated and subtracted which gives a paramagnetic background subtracted data as shown in Figure 6.19. The MHLs in this figure show broader widths for binary doped samples, especially for NdCa2. At 5 K and fields up to 2 T, the binary doped samples show broader magnetization loop width as compared to Nd4 wherein NdCa2 excels NdMg2. However, at higher fields above 2 T, there is a gradual decrease in the width of NdCa2 while the width remains almost constant for NdMg2. Since width of MHLs determines the vortex pinning capability of the system being studied, it can be inferred that the vortex pinning is

enhanced by CaF_2 doping over the entire field of study. But, upon increasing magnetic field, there is a higher rate of reduction in magnetization of NdCa2 compared to that of NdMg2 especially at 20 K. Thus, pinning ability of NdCa2 is seen to be coming down at higher fields and high measurement temperatures while NdMg2 maintains a lower but nearly constant magnetization at higher fields and measurement temperatures.

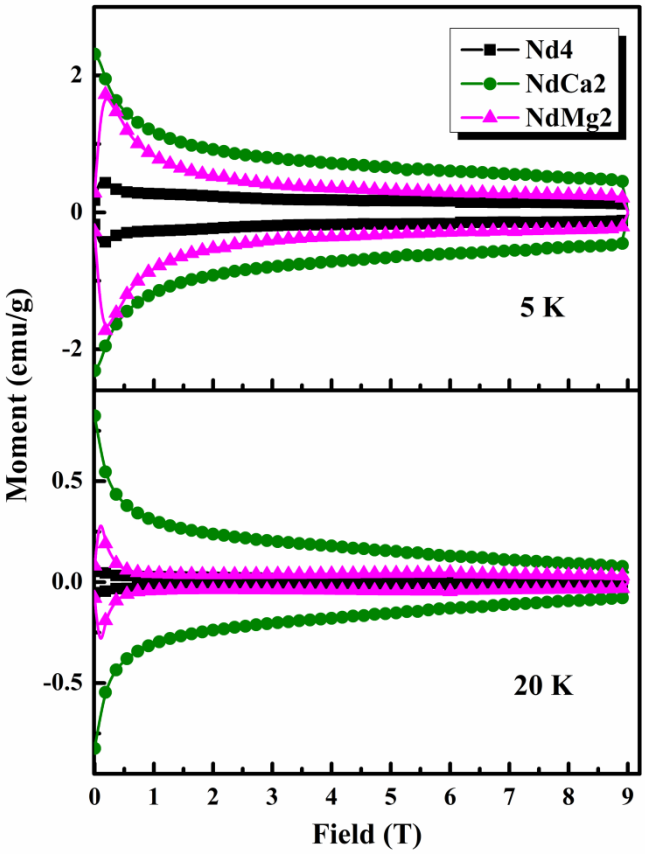

Figure 6.19: The paramagnetic background subtracted MHLs of Nd4, NdCa2 and NdMg2 at 5 & 20 K

Using the Bean critical state model, the intra-grain critical current density (J_C) or the J_C within the grains was calculated asLocal $J_C = \left(\frac{30\Delta M}{\langle d \rangle}\right)$, where ΔM (= $M^+ - M^-$) is the width of the MHLs (Figure 6.19) and $\langle d \rangle$ is the average grain size (estimated from SEM images). The local J_C with respect to applied field was then plotted as shown in Figure 6.20. As expected from the M-H data in Figure 6.19, the local J_C of the binary doped samples are higher than the F doped sample up to 9 T. At 5 K, the maximum self-field local J_C (~ 2.6×10^5 A/cm^2) is obtained for NdCa2 as compared to the F doped sample (5.9×10^4 A/cm^2). It may be noted from the previous chapter that the Ce and Gd doped $NdFeAsO_{0.7}F_{0.3}$ samples showed a constant $J_C(H)$ performance above 2 T. Whereas, here at 5 K, both NdCa2 and NdMg2 show a gradually decreasing J_C above 2 T. At 20 K,

though NdCa2 excels NdMg2 in terms of J_C, a constant $J_C(H)$ performance is exhibited by NdMg2 whereas the F doped sample Nd4 undergoes sudden drop in J_C at higher fields.

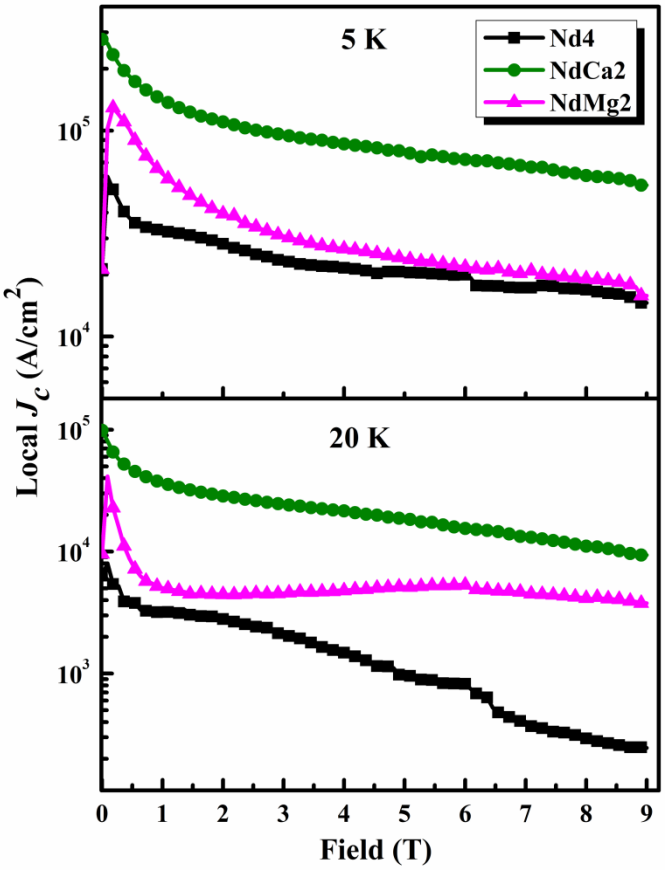

Figure 6.20: Local J_C of Nd4, NdCa2 and NdMg2 estimated using MHLs measured at 5 and 20 K

The $J_C(H)$ performance of the binary doped samples confirms that the lattice defects due to binary doping with CaF_2 and MgF_2 do create pinning centres which help in enhancing the in-field J_C of Nd4. But the pinning capability of NdCa2 and NdMg2 gradually decreases at higher fields and thus the in-field J_C is found to decrease at 5 K. At 20 K, NdCa2 follows similar behavior as observed at 5 K while the $J_C(H)$ variation of NdMg2 shows an initiation of peak effect above 4 T. However, there is an abrupt degradation in the $J_C(H)$ performance of the F doped sample Nd4 at 20 K and high fields, wherein the binary doped samples sustain a much enhanced in-field J_C. It is clear from the XRD that both F doped samples and binary doped samples contain the same kind of impurity phases which act as current blockers thereby inhibiting transport current. Besides, the $J_C(H)$ performance of Nd4 indicates that these impurity phases also give limited support to in-field J_C in the form of flux pinners. Hence, the enhanced $J_C(H)$ in binary doped samples is solely due to the combined effect of lattice defects created by the simultaneous substitution of Mg^{2+}/Ca^{2+} ions at Nd^{3+} site and O^{2-} at F^- site. Though substitutional lattice defects due to Mg^{2+}/Ca^{2+} ions at Nd^{3+} site in binary doped samples act

as better pinning centres compared to the solo substitution of fluorine in Nd4, these defects are not fully effective to maintain constant $J_C(H)$ at higher fields especially in NdCa2.

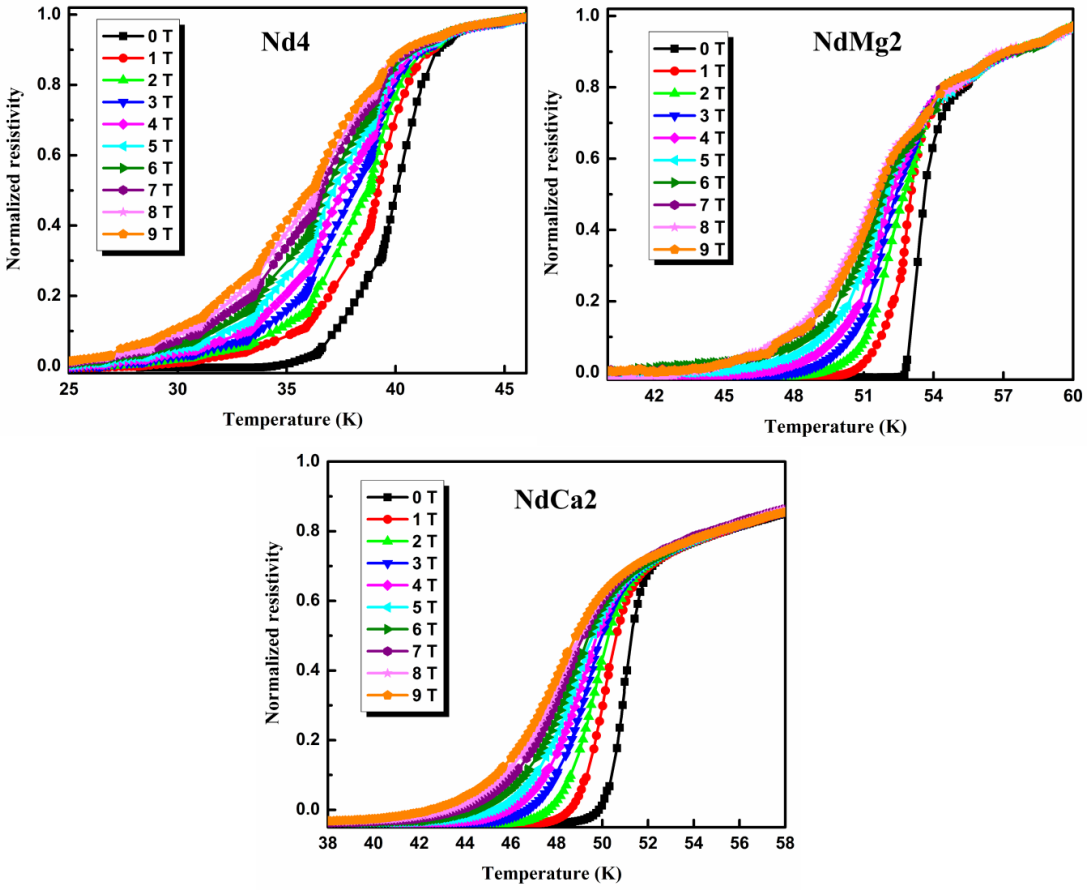

Figure 6.21: ρ-T plots of Nd4, NdCa2 and NdMg2 samples measured at fields 0-9 T

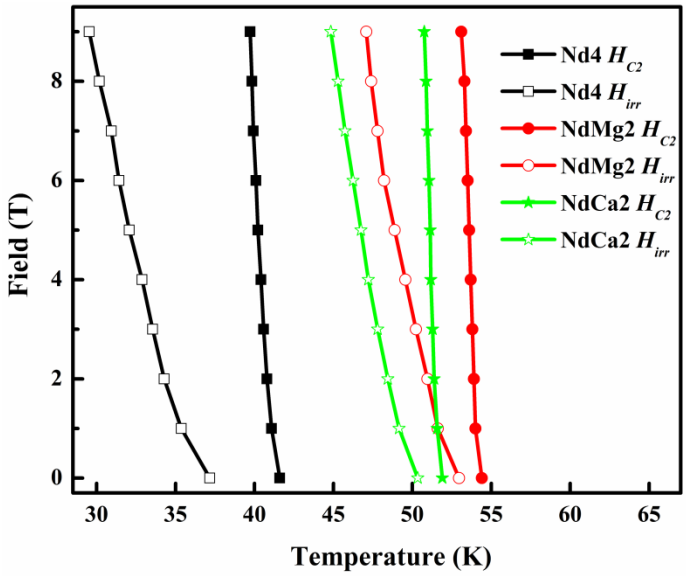

Figure 6.22: H-T phase diagram of Nd4, NdCa2 and NdMg2 samples measured at fields 0-9 T

Figure 6.21 shows the field dependent ρ-T plots of Nd4, NdCa2 and NdMg2 samples measured at fields 0-9 T. It is observed that superconducting transition at 0 T is

steeper, while on applying field there is a systematic broadening in the transition region. The rate of increase in broadening with respect to applied field determines the field withstanding capability of the superconductor, i.e. the upper critical field of the system can be estimated. An overall analysis of the ρ-T plots conclude that the broadening of transitions is maximum for Nd4, whereas it is minimized upon binary doping. This indicates the possibility of achievement of higher upper critical field, H_{C2} for the binary doped samples than the F doped one. Accordingly, the H_{C2} values were estimated using the WHH theory as detailed in the previous chapter. According to WHH theory, $H_{C2}(0) = -0.693T_C[d(H_{C2})/dT]$, the slope $d(H_{C2})/dT$ was estimated from the H-T phase diagram plotted using the 90% and 10% values of the normal state resistivity (ρ_n - normal state resistivity value just above the transition). Figure 6.22 gives the H-T plots in which the slopes of the curves corresponding to 90% ρ_n values of the samples give their respective H_{C2} values and that of 10% ρ_n values give the H_{irr} values. The slopes of H_{C2} curves obtained for Nd4, NdCa2 and NdMg2 are -4.9, -8.5 and -7.9 T/K that corresponds to H_{C2} values of 144, 310 and 300 T, respectively. Similarly, the slopes of H_{irr} curves were obtained as -1.2, - 1.6 and -1.5 T/K giving H_{irr} values of 36, 57.9 and 57.5 T, respectively. Such higher values of H_{C2} and H_{irr} again confirm the flux pinning ability of substitutional defects created by Mg^{2+}/Ca^{2+} ions at Nd^{3+} site.

6.6 Hall Effect measurement

Hall Effect measurement performed on a system having both holes and electrons as charge carriers can help in distinguishing the dominance of the type of carriers present in the system. In the present chapter, we have synthesized alkaline earth metal doped iron oxypnictides using binary dopants such as CaF_2 and MgF_2. The composition $Nd_{1-x}A_xFeAsO_{1-2x}F_{2x}$ (where A = Ca and Mg) itself gives a clear indication that the electrons imparted by fluorine doping are larger in number compared to holes created due to alkaline earth metal doping. However, a confirmation on the majority charge carriers through Hall measurement is desirable. Hence, the Hall voltage of selected samples i.e. the samples NdCa2 and NdMg2 were measured keeping the current flow and applied magnetic field mutually perpendicular. The transverse voltage is measured by sweeping the magnetic field from -9 to 9 T and Hall voltage is estimated by eliminating the longitudinal resistive contribution as discussed in *Chapter 5*. Figure 6.23 shows the field dependent transverse resistivity of the samples NdCa2 and NdMg2 measured from -9 to 9 T at 100 K. It is observed that samples exhibit negative resistivity with linear dependence on applied field. The slopes of the linear curves i.e. the Hall co-efficient (R_H) for NdCa2 and NdMg2 are

found to be -6.7 × 10^{-9} m^3/C and -5.9 × 10^{-9} m^3/C, respectively. The negative sign of the Hall co-efficient makes it clear that the dominant charge carriers are electrons. Though the values of R_H are very close, NdMg2 is having a relatively smaller R_H as compared to that of NdCa2. Thus, the estimated charge carrier density ($n = 1/eR_H$) is higher for NdMg2 (1.05 × 10^{27} /m^3) than NdCa2 (0.93 × 10^{27} /m^3). The smaller ionic size of Mg contracts the lattice which favors effective charge transfer and this can be accounted for the difference in carrier densities. The key observation is that though holes and electrons are induced deliberately through binary doping, electrons are the majority or dominant carriers in both CaF_2 and MgF_2 doped samples.

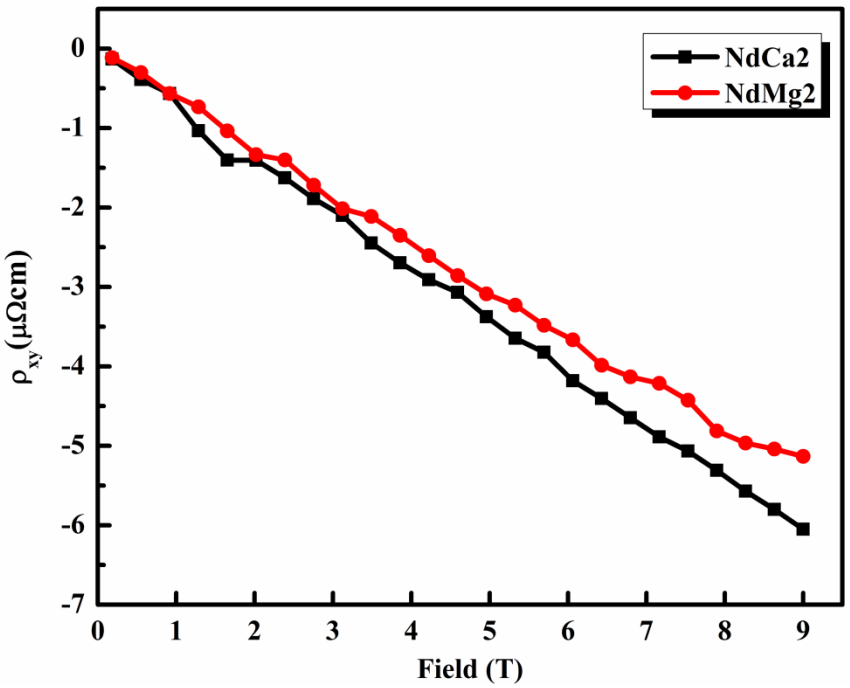

Figure 6.23: Transverse resistivity of NdCa2 and NdMg2 samples measured at 100 K

6.7 Summary and conclusions

Polycrystalline samples of F doped NdFeAsO: $NdFeAsO_{1-x}F_x$ (x = 0.3 and 0.4) and corresponding binary doped NdFeAsO: $Nd_{1-x}A_xFeAsO_{1-2x}F_{2x}$ (A = Ca, Mg; x = 0.15 and 0.2) were prepared using CaF_2 and MgF_2 as the binary dopant sources. Binary doping helped in providing a combined effect of introducing both holes and electrons into the system. Rather than the nature and density of charge carriers introduced, the use of the alkaline earth metal fluorides (CaF_2 and MgF_2) as a fluorine source refined the microstructure of the system tremendously in terms of grain size and grain connectivity along with the improvement in density and homogeneity. The preferential orientation of grains in CaF_2 doped samples was another interesting observation that needs to be further

tailored in future for application point of view. Moreover, enhanced superconducting and magnetic properties were observed for the binary doped systems as compared to the solo F doped sample. Maximum T_Cs of 52.3 and 54.7 K were observed for the binary doped samples NdCa2 and NdMg2, respectively. These samples also gave high transport J_C values of 1240 and 1150 A/cm^2 (at 12 K), respectively. The in-field J_C behavior derived through magnetization measurements and very high critical fields estimated using magneto-transport measurements also concluded that lattice defects due to binary doping acted as effective flux pinning centres.

CHAPTER 7

DEVELOPMENT OF $NdFeAsO_{1-x}F_x$ BASED CONDUCTORS IN WIRE AND TAPE FORMS

7.1 Introduction

Superconducting wire is the central and inevitable component for a wide variety of applications such as *ac* and *dc* power cables, power transformers, superconducting magnetic energy storage devices, fault current limiters, wind turbine generators etc. The low temperature superconductor Nb-Ti is still ruling the superconducting world, especially as superconducting magnets, because of its steady performance and easy fabrication both in mono and multifilamentary forms. However, the low values of T_C and H_{C2} make liquid Helium cooling mandatory and limit its application to lower fields. The limits on T_C, J_C and H_{C2} affect the maximum current and the maximum magnetic field that a superconductor can sustain which determine its value for practical applications. In view of the relatively high T_C and H_{C2} of iron based superconductors, persistent efforts towards the synthesis of phase pure $REFeAsO_{1-x}F_x$ (RE - rare earth) compounds capable of carrying high J_C are ongoing. The volatile nature of fluorine, toxicity and volatility of arsenic and high oxygen affinity of rare earths are the major hurdles. The gravity of these problems intensifies while considering the translation of these compounds into conductors suitable for practical applications. In order to evaluate the proficiency of iron based wires, the process of wire development needs to be optimized at the outset. Different wire development techniques such as coating method, diffusion, continuous tube filling and forming (CTFF) and powder-in-tube (PIT) exist for superconductors (Komori *et al.* 2002; Cunningham *et al.* 2001; Tomsic *et al.* 2007; Suo *et al.* 2001). Among these techniques, PIT technique following both *in situ* and *ex situ* methods is found to be more popular and efficient in achieving good quality wires. The *in situ* PIT method is preferred since it helps in achieving good inter-granular connectivity and makes doping of impurity elements easier to implement artificial pinning centres. On following *ex situ* method, the main issue lies with the volatility of arsenic and fluorine during the synthesis of the precursor powder which demands supplement of these elements in the form of binders (Fujioka *et al.* 2011a). However, for the successful fabrication of wires, a few critical issues are to be addressed. Firstly, superconductors that are hard and brittle in the bulk form require stabilization using a normal metal cladding intended for electrical, thermal and mechanical protection (Ma(a)

et al. 2011). After choosing the appropriate sheath metal, other processing conditions such as fabrication procedure, processing temperature and duration should be optimized to yield the best superconducting properties.

7.2 Preparation of mono-filamentary NdFeAsO$_{0.6}$F$_{0.4}$ wires

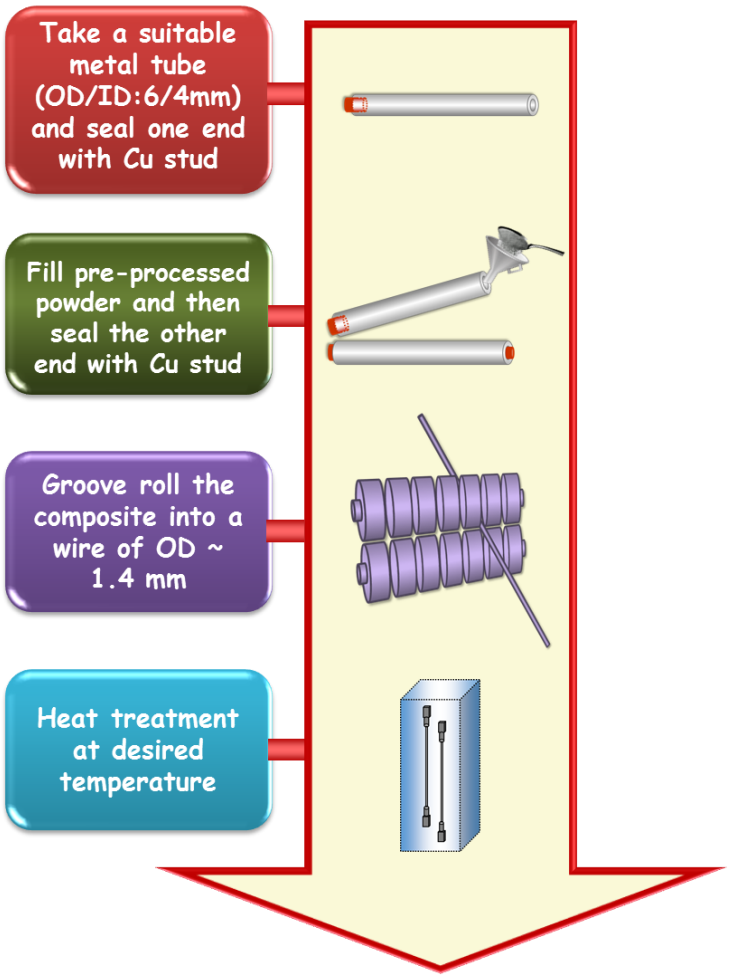

Figure 7.1: A schematic representation of the wire development procedure

The development of mono-filamentary wires has already been briefly discussed in *Chapter 3*. A schematic representation of the wire development procedure followed in the present work is given in Figure 7.1. Before initiating the wire making procedure, the precursor powder is prepared i.e. ingredients necessary for NdFeAsO$_{0.6}$F$_{0.4}$ is weighed stoichiometrically and mixed inside a glove box having inert atmosphere. The homogenous mixture is then pelletized and vacuum sealed in quartz tube. The sealed tube is then heat treated at 360 ºC for 5 h i.e. at the pre-processing temperature followed for the bulk sample preparation. The pre-processed pellet is again ground and homogenized to be used as the precursor for wire making. Then, a sheath metal tube of OD/ID (6/4 mm) is cut into an approximate length of 3 cm. One of the open ends of the tube is sealed effectively using a Cu stud. The precursor powder is then filled and compacted well in the tube. After sealing

the other end with another Cu stud, the composite is groove rolled until it reaches an outer diameter of 1.4 mm. The rolled long length wire is then cut into short pieces. The ends of the short pieces of wires are then end capped using Fe as shown in figure. The short pieces of these wires are then subjected to final heat treatment in inert atmospheres.

7.3 Optimization of sheath material and processing temperature for $NdFeAsO_{0.6}F_{0.4}$ wires

7.3.1 Introduction

In the previous section, the procedure for wire development makes it clear that for *in situ* PIT method the precursor powder can be realized into a wire only with the support of an appropriate metal cladding or sheath metal. Moreover, the sheath metal used for superconducting wires should be beyond an ordinary protective jacket. It should meet certain pre-requisites such as chemical compatibility with the superconductor, enough ductility to be drawn into thin wires and strength to withstand mechanical workability. In the present work, a set of five selected metals were used as sheath material for $NdFeAsO_{0.6}F_{0.4}$ in order to check the chemical compatibility and influence of these sheath metals on its superconducting properties. Initially, $NdFeAsO_{0.6}F_{0.4}$ wires were prepared using five different sheath metals such as Ag, Cu, Fe, Ni and SS hereafter referred as Ag, Cu, Fe, Ni and SS, respectively. Then, each metal sheathed wire was cut into three pieces of equal lengths. These short length wires were end capped and heat treated at different processing temperatures such as 850, 900 and 950 ºC, respectively.

7.3.2 Results and discussion

Samples for the x-ray diffraction (XRD) analysis were retrieved from the wires by mechanically peeling off the sheath metal and powdering the reacted core. The patterns were taken using a zero background holder. Figure 7.2 shows the XRD patterns of all the wire samples with different sheaths processed at 850 ºC for 40 h. The major phase in all the samples is indexed to be that of NdFeAsO and all the superconducting cores contain impurity phases such as FeAs and NdOF. However, it is clearly seen that except the Ag sheathed sample all the other metal sheathed samples contain impurity phases due to the sheath, that have been indexed. It is also observed that the amount of impurity phases is larger in Ni and SS sheathed samples. Thus, the XRD analyses of samples indicate that $NdFeAsO_{0.6}F_{0.4}$ is more chemically compatible to Ag sheath at elevated temperatures as compared to other sheaths.

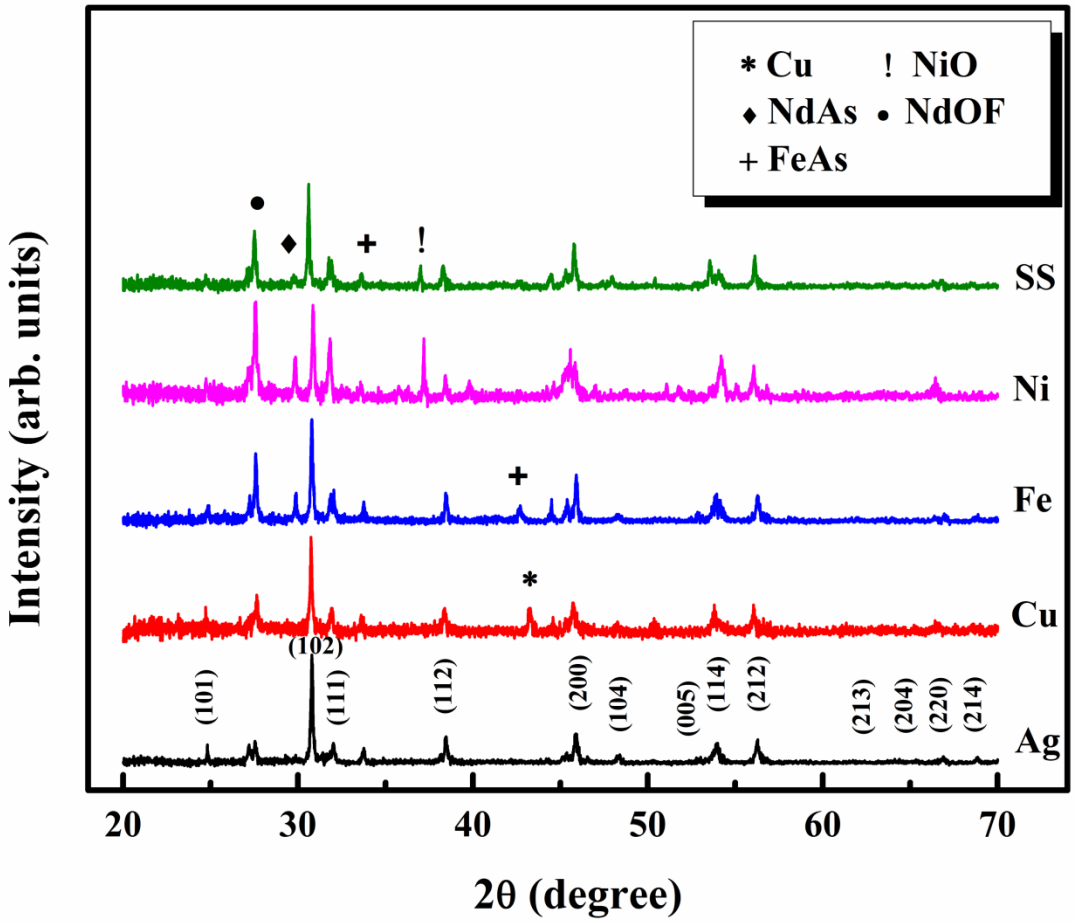

Figure 7.2: XRD patterns of different metal (Ag, Cu, Fe, Ni & SS) sheathed NdFeAsO$_{0.6}$F$_{0.4}$ samples

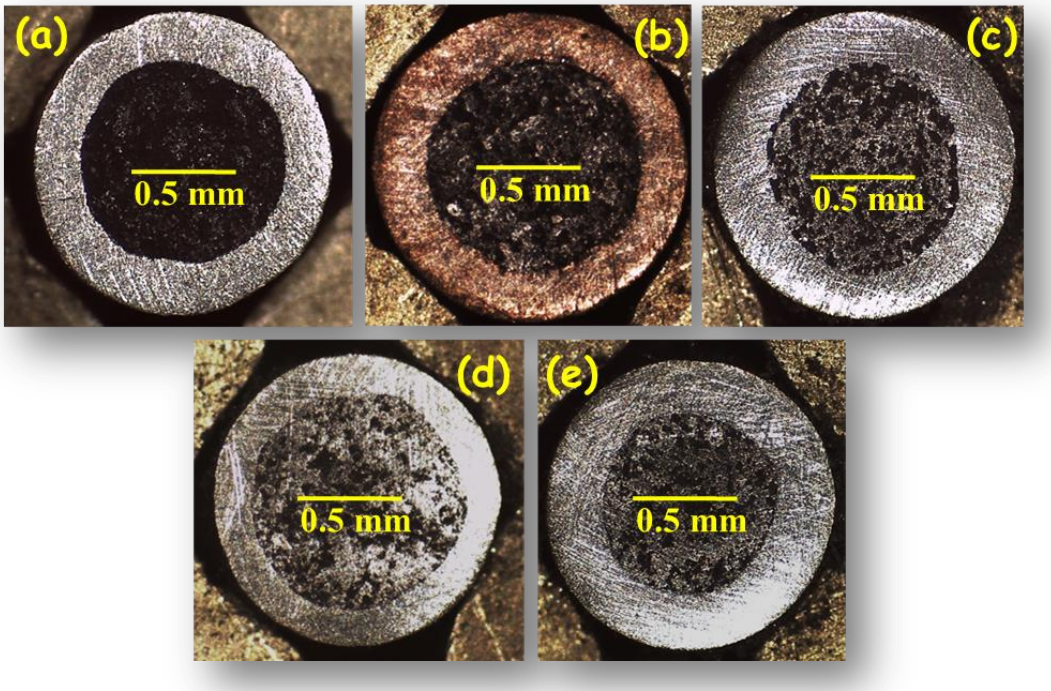

Figure 7.3: Optical images of the cross sectional area of (a) Ag, (b) Cu, (c) Fe, (d) Ni & (e) SS sheathed NdFeAsO$_{0.6}$F$_{0.4}$ wires

The optical images of the cross section of all the metal sheathed wires were also taken using an optical microscope (Leica EZ4 HD) and are shown in Figure 7.3. There is notable change in the superconducting core of the wires with respect to the outer sheath used. In Ag sheathed sample (Figure 7.3 (a)), the core is dense, black and homogeneous; while the density and homogeneity of the core are relatively poor for rest of the samples (Figure 7.3 (b)-(e)). Though significant interfacial reaction is not observed in the core-sheath boundary, the Ni and SS sheathed samples seem to have noticeable degradation of the core with respect to density and composition.

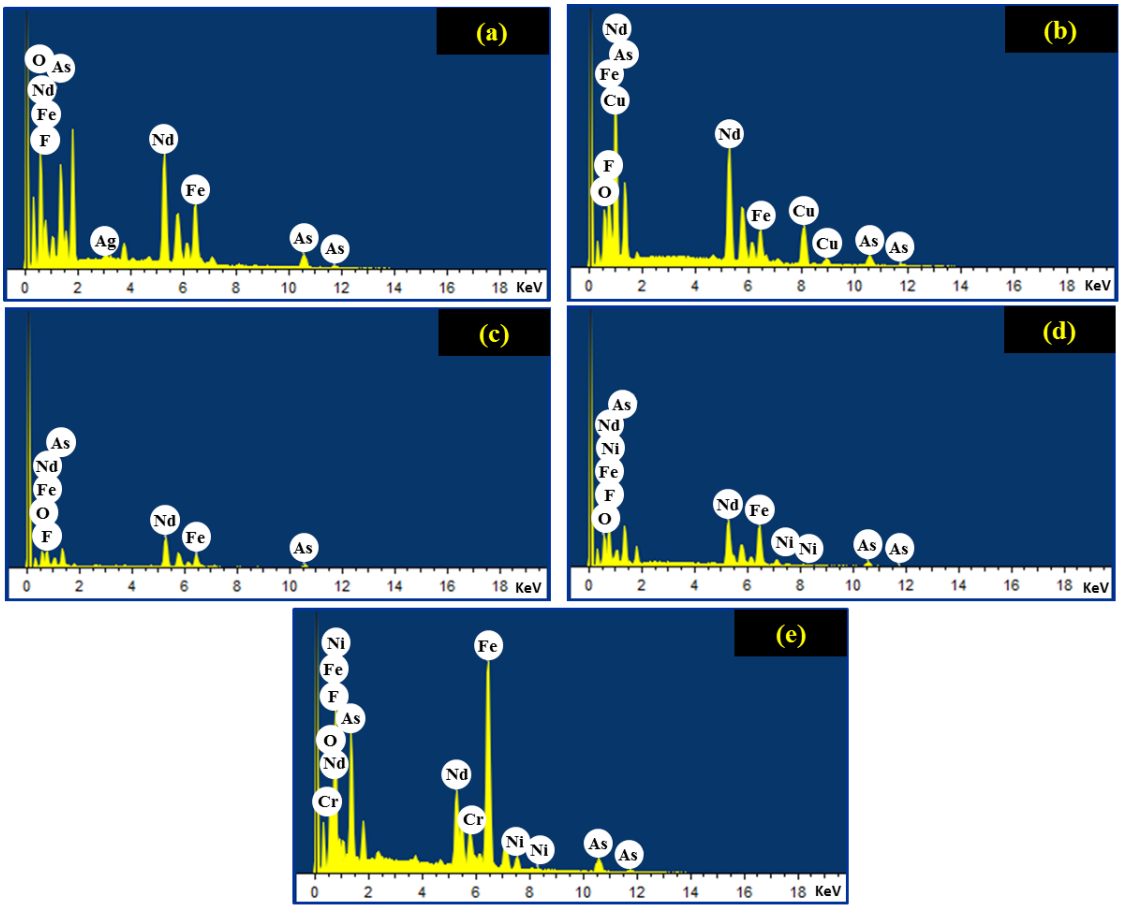

Figure 7.4: EDX of the superconducting core of (a) Ag, (b) Cu, (c) Fe, (d) Ni & (e) SS sheathed NdFeAsO$_{0.6}$F$_{0.4}$ wires

The superconducting core of the metal sheathed samples were subjected to EDX analysis to check the influence of the sheath metals on the composition of the core. The elemental analysis confirms the presence of Nd, Fe, As, O, F and the metal corresponding to the sheath. In the Ag and Fe sheathed samples (Figure 7.4 (a) and (c)), the content of Ag and Fe is found to be relatively low whereas rest of the samples show higher metal content corresponding to the sheath. The core of Ag sheathed wire shows little diffusion of Ag. Regarding the Fe sheathed wires, the diffusion of Fe is not expected to have adverse effects

on the superconductivity since Fe is an ingredient of the core itself. However; in Cu, Ni and SS sheathed wires the metal diffusion is relatively high. In SS sheathed samples, the presence of 8-10 wt% of Ni and 18-20 wt% Cr in SS can influence the superconducting properties of the SS sheathed wires. The presence of Ni and SS is well observed in the EDX spectrum which confirms the diffusion from SS into the core.

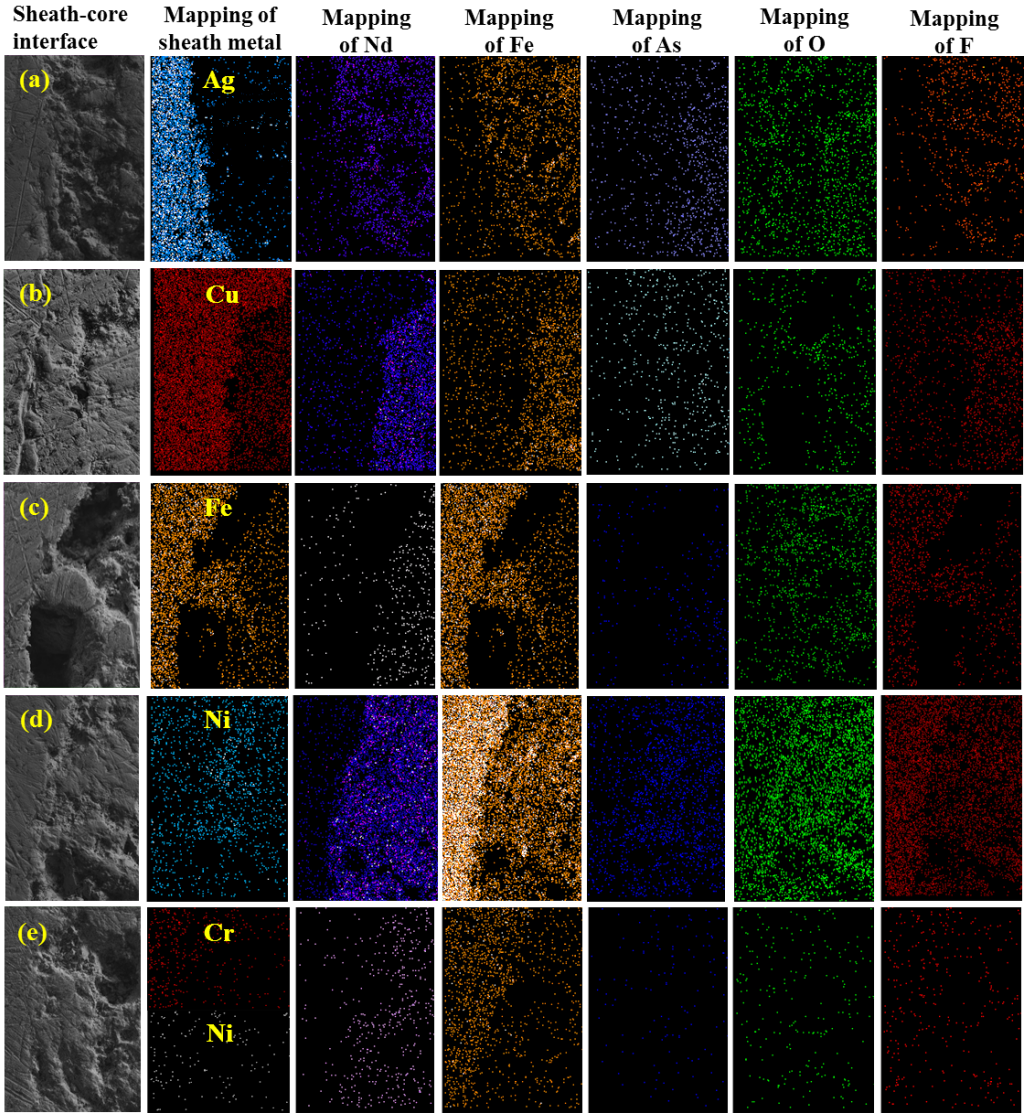

Figure 7.5: SEM images of the core sheath interface and mapping of the compositional elements near the boundary region of (a) Ag, (b) Cu, (c) Fe, (d) Ni & (e) SS sheathed NdFeAsO$_{0.6}$F$_{0.4}$ wires

Figure 7.5 shows the SEM images taken near the sheath-core boundary and the mapping of the constituent elements based on the EDX taken in that region. The coloured dot mapping on a black background is a convenient technique to represent the spatial distributions and local enrichments of the individual elements. Here, the coloured dots denote the presence of the element being mapped and the black background indicates its absence. According to the prerequisites for a metal to be considered as an appropriate

sheath for a superconductor, the chemical compatibility especially its inertness to the constituent elements is very essential. Hence, in the present analysis, it is preferred that the sheath metal distribution should be restricted in the sheath area and the $NdFeAsO_{0.6}F_{0.4}$ phase or specifically the elements must be distributed only in the core area. The diffusion of either of them into the other area is undesirable. In the case of Ag sheathed sample (Figure 7.5 (a)), mapping of the sheath metal i.e. shows a clear distribution of Ag along the sheath area and there is only a little presence of Ag within the core. Though Ag is a low melting metal, its diffusion into the core is minimal and similar is the case with metallic elements such as Nd and Fe. However, the distribution of the metalloid As, and non-metals such as O and F are found to be more even at both core and sheath area. This may be due to the volatile nature of As and F, the formation of an oxide on the metal area, and even due to smudging of the compound on the sheath area caused while polishing the cross section for the analysis. In the Cu and Fe sheathed samples (Figure 7.5 (b) and (c)), the distribution of the respective metal is denser in the sheath area while it is rarer in the core area. In Fe sheathed sample, the Fe distribution in the core is not solely due to the interdiffusion of the sheath into the core. Fe is present as an ingredient of the compound within the core and the chances of forming FeAs on the sheath are also significantly high. In, Ni and SS sheathed samples (Figure 7.5 (d) and (e)), there is no clear variation in the spatial distribution of the metal that distinguishes the core from the sheath. For SS sheathed samples, both Ni and Cr distribution has been mapped based on their presence in the EDX spectrum. The mapping of the constituent elements and sheath metals on the sheath-core boundary thus confirms interdifussion of the metals which is relatively high in Ni and SS sheathed samples. Ag, Cu and Fe sheathed samples are found to be relatively better, with Ag sheath being the best in terms of sheath metal diffusion into the core. The effect of the sheath diffusion into the core on the transport properties can be analysed only through superconducting characterizations.

In order to evaluate the influence of these sheath metals on the superconducting properties of $NdFeAsO_{0.6}F_{0.4}$ wires, the resistivity and transport I-V measurements were also done. The temperature dependent resistivity plots of the metal (Ag, Cu, Fe, Ni and SS) sheathed $NdFeAsO_{0.6}F_{0.4}$ wires processed at three different temperatures 850, 900 and 950 ^oC are shown in Figure 7.6 (a), 7.6 (b) and 7.6 (c), respectively. It is observed that the emergence of superconductivity is observed only in Fe and Ag sheathed samples whereas all the other samples are found to be nonsuperconducting and show metallic behavior down to the lowest measurement temperature. The Fe sheathed sample processed at 850 ^oC

does not show perfect superconductivity i.e. zero resistance, instead it shows a tendency of superconducting transition. While Fe sheathed samples processed at 900 ºC and 950 ºC are superconducting with a T_C around 33 K, Ag sheathed $NdFeAsO_{0.6}F_{0.4}$ wires processed at 850 ºC and 900 ºC show an onset T_C of 57 K and 55 K, respectively which are higher than the T_C obtained for the corresponding bulk samples. On increasing the processing temperature of the Ag sheathed sample to 950 ºC, a double step transition is observed in the ρ-T plot, which is unfavourable for the ampacity of the conductor.

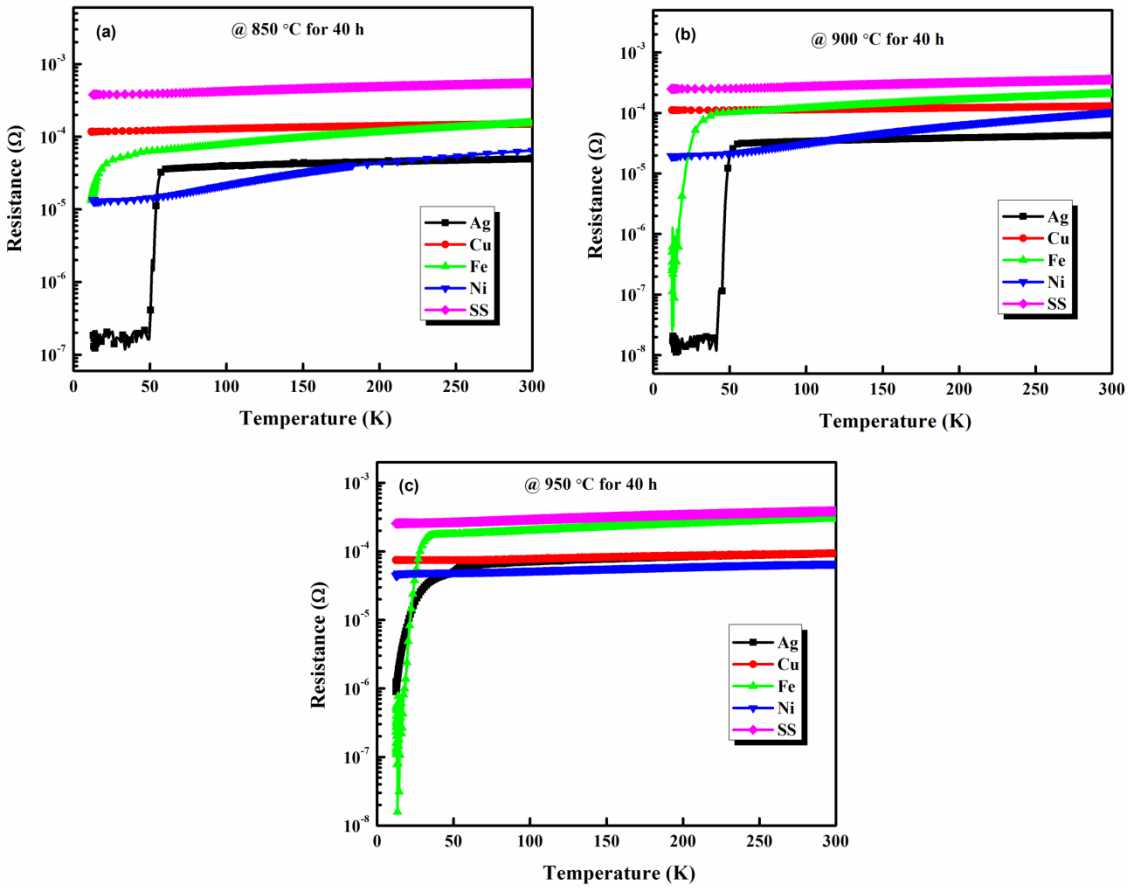

Figure 7.6: R-T plots of Ag, Cu, Fe, Ni and SS sheathed $NdFeAsO_{0.6}F_{0.4}$ wires processed at (a) 850 (b) 900 and (c) 950 ºC

The Ag and Fe sheathed superconducting wires were then subjected to I-V measurements at 12 K and the results are shown in Figure 7.7. The critical current I_C of the samples were determined on the basis of the standard 1 μV/cm criterion. The critical currents, I_Cs of 25, 28 and 13 A were measured in Ag sheathed samples processed at 850, 900 and 950 ºC, respectively. This corresponds to a critical current densities J_Cs ($J_C = I_C/A$ where A is the cross sectional area of the superconducting core) of 3250, 3640 and 1690 A/cm^2, respectively. The T_C and J_C values obtained for the wire samples are higher than the bulk samples having the same stoichiometry. However, the I_C values (~ 2 A) and the

corresonding J_C values (260 A/cm^2) obtained for the Fe sheathed wires processed at both 900 and 950 ºC are much lower as compared to the Ag sheathed samples. The influence of Fe sheath metal on the phase formation i.e. the formation of the secondary phase FeAs (as observed in XRD) is presumed to be the major reason for the decrease in superconducting volume fraction, thereby affecting the T_C. Moreover, FeAs acts as a current blocking wet phase which results in the substantial decrease of I_C. Whereas Ag sheath remains chemically inert to $NdFeAsO_{0.6}F_{0.4}$ and supports relatively high J_C as compared to Fe sheathed wires. Nevertheless, higher processing temperature makes Ag sheath more permeable causing heavy volatile loss of fluorine and secondary phase formation. Thus, both T_C and I_C values are found to depreciate, at a processing temperature of 950 ºC.

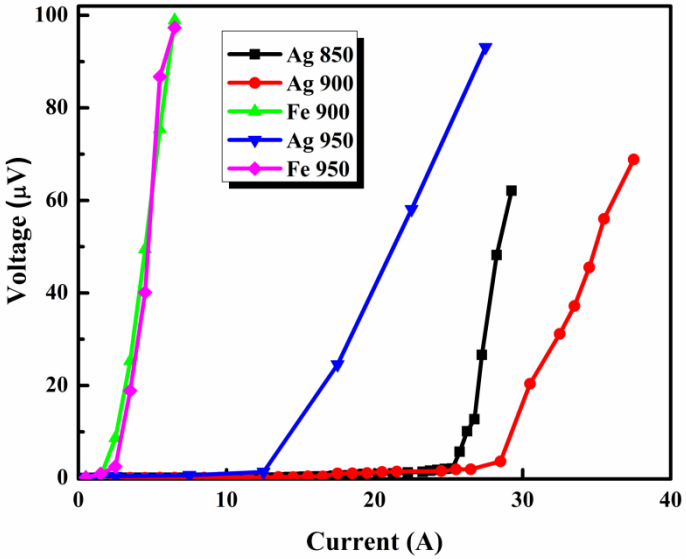

Figure 7.7: I-V plots of Ag and Fe sheathed $NdFeAsO_{0.6}F_{0.4}$ wires processed at 850, 900 and 950 ºC

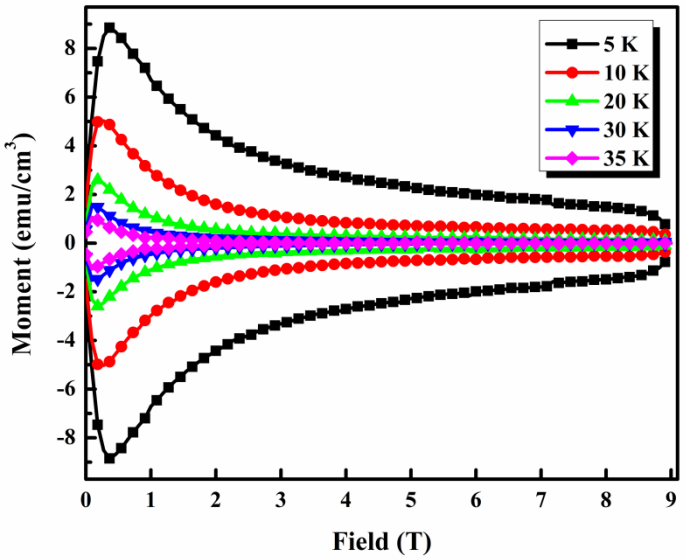

Figure 7.8: M-H plots of Ag sheathed $NdFeAsO_{0.6}F_{0.4}$ measured at different temperatures

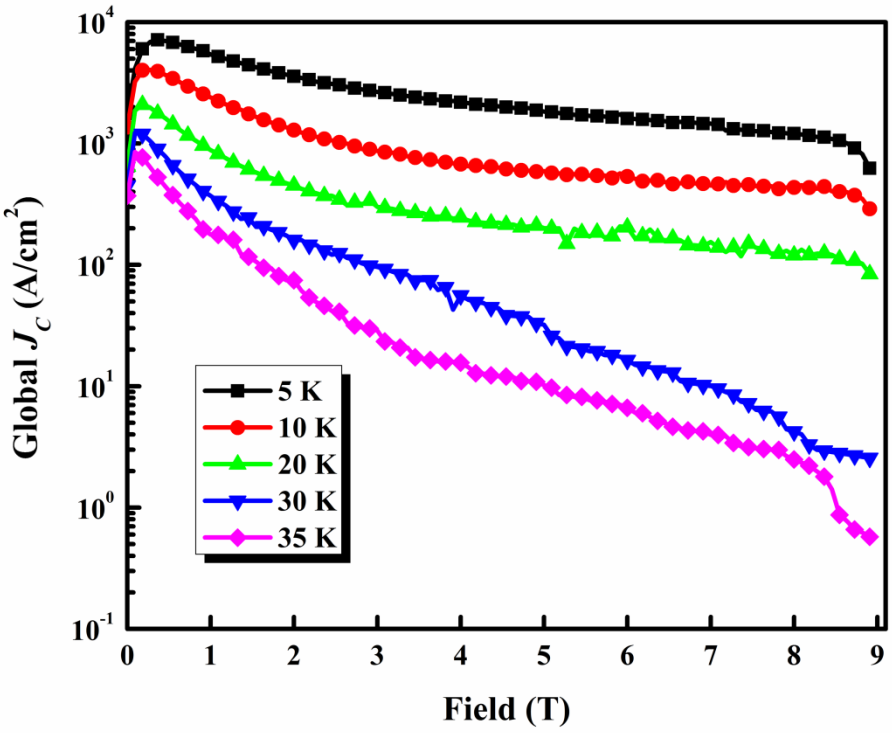

Figure 7.9: J_C-H plots of Ag sheathed NdFeAsO$_{0.6}$F$_{0.4}$ measured at different temperatures

The magnetic measurements of Ag sheathed NdFeAsO$_{0.6}$F$_{0.4}$ sample with maximum transport J_C were also conducted at different measurement temperatures 5, 10, 20, 25, 30 and 35 K. The paramagnetic background subtracted M-H curves are given in Figure 7.8. The width of the hysteresis loops is larger at lower temperatures and systematically narrows down with increase in measurement temperature. This decrease in loop width signifies the decrease in bulk vortex pinning with increasing temperature. Moreover, the loop width is broader at self-field and has a sharp decrease on increasing the field. Above 4 T, the magnetic moment remains almost constant up to 9 T. The critical current density derived from the M-H loop using Bean's Critical state model is also shown in Figure 7.9. The global J_C estimated for the sample shows a sudden decrease on increasing the field, however, the $J_C(H)$ behavior is almost constant above 4 T for the measurements up to 20 K. At higher measurement temperatures, the J_C shows severe degradation with respect to field. The maximum magnetic J_C obtained for Ag sheathed NdFeAsO$_{0.6}$F$_{0.4}$ wire at 5 K is around 7000 A/cm^2. This magnetic J_C is much higher than that observed in bulk NdFeAsO$_{0.6}$F$_{0.4}$ at 5 K (*Chapter 4*). The metal sheath has helped in reducing the volatile loss of fluorine and arsenic and has also improved the density. But, there is still a difference between magnetic J_C and transport J_C which is mainly due to the electromagnetic granularity or weak links at grain boundaries created by wet phases such as FeAs and impurity phases such as NdOF.

7.3.3 Conclusions

The influence of reactivity of selected sheath metals such as Ag, Cu, Fe, Ni and SS on both the structural and superconducting properties of $NdFeAsO_{0.6}F_{0.4}$ was investigated. Fe and Ag metals were found to be chemically compatible sheath materials for $NdFeAsO_{0.6}F_{0.4}$ wires supporting the occurrence of superconductivity. However, Ag sheath stands superior in terms of chemical inertness and mechanical workability which helps in exhibiting the maximum T_C and supports the maximum possible J_C as compared to other sheath metals.

7.4 Effect of metal addition on the transport properties of $NdFeAsO_{0.6}F_{0.4}$ tapes

7.4.1 Introduction

The achievement of high transport critical current density is of immense significance in view of conductors for practical applications. But, iron pnictides including the RE1111 systems are found to be inferior in terms of transport J_C when compared to the J_C derived using magnetization measurements. The ostensible reasons for this substantial difference between the transport and magnetic J_C is the formation of impurity phases such as FeAs, REAs and REOF which create current blocking networks, the inherent electromagnetic granularity and weak link behavior which again reduces the inter-grain coupling at the grain boundaries. The XRD results, magnetization measurements and the double step transition in *ac* susceptibility plots (presented in the *previous chapters)* evidence the same. Also, the volatile loss of fluorine decreases the inherent T_C of the system which also indirectly limits the transport J_C. The highest transport J_C reported for RE1111 system without any binder or chemical addition is 1.3×10^3 A/cm^2 at 4.2 K (Wang(d) *et al.* 2010). Though iron pnictides have very high upper critical fields, the lower transport J_C is a constraint in their development as practically viable conductors.

The possible ways to circumvent the issues inhibiting transport J_C include the addition of excess ingredients that are prone to volatile loss or the addition of selective chemical dopants that prevent the volatile loss and simultaneously form phases favorable in enhancing the current networking between the superconducting grains. From the age of high T_C superconductivity, there exists a practice of using metal additives having relatively low melting point and high conductivity, for instance, metals such as Ag, Pb, and Cu depending upon their reactivity with the superconducting compound and compatibility with the sheath in case of conductors such as wires and tapes (Gao *et al.* 1992; Neson *et al.* 2011). In the previous *Section 7.3*, it was observed that both Fe and Ag are suitable

candidates as sheath metals. But, Fe sheathed wires were found to have relatively low T_C and transport J_C. In this context, we made an attempt to incorporate certain metal additives such as Mg, Sn and Pb, which may enhance the transport properties of Fe sheathed $NdFeAsO_{0.6}F_{0.4}$ in tape geometry. But the preliminary studies showed that Mg and Pb addition destroyed the superconductivity in $NdFeAsO_{0.6}F_{0.4}$, while Sn addition showed encouraging results. Hence, the present section discusses only the effect of Sn addition on the transport properties of Fe sheathed $NdFeAsO_{0.6}F_{0.4}$ tapes.

7.4.2 Preparation procedure of Sn added Fe sheathed $NdFeAsO_{0.6}F_{0.4}$ tapes

The preparation of Sn added Fe sheathed mono-filamentary wires basically follow the same scheme as detailed in *Section 7.2*. Then, the required amount of Sn powder was weighed according to the wt% of Sn. The $NdFeAsO_{0.6}F_{0.4}$ powder processed at 360 ºC was then ground and homogenously mixed along with the Sn filings. This precursor powder was then filled in Fe tubes (OD/ID: 6/4 mm). The tubes were then groove rolled in to wires having an outer diameter of 1.4 mm following which the wires were flat rolled with an average thickness of 0.7 mm. For Sn added Fe sheathed $NdFeAsO_{0.6}F_{0.4}$ samples, 10, 20, and 30 wt% of Sn were added to the pre-processed $NdFeAsO_{0.6}F_{0.4}$ and labeled as Nd4Sn1, Nd4Sn2 and Nd4Sn3, respectively. As a reference, Fe sheathed $NdFeAsO_{0.6}F_{0.4}$ without Sn was also prepared identically and labeled as Nd4. The short length pieces of these tape samples were end capped and heat treated at 900 ºC for 40 h under inert atmosphere. The samples were then subjected to transport measurements such as ρ-T and I-V. The Sn added $NdFeAsO_{0.6}F_{0.4}$ sample, retrieved by peeling of the sheath metal, was subjected to XRD analysis.

7.4.3 Structural and transport properties of Sn added $NdFeAsO_{0.6}F_{0.4}$/Fe tapes

Figure 7.10 shows the temperature dependent resistivity of pure and Sn added $NdFeAsO_{0.6}F_{0.4}$ tapes and the inset shows the enlarged view around T_C. All the samples show metallic behavior down to their respective transition temperatures. The normal state resistivity of Sn added tapes are found to be relatively lower than that of the pure sample. However, the 30 wt% Sn added sample shows an increase in normal state resistivity, still lower than the pure sample. The relatively low electrical resistivity of Sn is presumed to be the reason for the decrease in normal state resistivity of the tapes. It is also observed that the pure sample Nd4 shows a T_C of 42.2 K; while the Sn added samples Nd4Sn1 and Nd4Sn2 have transitions at 49.3 and 52.5 K, respectively. On 30 wt% addition of Sn, the T_C was found to drop and the sample did not reach zero resistance. The transition width is

also found to increase on increasing Sn addition above 10 wt%. The maximum T_C observed in Sn added tape (52.5 K) is comparable to the T_C (52 K) obtained for the bulk sample with the same stoichiometry (*Chapter 4*). Though Sn addition is not causing a remarkable T_C enhancement, it is definitely assisting the system in maintaining a relatively high T_C by controlling the volatile loss of fluorine. Nevertheless, besides T_C enhancement, the influence of Sn incorporation on the transport current is of higher concern.

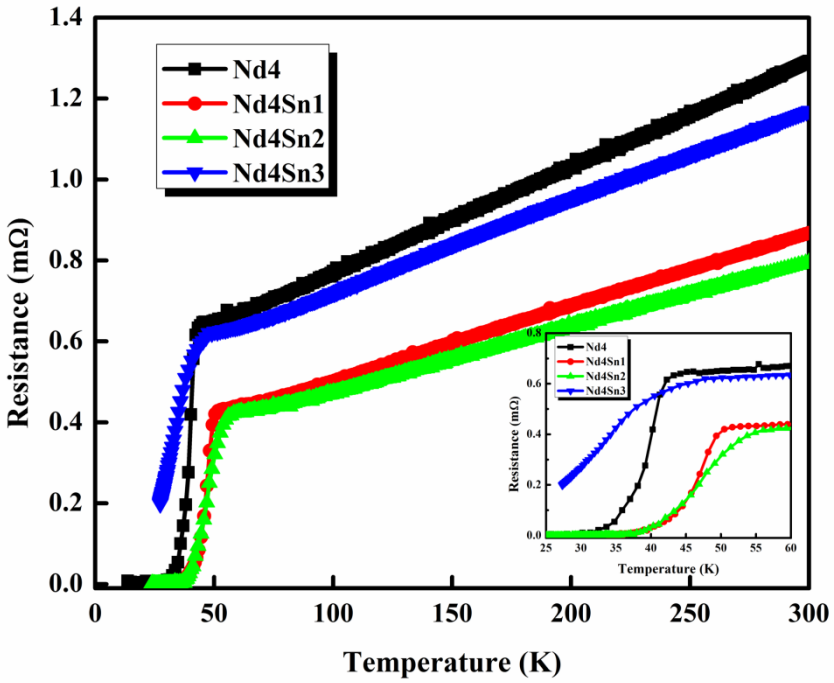

Figure 7.10: R-T plots of Fe sheathed NdFeAsO$_{0.6}$F$_{0.4}$ tapes with varying Sn addition

The transport I-V measurements of Sn added Fe sheathed tape samples were carried out at 12 K and the I-V characteristics are shown in Figure 7.11. Since the sample with 30 wt% Sn addition did not give a zero resistance, its I-V measurement was not taken. The I-V characteristics of the rest of the samples taken in self-field shows that the Sn added samples (both 10 and 20 wt%) transport higher critical currents as compared to the pure sample. In the pure tape sample (Nd4), the I_C obtained is 4 A which is higher than that of the same sample in the wire form, ~ 2 A (*given in Figure 7.6, Section 7.3.1*). The corresponding J_C is found to be 660 A/cm^2. The increase in transport J_C may be due to the flat rolling undergone during tape fabrication which improves the density of the sample. Moreover, the flat rolling enables the misoriented grains to align along the rolling direction. Upon Sn addition, the critical currents and corresponding J_C are found to increase significantly. The transport I_C values for 20 and 30 wt% Sn added samples are found to be 8 and 11.8 A, respectively. The corresponding transport J_C (J_C = I_C/A, where 'A' is the cross sectional area of the superconducting core of the tape) values of the pure

and Sn added samples are found to be 1330 and 1960 A/cm^2, respectively. The formation of liquid phase such as $FeSn_2$ helps in reducing current blocking wet phases such as FeAs, thereby facilitating better grain-to-grain connectivity. Though the maximum transport J_C achieved is not high as compared to the Ag sheathed wire samples, the relative increase in J_C due to Sn addition using an inexpensive sheath metal Fe is promising.

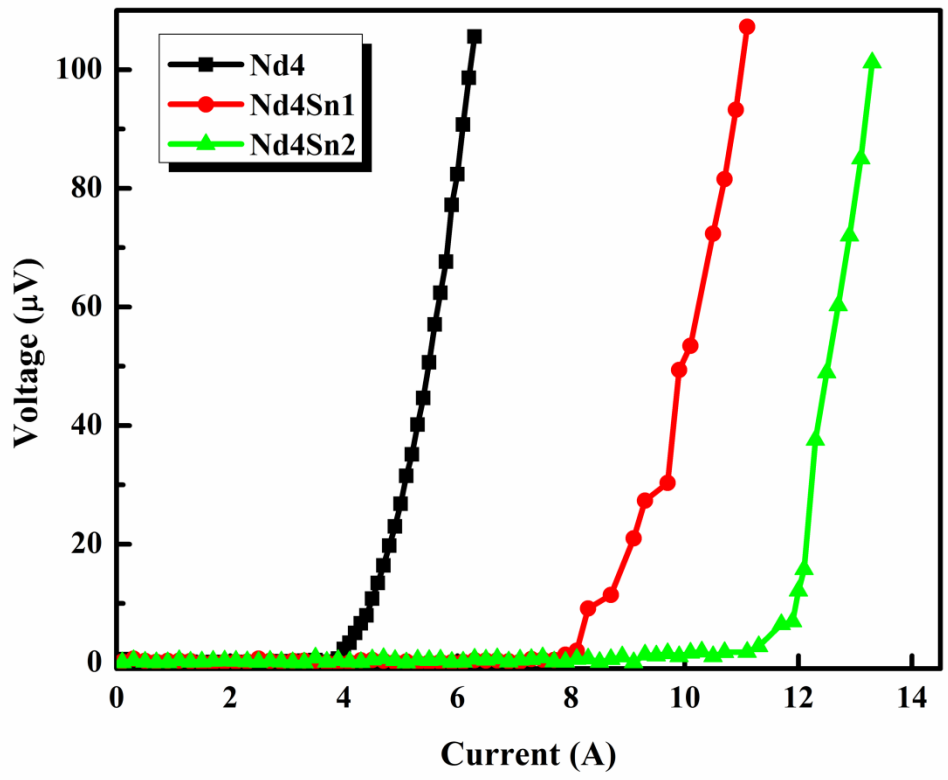

Figure 7.11: I-V plots of Fe sheathed NdFeAsO$_{0.6}$F$_{0.4}$ tapes with varying Sn addition

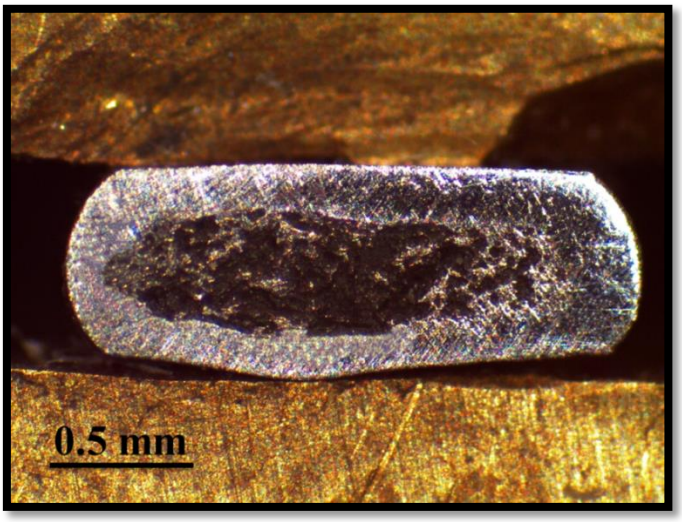

Figure 7.12: Optical image of the cross sectional area of the 20 wt% Sn added NdFeAsO$_{0.6}$F$_{0.4}$ tape

Figure 7.12 shows the optical image of the cross sectional area of Sn added $NdFeAsO_{0.6}F_{0.4}$ tape, i.e. Nd4Sn2 which exhibited the highest T_C and transport J_C. The

core-sheath boundary is very distinct. The presence of fused metal (Sn) can be observed as shiny patches within the core and at boundary regions. The black dense area represents NdFeAsO$_{0.6}$F$_{0.4}$ matrix. Figure 7.13 shows the XRD pattern of the superconducting core retrieved from the tape sample (Nd4Sn2 i.e. 20 wt% Sn added sample) taken on a zero background holder. The major phase belongs to that of NdFeAsO. The secondary phases such as NdAs, $FeSn_2$ and NdOF can be observed. The presence of Fe is also very prominently observed; due to the Fe sheath used for tape fabrication.

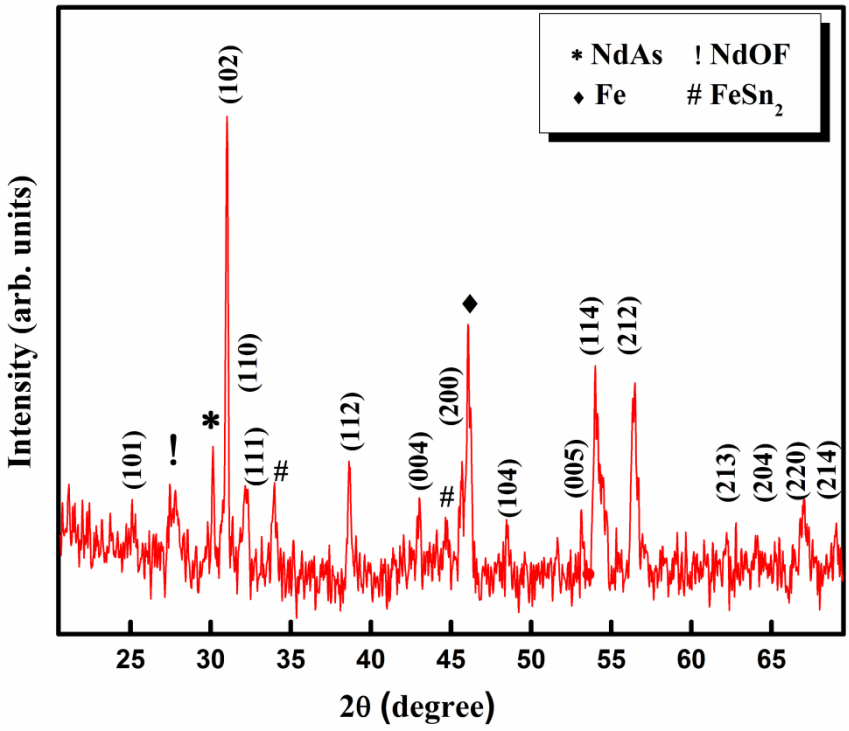

Figure 7.13: XRD pattern of the 20 wt% Sn added NdFeAsO$_{0.6}$F$_{0.4}$ tape

7.4.4 Conclusions

Fe sheathed NdFeAsO$_{0.6}$F$_{0.4}$ tapes were developed successfully with varying wt% (10, 20 and 30) of Sn addition. 20 wt% of Sn addition exhibited the maximum T_C and transport J_C. The addition of Sn is found to decrease the weak links between grain boundaries and has helped in preventing excessive fluorine loss, thus improving the transport properties.

7.5 Summary

As an initial step towards conductor development, a detailed study on sheath reactivity with NdFeAsO$_{0.6}$F$_{0.4}$ was carried out using selected sheath metals such as Ag, Cu, Fe, Ni and SS at different processing temperatures. Fe and Ag were identified as possible candidates as sheath metals supporting the superconductivity in NdFeAsO$_{0.6}$F$_{0.4}$.

Ag sheath exhibited commendable chemical compatibility and the best superconducting properties at a processing temperature of 900 ºC. After fixing the sheath and processing temperature, an effort towards improving the transport properties of $NdFeAsO_{0.6}F_{0.4}$ in tape geometry, through selective metal addition was also done. Addition of 20 wt% Sn in Fe sheathed $NdFeAsO_{0.6}F_{0.4}$ tape displayed the maximum transport J_C. Sn addition was found to form a liquid phase $FeSn_2$ which could help in preventing excessive volatile loss of fluorine and channelizing current flow at grain boundaries. However, systematic and persistent investigations are essential to make Nd1111 based conductors fit for practical applications.

CHAPTER 8

SUMMARY AND CONCLUSIONS

8.1 Summary

The thesis mainly focuses on the synthesis of the $NdFeAsO_{1-x}F_x$ based iron pnictides at ambient conditions and the studies on their structural, transport and magnetic properties. Nd1111 based compounds were reported to exhibit better properties on being synthesized at an applied pressure of about 6 GPa and temperatures around 1300 ºC. Hence, the main objective of the thesis was to prepare good quality $NdFeAsO_{1-x}F_x$ at relatively low processing temperature and ambient pressure. Further, to enhance the inherent transport and magnetic properties which are embodied by critical factors such as T_C, J_C and H_{C2} through the incorporation of appropriate dopants. The realization of $NdFeAsO_{1-x}F_x$ based wires and tapes suitable for practical applications was also assumed as a significant objective due to the inferior status of conductor development.

The volatile loss of fluorine and the apparent difference between the real and nominal content of fluorine is reported to affect the transport properties of Nd1111. Hence, optimizing the fluorine content has become the prime initiative. The first chapter deals with the influence of fluorine variation on the structural and superconducting properties $NdFeAsO_{1-x}F_x$ with x = 0, 0.1, 0.2, 0.3 and 0.4. The Nd1111 compounds of varying fluorine concentration were synthesized using a pre-processing technique developed by our group and subjected to structural, transport and magnetic characterizations.

After identifying the stoichiometry which yielded the maximum T_C (here x = 0.3), chemical doping at rare earth site was attempted using selected isovalent rare earth dopants such as Yttrium (Y), Cerium (Ce) and Gadolinium (Gd) with an aim to further enhance T_C, J_C and H_{C2}. Thus, the compound $NdFeAsO_{0.7}F_{0.3}$ was doped at rare earth site and the doped variants $Nd_{1-x}RE_xFeAsO_{0.7}F_{0.3}$ (where RE = Y, Ce and Gd) were characterized to analyze the effect of single site doping on the structural and superconducting properties.

Besides isovalent doping, simultaneous doping at two sites i.e. binary doping at Nd and O sites with a single source was also tried. For this, alkaline earth metal fluorides such as CaF_2 and MgF_2 were considered so as to incorporate Ca^{2+}/Mg^{2+} ions and F^- ions at Nd^{3+} and O^{2-} sites, respectively. Since the alkaline earth metal ion has a difference in valency as compared to Nd^{3+} ions, binary doping changes the charge carrier concentration along with the creation of defects. Thus, the influence of binary doping on the structural and magneto-transport properties of $Nd_{1-x}A_xFeAsO_{1-2x}F_{2x}$ (x = 0.15 and 0.2) was investigated.

On an application point of view, an effort towards conductor development was also made. As an initial step towards wire fabrication, a sheath reactivity study was done to identify a metal sheath suitable for $NdFeAsO_{1-x}F_x$ based compounds in terms of chemical compatibility, mechanical workability and influence on transport properties. The metals such as Ag, Fe, Cu, Ni and SS were tried and their influence on $NdFeAsO_{0.6}F_{0.4}$ was studied. Among these, Ag and Fe were found to be promising and hence these were chosen as outer sheath for further studies on $NdFeAsO_{0.6}F_{0.4}$ based conductors. In order to enhance the transport J_C, selected low melting metal additives such as Mg, Pb and Sn were chosen. Among which Sn addition was found to be favorable and thus Fe sheathed $NdFeAsO_{0.6}F_{0.4}$ tapes with varying wt% of Sn addition were fabricated. Both the wire and tape samples were characterized by transport and magnetic measurements.

8.2 Conclusions

- *Polycrystalline samples of $NdFeAsO_{1-x}F_x$ (Nd1111) with x = 0, 0.1, 0.2, 0.3, and 0.4 were synthesized using a pre-processing technique at ambient pressure. The transport and magnetic properties observed for each stoichiometry showed remarkable correlation with their corresponding structural and microstructural aspects.*
- *A maximum transition temperature (T_C) of 52.0 K and a transport J_C of 1050 A/cm^2 at 12 K were observed for x = 0.3 and 0.4, respectively. Moreover, the superconducting properties exhibited in this material, processed at a relatively low temperature of 1000 °C, are competitive as compared to the existing reports wherein high pressures/temperatures are inevitable.*
- *Selected rare earths such as Yttrium (non 4f element) and 4f elements such as Cerium and Gadolinium having ionic radii in the order Ce > Nd > Gd were doped at Nd^{3+} site in $Nd_{1-x}RE_xFeAsO_{0.7}F_{0.3}$ in order to enhance the critical parameters such as T_C, J_C and H_{C2}.*
- *The transition temperatures of the yttrium doped samples were found to increase monotonically with increase in Y and attained a maximum of 53.3 K for 30% yttrium doping i.e. x = 0.3. Yttrium doping is found to decrease the lattice parameters of the system; causing an inner chemical pressure and thereby accomplishing a T_C enhancement.*

- *The substitution of relatively smaller yttrium ion at Nd site also created lattice defects which act as effective pinning centers thereby enhancing the $J_C(H)$ performance of the system.*
- *The influence of 4f rare earth doping at Nd site in $NdFeAsO_{0.7}F_{0.3}$ superconductor was also investigated wherein Ce and Gd have ionic radii in the order Ce > Nd > Gd. It was observed that Ce doping enhances the T_C of $Nd_{1-x}RE_xFeAsO_{0.7}F_{0.3}$ to a maximum of 53.6 K at x = 0.1 while Gd doping attains a T_C of 55.1 K at x = 0.15.*
- *The relatively small ionic size of Gd and yttrium cause lattice shrinkage helping in effective charge transfer between the charge reservoir and conducting layers, whereas the multivalent nature of Ce is found to enhance the charge density; both of which result in T_C enhancement.*
- *The lattice defects due to Y, Ce and Gd doping at Nd site, irrespective of their ionic size, assisted in effective pinning of the flux lines thereby exhibiting an enhanced $J_C(H)$ performance especially at high fields. Very high upper critical fields of 335 and 360 T were also estimated for Gd and Ce doped samples, respectively.*
- *Polycrystalline samples of $Nd_{1-x}A_xFeAsO_{1-2x}F_{2x}$ (A = Ca & Mg) superconductors were also synthesized by simultaneous doping of holes and electrons at Nd^{3+} and O^{2-} sites with Ca^{2+}/Mg^{2+} and F^-, respectively, using CaF_2 and MgF_2 as binary dopants.*
- *Alkaline earth metal fluorides used as binary dopants not only introduced a change in charge carrier concentration but also refined the microstructure of the system tremendously in terms of grain size and grain connectivity along with the improvement in density and homogeneity. The preferential orientation of grains in CaF_2 doped samples was another interesting observation that needs to be further tailored in future for application point of view.*
- *Enhanced superconducting and magnetic properties were also observed for the binary doped systems as compared to the solo F doped sample. Maximum T_Cs of 52.3 and 54.7 K were observed for the binary doped samples NdCa2 and NdMg2, respectively. These samples also gave high transport J_C values of 1240 and 1150 A/cm^2 (at 12 K), respectively.*

- *The $J_C(H)$ behavior derived through magnetization measurements and very high critical fields (~ 300 T) estimated using magneto-transport measurements also concluded that lattice defects due to binary doping acted as effective flux pinning centres.*

- *For the development of $NdFeAsO_{0.6}F_{0.4}$ based wires, the sheath reactivity and temperature optimization studies were conducted. Five different sheath metals such as Ag, Fe, Cu, Ni and SS were chosen and the metal sheathed wires were processed at 850, 900 and 950 ºC. Fe and Ag sheathed wires were found to support superconductivity in $NdFeAsO_{0.6}F_{0.4}$ wires, while Cu, Ni and SS showed no signs of superconductivity. However, Ag sheathed wires processed at 900 ºC were better in terms of superconducting properties such as T_C (57 K) and transport J_C (3640 A/cm^2 at 12 K).*

- *Fe sheathed $NdFeAsO_{0.6}F_{0.4}$ tapes with Sn addition of varying wt% (10, 20 and 30) were fabricated. 20 wt% addition of Sn was found to exhibit a maximum T_C of 52.5 K and a transport J_C of 1960 A/cm^{2}at 12 K. The formation of liquid phase such as $FeSn_2$ could minimize the weak links between grains thereby yielding an improved transport J_C compared to Fe sheathed tapes without Sn.*

8.3 Future directions

In the present work, $NdFeAsO_{1-x}F_x$ based iron pnictides were synthesized at ambient pressures and the optimum fluorine contents for maximum T_C and J_C were identified. Thereafter, the critical properties especially T_C, magnetic J_C and H_{C2} were enhanced by rare earth site doping. Binary doping using alkaline earth metal fluorides was found to achieve remarkable increase in transport J_C through microstructural refinement. Moreover, wires and tapes were developed using $NdFeAsO_{0.6}F_{0.4}$ at a relatively low temperature of 900 ºC and the transport J_C was also improved using Sn addition.

But there are a number of issues which need to be addressed and a few are suggested below:

- The problems such as electromagnetic granularity and weak link nature of Nd1111 are intrinsic; however, the inevitable impurity phases such as NdOF and FeAs which act as current blockers between grains need to be minimized by developing novel synthesis techniques.

- Appropriate chemical dopants are to be identified for further enhancement of all the critical properties such as T_C, J_C and H_{C2} in the bulk forms of Nd1111.
- CaF_2 was identified as a promising dopant in terms of microstructural refinement; hence the translation of CaF_2 doped $NdFeAsO_{0.6}F_{0.4}$ into tapes needs to be optimized.
- A relatively cheap outer sheath suitable for $NdFeAsO_{0.6}F_{0.4}$ wires is to be explored which exhibits transport J_C even better compared to that achieved using Ag sheath.
- Focused efforts are to be made for enhancing the superconducting properties of wires by finding more appropriate metal additives and innovative conductor development techniques.

REFERENCES

Abrikosov, A. A.; Nobel Lecture: Type-II superconductors and the vortex lattice, *Rev. Mod. Phys.* **2004**, *76*, 975-979.

Abrikosov, A. A.; On the magnetic properties of superconductors of the second group, *Sov. Phys. JETP* **1957a**, *5*, 1174-1182.

Abrikosov, A. A.; On the magnetic properties of superconductors of the second group, *Zh. Eksp. Teor. Fiz.* **1957b**, *32*, 1442-1452.

Alam, A.; Johnson, D. D.; Mixed valency and site-preference chemistry for cerium and its compounds: A predictive density-functional theory study, *Phys. Rev. B* **2014**, *89*, 235126 (4pp).

Altay, A.; Gulgun, M. A.; Microstructural Evolution of calcium-doped-alumina, *J. Am. Ceram. Soc.* **2003**, *86*, 623-629.

Anderson, P. W.; Resonating valence bond: a new kind of insulator, *Mat. Res. Bull.* **1973**, *8*, 153-160.

Anderson, P. W.; The resonating valence bond state in La_2CuO_4 and superconductivity, *Science* **1987**, *235*, 1196-1198.

Anderson, P.W.; The theory of superconductivity in High-T_C cuprates superconductors (Princeton University Press. Princeton, 1997)

Anderson, P.W.; Theory of flux creep in hard superconductors, *Phys. Rev. Lett.***1962**, *9*, 309-311.

Anooja, J. B.; Aswathy, P. M.; Sarun, P. M.; Syamaprasad, U.; A novel low temperature synthesis route for $SmFeAsO_{1-x}F_x$ bulk superconductor with improved transport properties, *J. Alloys Compd.* **2012**, *514*, 1-5.

Askerzade, I.; Unconventional superconductors, Springer Series in Materials Science 153, 2012.

Aswathy, P. M.; Anooja, J. B.; Sarun, P. M.; Syamaprasad, U.; An overview on iron based superconductors, *Supercond. Sci. Technol.* **2010**, *23*, 073001.

Aswathy, P. M.; Anooja, J. B.; Syamaprasad, U.; $NdFeAsO_{1-x}F_x$ superconductor – impact of fluorine variation on microstructure and transport properties, *J. Am. Ceram. Soc.* **2013**, *96*, 1176-1180.

Awana, V. P. S.; Vajpayee, A.; Mudgel, M.; Kumar, A.; Meena, R. S.; Tripathi, R.; Kumar, S.; Kotnala, R. K.; Kishan, H.; One-step atmospheric pressure synthesis of the ground state of Fe based $LaFeAsO_{1-\delta}$, *J. Supercond. Novel Magn.* **2008**, *21*, 167-169.

Backen, E.;, Haindl, S.; Niemeier, T.; Huhne, R.; Freudenberg, T.; Werner, J.; Behr, G.; Schultz, L.; Holzapfel, B.; Growth and anisotropy of La(O,F)FeAs thin films deposited by pulsed laser deposition, *Supercond. Sci. Technol.* **2008**, *21*, 122001.

Bardeen, J.; Cooper, L. N.; Schreiffer, J. R.; Theory of superconductivity, *Phys. Rev.* **1957a**, *108*, 1175-1204.

Bardeen, J.; Cooper, L. N.; Shrieffer, J. R.; Microscopic theory of superconductivity, *Phys. Rev.* **1957b**, *106*, 162-164.

Bean, C. P.; Livingston, J. D.; Surface barrier in type-II superconductors, *Phys. Rev. Lett.* **1964**, *12*, 14–16.

Bean, C. P.; Magnetization of hard superconductors, *Phys. Rev. Lett.* **1962**, *8*, 250-253.

Bednorz, G.; Muller, K. A.; Possible high T_C superconductivity in the Ba-La-Cu-O system, *Z. Phys. B* **1986**, *64*, 189-193.

Bharathi, A.; Sharma, S.; Paulraj, S.; Satya, A.T.; Hariharan, Y.Sundar, C.S.; Critical properties of superconducting $Ba_{1-x}K_xFe_2As_2$, *Physica C* **2010**, *470*, 8–11.

Bhoi, D.; Sharath Chandra, L. S.; Choudhury, P.; Ganesan, V.; Mandal, P.; The magnetoresistance of a $PrFeAsO_{1-x}F_y$ superconductor, *Supercond. Sci. Technol.* **2009**, *22*, 095015.

Blatter, G.; Feigelman, M. V.; Geshkenbein, V. B.; Larkin, A. I.; Vinokur, V. M.; Vortices in high temperature superconductors, *Rev. Mod. Phys.* **1994**, *66*, 1125–1388.

Bonsignore, G.; Gallitto, A. A.; Vigni, M. L.; Luo, J. L.; Chen,G. F.; Wang, N. L.; Shovkun, D. V.; Intergrain effects in the *ac* susceptibility of polycrystalline $LaFeAsO_{0.94}F_{0.06,}$ *J. Low Temp. Phys.* **2011**, *162*, 40-51.

Brandt, E. H.; The flux-line lattice in superconductors, *Rep. Prog. Phys.***1995**, *58*, 1465–1594.

Brinkman, W. F.; Rice, T. M.; Application of Gutzwiller's Variational method to the metal-insulator transition, *Phys. Rev. B* **1970**, *2*, 4302-4304.

C¸elebi, S.; Nezir, S.; Gencer, A.; Yanmaz, E.; Altunbas, M.; AC losses and irreversibility line of Bi(Pb)SrCaCuO high-T_C superconductors, *J. Alloys Compd.***1997**, *255*, 5-10.

Calderón, M. J.; Valenzuela, B.; Bascones, E.; Effect of tetrahedral distortion on the electronic properties of iron pnictides, *New J. Phys.* **2009**, *11*, 013051 (9pp).

Canfield, P. C.; Bud'ko, S. L.; FeAs-based superconductivity: A case study of the effects of transition metal doping on $BaFe_2As_2$, *Annual Review of Condensed Matter Physics* **2010**, *1*, 27-50.

Celebi, S.; Karaca, I.; Aksu, E.; Gencer, A.; Frequency dependence of the intergranular *ac* loss peak in a high-T_C Bi–(Pb)–Sr–Ca–Cu–O bulk superconductor, *Physica C* **1998**, *309*, 131–137.

Chaddah, P.; Critical current densities in superconducting materials, *Sadhana* (Springer) **2003**, *28*, 273–282.

Chen (b), G. F.; Li, Z.; Li, G.; Zhou, J.; Wu, D.; Dong, J.; Hu, W. Z.; Zheng, P.; Chen, Z. J.; Yuan, H. Q.; Singleton, J.; Luo, J. L.; Wang, N. L.; Superconducting properties of the Fe-based layered superconductor $LaFeAsO_{0.9}F_{0.1-\delta}$, *Phys. Rev. Lett.* **2008a**, *101*, 057007.

Chen(a), D. X.; Pardo, E.; Sanchez, A.; Flux-flow critical-state susceptibility of superconductors, *Appl. Phys. Lett.* **2005**, *86*, 242503.

Chen(b), G. F.; Li, Z.; Wu, D.; Li, G.; Hu, W. Z.; Dong, J.; Zheng, P.; Luo, J. L.; Wang, N. L.; Superconductivity at 41 K and its competition with spin-density-wave instability in layered $CeO_{1-x}F_xFeAs$, *Phys. Rev. Lett.* **2008b**, *100*, 247002.

Chen(c), X. H.; Wu, T.; Wu, G.; Liu, R. H.; Chen, H.; Fang, D. F.; Superconductivity at 43 K in $SmFeAsO_{1-x}F_x$, *Nature* **2008**, *453*, 761-762.

Chen(d), Y. L.; Cui, Y. J.; Cheng, C. H.; Yang, Y.; Wang, L.; Li, Y. C.; Zhang, Y.; Zhao, Y.; Low temperature preparation and superconductivity of F-doped SmFeAsO, *Physica C* **2010a**, *470*, 989-992.

Chen(d), Y. L.; Cui, Y. J.; Cheng, C. H.; Yang, Y.; Zhang, Y.; Zhao, Y.; Effect of Y Doping on Superconductivity and Spin-Density-Wave States in $Sm_{1-x}Y_xFeAsO_{0.8}F_{0.2}$ and $Sm_{1-x}Y_xFeAsO$, *J. Supercond. Novel Magn.* **2010b**, *23*, 621–624.

Chen(d), Y. L.; Cui, Y. J.; Yang, Y.; Zhang, Y.; Wang, L.; Cheng, C. H.; Sorrell, C.; Zhao, Y.; Peak effect and superconducting properties of $SmFeAsO_{0.8}F_{0.2}$ wires, *Supercond. Sci. Technol.* **2008**, *21*, 115014 (6pp).

Chen(e), Y.; Lynn, J. W.; Li, J.; Li, G.; Chen, G. F.; Luo, J. L.; Wang, N. L.; Dai, P. C.; de la Cruz, C.; Mook, H. A.; Magnetic order of the iron spins in NdFeAsO, *Phys. Rev. B* **2008**, *78*, 064515.

Cheng, P.; Yang, H.; Jia, Y.; Fang, L.; Zhu, X.; Mu, G.; Wen, H. H.; Hall effect and magneto-resistance in single crystals of $NdFeAsO_{1-x}F_x$ (x=0 and 0.18), *Phys. Rev. B* **2008**, *78*, 134508.

Choi, E.; Jung, S.; Lee, N. H.; Kwon, Y.; Kang, W. N.; Kim, D. H.; Jung, M.; Lee, S.; Sun, L.; *In situ* fabrication of cobalt-doped $SrFe_2As_2$ thin films by using pulsed laser deposition with excimer laser, *Appl. Phys. Lett.* **2009**, *95*,062507.

Clem, J. R.; Hein, R.A.; Francavilla, T.L.; Liebenberg, D.H.; Magnetic susceptibility of superconductors and other spin systems, Plenum, New York, 1991.

Cui, Y. J.; Chen, Y. L.; Cheng, C. H.; Yang, Y.; Zhang, Y.; Zhao, Y.; Magnetic properties and superconductivity in $GdFeAsO_{1-x}F_x$, *J. Supercond. Nov. Magn.* **2010**, *23*, 625-628.

Cunningham, C. E.; Petrovic, C.; Lapertot, G.; Bud'ko, S. L.; Laabs, F.; Straszheim, W.; Finnemore, D. K.; Canfield, P. C.; Synthesis and processing of MgB_2 powders and wires, *Physica C* **2001**, *353*, 5-9.

Day, C.; Iron-based superconductors, *Physics Today*, **2009**, *62*, 36-40.

de la Cruz, C.; Huang, Q.; Lynn, J. W.; Li, J. Y.; Ratcliff, W.; Zarestky, J. L.; Mook, H. A.; Chen, G. F.; Luo, J. L.; Wang, N. L.; Dai. P.; Magnetic order close to superconductivity in the iron based layered $LaO_{1-x}F_xFeAs$ systems, *Nature* **2008**, *453*, 899–902.

Ding, Y.; Sun, Y.; Wang, X. D.; Shi, Z. X.; Ren, Z. A.; Yang, J.; Lu, W.; Magnetic characterization of polycrystalline $NdFeAsO_{0.88}F_{0.12}$ oxypnictide superconductor, *J. Alloys Compd.* **2011**, *509*, 24-29.

Edegger, B.; Muthukumar V. N.; Gros, C.; Gutzwiller–RVB theory of high temperature superconductivity: Results from renormalized mean-field theory and variational Monte Carlo calculations, *Adv. Phys.* **2007**, 56, 927-1033.

Eisenstein, J.; Superconducting Elements, *Rev. Mod. Phys.* **1954**, *26*, 277-291.

Emmen, J.H.P.M.; Stollman, G. M.; de Jonge, W. J. M.; Frequency and field dependence of the irreversibility line in a $YBa_2Cu_3O_{7-\delta}$ film, *Physica C* **1990**, *169*, 418-424.

Fang(a), A. H.; Huang, F. Q.; Xie, X. M.; Jiang, M. H.; Low-temperature rapid synthesis and superconductivity of Fe-based oxypnictide superconductors, *J. Am. Chem. Soc.* **2010**, *132*, 3260-3261.

Fang(b), L.; Cheng, P.; Jia, Y.; Zhu, X.; Luo, H.; Mu, G.; Gu, C.; Wen, H. H.; Growth of image single crystals at ambient pressure and their transport properties, *J. Cryst. Growth* **2009**, *311*, 358-361.

Flukiger, R.; Suo, H. L.; Musolino, N.; Beneduce, C.; Toulemonde, P.; Lezza, P.; Superconducting properties of MgB_2 tapes and wires, *Physica C* **2003**, *385*, 286-305.

Fuchs, G.; Drechsler, S. L.; Kozlova, N.; Behr, G.; Köhler, A.; Werner, J.; Nenkov, K.; Klingeler, R.; Hamann-Borrero, J.; Hess, C.; Kondrat, A.; Grobosch, M.; Narduzzo, A.; Knupfer, M.; Freudenberger, J.; Büchner, B.; Schultz, L.; High-field pauli-limiting behavior and strongly enhanced upper critical magnetic fields near the transition temperature of an arsenic-deficient $LaO_{0.9}F_{0.1}FeAs_{1-\delta}$ superconductor, *Phys. Rev. Lett.* **2008**, *101*, 237003.

Fujioka, M.; Kota, T.; Matoba, C.; Ozaki, T.; Takano, Y.; Kumakura, H.; Kamihara, Y.; Effective ex-situ fabrication of F doped SmFeAsO wire for high transport critical current density, *Appl. Phys. Express* **2011a**, *4*, 063102.

Fujioka, M.; Matoba, M.; Ozaki, T.; Takano, Y.; Kumakura, H.; Kamihara, Y.; Analysis of interdiffusion between $SmFeAsO_{0.92}F_{0.08}$ and metals for ex situ fabrication of superconducting wire, *Supercond. Sci. Technol.* **2011b**, *24*, 075024.

Ganguli, A. K.; Prakash, J.; Iron-based superconductors with extended FeX_4(X = As and Se) tetrahedra, *Eur. J. Inorg. Chem.* **2011**, 3868–3876.

Ganguli, A. K.; Prakash, J.; Singh, S. J.; Patnaik, S.; Role of chemical pressure in enhancing the transition temperature (T_C) and upper critical field (H_{C2}) in the Y-doped Ce-oxyfluoride superconductor, *Eur. Phys. J. B* **2010**, *73*, 177–184.

Gao, W.; Li, S. C.; Rudman, D. A.; Sande, J. B. V.; The effect of Ag on the microstructure and properties of Bi(Pb)-Sr-Ca-Cu oxide/Ag superconducting microcomposites produced by oxidation of metallic precursor alloys, *Physica C*, **1990**, 167, 395-407.

Gao, Z. S.; Ma, Y. W; Yao,C.; Zhang, X. P.; Wang, C. L.; Wang, D. L.; Awaji, S.; Watanabe, K.; High critical current density and low anisotropy in textured $Sr_{1-x}K_xFe_2As_2$ tapes for high field applications, *Scientific Reports* **2012**, *2*, 998.

Gao, Z. S.; Wang, L.; Qi, Y. P.; Wang, D. L.; Zhang, X. P.; Ma, Y. W.; Preparation of $LaFeAsO_{0.9}F_{0.1}$ wires by the powder-in-tube method, *Supercond. Sci. Technol.* **2008a**, *21*, 105024.

Gao, Z. S.; Wang, L.; Qi, Y. P.; Wang, D. L.; Zhang, X. P.; Ma, Y. W.; Yang, H.; Wen, H. H.; Superconducting properties of granular $SmFeAsO_{1-x}F_x$ wires with Tc = 52 K prepared by the powder-in-tube method, *Supercond. Sci. Technol.* **2008b**, *21*, 112001.

Gao, Z. S.; Wang, L.; Yao,C.;Qi, Y. P.. Wan ; C. L.; Zhang, X. P.; Wang, D. L.; Wang, C. D.; Ma, Y. W.; High transport critical current densities in textured Fe-sheathed $Sr_{1-x}K_xFe_2As_2$+Sn superconducting tapes, *Appl. Phys. Lett.* **2011**, *99*, 242506.

Geim, A. K.; Grigorieva, I.V.; Dubonos, S.V.; Lok, J.G.S.; Maan, J. C.; Filippov, A. E.; Peeters, F. M.; Phase transitions in individual sub-micrometre superconductors, *Nature* **1997**, 390, 259-262.

Ginzburg, V. L.; Landau, L. D.; On the theory of superconductivity, *Zh. Eksp. Teor. Fiz.* **1950**, *20*, 1064-1082.

Ginzburg, V. L.; Nobel Lecture: On superconductivity and superfluidity (what I have and have not managed to do) as well as on the "physical minimum" at the beginning of the XXI century, *Rev. Mod. Phys.* **2004**, *76*, 981-998.

Gordon, R. T.; Kim, H.; Salovich, N.; Giannetta, R. W.; Fernandes, R. M.; Kogan, V. G.; Prozorov, T.; Bud'ko, S. L.; Canfield, P. C.; Tanatar, M. A.; Prozorov, R.; Doping evolution of the absolute value of the London penetration depth and superfluid density in single crystals of $Ba(Fe_{1-x}Co_x)_2As_2$, *Phys. Rev. B* **2010**, *82*, 054507.

Gor'kov, L. P.; Microscopic derivation of the Ginzburg-Landau equations in the theory of superconductivity, *Sov. Phys. JETP* **1959**, *9*, 1364-1367.

Gregersen, E.; The Britannica guide to electricity and magnetism, The Rosen Publishing Group, 2011

Gurevich, A. Iron-based superconductors at high magnetic fields, *Rep. Prog. Phys.* **2011**, *74*, 124501 (19pp).

Gurevich, A.; Upper critical field and the Fulde-Ferrel-Larkin-Ovchinnikov transition in multiband superconductors, *Phys. Rev. B* **2010**, *82*, 184504.

Gutzwiller, M. C.; Effect of correlation on the ferromagnetism of transition metals, *Phys. Rev. Lett.* **1963**, *10*, 159-162.

Haindl, S.; Kidszun, M.; Kauffmann, A.; Nenkov, K.; Kozlova, N.; Freudenberger, J.; Thersleff, T.; Hänisch, J.; Werner, J.; Reich, E.; Schultz, L.; Holzapfel, B.; High upper critical fields and evidence of weak-link behavior in superconducting $LaFeAsO_{1-x}F_x$ Thin Films, *Phys. Rev. Lett.* **2010**, *104*, 077001.

Han, F.; Zhu, X.; Cheng, P.; Mu, G.; Jia, Y.; Fang, L.; Wang, Y.; Luo, H.; Zeng, B.; Shen, B.; Shan, L.; Ren, C.; Wen, H. H.; Superconductivity and phase diagrams of the 4d- and 5d-metal-doped iron arsenides $SrFe_{2-x}M_xAs_2$ (M=Rh,Ir,Pd), *Phys. Rev. B* **2009**, *80*, 024506.

He, B.; Dong, C.; Cao, W.; Liao, C.; Yang, L.; Chen, H.; Enhancement of the critical current density and upper critical field in Zr and Mo co-doped Nb_3Sn, *Supercond. Sci. Technol.* 2**010**, *23* 025016.

Hikata, T.; Nishikawa, T.; Mukai, H.; Sato, K.; Hitotsuyanagi, H.; Ag sheathed Bi-Pb-Sr-Ca-Cu-O Superconducting Wires with High Critical Current Density, *Jpn J. Appl. Phys.* **1989**, *28*, L82-L84.

Hiramatsu, H.; Katase, T.; Kamiya, T.; Hirano, M.; Hosono, H.; Superconductivity in epitaxial thin films of Co-doped $SrFe_2As_2$ with bilayered feas structures and their magnetic anisotropy, *Appl. Phys. Express* **2008**, *1*, 101702.

Hubbard, J.; Electron Correlations in Narrow Energy Bands, *P. Roy. Soc. (Lond)* **1963**, *A276*, 238-257.

Hunte, F.; Jaroszynski, J.; Gurevich, A.; Larbalestier, D. C.; Jin, R.; Sefat, A. S.; McGuire, M. A.; Sales, B. C.; Christen, D. K.; Mandrus, D.; Two-band superconductivity in $LaFeAsO_{0.89}F_{0.11}$ at very high magnetic fields, *Nature* **2008**, *453*, 903-905.

Ishida, K.; Nakai, Y.; Hosono, H.; To What extent iron-pnictide new superconductors have been clarified: A progress report, *J. Phys. Soc. Jpn* **2009**, *78*, 062001.

Jaroszynski, J.; Hunte, F.; Balicas, L.; Jo, Y.; Raičević, I.; Gurevich, A.; Larbalestier, D. C.; Balakirev, F. F.; Fang, L.; Cheng, P.; Jia, Y.; Wen, H. H.; Upper critical fields and thermally-activated transport of $NdFeAsO_{0.7}F_{0.3}$ single crystal, *Phys. Rev. B* **2008a**, *78*, 174523.

Jaroszynski, J.; Riggs, S. C.; Hunte, F.; Gurevich, A.; Larbalestier, D. C.; Boebinger, G. S.; Balakirev, F. F.; Migliori, A.; Ren, Z. A.; Lu, W.; Yang, J.; Shen, X. L.; Dong, X. L.; Zhao, Z. X.; Jin, R.; Sefat, A. S.; McGuire, M. A.; Sales, B. C.; Christen, D. K.; Mandrus, D.; Comparative high-field magnetotransport of the oxypnictide

superconductors $RFeAsO_{1-x}F_x$ (R=La, Nd) and $SmFeAsO_{1-\delta}$, *Phys. Rev. B* **2008b**, *78*, 064511.

Jia, Y.; Cheng, L.; Fang, L.; Yang, H.; Ren, C.; Shan, L.; Gu, C. Z.; Wen, H. H.; Angular dependence of resistivity in the superconducting state of $NdFeAsO_{0.82}F_{0.18}$ single crystals, *Supercond. Sci. Technol.* **2008b**, *21*, 105018.

Jia, Y.; Cheng, P.; Fang, L.; Luo, H.; Yang, H.; Ren, C.; Shan, L.; Gu, C.; Wen, H. H.; Critical fields and anisotropy of $NdFeAsO_{0.82}F_{0.18}$ single crystals, *Appl. Phys. Lett.* **2008a**, *93*, 032503.

Jo, Y. J.; Jaroszynski, J.; Yamamoto, A.; Gurevich, A.; Riggs, S. C.; Boebinger, G. S.; Larbalestier, D.; Wen, H. H.; Zhigadlo, N.D.; Katrych, S.; Bukowski, Z.; Karpinski, J.; Liu, R.H.; Chen, H.; Chen, X.H.; Balicas, L.; High-field phase-diagram of Fe arsenide superconductors, *Physica C* **2009**, *469*, 566-574.

Johannes, M. D.; Mazin, I. I.; Microscopic origin of magnetism and magnetic interactions in ferropnictides, *Phys. Rev. B* **2009**, *79*, 220510.

Johnston, D. C.; The puzzle of high temperature superconductivity in layered iron pnictides and chalcogenides, *Adv. Phys.* **2010**, *59*, 803–1061.

Josephson, B. D.; Possible new effects in superconductive tunnelling, *Phys. Lett.* **1962**, *1*, 251-253.

Kachan, J.; Bosi, S.; The University of Australia (2008) www.physics.usyd.edu.au/~khachan/PTF/Superconductivity.pdf

Kamihara, Y.; Watanabe, T.; Hirano, M.; Hosono, H.; Iron-based layered superconductor $La[O_{1-x}F_x]FeAs$ (x = 0.05−0.12) with Tc = 26 K, *J. Am. Chem. Soc.* **2008**, *130*, 3296-3297.

Kamihara,Y.; Hiramatsu, H.; Hirano, M.; Kawamura, R.; Yanagi, H.; Kamiya, T.; Hosono, H.; Iron-based layered superconductor: LaOFeP, *J. Am. Chem. Soc.* **2006**, *128*, 10012-10013.

Kawaguchi, T.; Uemura, H.; Ohno, T.; Tabuchi, M.; Ujihara, T.; Takenaka, K.; Takeda, Y.; Ikuta, H.; In situ growth of superconducting NdFeAs(O,F) thin films by molecular beam epitaxy, *Appl. Phys. Lett.* **2010**, *97*, 042509.

Kemper, A. F.; Maier, T. A.; Graser, S.; Cheng, H. P.; Hirschfeld, P. J.; Scalapino, D. J.; Sensitivity of the superconducting state and magnetic susceptibility to key aspects of electronic structure in ferropnictides, *New J. Phys.* **2010**, 12, 073030.

Kidszun, M.; Haindl, S.; Reich, E.; Hanisch, J.; Iida, K.; Schultz, L.; Holzapfel, B.; Epitaxial $LaFeAsO_{1-x}F_x$ thin films grown by pulsed laser deposition, *Supercond. Sci. Technol.* **2010**, *23*, 022002.

Kim, Y. B.; Hempstead, C. F.; Strnad, A. R.; Critical persistent currents in hard superconductors, *Phys. Rev.* **1962**, *9*, 306-309.

Kimber, S. A. J.; Argyriou, D. N.; Yokaichiya, F.; Habicht, K.; Gerischer, S.; Hansen, T.; Chatterji, T.; Klingeler, R.; Hess, C.; Behr, G.; Kondrat, A.; Buchner, B.; Magnetic ordering and negative thermal expansion in PrFeAsO, *Phys. Rev. B* **2008**, *78*, 140503.

Kitazawa, K.; Superconductivity: 100th Anniversary of Its Discovery and Its Future, *Jpn. J. Appl. Phys.* **2012**, *51*, 010001.

Kito, H.; Eisaki, H.; Iyo, A.; Superconductivity at 54 K in F-Free $NdFeAsO_{1-y}$, *J. Phys. Soc. Jpn.* **2008**, *77*, 063707.

Koizumi, N.; Progress of ITER Superconducting Magnet Procurement, *Physics Procedia* **2013**, *45*, 225-228.

Komori, K.; Kawagishi, K.; Takano, Y.; Fujii, H.; Arisawa, S.; Kumakura, H.; Fukutomi, M.; Togano, K.; Approach for the fabrication of MgB_2 superconducting tape with large in-field transport critical current density, *Appl. Phys. Lett.* **2002**, *81*, 1047.

Kontani, H.; Onari, S.; Orbital-fluctuation-mediated superconductivity in iron pnictides: analysis of the five-orbital hubbard-holstein model, *Phys. Rev. Lett.* **2010**, *104*, 157001.

Kopaev, Y. V.; Belyavsky, V. I.; Kapaev, V. V.; With cuprate luggage to room-temperature superconductivity, *Physics -Uspekhi* **2008**, *51*, 191-198.

Kunzler, J. E.; Wernick, J. H.; Hsu, F. S. L.; Buehler, E.; Superconductivity in Nb_3Sn at high current density in a magnetic field of 88 KG, *Phys. Rev. Lett.* **1961**, *6*,89-91.

Lai, K.T.; Kwong, F. L.; Dickon, H. L.; Superconductivity in fluorine and yttrium co-doped SmFeAsO, *J. Appl. Phys.* **2012**, *111*, 093912 (5pp).

Larbalestier, D. C.; Cooley, L. D.; Rikel, M. O.; Polyanskii, A. A.; Jiang, J.; Patnaik, S.; Cai, X. Y.; Feldmann, D. M.; Gurevich, A.; Squitieri, A. A.; Naus, M. T.; Eom, C. B.; Hellstrom, E. E.; Cava, R. J.; Regan, K. A.; Rogado, N.; Hayward, M. A.; He, T.;Slusky, J. S.; Khalifah, P.; Inumaru, K.; Haas, M.; Strongly linked current flow in polycrystalline forms of the superconductor MgB_2, *Nature* **2001a**, *410*, 186-189.

Larbalestier, D. C.; Gurevich, A.; Feldmann, D. M.; Polyanskii, A.; High-T_C superconducting materials for electric power applications, *Nature* **2001b**, *414*, 368–377.

Larkin, A. I.; Varlamov, A. A.; Fluctuations in superconductors, (Oxford: Clarendon) 2007

Lebrun, Ph; LHC Project Report 441, Beijing International Conference on Cryogenics, 2000

Lee(a), C. C.; Yin, W. G.; Ku, W.; Ferro-orbital order and strong magnetic anisotropy in the parent compounds of iron-pnictide superconductor, *Phys. Rev. Lett.* **2009**, *103*, 267001.

Lee(b), C. H.; Iyo, A.; Eisaki, H.; Kito, H.; Fernandezdiaz, M. T.; Ito, T.; Kihou, K.; Matsuhata, H.; Braden, M.; Yamada, K.; Effect of structural parameters on superconductivity in fluorine-free $LnFeAsO_{1-y}$ (Ln = La, Nd), *J. Phys. Soc. Japan* **2008**, *77*, 083704.

Lee(c), C. Y.; Kao, Y. H.; Frequency dependence of the intergranular energy-loss peak in AC magnetic susceptibility of high-T_C superconductors, *Physica C* **1996**, *256*, 183-190.

Lee(d), H. S.; Park, J. H.; Lee, J. Y.; Kim, J. Y.; Sung, N. H.; Koo, T. Y.; Cho, B. K.; Jung, C. U.; Saini, S.; Kim, S. J.; Lee, H. J.; High-pressure growth of fluorine-free $SmFeAsO_{1-x}$ superconducting single crystals, *Supercond. Sci. Technol.* **2009,** *22*, 075023.

Lee(e), S.; Jiang, J.; Weiss, J. D.; Folkman, C. M.; Bark, C. W.; Tarantini, C.; Xu, A.; Abraimov, D.; Polyanskii, A.; Nelson, C. T.; Zhang, Y.; Baek, S. H.; Jang, H. W.; Yamamoto, A.; Kametani, F.; Pan, X. Q.; Hellstrom, E. E.; Gurevich, A.; Eom, C. B.; Larbalestier, D. C.; Weak-link behavior of grain boundaries in superconducting $Ba(Fe_{1-x}Co_x)_2As_2$ bicrystals, *Appl. Phys. Lett.* **2009**, *95*, 212505.

Li(a), L. J.; Li, Y. K.; Ren, Z.; Luo,Y .; Lin, X.; He, M.; Tao, Q.; Zhu, Z.; Cao, G.; Xu, Z.; Superconductivity above 50 K in $Tb_{1-x}Th_xFeAsO$, *Phys. Rev. B* **2008**, *78*, 132506.

Li(a), L. J.; Luo, Y. K.; Wang, Q. B.; Chen, H.; Ren, Z.; Tao, Q.; Li, Y. K.; Lin, X.; He, M.; Zhu, Z. W.; Cao, G. H.; Xu, Z. A.; Superconductivity induced by Ni doping in $BaFe_2As_2$ single crystals, *New J. Phys.* **2009**, *11*, 025008.

Li(b), W. H.; Chuang, W. Y.; Wu, S. Y.; Lee, K. C.; Lynn, J. W.; Tsay, H. L.; Yang, H. D.; Superconductivity, magnetic fluctuations, and magnetic order in $TbSr_2Cu_{2.69}Mo_{0.31}O_7$, *Phys. Rev. B* **1997**, *56*, 5631-5636.

Li(c), Y. K; Lin, X.; Zhou, T.; Shen, J. Q.; Tao, Q.; Cao, G. H.; Xu, Z. A.; Superconductivity induced by Ni doping in $SmFe_{1-x}Ni_xAsO$, *J. Phys.: Condens. Matter 2009*, *21*, 355702.

Li(d), Y. S.; Xin, L. J.; Spin fluctuations and unconventional superconducting pairing in iron-based superconductors, *Chin. Phys. B* **2013**, *22*, 087411.

Li(e), Y.; Lin, X.; Zhou, T.; Shen, J.; Luo, Y.; Tao, Q.; Cao, G.; Xu, Z.; Superconductivity in phosphorus-doped $SmFeAs_{1-x}P_xO$, *Physica C***2010**, *470*, S493-S494.

Liu(a), R. H.; Wu, G.; Wu, T.; Fang, D. F.; Chen, H.; Li, S. Y.; Liu, K.; Xie, Y. L.; Wang, X. F.; Yang, R. L.; Ding, L.; He, C.; Feng, D. L.; Chen, X. H.; Anomalous transport properties and phase diagram of the feas-based $SmFeAsO_{1-x}F_x$ superconductors, *Phys. Rev. Lett.* **2008**, *101*,087001 (4pp).

Liu(b), S. L.; Wu, J. G.; Xu, X. B.; Wu, J.; Shao, H. M.; Cai, Y. M.; Jin, X. C.; Frequency Response of AC susceptibility in melt textured YBCO superconductors, *J. Supercond.: Incorporating Novel Magnetism* **2005**, *18*, 281-285.

London, F.; London, H.; Supraleitung und diamagnetismus, *Physica* **1935a**, *2*, 341-354.

London, F.; London, H.; The electromagnetic equations of the superconductor, *Proc. Roy. Soc. A* **1935b**, *149*, 71.

Lorenz, B.; Sasmal, K.; Chaudhury, R. P.; Chen, X. H.; Liu, R. H.; Wu, T.; Chu, C.W.; Effect of pressure on the superconducting and spin-density-wave states of $SmFeAsO_{1-x}F_x$, *Phys. Rev. B* **2008**, *78*, 012505 (4pp).

Lu, W.; Yang, J.; Dong, X. L.; Ren, Z. A.; Che, G. C.; Zhao, Z. X.; Pressure effect on superconducting properties of $LaO_{1-x}F_xFeAs$ (x=0.11) superconductor, *New J. Phys.* **2008**, *10*, 063026.

Lumsden, M. D.; Christianson, A. D.; Magnetism in Fe-based superconductors, *J. Phys.: Condens. Matter* **2010**, *22*, 203203.

Ma(a), Y.; Progress in wire fabrication of iron-based superconductors, *Supercond. Sci. Technol.* **2012**, *25*, 113001.

Ma(a), Y.; Wang, L.; Qi, Y.; Gao, Z.; Wang, D.; Zhang, X.; Development of Powder-in-Tube Processed Iron Pnictide Wires and Tapes, *IEEE Trans. Appl. Supercond.* **2011**, *21*, 2878-2881.

Ma(b), F. J.; Lu, Z. Y.; Xiang, T.; Arsenic-bridged antiferromagnetic superexchange interactions in LaFeAsO, *Phys. Rev. B* **2008**, *79*, 224517.

Malavasi, L.; Artioli, G. A.; Ritter, C.; Mozzati, M. C.; Maroni, B.; Pahari, B.; Caneschi, A.; Phase diagram of $NdFeAsO_{1-x}F_x$: Essential role of chemical composition, *J. Am. Chem. Soc.* **2010**, *132*, 2417-2420.

Martin, C.; Tillman, M. E.; Kim, H.; Tanatar, M. A.; Kim, S. K.; Kreyssig, A.; Gordon, R. T.; Vannette, M. D.; Nandi, S.; Kogan, V. G.; Budko, S. L.; Canfield, P. C.; Goldman, A. I.; Prozorov, R.; Non-exponential london penetration depth of feas-based superconducting $RFeAsO_{0.9}F_{0.1}$ (R=La, Nd) single crystals, *Phys. Rev. Lett.* **2009**, *102*, 247002.

Matsuishi, S.; Inoue, Y.; Nomura, T.; Yanagi, H.; Hirano, M.; Hosono, H.; Superconductivity Induced by Co-Doping in Quaternary Fluoro-arsenide CaFeAsF, *J. Am. Chem. Soc.* 2008, 130, 14428-14429.

Matthias, B. T.; Geballe, T. H.; Compton, V. B.; Superconductivity, *Rev. Mod. Phys.* **1963**, *35*, 1-22.

Maxwell, E.; Isotope Effect in the Superconductivity of Mercury, *Phys. Rev.* **1950**, *78*, 477.

Mazin, I. I.; Schmalian, J.; Pairing symmetry and pairing state in ferropnictides: Theoretical overview, *Physica C* **2009**, *469*, 614–627.

Mazin, I. I.; Singh, D. J.; Johannes, M. D.; Du, M. H.; Unconventional superconductivity with a sign reversal in the order parameter of $LaFeAsO_{1-x}F_x$, *Phys. Rev. Lett.* **2008**, *101*, 057003.

McGuire, M. A.; Christianson, A. D.; Sefat, A. S.; Sales, B. C.; Lumsden, M. D.; Jin, R. Y.; Payzant, E. A.; Mandrus, D.; Luan, Y. B.; Keppens, V.; Varadarajan, V.; Brill, J. W.; Hermann, R. P.; Sougrati, M. T.; Grandjean , F.; Long, G. J.; Phase transitions in LaFeAsO: Structural, magnetic, elastic, and transport properties, heat capacity and Mössbauer spectra, *Phys. Rev. B* **2008**, *78*, 094517.

McGuire, M. A.; Hermann, R. P.; Sefat, A. S.; Sales, B. C.; Jin, R. Y.; Mandrus, D.; Grandjean, F.; Long, G. J.; Influence of the rare-earth element on the effects of the structural and magnetic phase transitions in CeFeAsO, PrFeAsO and NdFeAsO, *New J. Phys.* **2009**, *11*, 025011.

Meissner, W.; Oschenfeld, R.; A new effect upon the occurrence of superconductivity, *Naturwissenschaften* **1933**, 21, 787-788.

Moore, J.D.; Morrison, K.; Yates, K.A.; Caplin, A.D.; Yeshurun, Y.; Cohen, L. F.; Perkins, J. M.; McGilvery, C. M.; McComb, D. W.; Ren, Z. A.; Yang, J.; Lu, W.; Dong, X. L.; Zhao, Z. X.; Evidence for supercurrent connectivity in conglomerate particles in $NdFeAsO_{1-\delta}$, *Supercond. Sci. Technol.* **2008**, *21*, 092004 (5pp).

Müller, K. H.; Frequency dependence of AC susceptibility in high-temperature superconductors: Flux creep and critical state at grain boundaries, *Physica C* **1990**, *168*, 585-590.

Müller, K. H.; Nikolo, M.; Driver, R.; Flux pinning at grain boundaries in Bi-(Pb)-Sr-Ca-Cu-O ceramic superconductors, *Phys. Rev. B* **1991**, *43*, 7976-7979.

Muzikar, P.; Unconventional superconductivity, *J. Phys.: Condens. Matter* **1997**, *9*, 1159–1179.

Nagamatsu, J.; Nakagawa, N.; Muranaka, T.; Zenitani; Y.; Akimtsu, J.; Superconductivity at 39 K in magnesium diboride, *Nature* **2001**, *410*, 63-64.

Neson, V.; Vinod, K.; Rahul, S.; Devadas, K. M.; Syju, T.; Pradhan, S.; Syamaprasad, U.; Influence of nano-Cu additive on MgB_2 phase formation, processing temperature, and transport properties, *J. Appl. Phys.* **2011**, *109*, 033902.

Neson, V.; Vinod, K.; Shipra,Sundaresan, A.; Syamaprasad, U.; Burned Rice Husk: An effective additive for enhancing the electromagnetic properties of MgB_2 superconductor, *J. Am. Ceram. Soc.* **2010**, *9*, 732-736.

Ni, N.; Thaler, A.; Kracher, A.; Yan, J. Q.; Budko, S. L.; Canfield, P. C.; Phase diagrams of $Ba(Fe_{1-x}M_x)_2As_2$ single crystals (M=Rh and Pd), *Phys. Rev. B* **2009**, *80*, 024511.

Nikolo, M.; Goldfarb, R. B.; Flux creep and activation energies at the grain boundaries of Y-Ba-Cu-O superconductors, *Phys. Rev. B* **1989**, *39*, 6615-6618.

Nikolo, M.; Superconductivity: A guide to alternating current susceptibility measurements and alternating current susceptometer design, *Am. J. Phys* **1995**, *63*, 57-65.

Norman, M. R.; High-temperature superconductivity in the iron pnictides, *Physics* **2008**, *1*, 21.

Onnes, K. H.; The Superconductivity of Mercury, *Leiden Commun.* **1911**, *124*, 1226.

Orlando, T. P.; McNiff, E. J.; Foner, S.; Beasley, M. R.; Critical fields, Pauli paramagnetic limiting, and material parameters of Nb_3Sn and V_3Si, *Phys. Rev. B* **1979**, *19*, 4545–4561.

Ozawa, T.C.; Kauzlarich, S. M.; Chemistry of layered d-metal pnictide oxides and their potential as candidates for new superconductors, *Sci. Technol. Adv. Mater.* **2008**, *9*, 033003 (11pp).

Paglione, J.; Greene, R. L.; High-temperature superconductivity in iron-based materials, *Nature Phys.* **2010**, *6*, 645–658.

Parkin, S. S. P.; Lee, V. Y.; Engler, E. M.; Nazzal, A. I.; Huang, T. C.; Gorman, G.; Savoy, R.; Beyers, R.; Bulk Superconductivity at 125 K in $Tl_2Ca_2Ba_2Cu_3O_x$, *Phys. Rev. Lett.* **1988**, *60*, 2539-2542.

Pauling, L.; A resonating-valence-bond-theory of metals and intermetallic compounds, *Proc. Roy. Soc. London* **1949**, *A196*, 343-362.

Pauling, L.; A theory of ferromagnetism, *Proc. N. A. S.* **1953**, *39*, 551-560.

Pissas, M.; Stamopoulous, D.; Ren, Z. A.; Shen, X. L.; Yang, J.; Zhao, Z. X.; Magnetic measurements of superconducting $NdFeAsO_{0.82}F_{0.18}$ oxypnictide, *Supercond. Sci. Technol.* **2009**, *22*, 055008 (5pp).

Polichetti, M.; Adesso, M. G.; Zola, D.; Luo, J. L.; Chen, G. F.; Li, Z.; Wang, N. L.; Noce, C.; Pace, S.; Granularity and vortex dynamics in $LaFeAsO_{0.92}F_{0.08}$ probed by harmonics of the ac magnetic susceptibility, *Phys. Rev. B* **2008**, *78*, 224523 (10pp).

Polichetti, M.; Zola, D.; Luo, J.; Chen, G. F.; Li, Z.; Wang, N. L.; Noce, C.; Pace, S.; Frequency behavior of the AC magnetic response in $LaFeAsO_{0.92}F_{0.08}$ bulk and powders, *Physica C* **2010**, *470*, 929–931.

Poole, C. P.; Farach, H. A.; Creswick, R. J.; Superconductivity, Academic Press, California (1995)

Prakash, J.; Singh, S. J.; Banerjee, A.; Patnaik, S.; Ganguli, A. K.; Enhancement in transition temperature and upper critical field of $CeO_{0.8}F_{0.2}FeAs$ by yttrium doping, *Appl. Phys. Lett.* **2009**, *95*, 262507.

Prozorov, R.; Tillman, M. E.; Mun, E. D.; Canfield, P. C.; Intrinsic magnetic properties of the superconductor $NdFeAsO_{0.9}F_{0.1}$ from local and global measurements, *New J. Phys.* 2009, *11*, 035004 (9pp).

Putti, M.; Pallecchi, I.; Bellingeri, E.; Cimberle, M. R.; Tropeano, M.; Ferdeghini, C.; Palenzona, A.; Tarantini, C.; Yamamoto, A.; Jiang, J.; Jaroszynski, J.; Kametani, F.; Abraimov, D.; Polyanskii, A.; Weiss, J. D.; Hellstrom, E. E.; Gurevich, A.;

Larbalestier, D. C.; Jin, R.; Sales, B. C.; Sefat, A. S.; McGuire, M. A.; Mandrus, D.; Cheng, P.; Jia, Y.; Wen, H. H.; Lee, S.; Eom, C. B.; New Fe-based superconductors: properties relevant for applications, *Supercond. Sci. Technol.* **2010**, *23*, 034003.

Qi, Y. P.; Gao, Z. S.; Wang, L.; Wang, D. L.; Zhang, X. P.; Ma, Y. W.; Superconductivity at 34.7 K in the iron arsenide $Eu_{0.7}Na_{0.3}Fe_2As_2$, *New J. Phys.* **2008b**, *10*, 123003.

Qi, Y. P.; Zhang, X. P.; Gao, Z. S.; Zhang, Z. Y.; Wang, L.; Wang, D. L.; Ma, Y. W.; Superconductivity of powder-in-tube $Sr_{0.6}K_{0.4}Fe_2As_2$ wires, *Physica C* **2009b**, 469, 717-720.

Qi,Y. P.; Gao, Z.; Wang, L.; Wang, D; Zhang, X.; Ma, Y.; Superconductivity in Co-doped SmFeAsO, *Supercond. Sci. Technol.* **2008a**, *21*, 115016.

Qi,Y. P.; Wang, L.; Gao, Z.; Wang, D.; Zhang, X.; Ma, Y.; Superconductivity in Ir-doped $LaFe_{1-x}Ir_xAsO$, *Phys. Rev. B* **2009a**, *80*, 054502.

Raghu, S.; Qi, X. L.; Liu, C. X.; Scalapino, D. J.; Zhang, S. C.; Minimal two-band model of the superconducting iron oxypnictides, *Phys. Rev. B: Condens. Matter* **2008**, *77*, 220503.

Ren(a), Z. A.; Che, G. C.; Dong, X. L.; Yang, J.; Lu, W.; Yi, W.; Shen, X. L.; Li, Z. C.; Sun, L. L.; Zhou, F.; Zhao, Z. X.; Superconductivity and phase diagram in iron-based arsenic-oxides $ReFeAsO_{1-\delta}$ (Re = rare-earth metal) without fluorine doping, *Europhys. Lett.* **2008a**, *83*, 17002.

Ren(a), Z. A.; Lu, W.; Jie, Y.; Yi, W.; Shen, X. L.; Zheng, C.; Che G. C.; Dong X. L.; Sun, L. L.; Zhou, F.; Zhao, Z. X.; Superconductivity at 55 K in iron-based f-doped layered quaternary compound $Sm[O_{1-x}F_x]FeAs$, *Chinese Phys. Lett.* **2008b**, *25*, 2215-2216.

Ren(a), Z. A.; Yang, J.; Lu, W.; Yi, W.; Che, G. C.; Dong, X. L.; Sun, L. L.; Zhao, Z. X.; Superconductivity at 52 K in iron based F doped layered quaternary compound $Pr[O_{1-x}F_x]FeAs$, *Mater. Res. Innovations* **2008c**, *12*, 105-106.

Ren(a), Z. A.; Yang, J.; Lu, W.; Yi, W.; Shen, X. L.; Li, Z. C.; Che, G. C.; Dong, X. L.; Sun, L. L.; Zhou, F.; Zhao, Z. X.; Superconductivity in the iron-based F-doped layered quaternary compound $Nd[O_{1-x}F_x]FeAs$, *Eur. Phys. Lett.* **2008d**, *82*, 57002 (2pp).

Ren(a), Z. A.; Zhao, Z. X.; Research and prospects of iron-based superconductors, *Adv. Mater.* **2009**, *21*, 4584–4592.

Ren(b), Z.; Tao, Q.; Jiang, S.; Feng, C.; Wang, C.; Dai, J.; Cao, G.; Xu, Z.; Superconductivity induced by phosphorus doping and its coexistence with ferromagnetism in $EuFe_2(As_{0.7}P_{0.3})_2$, *Phys. Rev. Lett.* **2009**, *102*, 137002.

Reynolds, C. A.; Serin, B.; Wright, W. H.; Nesbitt, L. B.; Superconductivity of isotopes of mercury, *Phys. Rev.* **1950**, *78*, 487.

Rotter, M.; Tegel, M.; Johrendt, D.; Superconductivity at 38 K in the iron arsenide $(Ba_{1-x}K_x)Fe_2As_2$, *Phys. Rev. Lett.* **2008**,*101*, 107006.

Ryan, D. H.; Cadogan, J. M.; Ritter, C.; Canepa, F.; Palenzona, A.; Putti, M.; Coexistence of long-ranged magnetic order and superconductivity in the pnictide superconductor $SmFeAsO_{1-x}F_x$ (x=0, 0.15), *Phys. Rev. B* **2009**, *80*, 220503.

Salamati, H.; Kameli, P.; AC susceptibility study of YBCO thin film and BSCCO bulk superconductors, *J. Magn. Magn. Mater.* **2004**, *278*, 237-243.

Saleh, A. M.; Abu-Samreh, M. M.; Leghrouz, A. A.; Dependence of AC susceptibility of polycrystalline $RuSr_2GdCu_2O_8$ superconductor on magnetic field amplitudes and frequencies, *Physica C* **2003**, *384*,383–390.

Sanchez, D. R.; Alzamora, M.; Munevar, J.; Wang, N. L.; Cheng, G. F.; Baggio-Saitovitch, E.; Mössbauer study of superconducting $NdFeAsO_{0.88}F_{0.12}$ and its parent compound NdFeAsO, *J. Phys.: Condens. Matter* **2009**, *21*, 455701.

Sato, M.; Kobayashi, Y.; Lee, S. C.; Takahashi, H.; Satomi, E.; Miura, Y.; Studies on effects of impurity doping and nmr measurements of La1111 and/or Nd1111 Fe-pnictide superconductors, *J. Phys. Soc. Jpn.***2010**, *79*, 014710.

Schmidt, V. V.; Paul, M.; Ustinov, A. V.; The Physics of Superconductors: Type-II Superconductors **1997**, 101-137

Schnelle, W.; Leithejasper, A.; Gumeniuk, R.; Burkhardt, U.; Kasinathan, D.; Rosner, H.; Substitution-induced superconductivity in $SrFe_{2-x}Ru_xAs_2$ ($0 \le x \le 2$), *Phys. Rev. B* **2009**, *79*, 214516.

Sefat, A. S.; Mcguire, M. A.; Sales, B. C.; Jin, R.; Howe, J. Y.; Mandrus, D.; Electronic correlations in the superconductor $LaFeAsO_{0.89}F_{0.11}$ with low carrier density, *Phys. Rev. B* **2008**, *77*, 174503.

Senatore, C.; Cantoni, M.; Wu, G.; Liu, R. H.; Chen, X. H.; Flukiger, R.; Upper critical fields well above 100 T for the superconductor $SmFeAsO_{0.85}F_{0.15}$ with T_C=46 K, *Phys. Rev. B* **2008**, *78*, 054514.

Shahbazi, M.; Wang, X. L.; Shekhar, C.; Srivastava, O. N.; Dou, S. X.; Upper critical field, critical current density and thermally activated flux flow in fluorine doped CeFeAsO superconductors, *Supercond. Sci. Technol.* **2010**, *23*, 105008.

Shapira, Y.; Neuringer, L. J.; Upper Critical Fields of Nb-Ti Alloys: Evidence for the influence of Pauli paramagnetism, *Phys. Rev.* **1965**, *140*, A1638–A1644.

Sharma, S.; Vinod, K.; Sundar, C.S.; Bharathi, A.; Critical current density and magnetic phase diagrams of $BaFe_{1.29}Ru_{0.71}As_2$ single crystals, *Supercond. Sci. Technol.* **2013**, *26*, 015009 (6pp).

Shekhar, C.; Singh, S.; Siwach, P. K.; Singh, H. K.; Srivastava, O. N.; Synthesis and microstructural studies of iron oxypnictide $LaO_{1-x}F_xFeAs$ superconductors, *Supercond. Sci. Technol.* **2008**, *22*, 015005.

Shen, W., Coffey, M.; McGhee, W.; Development of 9.5 T NbTi cryogen-free magnet, *IEEE Trans. Appl. Supercond.* **2001**, *11*, 2619-2622.

Sheng, Z. Z.; Hermann, A. M.; Bulk superconductivity at 120 K in the Tl–Ca/Ba–Cu–O system, *Nature* **1988**, *332*, 138-139.

Shirage, P. M.; Miyazawa, K.; Kito, H.; Eisaki, H.; Iyo, A.; Superconductivity at 43 K at ambient pressure in the iron-based layered compound $La_{1-x}Y_xFeAsOy$, *Phys. Rev. B* **2008**, *78*, 172503.

Shlyk, L.; Wolff, K. K.; Bischoff, M.; Rose, E.; Schleid, T.; Niewa, R.; Crystal structure and superconducting properties of hole-doped $Ca_{0.89}Na_{0.11}FFeAs$ single crystals, *Supercond. Sci. Technol.***2014**, *27*, 044011.

Shuba, R.; Chen, I. W.; Effect of seeding on the microstructure and mechanical properties of α-SiAlON: II, Ca-α-SiAlON, *J. Am. Ceram. Soc.* **2002**, *85***,** 1260-1267.

Singh, D. J.; Du, M. H.; Density Functional Study of $LaFeAsO_{1-x}F_x$: A low carrier density superconductor near itinerant magnetism, *Phys. Rev. Lett.* **2008**, *100*, 237003.

Solovjov, A. L.; Sidorov, S. L.; Tarenkov, Y. V.; D'yachenko, A. I.; Possibility of local pair existence in optimally doped $SmFeAsO_{1-x}$ in pseudogap regime, *arXiv*:1012.1252v1.

Song, X.; Daniels, G.; Feldmann, D. M.; Gurevich, A.; Larbalestier, D. C.; Electromagnetic, atomic structure and chemistry changes induced by Ca-doping of low-angle $YBa_2Cu_3O_{7-\delta}$ grain boundaries, *Nature Mater.* **2005**, *4*, 470–475.

Spalek, J.; t-J model then and now: A personal perspective from the pioneering times, *Acta Physica Polonica A* **2007**, *111*, 409-424.

Sun, Y.; Ding, Y.; Zhuang, J. C.; Cui, L. J.; Yuan, X. P.; Shi, Z. X.; Ren, Z. A.; An anomalous tail effect in the resistivity transition and weak-link behavior of superconducting $NdFeAsO_{0.88}F_{0.12}$, *Supercond. Sci. Technol.* **2011**, *24*, 085011 (5pp).

Suo, H. L.; Beneduce, C.; Dhallé, M.; Musolino, N.; Genoud, J. Y.; Flükiger, R.; Large transport critical currents in dense Fe- and Ni-clad MgB_2 superconducting tapes, *Appl. Phys. Lett.* **2001**, *79*, 3116.

Superconductivity to meet humanity's greatest challenges, News September 2013 archive, http://iopscience.iop.org/0953-2048/

Takabayashi, Y.; Mcdonald, M. T.; Papanikolaou, D.; Margadonna, S.; Wu, G.; Liu, R. H.; Chen, X. H.; Prassides, K.; Doping dependence of the pressure response of T_C in the $SmO_{1-x}F_xFeAs$ superconductors, *J. Am. Chem. Soc.* **2008**, *130*, 9242-9243.

Takahashi, H.; Igawa, K.; Arii, K.; Kamihara, Y.; Hirano, M.; Hosono, H.; Superconductivity at 43 K in an iron-based layered compound $LaO_{1-x}F_xFeAs$, *Nature* **2008**, *453*, 376-378.

Takeda, S.; Ueda, S.; Takano, S.; Yamamoto, A.; Naito, M.; Growth of superconducting SmFeAs(O,F) epitaxial films by F diffusion, *Supercond. Sci. Technol.***2012**, *25*, 035007 (6pp).

Tang, C. C.; Li, Y. X.; Du, J. G.; Wu, H.; Zhan, W. S.; Effects of rare-earth substitution in : mixed-valence and magnetic properties, *J. Phys.: Condens. Matter*, **1999**, *11*, 2027.

Tani, T.; Itahara, H.; Kadoura, H.; Asahi, R.; Crystallographic orientation analysis on calcium cobaltite ceramic grains textured by reactive-templated grain growth, *Int. J. Appl. Ceram. Technol.***2007**, *4*, 318-325.

Tarantini, C.; Gurevich, A.; Larbalestier, D. C.; Ren, Z. A.; Dong, X. L.; Lu, W.; Zhao, Z. X.; Superconductivity and antiferromagnetic ordering in the high-field paramagnetic oxypnictide $NdFeAsO_{0.94}F_{0.06}$, *Phys. Rev. B*, **2008**, *78*, 184501.

Timm, C.; Theory of Superconductivity, Dresden Institute of Theoretical Physics, Wintersemester 2011/2012

Tinkham, M.; Introduction to superconductivity (McGraw Hill, New York, 1975)

Togano, K.; Matsumoto, A.; Kumakura, H.; Large transport critical current densities of Ag sheathed $(Ba,K)Fe_2As_2$+Ag superconducting wires fabricated by an ex-situ powder-in-tube process, *Appl. Phys. Express* **2011**, *4*, 043101.

Tomsic, M.; Rindfleish, M.; Yue, J.; McFadden, K.; Phillips, J.; Sumption, M. D.; Bhatia, M.; Bohnenstiehl, S.; Collings, E. W.; Overview of MgB_2 superconductor applications, *Int. J. Appl. Ceram. Technol.* **2007**, *4*, 250-259.

Tropeano, M.; Fanciulli, C.; Canepa, F.; Cimberle, M. R.; Ferdeghini, C.; Lamura, G.; Martinelli, A.; Putti, M.; Vignolo, M.; Palenzona, A.; Effect of chemical pressure on spin density wave and superconductivity in undoped and 15% F-doped $La_{1-y}Y_yFeAsO$ compounds, *Phys. Rev. B* **2009**, *79*, 174523 (6pp).

Tsuei, C. C.; Kirtley, J. R.; Pairing symmetry in cuprate superconductors, *Rev. Mod. Phys.* **2000**, *72*, 969-1016.

Ueda, S.; Takeda, S.; Takano, S.; Yamamoto, A.; Naito, M.; High-T_C and high-J_C SmFeAs(O,F) films on fluoride substrates grown by molecular beam epitaxy, *Appl. Phys. Lett.* **2011**, *99*, 232505.

Van der Beek, C. J.; Rizza, G.; Konczykowski, M.; Fertey, P.; Monnet, I.; Klein, T.; Okazaki, R.; Ishikado, M.; Kito, H.; Iyo, A.; Eisaki, H.; Shamoto, S.; Tillman, M. E.; Bud'ko, S. L.; Canfield, P. C.; Shibauchi, T.; Matsuda, Y.; Flux pinning in $PrFeAsO_{0.9}$ and $NdFeAsO_{0.9}F_{0.1}$ superconducting crystals, *Phys. Rev. B* **2010**, *81*, 174517

Vinod, K.; Varghese, N.; Syamaprasad, U.; Superconductivity of MgB_2 in the BCS framework with emphasis on extrinsic effects on critical temperature, *Supercond. Sci. Technol.* **2007**, *20*, R31–R45.

Vinu, S.; Sarun, P. M.; Shabna, R.; Aswathy, P. M.; Anooja, J. B.; Syamaprasad, U.; Suppression of flux-creep in (Bi,Pb)-2212 superconductor by holmium doping, *Physica B* **2010**, *405*, 4355-4359.

Wang(a), C. L.; Gao, Z. S.; Qi, Y; Zhang, X.; Wang, D.; Ma, Y.; Structural and critical current properties in polycrystalline $SmFeAsO_{1-x}F_x$, *Supercond. Sci. Technol.* **2009**, *22*, 015019 (6pp).

Wang(a), C. L.; Qi, Y. P.; Wang, D. L.; Zhang, X. P.; Gao, Z. S.; Zhang, Z. Y.; Ma, Y. W.; Awaji, S.; Nishijima, G.; Watanabe, K.; Large transport critical currents of powder-in-tube $Sr_{0.6}K_{0.4}Fe_2As_2$/Ag superconducting wires and tapes, *Physica C* **2010**, *470*, 183-186.

Wang(a), C. L.; Yao, C.; Zhang, X. P.; Gao, Z. S.; Wang, D. L.; Wang, C. D.; Lin, H.; Ma, Y. W.; Awaji, S.; Watanabe, K.; Effect of starting materials on the superconducting properties of $SmFeAsO_{1-x}F_x$ tapes, *Supercond. Sci. Technol.* **2012**, *25*, 035013.

Wang(a), C. L.; Yao,C.; Lin, H.; Zhang, X. ; Zhang, Q.; Wang, D.; Ma,Y.; Awaji, S.; Watanabe, K.; Tsuchiya, Y.; Sun, Y.; Tamegai, T.; Large transport J_C in Sn-added $SmFeAsO_{1-x}F_x$ tapes prepared by an ex situ PIT method, *Supercond. Sci. Technol.***2013**, *26*, 075017.

Wang(b), C.; Jiang, S.; Tao, Q.; Ren, Z.; Li, Y.; Li, L.; Feng, C.; Dai, J.; Cao, G.; Xu, Z.; Superconductivity in $LaFeAs_{1-x}P_xO$: Effect of chemical pressures and bond covalency, *Europhys. Lett.* **2009a**, *86*, 47002.

Wang(b), C.; Li, L.; Chi, S.; Zhu, Z.; Ren, Z.; Li, Y.; Wang, Y.; Lin, X.; Luo, Y.; Jiang, S.; Xu, X.; Cao, G.; Xu, Z.; Thorium-doping–induced superconductivity up to 56 K in $Gd_{1-x}Th_xFeAsO$, *Europhys. Lett.* **2008**, *83*, 67006.

Wang(b), C.; Li, Y. K., Zhu, Z. W.; Jiang, S.; Lin, X.; Luo, Y. K.; Chi, S.; Li, L. J.; Ren, Z.; He, M.; Chen, H.; Wang, Y. T.; Tao, Q.; Cao, G. H.; Xu, Z. A.; Effects of cobalt doping and phase diagrams of $LFe_{1-x}Co_xAsO$ (L=La and Sm), *Phys. Rev. B* **2009b**, *79*, 054521.

Wang(c), X.; Ghorbani, S. R.; Peleckis, G.; Dou, S.; Very high critical field and superior J_C-field performance in $NdFeAsO_{0.82}F_{0.18}$ with T_C of 51 K, *Adv. Mater.* **2009**, *21*, 236-239.

Wang(d), L.; Qi, Y; Wang,D.; Gao, Z.; Zhang, X.;Zhang, Z.; Wang, C.; Ma, Y.; Low-temperature synthesis of $SmFeAsO_{0.7}F_{0.3-\delta}$ wires with a high transport critical current density, *Supercond. Sci. Technol.* **2010**, *23*, 075005 (4pp)

Wei, B.; Physics picture from neutron scattering study on Fe-based superconductors, *Chin. Phys. B* **2013**, 22, 087405.

Wei, Z.; Li, W.; Hong, L.; Lv, Z. M.; Wu, H. Y.; Guo, X. F.; Ruan, K. Q.; Superconductivity at 57.3 K in La-doped iron-based layered compound $Sm_{0.95}La_{0.05}O_{0.85}F_{0.15}FeAs$, *J. Supercond. Novel Magn.* **2008**, *21*, 213-215.

Weiss, J. D.; Tarantini, C.; Jiang, J.; Kametani, F.; Polyanskii, A. A.; Larbalestier, D. C.; Hellstrom, E. E.; High intergrain critical current density in fine-grain $(Ba_{0.6}K_{0.4})Fe_2As_2$ wires and bulks, *Nature Mater.* **2012**, *11*, 682-685.

Welp, U.; Mu, G.; Xie, R.; Koshelev, A. E.; Kwok, W. K.; Luo, H. Q.; Wang, Z. S.; Cheng, P.; Fang, L.; Ren, C.; Wen, H. H.; Specific heat and phase diagrams of single crystal iron pnictide superconductors, *Physica C* **2009**, *469*, 575-581.

Welp, U.; Xie, R.; Koshelev, A. E.; Kwok, W. K.; Cheng, P.; Fang, L.; Wen, H. H.; Calorimetric determination of the upper critical fields and anisotropy of $NdFeAsO_{1-x}F_x$ single crystals, *Phys. Rev. B* **2008**, *78*, 140510R.

Wen, H. H.; Mu, G.; Fang, L.; Yang, H.; Zhu, X.; Superconductivity at 25 K in hole-doped $(La_{1-x}Sr_x)OFeAs$, *Europhys. Lett.***2008**, 82, 17009.

Werthamer, N. R.; Helfand, E.; Hohenberg, P. C.; Temperature and purity dependence of the superconducting critical field, H_{C2}. III. Electron spin and spin-orbit effects, *Phys. Rev.* 1966, 147, 295-302.

Williamson, G. K.; Hall, W. H.; X-ray line broadening from filed aluminium and wolfram, *Acta Metall.* **1953**, *1*, 22-31.

Wu(a), M. K.; Ashurn, J. R.; Torng, C. J.; Hor, P. H.; Meng, R. L.; Gac, L.; Huang, Z. J.; Wang, Y. Q.; Chu, C. W.; Superconductivity at 93 K in a new mixed-phase Y-Ba-Cu-O compound system at ambient pressure, *Phys. Rev. Lett.* **1987**, *58*, 908-910.

Wu(b), C. C.; Chaudhury, R. P.; Chen, F.; Gooch, M.; Guloy, A.; Lorenz, B.; Bing L.; Sasmal, K.; Tang, Z.; Wang, L.; Xue, Y.Y.; Superconductivity in R(O,F)FeAs, AFe_2As_2, $(A,A')Fe_2As_2$, AFeAs and LaNFeAs, where R = Rare Earth, A = Alkaline, and A = Alkaline Earth, *J. Phys. Soc. Japan* **2008**, *77*, 72.

Yamamoto, A.; Jiang, J.; Kametani, F.;Polyanskii, A.; Hellstrom, E.; Larbalestier, D.; Martinelli, A.; Palenzona, A.; Tropeano, M.; Putti, M.; Evidence for electromagnetic granularity in polycrystalline Sm1111 iron-pnictides with enhanced phase purity, *Supercond. Sci. Technol.***2011**, *24*, 045010 (7pp).

Yamamoto, A.; Polyanskii, A. A.; Jiang, J.; Kametani, F.; Tarantini, C.; Hunte, F.; Jaroszynski, J.; Hellstrom, E. E.; Lee, P. J.; Gurevich, A.; Larbalestier, D. C.; Ren, Z. A.; Yang, J.; Dong, X. L.; Lu, W.; Zhao, Z. X.; Evidence for two distinct scales of current flow in polycrystalline Sm and Nd iron oxypnictides, *Supercond. Sci. Technol.***2008**, *21*, 095008

Yan, J. Q.; Jensen, B.; Dennis, K. W.; McCallum, R. W.; Lograsso, T. A.; Flux requirements for the growth of RFeAsO (R=rare earth) superconductors, *Appl. Phys. Lett.* **2011**, *98*, 072504.

Yang(a), J. L.; Ren, W. J.; Li, D.; Hu, W. J.; Li, B.; Zhang, Z. D.; Superconductivity modulated by internal pressure in $Ce_{1-x}Gd_xFeAsO_{0.84}F_{0.16}$ compounds, *Supercond. Sci. Technol.* **2010**, *23*, 025003.

Yang(b), J.; Li, Z. C.; Lu, W.; Yi, W.; Shen, X. L.; Ren, Z. A.; Che, G. C.; Dong, X. L.; Sun, L. L.; Zhou, F.; Zhao, Z. X.; Superconductivity at 53.5 K in $GdFeAsO_{1-\delta}$, *Supercond. Sci. Technol.* **2008a**, *21*, 082001.

Yang(b), J.; Ren, Z. A; Che, G. C.; Lu, W.; Shen, X. L.; Li, Z. C.; Yi, W.; Dong, X. L.; Sun, L. L.; Zhou, F.; Zhao, Z. X.; The role of F-doping and oxygen vacancies on the superconductivity in SmFeAsO compounds, *Supercond. Sci. Technol.* **2009**, *22*, 025004.

Yang(b), J.; Shen, X. L.; Lu, W.; Yi, W.; Li, Z. C.; Ren, Z. A.; Che, G. C.; Dong, X. L.; Sun, L. L.; Zhou, F.; Zhao, Z. X.; Superconductivity in some heavy rare-earth iron arsenide $REFeAsO_{1-\delta}$ (RE = Ho, Y, Dy and Tb) compounds, *New J. Phys.* **2008b**, *11*, 025005.

Yeshurun, Y.; Malozemoff, A. P.; Shaulov, A.; Magnetic relaxation in high-temperature superconductors, *Rev. Mod. Phys.* **1996**, *68*, 911–949.

Yildirim, T.; Origin of the 150-K Anomaly in LaFeAsO: competing antiferromagnetic interactions, frustration, and a structural phase transition, *Phys. Rev. Lett.* **2008**, *101*, 057010.

Yu,V.; Kopaev; Belyavsky, V. I.; Kapaev, V. V.; *Physics -Uspekhi* **2008**, *51*, 191.

Yuan, H. Q.; Singleton, J.; Balakirev, F. F.; Baily, S. A.; Chen, G. F.; Luo, J. L.; Wang, N. L.; Nearly isotropic superconductivity in $(Ba,K)Fe_2As_2$, *Nature* **2009**, *457*, 565-568.

Zhang(a), L.; Leng, X.; Ding, S. Y.; Zhu, X. B.; Sun, Y. P.; AC susceptibility in an inhomogeneous superconductor, *Supercond. Sci. Technol.* **2010**, *23*, 065020 (6pp).

Zhang(b), X. P.; Wang, L.; Qi, Y. P.; Wang, D. L.; Gao, Z. S.; Zhang, Z. Y.; Ma, Y. W.; Effect of sheath materials on the microstructure and superconducting properties of $SmO_{0.7}F_{0.3}FeAs$ wires, *Physica C* **2010**, *470*, 104-108.

Zhao(a), J.; Huang, Q.; de la Cruz, C.; Lynn, J. W.; Lumsden, M. D.; Ren, Z. A.; Yang, J.; Shen, X. L.; Dong, X. L.; Zhao, Z. X.; Dai, P. C.; Lattice and magnetic structures of PrFeAsO, $PrFeAsO_{0.85}F_{0.15}$, and $PrFeAsO_{0.85}$, *Phys. Rev. B* **2008a**, *78*, 132504.

Zhao(a), J.; Huang, Q.; de la Cruz, C.; Li, S. L.; Lynn, J. W.; Chen, Y.; Green, M. A.; Chen, G. F.; Li, G.; Li, Z.; Luo, J. L.; Wang, N. L.; Dai, P. C.; Structural and magnetic phase diagram of $CeFeAsO_{1-x}F_x$ and its relation to high-temperature superconductivity, *Nature Mater.* **2008b**, *7*, 953–959.

Zhao(b), L. D.; Berardana, D.; Dragoea, N.; Electrical transport properties of F-doped LaFeAsO oxypnictide, *J. Alloys Compd.* **2010,** *508*, 606-609.